UNIVERSITY OF SOUTHAMPTON

Active vibration control using a nonlinear inertial actuator

by

Mattia Dal Borgo

Thesis for the degree of Doctor of Philosophy

Faculty of Engineering and Physical Sciences
Institute of Sound and Vibration Research

February 2019

UNIVERSITY OF SOUTHAMPTON

ABSTRACT

FACULTY OF ENGINEERING AND PHYSICAL SCIENCES
INSTITUTE OF SOUND AND VIBRATION RESEARCH

Doctor of Philosophy

Active vibration control using a nonlinear inertial actuator

by Mattia Dal Borgo

This thesis presents a theoretical and experimental study of a stroke limited inertial actuator used in active vibration control. The active control system under investigation consists of an inertial actuator attached to a lightweight flexible structure, a collocated vibration sensor and a velocity feedback controller (VFC). Since the control force is generated by accelerating the proof mass, controlling low frequency motions or large amplitude vibrations requires a very long stroke for the proof mass. One of the main limitations of inertial actuators is that the stroke length is finite, however. This not only limits the amount of force available from the actuator but also when the proof mass hits the end-stops it causes impulse-like excitations that are transmitted to the structure and may result in damage. Additionally, the shocks produced by the impacts between the proof mass and the end-stops are in phase with the velocity of the structure, leading to a reduction of the overall damping of the system, which can give rise to instability of the system and limit cycle oscillations.

This research examines the implementation of a nonlinear feedback controller to avoid collisions of the proof mass with the actuator's end-stops, thus preventing this instability.

The nonlinear model of a stroke limited inertial actuator is first identified using base and direct excitation experiments and a parameter estimation process. A nonlinear feedback control (NLFC) strategy is then presented, which actively increases the internal damping of the actuator when the proof mass approaches the end-stops. The experimental implementation of the NLFC is investigated for the control of a cantilever beam, and it is shown that the robustness of the VFC system to external perturbations is much improved with the NLFC. Finally, a virtual sensing approach based on an extended Kalman filter algorithm is discussed for the real-time estimation of the states of the proof mass that is used to calculate the feedback signal of the NLFC. It is shown experimentally that larger velocity feedback gains can be used without the system becoming unstable when the NLFC is adopted and the theoretical reasons for this increase in stability margin are explored.

Contents

List of Figures

List of Tables

Declaration of Authorship

I, Mattia DAL BORGO, declare that the thesis entitled *Active vibration control using a nonlinear inertial actuator* and the work presented in the thesis are both my own, and have been generated by me as the result of my own original research. I confirm that:

- this work was done wholly or mainly while in candidature for a research degree at this University;
- where any part of this thesis has previously been submitted for a degree or any other qualification at this University or any other institution, this has been clearly stated;
- where I have consulted the published work of others, this is always clearly attributed;
- where I have quoted from the work of others, the source is always given. With the exception of such quotations, this thesis is entirely my own work;
- I have acknowledged all main sources of help;
- where the thesis is based on work done by myself jointly with others, I have made clear exactly what was done by others and what I have contributed myself;
- parts of this work have been published as:
  - M. Dal Borgo, M. Ghandchi Tehrani, and S. J. Elliott, "Dynamic analysis of nonlinear behaviour in inertial actuators," *in 12th International Conference on Recent Advances in Structural Dynamics (RASD 2016)*; 04 - 06 July 2016, Southampton, UK; Journal of Physics Conference Series, 2016,744:012027.
  - M. Dal Borgo, M. Ghandchi Tehrani, and S. J. Elliott, "Dynamic analysis of two nonlinear inertial actuators in active vibration control," *in 27th International Conference on Noise and Vibration Engineering (ISMA2016)*; 19 - 21 September 2016, Leuven, Belgium; pp. 1179-1193.
  - M. Dal Borgo, M. Ghandchi Tehrani, and S. J. Elliott, "Nonlinear control and stability analysis of a stroke limited inertial actuator in velocity feedback," *in 9th European Nonlinear Dynamics Conference (ENOC2017)*; 25 - 30 June 2017, Budapest, Hungary; pp. 1-10.
  - M. Dal Borgo, M. Ghandchi Tehrani, and S. J. Elliott, "Active nonlinear control of a stroke limited inertial actuator," *in International Conference on Engineering Vibration (ICoEV2017)*; 4 - 7 September 2017, Sofia, Bulgaria.

– M. Dal Borgo, M. Ghandchi Tehrani, and S. J. Elliott, "Experimental implementation of a nonlinear feedback controller for a stroke limited inertial actuator," *in 36th International Modal Analysis Conference (IMAC-XXXVI)*; 12 - 15 February 2018, Orlando, FL, USA; Structural Health Monitoring, Photogrammetry & DIC, 2019, vol. 6, pp. 163-177, Springer.

– M. Dal Borgo, G. Lapiccirella, J. Rohlfing, M. Ghandchi Tehrani, and S. J. Elliott, "Experimental identification of mechanical nonlinearities in a proof mass actuator," *in 25th International Congress on Sound and Vibration (ICSV25)*; 8 - 12 July 2018, Hiroshima, Japan; pp. 1-8.

– M. Dal Borgo, M. Ghandchi Tehrani, and S. J. Elliott, "Nonlinear feedback control of a stroke limited inertial actuator using a state estimation approach," *in 28th International Conference on Noise and Vibration Engineering (ISMA2018)*; 17 - 19 September 2018, Leuven, Belgium; pp. 341-354.

– M. Dal Borgo, M. Ghandchi Tehrani, and S. J. Elliott, "Identification and analysis of nonlinear dynamics of inertial actuators," *Mechanical Systems and Signal Processing*, 2019, vol. 115, pp. 338-360.

– M. Dal Borgo, M. Ghandchi Tehrani, and S. J. Elliott, "Active vibration control with a stroke limited inertial actuator using a nonlinear feedback law: theory and experiment," *Journal of Sound and Vibration*, (in preparation).

Signed: _____ Date: _____

Mattia DAL BORGO

Acknowledgements

I have always been a man of few words, but during the last three years I have benefited greatly from the help of a lot of people who deserve more than a "thank you all". I will try to express my gratitude to them here.

First of all I would like to thank Prof. Paolo Gardonio. Without his encouragement to join the Marie-Curie ITN program and the ISVR, I would have missed out on this extraordinary opportunity. Since the beginning of my studies at the University of Udine, he has spent huge amount of time in transferring to me his sound knowledge about mechanical vibrations and system's theory, with great passion. I will always remember his advice that any of my goals can be achieved with the correct mindset and strong commitment. I thank him unreservedly.

I gratefully acknowledge my supervisors Dr. Maryam Ghandchi Tehrani and Prof. Steve Elliott who have given me the opportunity to work with them during these years. Their motivation, guidance and support have helped shape the research and, most of all, build my technical background.

I would like to thank my internal reviewers Dr. Jordan Cheer, Dr. Neil Ferguson and Dr. Emiliano Rustighi for their extremely valuable comments, questions and suggestions during the regular review meetings. Also, most of the laboratory experiments were carried out using equipment borrowed from Dr. Jordan Cheer. Special thanks also to Dr. Michele Zilletti who helped me in many ways during the first stages of my PhD. I am also grateful to the staff and students of the Signal Processing and Control Group for the interesting discussions and meetings.

Thanks to Mr. Lawrence Miles of the ISVR electrical workshop and to Miss Harriet Gemmell of the administrative office who have always fulfilled my last minute requests.

A big thank goes to the European Commission for funding the Marie-Curie ITN FP7 ANTARES project (GA 606817), which shaped me both professionally and personally. I would like to extend my gratitude to the entire "ANTARES family" and in particular to the project coordinator Dr. Bert Pluymers. I feel enormously fortunate to have been given this opportunity.

The work presented in appendix A was carried out during a secondment at the Adaptronik department of the Fraunhofer LBF in Darmstadt (Germany), which is gratefully acknowledged. I am also grateful to Dr. Jens Rohlfing, Mr. Jonathan Millitzer and Mr. Giovanni Lapiccirella for their valuable support, supervision and collaboration during my research at Fraunhofer LBF.

Some of the results presented in chapters 3 and 4 were obtained using the NI2D software developed by the Space Structures and System Laboratory group (S3L) of the University

of Liège (Belgium), which is gratefully acknowledged. In particular, I would like to thank Prof. Gaëtan Kerschen, Dr. Jean-Philippe Noël and Dr. Thibaut Detroux for their course on nonlinearity in structural dynamics that has been a turnaround for my understanding of this topic.

A special thank you to my former colleagues at Deca Design and in particular to Mr. Deni De Cesero. His professional expertise as well as his unconditional support and constant strive for improvement will always be imprinted in my mind. It has been a privilege working under his guidance.

An enormous thank goes to my colleague and friend Mr. Stefano Camperi from whom I have learnt a lot both on professional and personal level. Our discussions in the coffee room and his advices have always been extremely helpful.

I would also like to thank my parents, Antonia and Gianni, and my brother Moreno, who have always supported me regardless of my decisions.

Thank you to my friends from home for their understanding that I cannot meet them every weekend as it used to be.

Above all, my deepest gratitude goes to Miss Stefania Del Fabbro for her love and unconditional support. The happiness and joy she spreads around her have always motivated and inspired me.

Nomenclature

Abbreviation	**Full-form**
ADC	Analogue-to-Digital Conversion
ADD	Active Damping Device
Back-emf	Back-Electromotive Force
B&K	Brüel & Kjær
DAC	Digital-to-Analogue Conversion
DoF	Degree of Freedom
DVF	Direct Velocity Feedback
FFT	Fast Fourier Transform
FRF	Frequency Response Function
HBM	Harmonic Balance Method
IA	Inertial Actuator
ICP®	Integrated Circuit Piezoelectric
ISVR	Institute of Sound and Vibration Research
MDoF	Multi Degree of Freedom
MIMO	Multi-Input Multi-Output
NFRC	Nonlinear Frequency Response Curve
NLFC	Nonlinear Feedback Controller
ODE	Ordinary Differential Equation
PBH	Popov-Belevitch-Hautus
PC	Personal Computer
PPC	POWER Performance Computing
PSD	Power Spectral Density
RFC	Relative Feedback Control
SDoF	Single Degree of Freedom
SISO	Single-Input Single-Output
TF	Transfer Function
THD	Total Harmonic Distortion
VFC	Velocity Feedback Controller

Symbol	Description	Unit
Latin letters		
b	Width of the beam, Fourier coefficient, parameter	$[m]$, [various], $[-]$
c	Damping coefficient	$[N s\, m^{-1}]$
e	Voltage, Napier's constant (2.71828...), error	$[V]$, $[-]$, [various]
f	Force, frequency	$[N]$, $[Hz]$
g	Fourier coefficient, gain	[various], $[-]$
h	Control gain, thickness of the beam	$[-]$, $[m]$
i	Current	$[A]$
j	Imaginary unit $\sqrt{-1}$	$[-]$
k	Stiffness	$[N\, m^{-1}]$
l	Length of the actuator's coil	$[m]$
m	Mass	$[kg]$
n	Nonlinear feedback gain	$[-]$
p	Parameter, exponent	$[-]$, $[-]$
q	Electrical charge	$[C]$
s	Laplace complex variable	$[-]$
t	Time	$[s]$
u	Input	[various]
v	Velocity, measurement noise	$[m\, s^{-1}]$, $[-]$
x	x-coordinate	$[m]$
y	y-coordinate, output	$[m]$, [various]
$\mathbf{y}$	Vector of states	
z	z-coordinate, complex variable for digital systems	$[m]$, $[-]$
A	System's matrix	$[-]$
B	Magnetic flux, input matrix	$[T]$, $[-]$
C	Output matrix	$[-]$
D	Feed-through term	$[-]$
E	Young modulus, electric field	$[Pa]$, $[N/C]$
$\mathbf{H}$	Matrix of control gains	$[-]$
K	Kalman gain	$[-]$
KE	Kinetic energy	$[J]$
L	Length of the beam, electrical inductance, open-loop TF	$[m]$, $[H]$, $[-]$
$\mathbf{I}$	Identity matrix	$[-]$
N	Number of modes considered, nonlinear function	$[-]$, [various]
Ob	Observability	$[-]$
$\mathcal{OR}$	Operating region	$[-]$
P	Disturbance amplitude	$[N]$
R	Electrical resistance	$[\Omega]$
T	Transmissibility, closed-loop	$[N\, A^{-1}]$, $[-]$

W	Process noise	$[-]$
Y	Mobility	$[m\,s^{-1}N^{-1}]$
Z	Impedance	$[Ns\,m^{-1}]$

Greek letters

ζ	Damping ratio	$[-]$
η	Loss factor, nonlinear gain	$[-]$, $[-]$
κ	Nonlinear stiffness	[various]
π	Ludolf's number	$[-]$
ρ	Mass density	$[kg\,m^{-3}]$
ϕ	Mode shapes, force factor	$[-]$, $[N/A]$
μ	Pre-warping coefficient	$[-]$
ψ	Wavelet, nonlinear feedback law	[-], $[V/V]$
ω	Angular frequency	$[rad\,s^{-1}]$
$\mathbf{\Omega}$	Matrix of modal resonant terms	$[-]$

Subscripts

0	Initial or boundary conditions
a	Referred to an inertial actuator, amplifier
acc	Accelerometer
b	Blocked, base
c	Control point, actuator casing (end-stops), crossing frequency
d	Displacement, digital
e	Electrical
$gauge$	Force gauge
L	Lossy-inductor
m	Mechanical, margin
o	Open-circuit
max	Maximum
min	Minimum
NL	Nonlinear
p	Primary point, proof mass
r	Relative
res	Resonance
RF	Restoring Force
s	Referred to a structure, shunted, saturation cut-off, sampling
sat	Saturation

Mathematical

x, X	Real or complex value x,X
$\Re\{X\}$	Real part of X

$\Im\{X\}$	Imaginary part of X
X^*	Complex conjugate of X
X^n	X to the power of n
$\exp(X)$	e to the power of X
$\text{sgn}(X)$	Sign of X
$\dot{X}$	Derivative of X in respect to time
X'	Spatial derivative of X
$\hat{X}$	Estimate of X
$\bar{X}$	Linearisation of X
d	Differential operator
$\mathbf{x}$	Vector x
$\mathbf{X}$	Matrix X
$\mathbf{X}^{-1}$	Inverse of matrix X
$\mathbf{X}^T$	Transpose of matrix X
$\mathbf{X}^H$	Hermitian (conjugate) transpose of matrix X
$\mathbf{E}[X]$	Expected value of X

Chapter 1

Introduction

1.1 Motivation

Active vibration control plays a vital role in the attenuation of unwanted vibrations in lightweight and flexible structures, as recognised by extensive research [1–8]. Velocity feedback controllers (VFCs) are a notable example of active solution that can increase the effective damping of a structure, reducing its level of resonant vibration [6].

A VFC typically consists of an electromagnetic inertial, or proof mass, actuator attached to a structure, a collocated vibration sensor and a controller, which feeds back the velocity of the structure to the actuator. The aim of the inertial actuator is to apply a control force to the structure proportional to its velocity for the purpose of vibration reduction. The operating principle of an inertial actuator is that an input current to the actuator generates a control force on the structure by means of an electromagnetic transducer, reacting against a proof mass, which starts to accelerate [8].

The internal dynamics of the inertial actuator is known to affect the stability and performance of the VFC, which then becomes only conditionally stable [9], so that there exists a maximum velocity feedback gain, above which the control system becomes unstable [10]. Previous research has established that higher feedback gains can be used if the inertial actuator has a low natural frequency and a well damped resonance [10].

On the other hand, this solution increases the proof mass static displacement and its response to low frequency excitations. In practical applications, however, the displacement that the proof mass can reach is limited by the stroke length between the end-stops of the actuator [11]. For very low frequency motions or high input currents, the proof mass can saturate in stroke as it hits the end-stops imparting large shocks to the structure, which may be damaged. Moreover, it has been observed both theoretically and experimentally that this nonlinear dynamic behaviour is also undesirable in terms of the stability of the closed-loop control system, because it can reduce the stability margin

of the velocity feedback loop, and in fact, enhance the level of vibration [12; 13]. The instability is due to the forces imparted during the collisions between the proof mass and end-stops being in-phase with the velocity of the structure, hence reducing the overall damping of the system. Over-designing the actuator may not be possible in practice [11] and allowing for a very large stroke may negate the weight benefits introduced by these active devices.

This motivates an investigation into the causes and the effects of stroke saturation, and the development of a control strategy that can contrast the instability by increasing the range of stable control gains.

In this thesis, the sources of mechanical and electromechanical nonlinearities in inertial actuators are investigated, where particular focus is given to stroke saturation. A methodology that allows the experimental characterisation and identification of the nonlinearity is derived. This permits one to build accurate nonlinear models that are useful to predict the dynamic behaviour of nonlinear inertial actuators and the stability margins of VFCs.

A novel nonlinear feedback control strategy is then proposed and investigated with the aim to prevent the collisions of the proof mass with the actuator end-stops. The nonlinear control strategy acts as a second feedback loop alongside the VFC and actively increases the internal damping of the actuator only when the proof mass gets closer to the end-stops.

The implementation of the control law requires real-time knowledge of the velocity and displacement of the proof mass, which often cannot be measured directly with a physical sensor, because the installation of an additional sensor would add mass and cost and take out space from the actuator. Thus, a virtual sensing approach is investigated, in which the states of the proof mass are estimated from the measurements of the other sensors and input signals making use of the identified nonlinear model of the inertial actuator. It is shown that the nonlinear feedback controller is able to increase the safe operating region of stroke limited inertial actuators. Hence, larger feedback gains can be used without the system becoming unstable if this nonlinear controller is used.

1.2 Aim and objectives

This thesis sets out a theoretical and experimental study on the active vibration control of a structure using a stroke limited inertial actuator. The aim of this research is to examine the implementation of a nonlinear control strategy to prevent stroke saturation of inertial actuators from occurring, thus enhancing their stability when used with VFCs.

The main objectives of the thesis can be summarised as follows:

1. Experimental characterisation and identification of nonlinearities of inertial actuators and numerical analysis comparing the identified nonlinear model with the underlying linear one;

2. Stability analysis of a single degree of freedom (SDoF) structure controlled by a nonlinear actuator in velocity feedback;

3. Investigation of a novel feedback control strategy to enhance the stability of VFCs using stroke limited inertial actuators;

4. Experimental implementation of the controller developed at the previous point on a structure controlled by a stroke limited actuator and comparing its stability with the direct velocity feedback controller;

5. Development of a state observer for the states of the system that cannot be measured directly.

1.3 Structure of the thesis

This thesis is organised in eight chapters:

Chapter 1 provides an introduction on the motivations for active vibration control. The aim and objectives together with the structure of this thesis are summarised and the original contributions are highlighted.

Chapter 2 briefly reviews the relevant literature on active vibration control, nonlinear structural dynamics, applied nonlinear control and electromagnetic proof mass actuators. Some among the many applications of inertial actuators are presented. Moreover, the nonlinearities that affect these devices are explained, in particular previous work on stroke saturation is discussed.

Chapter 3 investigates the nonlinear behaviour of inertial actuators and provides a methodology for identifying the nonlinearity. The experimental set-ups are described and the actuator's underlying linear parameters are identified using small excitation signals. The nonlinear dynamics is then explored using large excitation signals for the detection, characterisation and identification of the nonlinear parameters.

Chapter 4 presents a theoretical analysis comparing the nonlinear model of the inertial actuator identified in chapter 3 with its underlying linear model, both in time and frequency domains.

Chapter 5 derives the mathematical model of the system constituted by a nonlinear inertial actuator attached to a SDoF structure controlled using a velocity feedback loop. A theoretical investigation on the stability of the control loop is carried out comparing

the nonlinear actuator model with the underlying linear one. A nonlinear feedback control law is presented and analysed under different excitation conditions, whose aim is to prevent the instability of the system caused by stroke saturation and increase its operating region.

Chapter 6 describes the experimental study conducted on a cantilever beam controlled by a stroke limited inertial actuator in direct velocity feedback and excited by an instrumented hammer. The nonlinear feedback controller developed in chapter 5 is then introduced as a second loop in the control strategy and the stability of the system is assessed comparing the cases when the nonlinear controller is implemented or not under different excitation conditions.

Chapter 7 introduces the use of a state estimation algorithm for calculating the proof mass state required by the nonlinear controller implemented in chapter 6. Two different approaches are investigated. The first one uses the underlying linear model of the actuator to calculate the coefficients of a digital filter to be applied to the input signals of the actuator. The second approach considers an extended Kalman filter algorithm and the nonlinear model of the actuator to predict and update the state estimation.

Conclusions and indications of future work are summarised in chapter 8.

1.4 Contributions

The original contributions of the thesis are:

- An experimental methodology applicable to several inertial actuators for the identification of their mechanical nonlinearities using the restoring force and the back-electromotive force (back-emf) signals;
- A theoretical analysis of a novel nonlinear control law that aims to increase the safe operating range of inertial actuators by preventing their instability caused by stroke saturation;
- An experimental implementation of the nonlinear feedback controller on a stroke limited inertial actuator attached to a cantilever beam and the investigation of a virtual sensing strategy for the proof mass state estimation.

Some of this work has been published in refereed journals and conference proceedings and the references of these papers can be found in the Declaration of Authorship.

Chapter 2

Technical background

Vibration is commonly perceived as being an undesirable phenomenon. It can have unpleasant and even hazardous effects on health if applied to the human body. Hand-arm vibration and travel sickness are just two among many of them. Vibrating surfaces are noise sources over the audio-frequency band from 20 Hz to 20 kHz and noise can cause disturbing or undesirable effects to those who are exposed to it. Vibration can also be dangerous for the structural integrity of a large variety of mechanical systems. For example, fatigue damage of aircraft or harsh responses during lift-off of rocket launchers to on-board components can pose a limit to the operation of these structures. Thus, it is vital to develop methods for vibration control [1]. This chapter aims to present some of the literature that formed the technical background that motivated this research. A brief introduction to the field of active vibration control is given in section 2.1. Active vibration control relies on actuators to provide the control forces on the hosting structure. This thesis focuses on electromagnetic inertial actuators and an overview of their operating principle, areas of applications and nonlinear dynamic behaviour is presented in section 2.2. The major concern of this study is about the implications of harsh nonlinearities affecting inertial actuators, such as stroke saturation. An actuator that saturates in stroke not only is liable to damage, but also it may destabilise the active vibration control system. Hence, it is crucial to underpin the nonlinear dynamic behaviour of a stroke saturating inertial actuator and to develop a control strategy that prevents it from happening. An introduction to nonlinear structural dynamics is presented in section 2.3, which has been used for the characterisation and identification of the actuator nonlinearities. Applied nonlinear control is discussed in section 2.4, where several control strategies of nonlinear systems are compared. Some of these control strategies require the knowledge of some states of the system that, however, may not be possible to measure directly. Hence, an overview of virtual sensing techniques for the estimation of the states using remote sensors and the identified model of the system is presented in section 2.5.

2.1 Active vibration control

Nowadays, research and engineering development are moving onto smart mechatronic structures, which are lightweight, flexible and are required to perform multiple tasks such as reducing unwanted vibrations and structural health monitoring [7]. The characteristics of these structures, such as low weight and high flexibility, lead them to operate in an environment where their dynamic behaviour cannot be neglected [7]. As a result, these structures are susceptible to large amplitude vibrations that need to be controlled.

The use of passive treatments can be thought as a redesign process of changing either the mass, the damping, or the stiffness on an existing structure. Passive control is undoubtedly an efficient way to control the response of a structure, however, the constraints on the structure parameters are often such that the modification cannot be made. For example, passive treatments to control low frequency vibrations would typically add significant amount of mass to the structure, while the constraints might be low weight and flexibility [14]. Also, damping is a difficult parameter to adjust during the design process, especially if the structure is large and is made by a number of links and joints.

An alternative is found in active control, which applies dynamic forces to the structure to minimise its response. Active control gives more versatility than passive control in terms of shaping the desired response using a rule, namely control law, that can be different than a mere structural modification [3; 5]. The main differences between active and passive control are the use of an external energy source and the use of adjustable devices, namely actuators, to curb the vibration of a structure [5].

Active control of vibration has seen large interest and many industrial applications over the past decades [4]. Some typical applications include the reduction of low frequency vibration of space structures by use of lightweight vibration actuators, and the reduction of sway in tall buildings to contrast the oscillation induced by the wind [14]. Active control is found to be more effective at low frequencies compared to passive treatments [6], however, it can operate only over a limited frequency band, called bandwidth of the control system [8]. This is due to existing delays in the mechanical system or in the control path that lead to an increasing phase shift of the open-loop frequency response at higher frequencies [3]. In this case, the disturbance can even be amplified by the controller.

In general, an active vibration control system consists of a sensor, an electronic controller and an actuator. The sensor is used to detect the vibration of the structure due to the primary disturbance, the electronic controller manipulates the sensor signal with a predefined control law sending the modified signal to the actuator, which applies the control (also called secondary) force to the structure. There are two main families of control architecture, they are called feed-forward and feedback control and are shown in figure 2.1.

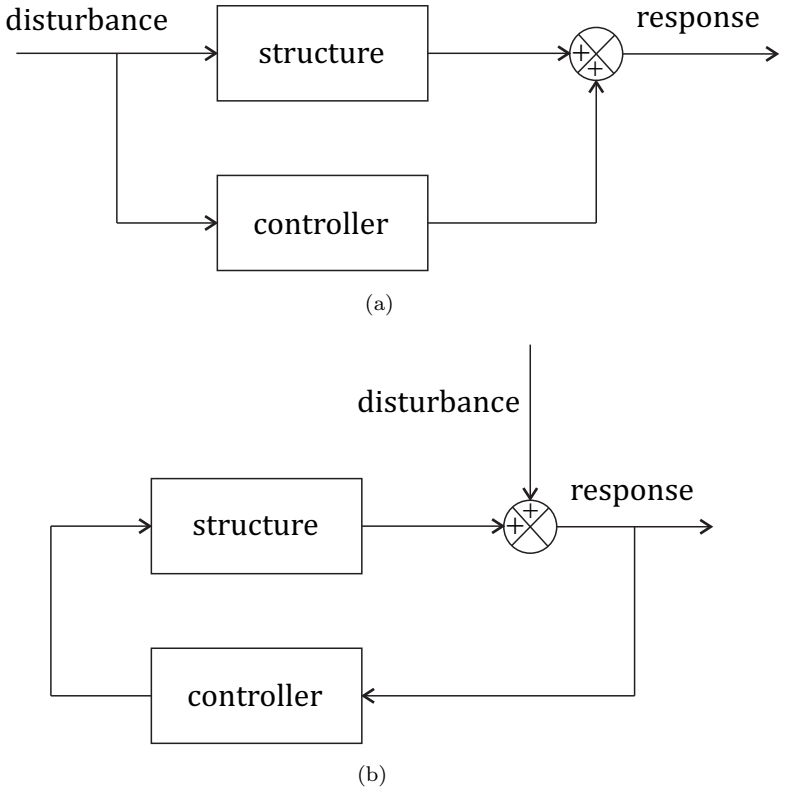

FIGURE 2.1: (a) General block diagram of active feed-forward control of vibration; (b) General block diagram of active feedback control of vibration.

The two differ for the direct availability of the primary disturbance signal. In fact, feedback controllers are not provided with reference sensors to get advance information about the disturbance being controlled. Feed-forward controllers instead, rely on the information about the primary excitation. The knowledge of the excitation can be obtained if either the disturbance is deterministic (future behaviour fully predicted by past behaviour) or a detection sensor can be used that measures the primary disturbance and is not affected by the secondary force. Hence, the success of feed-forward control depends on a delicate matching between the effects of the primary disturbance and the control input. On the other hand, feedback controllers use a sensor that measures the response of the system. Such measured signal is affected by both primary disturbance and secondary input, and it is fed back to the actuator [2–4; 8]. Feedback control is popular in the area of structural vibration because of its significant vibration attenuation performance without having to measure in advance a reference signal, for example when reducing the resonant response of an impulsively excited structure [14]. However, feed-forward control is usually to be preferred whenever an advance reference signal is available, because of its inherent stability characteristics and almost always superior performance [14].

Active vibration controllers can be divided into centralised, decentralised or distributed

and these have been widely compared by several researchers [15–17]. A centralised controller receives all sensor inputs and generates all controller output signals to drive the actuators, however, for a large number of sensors and actuators this strategy becomes computationally inefficient and heavy [14]. A decentralised controller, instead, is characterised by a set of individual controllers each of them operating on an input and output pair. This control configuration can show limited performance and stability issues if neighbouring controllers are significantly coupled [14]. The choice between centralised or decentralised depends on many factors, such as available number of controllers, number of modes to be controlled and coupling between the states of the system. In fact, if the optimal gain matrix of the controller is almost diagonal, then the centralised controller is almost decentralised and similar performance can be obtained. In this case, the latter should be preferred for its relative simplicity [17]. This thesis focuses on decentralised feedback control strategies, in which an individual control unit is investigated.

A common decentralised feedback control approach, which sometimes is referred to as low authority, is velocity feedback control (VFC) [18; 19]. The purpose of a VFC is to increase the effective damping of a structure, reducing its level of resonant vibration by using collocated sensors and actuators [4; 17]. A VFC consists of an inertial actuator attached to a structure, a collocated sensor of vibration and a controller, which feeds back the velocity of the structure to the actuator. The aim of the inertial actuator is to apply a control force to the structure proportional to its velocity for the purpose of vibration reduction. This control strategy would maintain the system stability if the sensor and actuator are collocated and if the transducer dynamics are neglected, regardless the number of structural modes considered and the inaccuracy of the parameters [19]. However, the inertial actuator internal dynamics play an important role and it has been shown that they can induce the instability of the VFC system [9; 10]. This thesis focuses on electromagnetic inertial actuators, however, feedback controllers can also be realised with other types of actuators. For example, hydraulic actuators are often used in the reduction of helicopter vibration [20], piezoelectric actuators are used for active vibration control of panels [21] and shape memory alloy actuators are used for vibration attenuation in micro-electromechanical devices [22].

2.2 Electromagnetic proof mass actuators

In this thesis, VFC is implemented using electromagnetic inertial, or proof mass, actuators. An inertial, actuator is a device that operates as a coil-magnet electromechanical transducer and it is attached to a structure, which requires a control force. The control force is produced by the interaction between the constant magnetic field given by a permanent magnet and the variable magnetic field given by the current flowing through a coil. The control force on the structure is generated by reacting off a proof mass,

which consequently starts to accelerate and a problem that sometimes occurs when controlling low frequency vibrations is that the proof mass experiences large amplitudes of motion, but in practice its travel is constrained by a limited stroke due to the presence of end-stops.

2.2.1 Concept

Electromagnetic inertial actuators have been widely used for the purpose of vibration suppression in lightweight, flexible and lightly damped structures [9; 23–39]. They are non-intrusive, because they can be attached to an existing structure without any structural modifications and they do not need an external mechanical connection to the ground or to another structure, hence the static behaviour of the structure does not change apart for the actuator mass. They have a wide frequency bandwidth of operation, resulting in a reduction of the vibration at several modes of the structure [40]. Moreover, they are suitable for lightweight and flexible structures due to their relatively large force-to-weight ratio [41].

An inertial actuator consists of a magnetic proof mass, an electrical winding and a suspension, which connects the proof mass to a casing or base mass [8]. An example of such a device is shown in figure 2.2(a) and its schematic representation is displayed in figure 2.2(b).

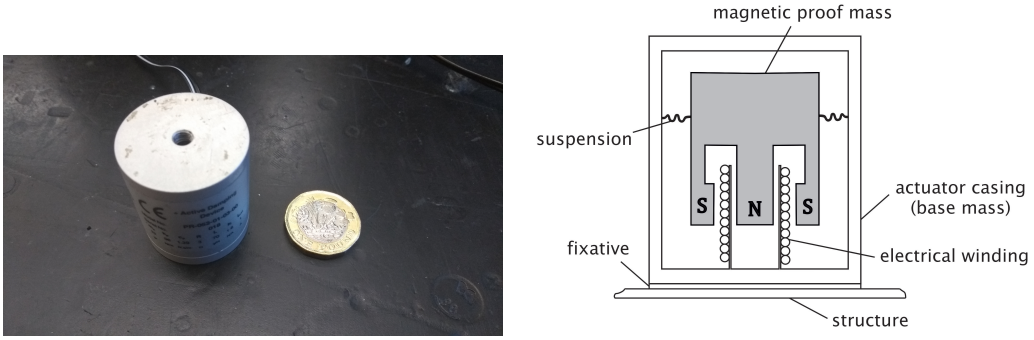

(a) (b)

FIGURE 2.2: (a) Picture of the Micromega Dynamics IA-01 inertial actuator [40]; (b) Schematic of an inertial actuator in cross-section.

The operating principle of an electromagnetic proof mass actuator is to convert electrical power into mechanical power according to Lorentz's force law. Hence, if an electrical charge q moves in a constant magnetic field, a force is generated on the charge, which is given by,

$$\mathbf{f} = q\mathbf{v} \times \mathbf{B}, \tag{2.1}$$

where $\mathbf{B}$ is the constant magnetic field (constant in the sense of time-invariant), $\mathbf{v}$ is the velocity of the electrical charge with respect to the magnetic field and eq. (2.1) can

be derived from the Maxwell's equation $\nabla \times \mathbf{E} = -\partial \mathbf{B}/\partial t$, where $\mathbf{E}$ is the electric field induced by the magnetic field.

Considering the case of figure 2.2(b), where a continuous flow of charges through the coil of the inertial actuator are subject to the constant magnetic flux, the force that acts on the charges in an infinitesimal length of the wire can be rewritten from eq. (2.1) as,

$$\mathrm{d}\mathbf{f} = \mathrm{d}l\mathbf{i_a} \times \mathbf{B}, \tag{2.2}$$

where $\mathrm{d}l$ is an infinitesimal length of the wire and $\mathbf{i_a}$ is the current flowing through the coil. Integrating eq. (2.2) over the whole length of the coil that is in the constant magnetic field region, a force is generated on the coil and hence on the actuator base, with an amplitude of,

$$f = Bl\ i_a, \tag{2.3}$$

where B is the constant magnetic field, l is the length of the coil exposed to the magnetic field, and according to Newton's third law, a force of the same magnitude but opposite direction reacts on the magnetic proof mass.

At the same time, according to Faraday's and Lenz's laws the relative motion between the magnetic field and an infinitesimal length of the wire exposed to such magnetic field generates a potential difference, which is given by,

$$\mathbf{E}\mathrm{d}l = \mathrm{d}l\mathbf{v} \times \mathbf{B}, \tag{2.4}$$

hence, integrating eq. (2.4) over the whole length of the coil, a voltage is generated at the terminals of the inertial actuator electrical winding, with an amplitude of,

$$e = Bl\ v, \tag{2.5}$$

where the voltage e is commonly called back electromotive force (back-emf) and v is the relative velocity between the magnet and the electrical winding.

Equations (2.3) and (2.5) describe the behaviour of the electromechanical conversion of the transducer, however, the dynamic behaviour of the inertial actuator is also affected by the mechanical and electrical impedances of the device as well as the presence of nonlinearities. On the mechanical side the actuator is usually modelled as a spring mass damper system, whereas the coil is usually modelled as a series ideal inductor and resistor. The mechanical and electrical side are then coupled by the transducer eqs. (2.3) and (2.5). The inertial actuator linear dynamic behaviour is usually studied considering its two-port network, because it is relatively easy to obtain the impedances of the different elements by setting the open-circuit or the short-circuit of each of the two ports. A complete and detailed treatment on the derivation of the two-port network of a linear inertial actuator can be found in [25; 42–46].

The internal dynamics of the actuator is characterised by a phase shift at the proof mass resonance frequency that can cause instability if the actuator is used in high gain VFC systems. To mitigate this problem, it is important that the natural frequency of the actuator is lower than the fundamental frequency of the structure and its resonance is well-damped [10; 47]. However, a low natural frequency of the actuator results in a high static deflection of the proof mass. Some solutions were proposed by [47; 48] to use a displacement feedback and a PID controller and by [26] to use an electronic compensator, however, all of these solutions increased the level of the feedback signal at low frequency and potentially the instability of the system if it was excited at this frequency. Another problem that is encountered in an inertial actuator is the limited stroke permitted to the proof mass, which together with other nonlinearities may affect its dynamic response and even change dramatically the stability conditions when it is used in VFCs. The nonlinear dynamic behaviour of an inertial actuator is discussed in greater detail in section 2.3 and then in chapters 3 and 4.

2.2.2 Applications

Electromagnetic proof mass actuators have a wide range of applications. For example they can be used in: active vibration attenuation of space structures or satellites, active reduction of human induced vibration on floors of open-space buildings or on stadia, active or hybrid vibration control of skyscrapers swing induced by wind excitation, internal noise reduction in aircraft and active vibration isolation between the gearbox and the cabin of helicopters.

For example, figure 2.3 displays an application of inertial actuators on a large space structure called “mast flight system” studied in [31]. The authors referred to the “mast flight system” as a lattice structure 60 m long and attached to the shuttle orbiter, which is provided with a deployment/retraction mechanism. Since the structure is lightweight and lightly damped, it requires an active vibration control system during on-orbit operations. The authors used a set of inertial actuators guided in decentralised velocity feedback with fixed gains to provide five percent of structural damping to the first ten bending and torsional modes of the structure. Other applications of inertial actuators in space structures are reported in [30; 32; 35; 37–39; 49–52].

In civil engineering there is a lot of ongoing research on human induced vibration [53]. Figure 2.4 shows a hybrid device, which is composed of a passive tuned mass damper with an active inertial actuator, developed in [36] to reduce floor vibrations generated by a crowd. The authors have compared experimentally the performance of the hybrid tuned mass damper with the performance of a passive tuned mass damper. The hybrid system has been found to be more effective to reduce the vibration in the frequency range of interest, in the sense that more vibration attenuation has been obtained for

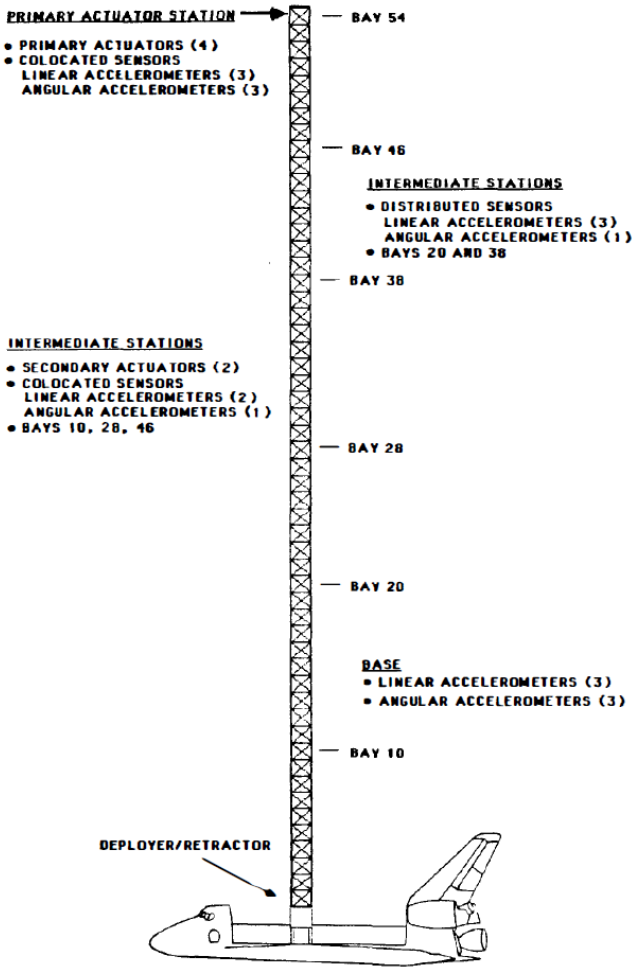

FIGURE 2.3: An application of electromagnetic proof mass actuators on a large space structure: a mast flight system. Reproduced from [31].

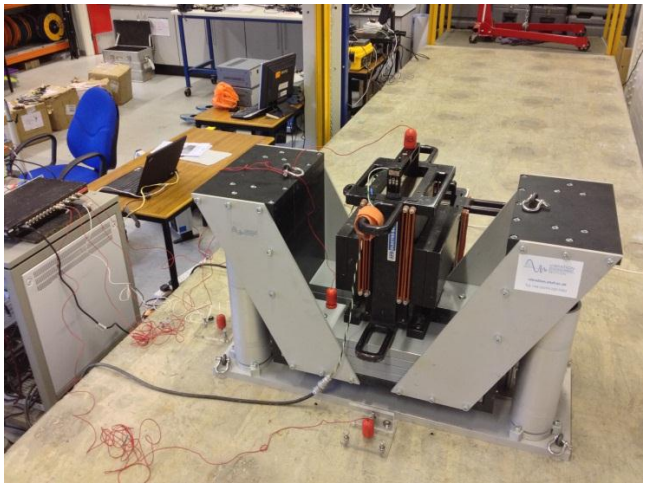

FIGURE 2.4: An application of electromagnetic proof mass actuators in civil structures: a hybrid tuned mass damper for floor vibration reduction. Reproduced from [36].

the same total mass of the devices. Other civil engineering applications where electromagnetic proof mass actuators are used can be found for example in [34; 54–63]. Also,

many practical applications of inertial actuators in civil engineering can be found for the suppression of flexural and torsional vibrations in tall buildings subject to small earthquakes and strong wind excitations [64].

Another application of proof mass actuators can be found in active noise reduction in aircraft, as reported in [24]. For example, in [33] the authors used a set of inertial actuators attached to the frame between the aircraft fuselage and the trim panel for the reduction of the cabin noise due to the blade passing excitation of a propeller aircraft, as shown in figure 2.5. Application of this active noise control system can be found nowadays on the Bombardier Dash8 Q400 aircraft [24; 33; 65]. Other applications where electromagnetic proof mass actuators are used to reduce the cabin noise in aircraft can be found for example in [66–69]. The isolation of helicopter cabins from the transmission

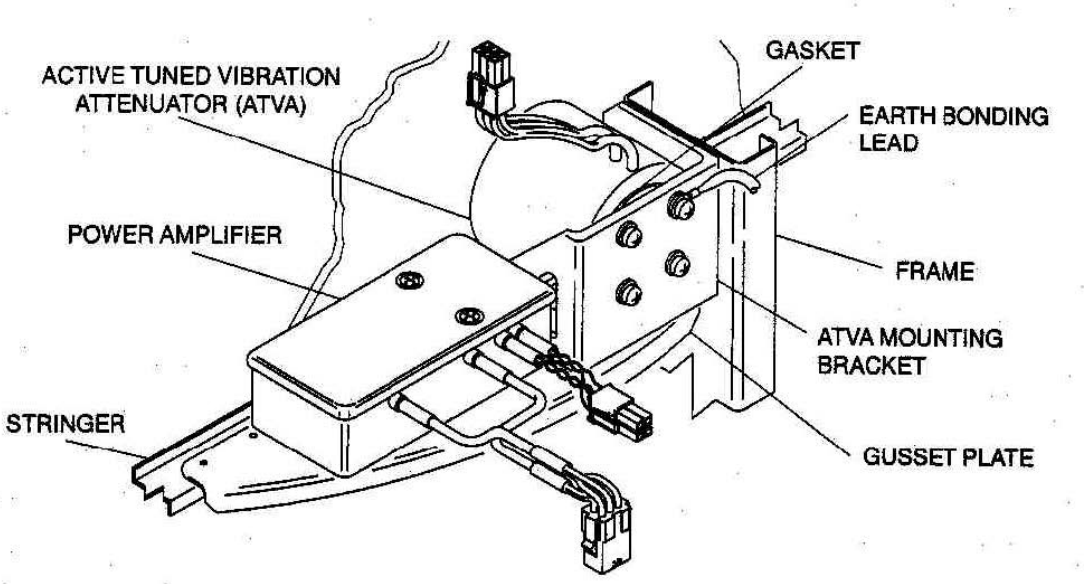

FIGURE 2.5: An application of electromagnetic proof mass actuators for internal noise reduction in aircraft: an active tuned vibration absorber. Reproduced from [33].

of rotor and gearbox vibration is another application problem that can be tackled using electromagnetic inertial actuators [24]. Figure 2.6 shows a prototype inertial actuator with a dual-loop controller, one that implements a negative stiffness feedback and one that provide a direct velocity feedback [70]. The inertial actuator was attached at the bottom of the main gearbox of an helicopter and its natural frequency was tuned to a specific resonance of the helicopter in order to damp the vibration of a specific mode [70; 71].

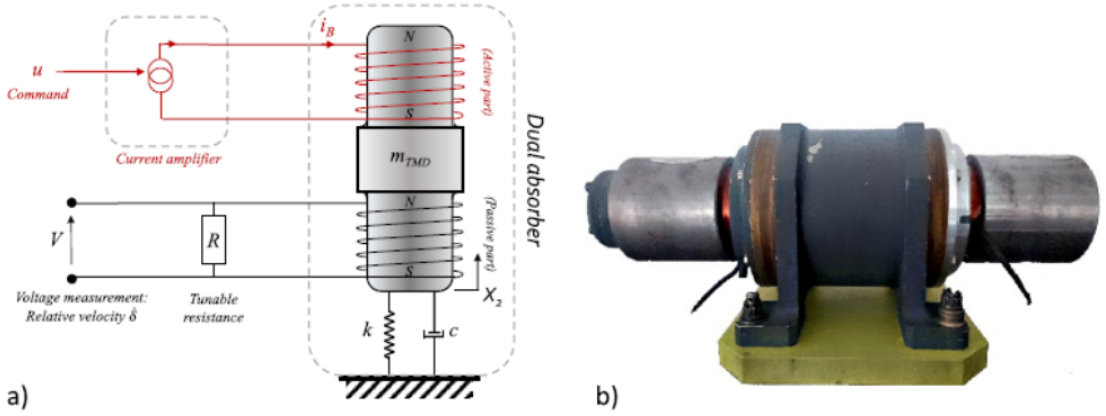

FIGURE 2.6: An application of electromagnetic proof mass actuators for active vibration control in helicopters: a dual loop hybrid mass damper. Reproduced from [70].

2.2.3 Nonlinear dynamics

The dynamic behaviour of inertial actuators is not always well described by linear mathematical models [11; 12; 72–75]. In fact, the assumption of linearity in the model holds only for small amplitude signals. If the actuator is subject to large amplitude signals instead, then a nonlinear model is required to reliably predict its dynamic behaviour, which is crucial when investigating instabilities or large amplitude of motion.

Common sources of loudspeaker's nonlinearity, whose operation is similar to inertial actuators include [76]:

- Nonlinear restoring force (force that moves the proof mass back to its equilibrium position), hence nonlinear stiffness and damping that depends on the proof mass displacement, as shown for example in figure 2.7(a);
- Nonlinear transduction coefficient that depends on the proof mass position and temperature of the actuator (or current circulating through the coil), as shown for example in figure 2.7(b);
- Nonlinear inductance that depends on the proof mass displacement and current flowing through the coil, as shown for example in figures 2.7(c) and 2.7(d);
- Nonlinear resistance that depends on the current flowing through the coil.

There exists an international standard, namely the IEC 62458:2010(E) [78], which gives the guidelines on how to perform the measurements to assess the nonlinearities of an electromechanical transducer, however, it is mainly based on the studies and methodologies developed by Klippel [76; 77; 79; 80] for loudspeaker systems. Even though loudspeakers and inertial actuators are very similar devices, there are some practical differences that

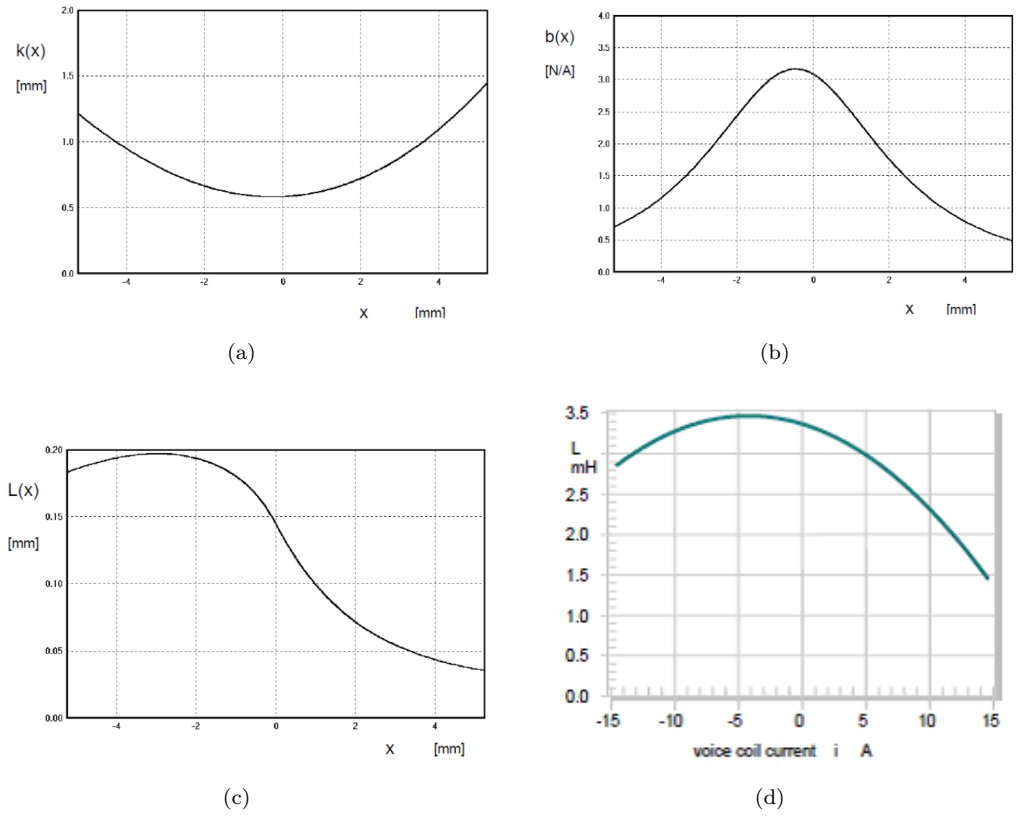

(a) (b) (c) (d)

FIGURE 2.7: (a) Suspension stiffness as function of relative coil-magnet displacement for a loudspeaker; (b) Transduction coefficient as function of relative coil-magnet displacement for a loudspeaker; (c) Coil inductance as function of relative coil-magnet displacement for a loudspeaker; (d) Coil inductance as function of current flowing through the coil for a loudspeaker. All figures taken from [76; 77]

motivate for the development of a different methodology to assess the nonlinearities of inertial actuators. Firstly, some inertial actuators are enclosed in a casing that is welded in place, hence there is not access to measure directly the displacement of the proof mass. Secondly, the underlying linear parameters of inertial actuators are commonly measured using base and direct excitations experiments, hence it would be convenient to use the same for the identification of the nonlinear parameters. Finally, the most important nonlinearity encountered by the author that affects the dynamic behaviour of inertial actuators is of the saturation type, which can be better investigated with a dynamic measurement methodology such as the one presented in chapter 3.

Saturation nonlinearity in inertial actuators comes as a limitation on the force that they can deliver. This is due to either the saturation of the power electronics or the finite stroke length between the actuator end-stops. The saturation of the power electronics gives a limitation on the electromechanical conversion, hence a maximum actuation force can be obtained for a given transduction coefficient and a maximum input current to the actuator coil. The saturation of the stroke instead gives a limitation of the inertial force

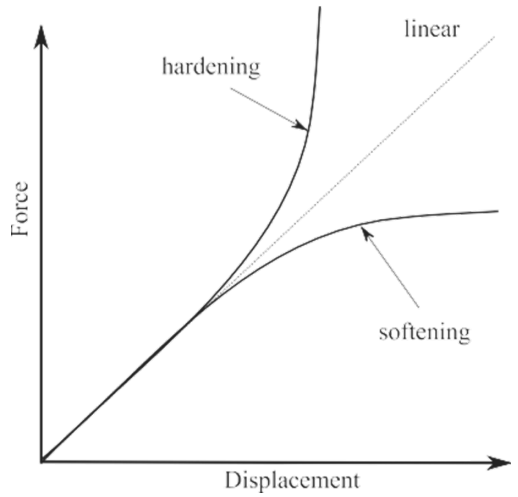

FIGURE 2.8: Nonlinear relationship between force and displacement of a spring. Reproduced from [7].

of the proof mass at low frequency, below the cut-off frequency where power electronic saturation and stroke saturation coincides.

Stroke saturation in inertial actuators has been previously investigated in [12; 72; 75; 81; 82], which pointed out that its implication is not only the limitation on the control force that the actuator can deliver at low frequency. In fact, stroke saturation is a non-smooth nonlinearity that is due to the proof mass hitting the actuator end-stops, potentially imparting large shocks to the structure, which may be damaged. Moreover, it has been shown both theoretically and experimentally that the shocks generated by stroke saturation can destabilise the closed-loop control system when an inertial actuator is used in a VFC [12; 83]. Over-designing the actuator may not be possible in practice [11] and allowing for very large stokes may negate the weight benefits introduced by these active devices.

It is worth to mention that stroke saturation is not always a problem to be avoided, instead, it can be beneficial for certain engineering applications. Self-propelled capsule systems for gastrointestinal endoscopy or for pipeline inspection use a vibro-impact oscillator (stroke saturating inertial actuator) where the impacting behaviour is used for the forward or backward motion of the capsule [84–88].

2.3 Nonlinear structural dynamics

Nonlinear systems are systems in which the assumption of linearity does not hold. Common properties of linear systems, such as the superposition principle, the uniqueness of solution for harmonic oscillations and the invariance of frequency response functions (FRFs) and modal parameters, are not observed in nonlinear systems.

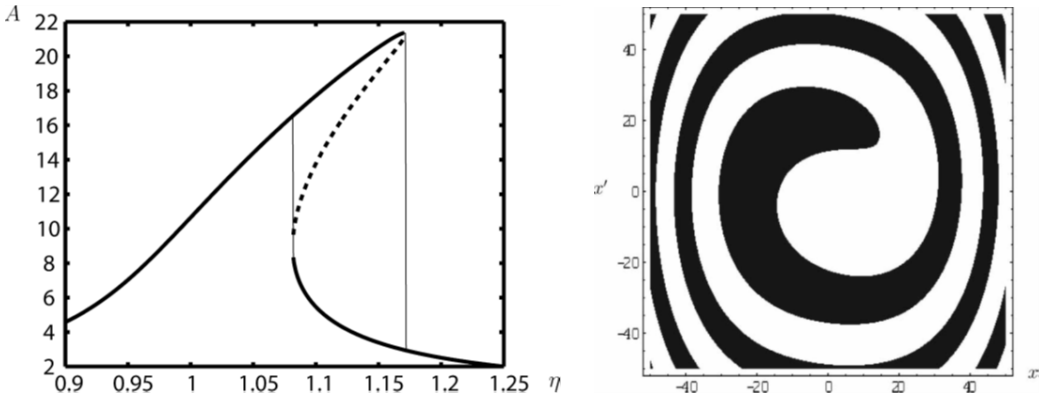

(a) (b)

FIGURE 2.9: (a) Nonlinear frequency response curve for a hardening Duffing oscillator; (b) Basins of attraction of the Duffing oscillator in figure (a) for $\eta = 1.12$; initial conditions identified with black points stabilise un the upper branch. Reproduced from [89].

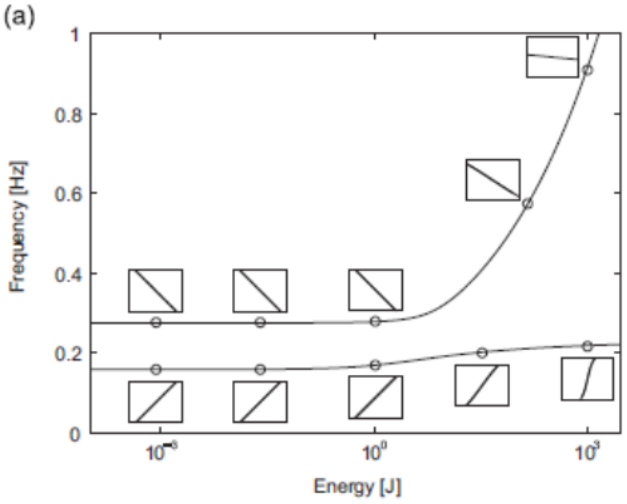

FIGURE 2.10: Frequency-energy plot of in-phase and out-of-phase nonlinear normal modes of a two degree of freedom nonlinear system. Reproduced from [90].

In fact, nonlinear systems exhibit non-proportional input-output relationships, as shown in figure 2.8. The steady state response of nonlinear systems depends on the initial conditions and hence harmonic oscillations can have multiple co-existing solutions, as illustrated in figure 2.9. Additionally, the frequency response of nonlinear systems is amplitude dependent, which means that the resonance frequencies and modal parameters can change with the energy input into the system, as shown in figure 2.10. Moreover, harmonic excitations of nonlinear systems can generate harmonic responses at higher or lower frequencies, as shown in figure 2.11.

Nonlinearity is significantly different from the more common linear dynamics, as new dynamic phenomena can be observed. Nonlinear dynamic behaviours include: "jumps" from higher to lower response levels or vice-versa, "bifurcations" that delineate a change

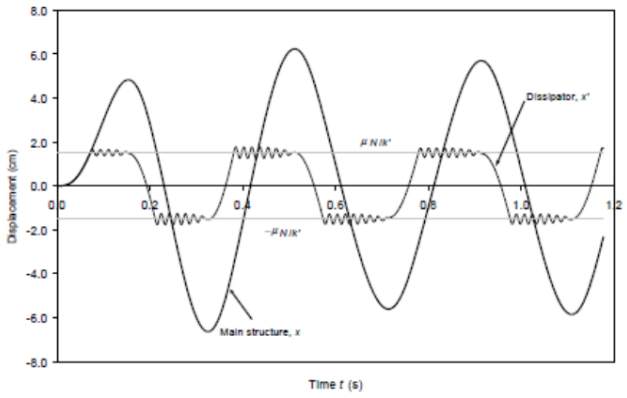

FIGURE 2.11: Time history response of a dissipation device due to a harmonic excitation of the main structure, where the nonlinearity of the device generates higher harmonics in the response. Reproduced from [91].

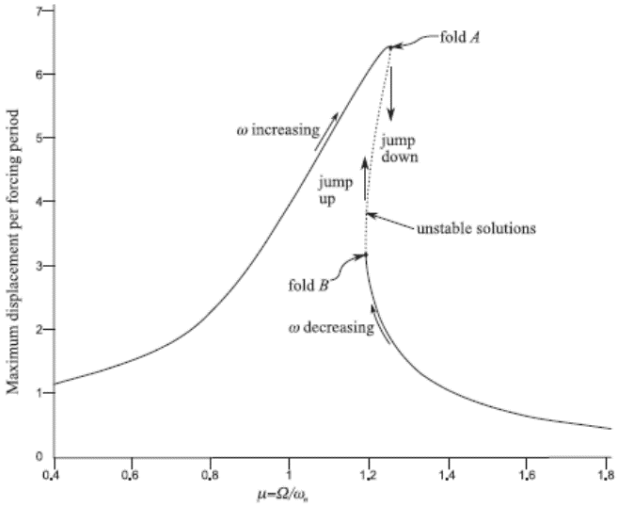

FIGURE 2.12: Frequency response curve of a nonlinear systems showing fold bifurcations, multiple solutions and jump responses. Reproduced from [7].

in the dynamic behaviour (e.g. from one to multiple co-existing solutions), "internal resonances" that are activated by the super- or sub-harmonics, "detached resonant curves" that are isolated solutions in the nonlinear frequency response curves, "quasi-periodic motion" where frequency components at non-integer multiples of the fundamental frequency are observed, and "chaos" where small changes in the initial conditions lead to very different responses [7; 90; 92–98].

For example, figure 2.12 shows a typical nonlinear frequency response curve, where multiple solutions, bifurcations and jumps are present. Increasing the forcing frequency Ω beyond the resonance peak corresponding to the fold bifurcation A leads the response to jump down to the lower branch [7]. A similar behaviour is obtained when decreasing the forcing frequency through the fold bifurcation B, but in this case the response jumps up to the higher branch. Figure 2.13, instead, shows a nonlinear frequency response curve

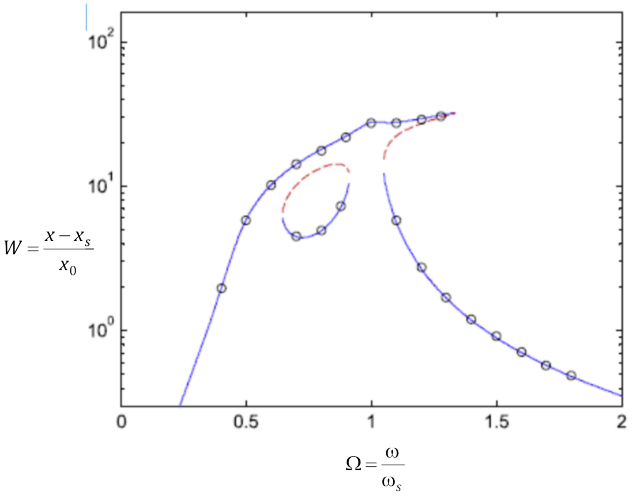

FIGURE 2.13: Nonlinear frequency response curves where an isolated branch is present. Normalised relative displacement W as function of the normalised frequency, where $x - x_s$ is the relative displacement and x_0 is the relative static displacement. Ω is the normalised frequency between the excitation frequency ω and the first natural frequency of the underlying linear system ω_s. Reproduced from [97].

where a detached resonance curve lies inside the main resonance curve [97]. In this case, a sweep-up or -down results in multiple jumps in the response of the nonlinear system.

The mechanical nonlinearities of inertial actuators can be investigated with the nonlinear structural dynamics tools. As it is shown in figure 2.14 the identification process consists of three steps, namely detection, characterisation and parameter estimation, as proposed in [99–101]. The nonlinear behaviour is detected in various manner, one can look at the coherence between the input and output signals, or at the total harmonic distortion (THD) of the output signal when the system is harmonically excited [102]. After the detection step, the nonlinearity has to be located, usually as a non-distributed element between two degrees of freedom so that a lumped parameter model can be built. Using different excitations (sine-sweep, stepped sine, random, impulse) and excitation levels, the type and form of nonlinearity can be determined concluding the characterisation step. The nonlinear parameters of the model are then estimated using different techniques, for example the restoring force surface method [99–101; 103–105] and a simple least-square fitting or a frequency-domain subspace identification approach [106].

The experimental identification process allows obtaining an accurate nonlinear lumped parameter model of the nonlinear system, which can be further investigated using numerical and analytical simulation tools.

The nonlinear model can be used to simulate the response both in time and frequency domains. Time domain solutions can be rarely obtained in an analytical closed form, they are usually calculated by numerical integration of the ordinary differential equations (ODEs) that constitutes the equations of motion, see appendix C or [107; 108]. Periodic solutions, instead, are commonly computed using the harmonic balance method (HBM)

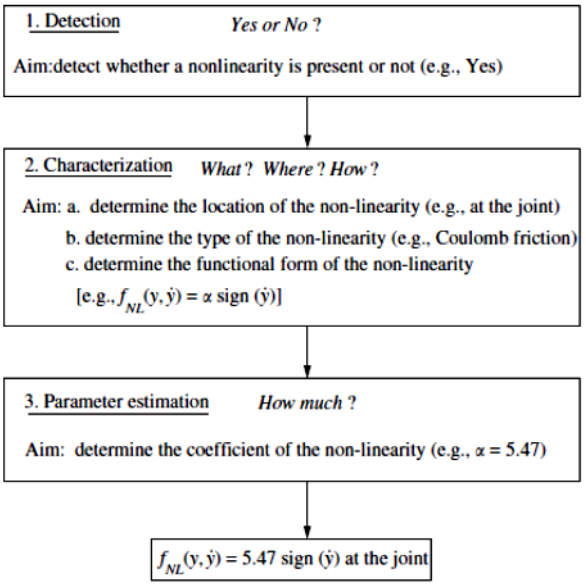

FIGURE 2.14: The nonlinear identification process. Reproduced from [100].

at each frequency and level of excitation [109–116]. Other approaches to calculate the periodic solutions are the shooting technique and orthogonal collocation [93; 94; 117]. The HBM permits the construction of nonlinear frequency response curves (NFRC) that are useful for a deeper understanding of the nonlinear behaviour of the system, such as determining the location of the bifurcations and the nonlinear resonances and the frequency range at which several solutions co-exist. A global analysis can also be performed to investigate which initial conditions of the system stabilise on which stable branch of the NFRC [101; 104; 105]. A frequency domain method that is commonly applied in the analysis of nonlinear system is the describing function method [118]. The describing function method approximates the response of a nonlinear system by neglecting the contribution of the higher or lower harmonics. For example, the nonlinear function $N(a)$ can be expressed as,

$$N(a) = K_{eq}(A)a + N_d(a), \tag{2.6}$$

where $K_{eq}a$ is a quasilinear term, $N_d(a)$ is a distortion term and $a = A\sin\omega t$. The first term represents the fundamental component of the nonlinearity and the gain K_{eq} is named describing function of the nonlinearity. It has been shown that in order to minimize the distortion term $N_d(a)$ in a mean-square sense, the describing function has to be the Fourier-series coefficient of the fundamental component of the nonlinearity [118]. The describing function can then written as,

$$K_{eq}(A) = g(A) + jb(A), \tag{2.7}$$

where,

$$g(A) = \frac{1}{\pi A}\int_0^{2\pi/\omega} N\left(A\sin\omega t\right)\sin\omega t\mathrm{d}t \tag{2.8a}$$

$$b(A) = \frac{1}{\pi A}\int_0^{2\pi/\omega} N\left(A\sin\omega t\right)\cos\omega t\mathrm{d}t \tag{2.8b}$$

,

are the Fourier coefficients. The describing functions of most common nonlinearities, such as saturation, Coulomb friction, backlash and hysteresis are shown in table 2.1.

TABLE 2.1: Describing functions of most common nonlinearities [119].

Nonlinearity	Schematic	Describing function
Saturation	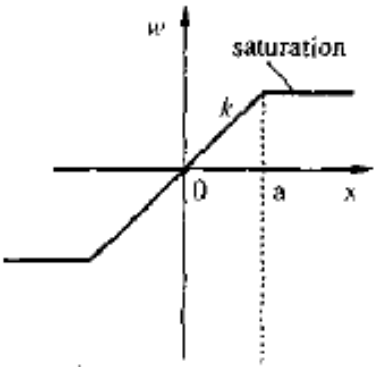	$K_{eq} = \frac{2k}{\pi}\left[\arcsin(\frac{a}{A}) + \frac{a}{A}\sqrt{1-\frac{a^2}{A^2}}\right]$
Backlash and hysteresis	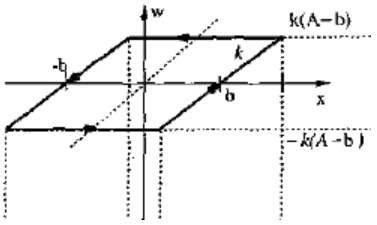	$K_{eq} = \frac{4kb}{\pi}(\frac{b}{A}-1) + j\frac{Ak}{\pi}$ $+[\frac{\pi}{2} - \arcsin(\frac{2b}{A}-1)+$ $-(\frac{2b}{A}-1)\sqrt{1-(\frac{2b}{A}-1)^2}]$
Coulomb friction	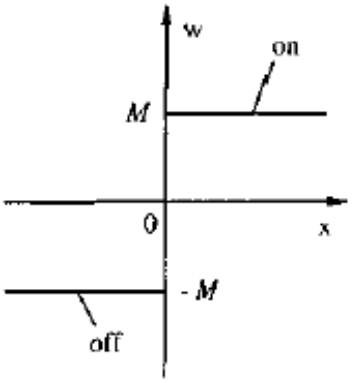	$K_{eq} = \frac{4M}{\pi A}$

2.4 Applied nonlinear control

Nonlinear control investigates control systems in which there is at least one nonlinear element. Nowadays, control strategies for linear systems are well-established, however, nonlinear control strategies are still matter of on-going research [119]. Switching from linear to nonlinear active control may be interesting for improving the existing control system, such as when the required operation range becomes larger. If the system is subject to discontinuous nonlinearities that are not linearisable, then nonlinear analyses have to be used to investigate the system. Additionally, nonlinear control methodologies can also outperform linear control strategies when dealing with model uncertainties [119].

The stability of nonlinear systems can be analysed with several mathematical tools, such as the Lyapunov's direct and indirect methods [119; 120], the analysis of phase-space trajectories [121], the circle and Popov criteria [120], or the describing function analysis [108; 119].

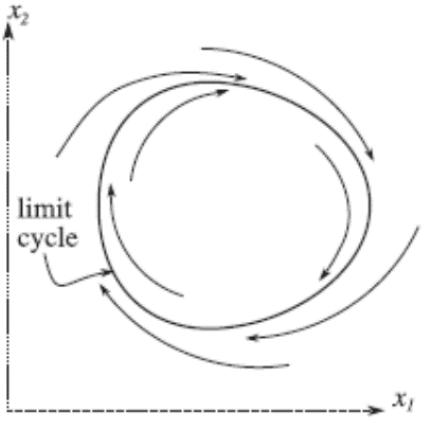

FIGURE 2.15: An example of a limit cycle oscillation. Reproduced from [7].

Lyapunov's indirect method is used to linearise the nonlinear system around an equilibrium point and to investigate the local stability by evaluating the eigenvalues of the linearised state matrix, which can be a closed-loop state matrix if a VFC is implemented for example. Lyapunov's direct method instead, is used to assess the global stability of the nonlinear system by searching a function that satisfies a set of rules [119]. Lyapunov's direct method is a powerful tool to investigate the stability of nonlinear systems, however, it is usually difficult to find a suitable candidate function. The circle and Popov criteria make use of Lyapunov's direct method to define a boundary between stable and unstable regions [120].

An interesting method to assess the stability of nonlinear systems is the describing function analysis, which is used for the detection of limit cycle oscillations. Limit cycles are trajectories of the nonlinear system in which the energy of the system does not change over the cycle. A qualitative representation of limit cycle oscillations is given in figure 2.15. A nonlinear system that contains a single nonlinearity can be represented by

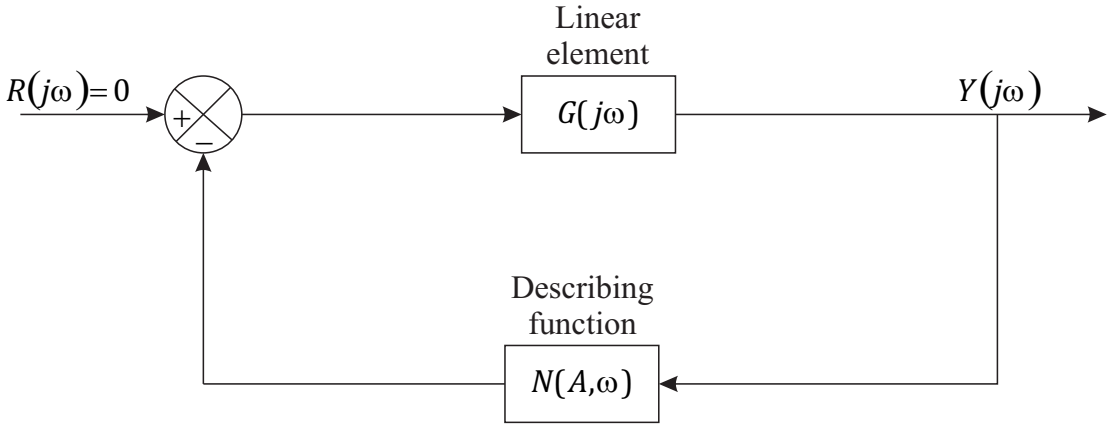

FIGURE 2.16: Block diagram of the describing function analysis for the prediction of limit cycle oscillations.

a transfer function that groups all the underlying linear dynamics and a feedback loop that contains the describing function of the nonlinearity [118], as shown in figure 2.16. The condition for the existence of limit cycles is given for the intersection between the negative inverse of the describing function with the transfer function of the underlying linear system [119]. However, due to the approximate nature of this analysis, it is important to check the results with direct numerical simulations if they are not too computationally expensive.

Several attempts have been made to overcome the issue of stroke saturation in inertial actuators with the aid of active nonlinear control methods. The first study on this extent can be found in [37], where a suboptimal feedback position controller of a beam with a proof mass actuator was designed using a linear programming algorithm. This approach, however, severely limits the performance of the inertial actuator. Later studies developed the idea of adding a nonlinear feedback control loop to the VFC loop [41; 122–125], but there is no record of experimental work using these controllers. Another approach that has been used is the on/off controller, which deactivates the VFC if stroke saturation is detected [83; 126]. A similar, but less dramatic strategy, namely gain scheduling, was first introduced by [127] and then adopted by [54; 128], where the VFC gain is reduced by a certain amount the more the proof mass gets close to the end-stops and eventually going to zero so that the system becomes passive.

2.5 Virtual sensing

Active vibration control applications often require the real-time knowledge of the states and parameters of the system being controlled. However, in many applications it is impossible to directly measure such quantities for many reasons. It could be that direct measurements require the use of costly sensors, or the integration of such sensors in the

system is not feasible, or even that a particular sensor does not exist [129]. Hence, the required variables have to be estimated from other measured variables using a model of the system. Usually in structural dynamics, the estimated variables are the states of the system, but they can also be the input forces or displacements, or the system parameters [129].

For example, a virtual sensing approach has been developed in [130] for the estimation of wheel centre loads on a MacPherson suspension, which is shown in figure 2.17. In fact, current practice is to instrument the vehicle wheel with a force transducer, but this solution is extremely expensive, intrusive (in the sense that it affects the measurements) and time consuming for the installation. Since the vehicle is already instrumented with many other sensors during the test campaign, researchers are investigating alternative approaches that make use of virtual sensors to estimate the wheel centre loads [130]. Another interesting application of virtual sensing techniques is the estimation of frictional contact forces in guiding rails of vertical transportation systems [131]. This allows one to monitor the condition of the system, in order to guarantee safety and efficiency by detecting any faults or degradation in the vertical transportation system.

The nonlinear control strategy developed in this thesis and some of the control strategies discussed in the previous section to prevent stroke saturation in inertial actuators require the real-time knowledge of the proof mass states. However, inertial actuators are commonly supplied without an internal sensor that measures the proof mass displacement. This can be because an additional sensor raises the price of the actuator, it may be subject to failures and it increases the mass of the device. Fitting an additional sensor to an inertial actuator is not always easy and without compromises, for example, the inertial actuator in figure 2.2 has a welded casing that protects the proof mass, which is therefore not accessible to be instrumented without tearing off the casing. Virtual sensing, instead, can provide an estimation of the proof mass states by using the already available measurements and the nonlinear model of the actuator without having to fit any additional physical sensors.

Virtual sensing usually refers to the use of observers [132] or estimators [133] for the state estimation of a system when the state measurements with physical sensors are not available. An observer is usually derived from the state space equations using the identified system matrices, the known input and the measured output of the system, such that,

$$\begin{cases} \dot{\hat{\mathbf{x}}} = \mathbf{A}\hat{\mathbf{x}} + \mathbf{B}u + \mathbf{L}(y - \hat{y}) & \text{(2.9a)} \\ \hat{y} = \mathbf{C}\hat{\mathbf{x}} & \text{(2.9b)} \end{cases},$$

where $\hat{\mathbf{x}}$ are the estimated states of the system, $\mathbf{A}, \mathbf{B}, \mathbf{C}$ are the system matrices, u is the input, y is the measured output and $\hat{y}$ is the estimated output. The convergence of the estimated states to those of the physical system, denoted by $\mathbf{x}$, is given by the $\mathbf{L}(y - \hat{y})$ term in eq. (2.9a) where the matrix $\mathbf{L}$ can be chosen by studying the observer

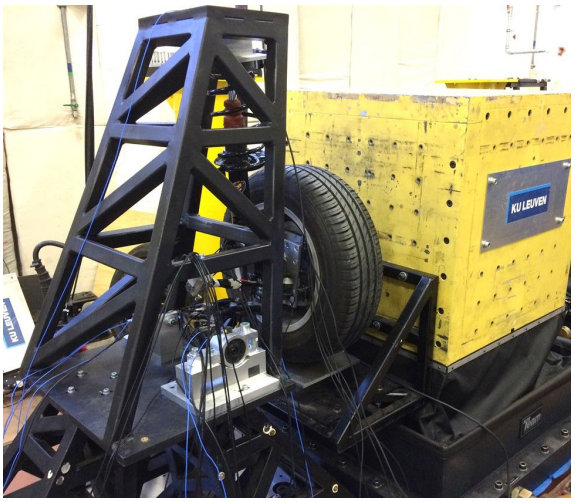

FIGURE 2.17: Test-rig for the virtual sensing of wheel centre loads on a MacPherson suspension attached to a rigid frame and excited by an hydraulic shaker. Reproduced from [130].

error dynamics [132],

$$\dot{\mathbf{e}} = (\mathbf{A} - \mathbf{LC})\,\mathbf{e}, \tag{2.10}$$

where $\mathbf{e} = \mathbf{x} - \hat{\mathbf{x}}$ is the observer error. Hence, $\mathbf{L}$ can be chosen to tune the eigenvalues of the matrix $(\mathbf{A} - \mathbf{LC})$ in order to achieve faster or slower convergence of the estimated states [132]. The block diagram of such an observer for a feedback control system is shown in figure 2.18.

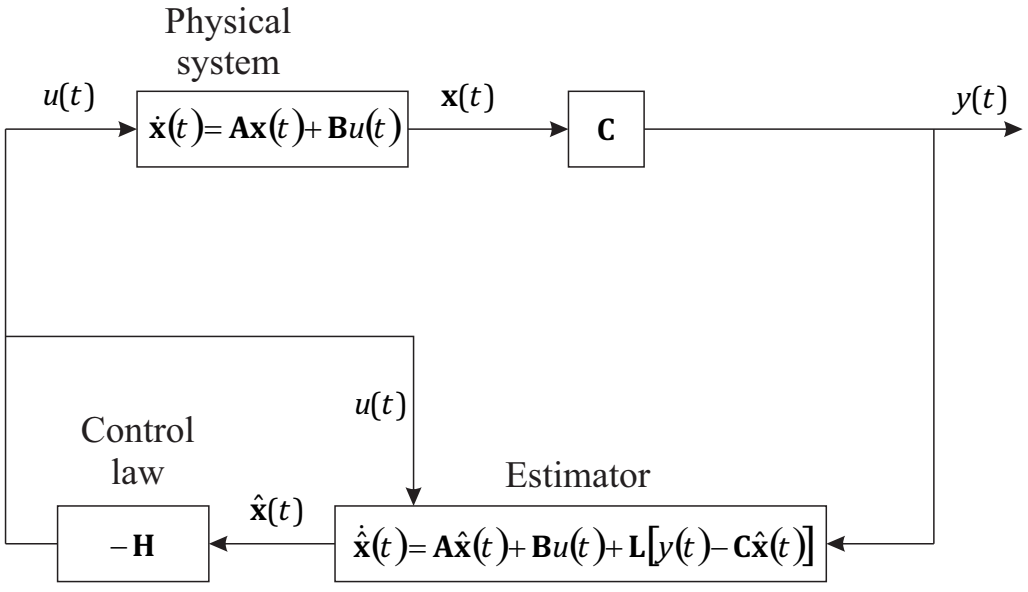

FIGURE 2.18: Block diagram of a feedback controller with a state estimator.

The observer shown in figure 2.18 is typically used for linear deterministic systems, however, in reality many systems behave nonlinearly and are subject to noise. In the 1960s optimal state estimators were developed, known as Kalman filters [133–135]. A

Kalman filter aims to obtain the optimal estimate (in the sense of minimum standard deviation of variables affected by Gaussian noise) of the states of a system and the covariances of the states based on the knowledge of the system matrices, the input and output of the system and the covariances of the measurement noise and process noise [133]. It cannot be directly applied to nonlinear systems since the propagation of the system states and covariances would not be Gaussian, however, if the nonlinear system is differentiable, it can also be linearised at each time step around the estimation point and the Kalman filter can be applied. This method, also known as extended Kalman filter (EKF) [133] is implemented in chapter 7 for the estimation of the states of the proof mass.

Chapter 3

Characterisation and modelling of nonlinear dynamics of inertial actuators

A large amount of literature has shown that the internal dynamics of inertial actuators affects the stability and performance of VFCs [9; 10; 12; 39]. This motivates the need for accurate models of inertial actuators and in particular characterising the nonlinearities that may affect the dynamics of such devices for large excitation signals. Although there exists a few publications based on experiments [81; 82; 136], a systematic methodology of measuring and identifying the nonlinearity in inertial actuators is still lacking. This chapter aims to determine the mechanical nonlinearities of inertial actuators through the detection, characterisation and identification of nonlinear parameters. The electrical nonlinearities are neglected since they mainly affect the behaviour at high frequencies, which are beyond the frequency region where the instability occurs. The inertial actuator used in the initial experiments is a Micromega Dynamics IA-01, which is shown in figure 2.2(a) and is documented in [40]. The nonlinear identification is explained in detail for this specific actuator, however, the methodology presented in this chapter can be applied to other actuators with weaker and different type of nonlinearities [137]. As evidence, a number of different actuators have been tested and their results are provided in appendices A and B. The experimental set-up is shown in section 3.1 and the underlying linear dynamics of the actuator is identified in section 3.2. The nonlinear dynamic behaviour is then investigated in sections 3.3 and 3.4 considering the response of the actuator to large amplitude signals.

3.1 Experimental set-up

In this section the experimental set-up for the identification of the linear and nonlinear dynamics of an inertial actuator is presented. In order to characterise the inertial actuator, two experiments are required. The first experimental set-up is used to measure the structural response of the actuator to a base excitation, as shown in figures 3.1(a) and 3.1(b). In this case, the actuator is mounted on a PCB Piezotronics 208C01 ICP

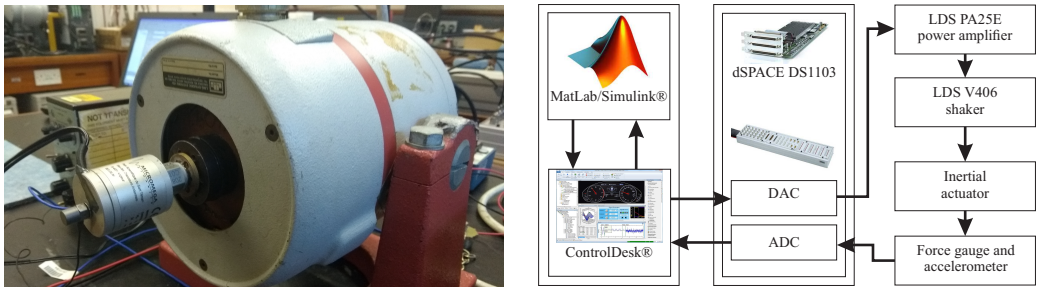

(a) (b)

FIGURE 3.1: (a) Picture of the base excitation experimental set-up; (b) Block diagram of the base excitation experiment.

force sensor, which is rigidly connected to an LDS V406 electrodynamic shaker. The shaker is powered by an LDS PA25E voltage driven voltage amplifier. A B&K Type 4375 accelerometer is attached to the actuator casing in order to measure the acceleration of the base mass. The actuator's coil terminals are initially left open to measure the voltage due to the back-emf. The output force, acceleration and voltage signals are acquired by a dSPACE DS1103 PPC Controller Board. The dSPACE operates the analogue-to-digital and digital-to-analogue conversions (ADC/DAC) of the input and output signals at a sampling frequency of 10 kHz. The dSPACE is also connected to a PC workstation. A model of the experiment is created in Matlab/Simulink in order to generate the adequate input signal and to acquire the signals from the measurement channels. The simulink model is then uploaded on the ControlDesk software for communicating with the dSPACE board. The driving signal generated by the dSPACE board is low-pass filtered with a 1 kHz cut-off frequency using a Kemo VBF8 filter before entering the power amplifier and then the shaker. A constant voltage signal input to the amplifier is thus converted to a constant displacement signal input to the shaker moving mass and to the actuator base mass. The second experimental set-up is used to measure the response of the actuator to a direct (current) excitation, as shown in figures 3.2(a) and 3.2(b). Since the aim of this experiment is to measure the blocked force, the actuator is fixed to a rigid clamped mass and the force at the actuator base is measured by a PCB 208C01 ICP force cell positioned between the actuator and the blocked mass. In this experiment, the signal generated by the dSPACE is low-pass filtered with a 4

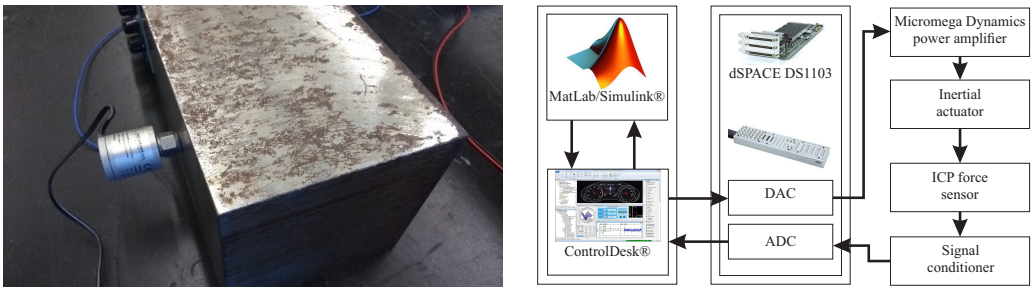

(a) (b)

FIGURE 3.2: (a) Picture of the direct excitation experimental set-up; (b) Block diagram of the direct excitation experiment.

kHz cut-off frequency and amplified by a Micromega Dynamics PR-052-01-04-03 voltage driven current amplifier [138] shown in figure 3.3 before entering the actuator leads. Considering this set-up, a constant voltage signal input from the dSPACE to the amplifier is converted to a constant current signal input to the actuator's coil. The amplifier has also an output monitoring port for measuring the current of the load, as shown in figure 3.3(a). Again, the current and voltage are acquired by the dSPACE board at a rate of 10 kHz. The underlying linear parameters of the actuator for both tests have

(a) (b)

FIGURE 3.3: Pictures of the Micromega Dynamics PR-052-01-04-03 current amplifier. (a) Front panel connections; (b) Back panel connections.

been measured by applying a broadband white noise excitation with a cut-on frequency of 2 Hz and a cut-off frequency of 4 kHz and recording the measurements for 60 s and taking averages. For the direct excitation experimental set-up, the only constraint is that the base mass of the actuator is fixed to the ground. Several other excitations under different constraints have been used for the base excitation experiments in order to better investigate both the linear and the nonlinear regimes of motion. In particular, for the underlying linear parameter identification, the actuator's coil terminals are first left open (zero current circulating) and then shunted (zero voltage across the terminals) in order to see the additional damping introduced by the electromechanical coupling. In order to identify the nonlinear behaviour, the actuator's coil terminals are left open circuit allowing to measure the back-emf. Initially, the excitation is chosen to be harmonic for detecting any nonlinearities. The investigation is followed by sine-sweep excitation

experiments, both up and down in frequency, allowing one to gain information about the instantaneous frequencies in the response. In this case the experiments are 60 s long each for linearly sweeping up (down) from 5 Hz (25 Hz) to 25 Hz (5 Hz) at a rate of 40 Hz/min (-40 Hz/min).

3.2 Underlying linear parameter identification

The operating principle of an electromagnetic proof mass actuator is to convert electrical power into mechanical power, which is described by the Lorentz force law. In such a system, a current flowing through a coil is exposed to a uniform magnetic flux, which is generated by the magnetic proof mass [139]. The electromechanical linear lumped parameter model of the actuator is shown in figure 3.4, where m_b is the base mass of the actuator and m_p the proof mass. The base and proof mass displacements are x_b and x_p, respectively, and the relative motion of the proof mass with respect to the actuator's base is $x_r = x_p - x_b$. The stiffness and damping parameters of the actuator's suspension are k_p and c_p, respectively. The external force applied to the base for the equilibrium is denoted with f, which is the opposite of the control force f_c that the actuator applies on the structure. The variable i_a represents the current flowing through the coil and e_a is the voltage across the coil terminals. The transduction coefficient is $\phi = Bl$, where B is the magnetic flux of the permanent magnet and l is the length of the coil exposed to the magnetic flux B. The voice coil electrical impedance is typically modelled as an ideal inductance L_e and resistance R_e in series. Assuming the system in figure 3.4 is linear

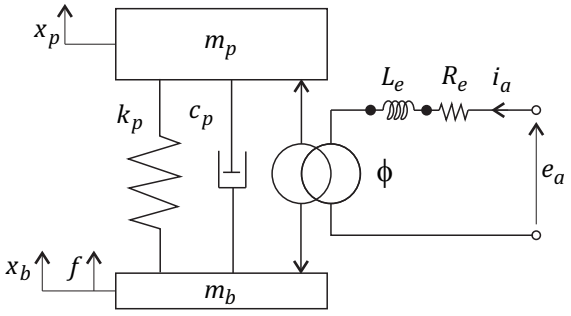

FIGURE 3.4: Electromechanical linear lumped parameter model of the inertial actuator.

and time-invariant as well as assuming that the electrical and mechanical variables are proportional to $e^{j\omega t}$, where ω is the angular frequency, the dynamic equilibrium equations in frequency domain can be written as,

$$\begin{cases} j\omega m_p \dot{X}_p(j\omega) = \phi I_a(j\omega) - \left[c_p + \dfrac{k_p}{j\omega}\right] \dot{X}_r(j\omega) & \text{(3.1a)} \\ F(j\omega) = \phi I_a(j\omega) - \left[c_p + \dfrac{k_p}{j\omega}\right] \dot{X}_r(j\omega) + j\omega m_b \dot{X}_b(j\omega)\text{,} & \text{(3.1b)} \\ E_a(j\omega) = \phi \dot{X}_r(j\omega) + \left[R_e + j\omega L_e\right] I_a(j\omega) & \text{(3.1c)} \end{cases}$$

where $\phi I_a(j\omega)$ is the force generated by the transducer according to the Lorentz force law and $\phi \dot{X}_r(j\omega)$ is the back-emf caused by the relative coil-magnet motion according to the Faraday's law. The notation in eq. (3.1) as for the whole thesis is that upper-case letters are used for variables in frequency domain and lower-case letters are used for variables in time-domain. Also, an abuse of notation has been made for $\dot{X}_p(j\omega)$ to indicate the Fourier transform of the velocity of the proof mass[1]. The dynamic behaviour of the system in figure 3.4 is well described by six frequency response functions (FRFs). These are the transmissibility between the mechanical and electrical ports and the driving-point impedances at either the electrical or mechanical terminals of the device and their mathematical derivation follows directly from eq. (3.1). The calculations can be found in the textbooks of Hunt [42] and Crandall [43], and in the research papers [25; 44], here the resulting formulation is reported. The electrical driving-point impedance $Z_{ee}(j\omega)$ defined as the ratio between the voltage across the coil terminals and the current flowing through the winding for the blocked actuator's base ($\dot{X}_b(j\omega) = 0$) is derived from eq. (3.1) as,

$$Z_{ee}(j\omega) = \left.\frac{E_a(j\omega)}{I_a(j\omega)}\right|_{\dot{X}_b(j\omega)=0} = (R_e + j\omega L_e) + \frac{\phi^2}{j\omega m_p + c_p + \frac{k_p}{j\omega}}. \tag{3.2}$$

Similarly, the mechanical driving-point impedance $Z_{mm}(j\omega)$ defined as the ratio between the transmitted force to the hosting structure and the base mass velocity for the open circuit electrical port ($I_a(j\omega) = 0$) is obtained from eq. (3.1) and results in,

$$Z_{mm,o}(j\omega) = \left.\frac{F(j\omega)}{\dot{X}_b(j\omega)}\right|_{I_a(j\omega)=0} = j\omega m_b + \frac{j\omega m_p \left(c_p + \frac{k_p}{j\omega}\right)}{j\omega m_p + c_p + \frac{k_p}{j\omega}}. \tag{3.3}$$

The mechanical driving-point impedance can also be calculated for the short-circuited electrical port ($E_a(j\omega) = 0$) from eq. (3.1) and it can be written as,

$$Z_{mm,s}(j\omega) = \left.\frac{F(j\omega)}{\dot{X}_b(j\omega)}\right|_{E_a(j\omega)=0} = j\omega m_b + \frac{j\omega m_p \left(c_p + \frac{k_p}{j\omega} + \frac{\phi^2}{R_e + j\omega L_e}\right)}{j\omega m_p + c_p + \frac{k_p}{j\omega} + \frac{\phi^2}{R_e + j\omega L_e}}. \tag{3.4}$$

The transmissibility between the electrical and mechanical ports for the base driven actuator $T_{\dot{X}_b}(j\omega)$ is defined as the ratio between the voltage across the coil terminals and the velocity of the base mass for the open-circuit electrical port and from eq. (3.1) it results in,

$$T_{\dot{X}_b}(j\omega) = \left.\frac{E_a(j\omega)}{\dot{X}_b(j\omega)}\right|_{I_a(j\omega)=0} = \frac{-j\omega m_p \phi}{j\omega m_p + c_p + \frac{k_p}{j\omega}}. \tag{3.5}$$

The transmissibility between the mechanical and electrical ports for the direct driven

[1] If $X_p(j\omega)$ is the Fourier transform of $x_p(t)$, then using $\dot{X}_p(j\omega)$ for the Fourier transform of $\dot{x}_p(t)$ can be confusing. In fact, one can point out that the time derivation of $X_p(j\omega)$ does not exist, since $j\omega$ is an algebraic value. In this thesis the following notation will be used: $X(j\omega)$, $\dot{X}(j\omega)$, $\ddot{X}(j\omega)$ for the Fourier transform of $x(t)$, $\dot{x}(t)$, $\ddot{x}(t)$, respectively.

actuator $T_{I_a}(j\omega)$ defined as the ratio between the force transmitted to the hosting structure and the input current for the blocked actuator's base can be written as,

$$T_{I_a}(j\omega) = \left.\frac{F(j\omega)}{I_a(j\omega)}\right|_{\dot{X}_b(j\omega)=0} = \frac{-j\omega m_p \phi}{j\omega m_p + c_p + \frac{k_p}{j\omega}}. \tag{3.6}$$

Depending on the type of the power amplifier used to operate the device it can be useful to calculate the expression of the transmissibility for the direct driven actuator with respect to an input voltage instead of an input current. Hence, from eq. (3.1), the transmissibility between the mechanical and electrical ports for the direct driven actuator, $T_{E_a}(j\omega)$, defined as the ratio between the force transmitted to the hosting structure and the input voltage for the blocked actuator's base can be written as,

$$T_{E_a}(j\omega) = \left.\frac{F(j\omega)}{E_a(j\omega)}\right|_{\dot{X}_b(j\omega)=0} = \frac{1}{(R_e + j\omega L_e)} \frac{-j\omega m_p \phi}{\left(j\omega m_p + c_p + \frac{k_p}{j\omega} + \frac{\phi^2}{R_e + j\omega L_e}\right)}, \tag{3.7}$$

which shows that a voltage driven actuator presents an increased internal damping and a decreased force output at high frequencies due to the electromechanical coupling, when compared to the same actuator but current driven. The FRFs described by eqs. (3.2)

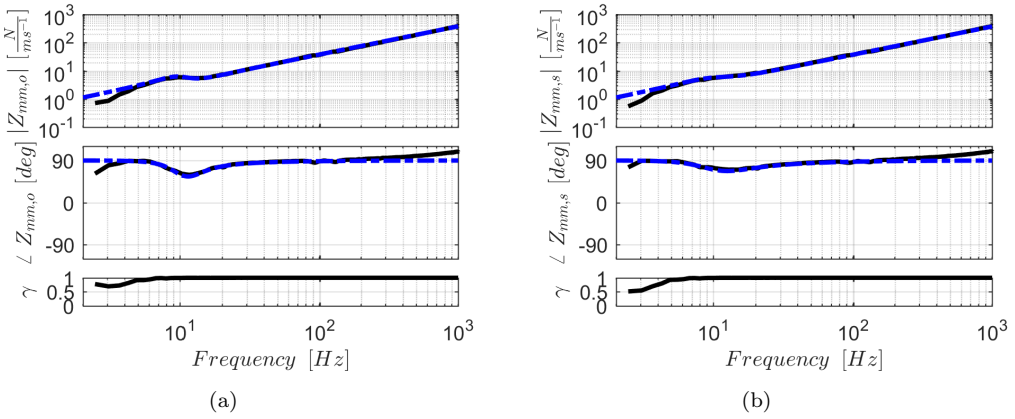

FIGURE 3.5: Magnitude, phase and coherence of the measured mechanical driving-point impedance (black solid line) and identified model (blue dash-dotted line). (a) Open-circuit mechanical impedance; (b) Short-circuit mechanical impedance.

to (3.7) have been measured using a broadband white noise excitation. In particular, $Z_{mm,o}(j\omega)$, $Z_{mm,s}(j\omega)$ and $T_{\dot{X}_b}(j\omega)$ have been measured using the base excitation set-up shown in figure 3.1 and $Z_{ee}(j\omega)$, $T_{I_a}(j\omega)$, $T_{E_a}(j\omega)$ have been measured using the direct excitation set-up shown in figure 3.2. The experimental results of the Micromega Dynamics IA-01 actuator are shown in figs. 3.5 to 3.7 with a black solid line, where the magnitude, phase and coherence are displayed for each measured FRF, taking the average of 8 measurements, each one being 60 s long. The measured FRFs have been fitted with the analytical FRFs given by eqs. (3.2) to (3.7) and are shown in figs. 3.5 to 3.7 with blue dashed lines. A least-square-error method between the analytical and

experimental FRFs has been implemented for the underlying linear model identification of the best fitting parameters [140], which are summarised in table 3.1. There is a very

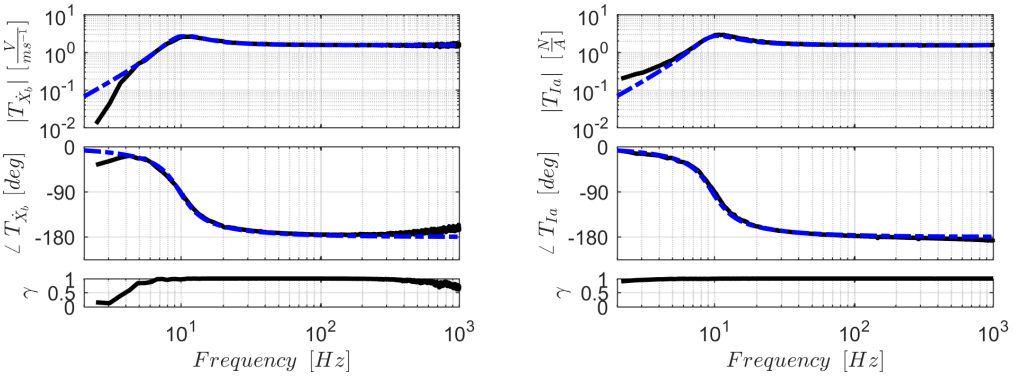

(a) (b)

FIGURE 3.6: Magnitude, phase and coherence of the measured transmissibility (black solid line) and identified model (blue dash-dotted line). (a) Base excitation experiment; (b) Direct (current) excitation experiment.

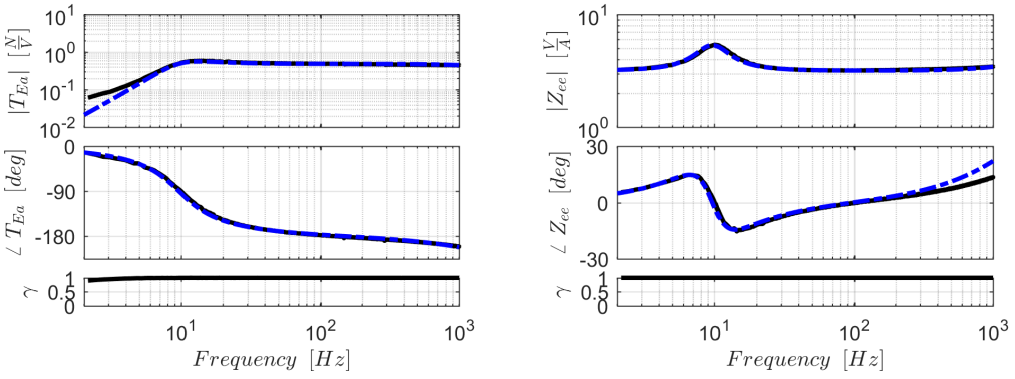

(a) (b)

FIGURE 3.7: Magnitude, phase and coherence of the measured transmissibility and electrical impedance (black solid line) and identified model (blue dash-dotted line). (a) Transmissibility for the direct (voltage) excitation experiment; (b) Electrical impedance for the direct (current) excitation experiment considering an ideal inductance model.

good agreement between the experimental and the analytical FRFs shown in figures 3.5 and 3.6 and eq. (3.7) above 5 Hz, where the coherence becomes closer to 1. In particular, figure 3.5(a) shows the mechanical driving-point impedance also given by eq. (3.3) for an open-circuit electrical port. At low frequency, the mechanical impedance converges towards the impedance of the total mass of the actuator, whereas at high frequency it converges towards the impedance of the base mass. The plot in figure 3.5(b) showing the mechanical driving-point impedance for a short-circuited electrical port looks almost identical to the plot in figure 3.5(a), but it differs for the additional damping introduced by the electromechanical coupling, as can be also seen in eq. (3.4), where the amplitude

of the resonance peak is reduced. This is not evident when comparing figure 3.5(a) with figure 3.5(b), because the Micromega actuator has a relatively high damping and low ϕ/R_e, however, it can be easily seen in the other actuators in appendices A and B. The plots in figures 3.6(a) and 3.6(b) are the mechanical to electrical transmissibility and the electrical to mechanical transmissibility for a current driven actuator, respectively, and they are given by eqs. (3.5) and (3.6). As expected, they give the same response that is characterised by in phase input-output FRF at low frequency and out of phase input-output FRF at frequencies above the resonance where the spectrum is also flat. Figure 3.7(a), instead, shows the electrical to mechanical transmissibility for a voltage driven actuator that is also given by eq. (3.7). Comparing this plot with the one in figure 3.6(b), it can be noticed that the resonance peak is reduced in magnitude because of the additional damping. Additionally, the transmissibility above the resonance decreases as the frequency increases. This is more evident for the actuators in appendices A and B. The electrical impedance of the blocked actuator is shown in figure 3.7(b), which is also given by eq. (3.2). At low frequency the electrical impedance can be approximated as the resistance of the coil and as the frequency increases a peak rises that is due to the electromechanical coupling. For higher frequencies the electrical impedance should tend to the ideal inductance impedance as predicted by eq. (3.2), however, there is a disagreement between the measured and identified FRFs that is even more evident for the actuators in appendices A and B. The discrepancy can be due to the inductance losses as a consequence of the eddy currents circulating in the magnetic proof mass and is investigated in the next section 3.2.1. Considering eqs. (3.2) to (3.7), the linear response of the base driven inertial actuator can be conveniently defined by the following two-port network equation [42; 45],

$$\begin{array}{ll} F(j\omega) & = T_{me} I_a(j\omega) + Z_{mech} \dot{X}_b(j\omega) \\ E_a(j\omega) & = Z_{elec} I_a(j\omega) + T_{em} \dot{X}_b(j\omega) \end{array} , \tag{3.8}$$

which is also shown in the block diagram of figure 3.8, where the electrical driving-point impedance $Z_{elec} = Z_{ee}$ is given by eq. (3.2), the electrical to mechanical and the mechanical to electrical transmissibility $T_{me} = T_{em} = T_{\dot{X}_b} = T_{I_a}$ are given by eqs. (3.5) and (3.6) and the mechanical driving-point impedance can either be $Z_{mech} = Z_{mm,o}$ for the open-circuit electrical port, which is given by eq. (3.3), or $Z_{mech} = Z_{mm,s}$ for the short-circuited electrical port, which is given by eq. (3.4).

3.2.1 Inductance losses due to eddy currents

As anticipated at the end of section 3.2, the series ideal inductance and resistance model of the voice coil does not always represent accurately the dynamic behaviour of the actuator, especially at high frequency [79; 141]. This can be identified by the mismatch of the experimental and analytical electrical impedance shown in figure 3.7(b). In fact, the voice coil is not operating in free air, but close to the magnetic pole structure.

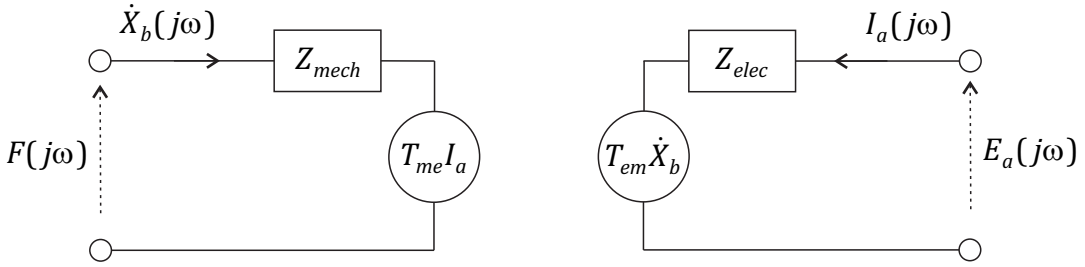

FIGURE 3.8: Two-port network parameters of a base driven inertial actuator.

TABLE 3.1: Identified underlying linear model parameters for the Micromega Dynamics IA-01 [40].

Parameter	Symbol	Value	Units
Base mass	m_b	0.054	kg
Proof mass	m_p	0.031	kg
Transduction coefficient	ϕ	1.55	N/A
Natural frequency	ω_p	9.7	Hz
Damping ratio	ζ_p	30%	–
Coil resistance	R_e	3.2	Ω
Coil inductance	L_e	211	μH

Hence, the variable magnetic field generated by the current flowing through the coil induces eddy currents in the solid iron pole structure due to Faraday's law. The eddy currents circulating through the resistance of the iron pole dissipate energy by heating the iron pole itself. In loudspeaker driver investigations, this is commonly taken into account by modifying the topology of the electrical port adding lossy inductors in the model, that are, inductors with a shunting parallel resistance [142–144]. Thus, adding in series to the ideal inductance L_e displayed in figure 3.4 a lossy inductor results in an equivalent impedance,

$$Z_{L,LR-2}(j\omega) = j\omega L_e + \frac{j\omega L_2 R_2}{j\omega L_2 + R_2}, \tag{3.9}$$

which has the topology shown in figure 3.9(a) and is usually referred as LR-2 model [143; 144]. Further investigations on loudspeaker drivers showed the development of several linear models to describe the inductance losses due to eddy currents in the iron pole. In fact, Vanderkooy [142] derived a mathematical formulation that models the behaviour of the voice coil as a series resistor and semi-inductor, which has an impedance,

$$Z_{L,Vanderkooy}(j\omega) = K\sqrt{j\omega}, \tag{3.10}$$

as shown in figure 3.9(b), where K is the semi-inductance parameter. Subsequently, Wright proposed a model with separated power functions for the real and imaginary

part of the electrical impedance [145] that can be written as,

$$Z_{L,Wright}(j\omega) = K_r\omega^{\eta_r} + jK_i\omega^{\eta_i}, \tag{3.11}$$

which however requires the identification of the four parameters K_r, K_i, η_r, η_i. A similar model was developed by Leach [146], where the electrical impedance takes the form,

$$Z_{L,Leach}(j\omega) = K(j\omega)^{\eta}, \tag{3.12}$$

which requires the identification of the parameters K and η. Leach also proposed a model described by a series effective inductance and resistance in which the inductance and resistance vary with frequency [147], as shown in figure 3.9(c). Thus, it can be written as,

$$Z_{L,eff}(j\omega) = L_{eff}(\omega)j\omega + R_{eff}(\omega), \tag{3.13}$$

where a large amount of parameters are requires for $L_{eff}(\omega)$ and $R_{eff}(\omega)$: two for each frequency point. Considering the inductance losses, the analytical driving-point

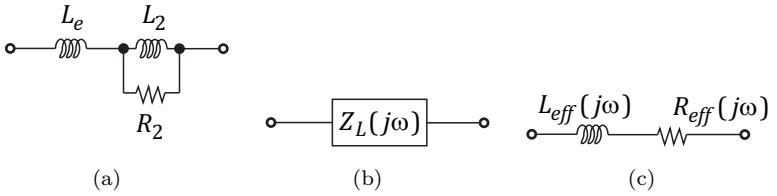

FIGURE 3.9: Topology of the voice coil electrical impedance considering the inductance losses due to eddy currents in the magnetic iron pole. (a) LR-2 model; (b) Wright and Leach frequency dependent models; (c) Effective inductance model.

electrical impedance of the inertial actuator given by eq. (3.2) becomes,

$$Z_{ee,L}(j\omega) = (R_e + Z_L(j\omega)) + \frac{\phi^2}{j\omega m_p + c_p + \frac{k_p}{j\omega}}, \tag{3.14}$$

where $Z_L(j\omega)$ is given by eqs. (3.9) to (3.13). Any of these models can be used for describing the inductance losses and in fact, it has been observed that the choice of each model strongly depends on the actuator design. The Micromega Dynamics IA-01 driving-point electrical impedance has been fitted using the Leach model given by eq. (3.12) [146] and the result of the fitting is shown in figure 3.10 with the red dashed line, where the frequency range has been increased up to 4kHz. The semi-inductance and the exponent used in the Leach model given by eq. (3.12) are $K = 4.5 \cdot 10^{-4}$ and $\eta = 0.85$. It is evident that including the inductance losses in the model will give a better prediction of the device electrical impedance at high frequency with respect to the ideal inductance model shown in figure 3.10 with the blue dash-dotted line. This can be useful when estimating the active and reactive electrical power required by the device for suppressing the vibration of a structure. However, for the sake of simplicity,

throughout this thesis the ideal inductance model is used, as shown in figure 3.4, and the effect of the eddy currents is neglected, being the focus of the thesis on a lower frequency range.

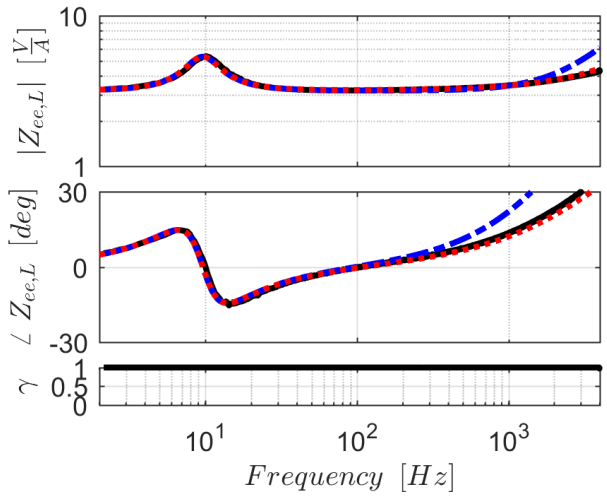

FIGURE 3.10: Magnitude, phase and coherence of the measured driving-point electrical impedance (black solid line), identified ideal model (blue dash-dotted line) and identified model considering the inductance losses due to the eddy currents (red dashed line).

3.3 Limits of linear analysis

The dynamic behaviour of inertial actuators is not always well described by linear mathematical models. These devices are subject to strong nonlinearities due to the saturation of the force they can generate, which is due to either the saturation of the power electronics or the saturation of the available stroke [11]. Considering the actuator in the direct excitation configuration, from eq. (3.1) the blocked force can be written as,

$$F_b(j\omega) = \begin{cases} -\left[j\omega c_p + k_p\right] X_p(j\omega) + \phi I_a(j\omega) & \text{(3.15a)} \\ \omega^2 m_p X_p(j\omega) & \text{(3.15b)} \end{cases}.$$

Also, according to Newton's second law, the equation of motion of the proof mass can be written as,

$$\left[-\omega^2 m_p + j\omega c_p + k_p\right] X_p(j\omega) = \phi I_a(j\omega), \tag{3.16}$$

thus,

$$X_p(j\omega) = \frac{\phi I_a(j\omega)}{-\omega^2 m_p + j\omega c_p + k_p}. \tag{3.17}$$

Substituting eq. (3.17) into eq. (3.15a) and rearranging the terms, provides the maximum blocked force that the actuator can deliver without exceeding its limits,

$$F_{b,max}(j\omega) = \begin{cases} F_{b,max1}(j\omega) = \phi I_{a,max} \left(\dfrac{\omega^2}{-\omega^2 + j\omega 2\zeta_p \omega_p + \omega_p^2} \right), & \text{(3.18a)} \\ F_{b,max2}(j\omega) = \omega^2 m_p x_0 & \text{(3.18b)} \end{cases}$$

where x_0 is half of the stroke length, $\omega_p = \sqrt{k_p/m_p}$ is the natural frequency and $\zeta_p = c_p/(2m_p\omega_p)$ is the damping ratio of the device. The force limit due to the power electronic saturation and the stroke saturation are $F_{b,max1}(j\omega)$ and $F_{b,max2}(j\omega)$, respectively. The power electronic saturation is a limitation on the electromechanical conversion, which is given by the maximum actuation force that the transducer can generate, which is,

$$F_{a,max}(j\omega) = \phi I_{a,max}, \tag{3.19}$$

where $I_{a,max}$ is the maximum input current flowing into the actuator coil. Stroke saturation, instead, gives a limitation on the maximum displacement allowed to the proof mass that is given by,

$$X_{p,max}(j\omega) = x_0. \tag{3.20}$$

The results of this analysis are shown in figure 3.11(a) for a Micromega Dynamics IA-01 actuator driven by a current amplifier. The dotted and dash-dotted blue lines in figure 3.11(a) show the spectrum of the actuation force $F_{a,max}(j\omega)$ and the blocked force $F_{b,max1}(j\omega)$ in a logarithmic scale when the actuator is driven by the maximum current of 1 A [40]. The dashed red line shows, instead, the spectrum of the blocked force $F_{b,max2}(j\omega)$, when the actuator is driven at the maximum stroke allowed to the proof mass ($x_0 = 1.25$ mm). A combination of these two limitations results in a region where the actuator follows the linear equation of motions, which is defined by the black solid line. The upper limit $F_{a,max}$, which has a flat dynamic behaviour over the whole frequency range, is indeed a limitation on the temperature and heating of the actuator. In fact, an increase in the input power to the actuator's coil would produce a temperature rise of its components [73; 74]. The maximum current value is given by the maximum temperature rise that does not lead to demagnetisation of the proof mass caused by passing the Curie temperature (80 °C for most of the permanent magnets), when the atoms of the material deviate from the magnetic alignment. An ultimate limit is then given by the melting temperature of the wire insulation, which is about 150 °C for common materials [74]. The force limit due to stroke saturation shown in figure 3.11(a) appears to be an effective limit at low frequency, instead. The plot of figure 3.11(a) can thus be divided into two regions: below the saturation cut-off frequency ω_s and, where the limitation on the blocked force is given by stroke saturation; and above ω_s, where

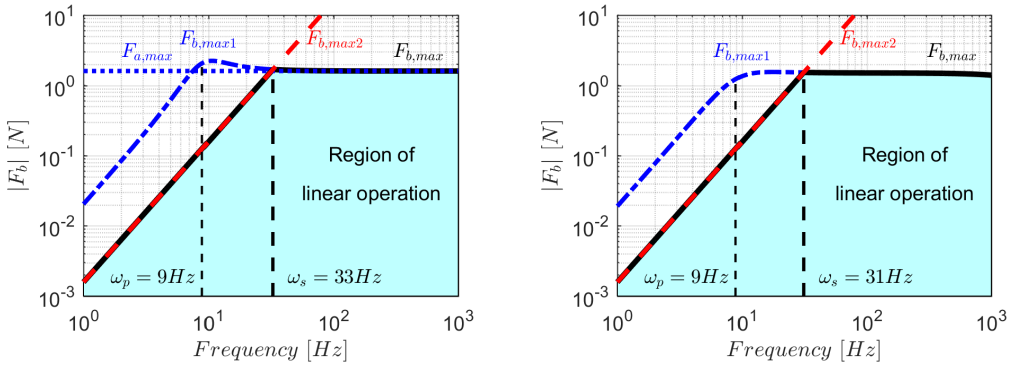

FIGURE 3.11: Limitation of the linear analysis for a proof mass actuator. Dotted and dash-dotted blue lines represent the limitation on the maximum force due to the power electronics saturation; red dashed lines display the limitation due to the maximum stroke; black solid lines are the combination of the two previous constraints and define a region where the actuator behaves linearly (cyan area). (a) Current driven actuator; (b) Voltage driven actuator.

the limitation is given by the saturation of the current. This can be summarised as,

$$F_{b,max}(j\omega) = \begin{cases} \phi I_{a,max} & \omega > \omega_s \quad (3.21a) \\ \omega^2 m_p x_0 & \omega \leq \omega_s \quad (3.21b) \end{cases}.$$

The saturation cut-off frequency can be calculated at the intersection point between the two limits by setting,

$$\omega_s^2 m_p x_0 = \phi I_{a,max}, \tag{3.22}$$

which gives,

$$\omega_s = \sqrt{\frac{\phi I_{a,max}}{m_p x_0}}. \tag{3.23}$$

If the saturation cut-off frequency is lower than the natural frequency of the actuator it means that the device has a large stroke and the only limitation on the blocked force is given by the power electronic saturation. However, for the Micromega Dynamics IA-01 actuator and for the majority of these devices, the saturation cut-off frequency is larger than their natural frequency, as shown in figure 3.11(a). Hence, in any practical application the control range should be above the saturation cut-off frequency for exploiting the maximum actuator authority. In order to avoid stroke saturation, the device could be redesigned allowing for a larger stroke that can be estimated by setting $\omega_s = \omega_p$, hence from eq. (3.22) results,

$$x_{0,new} = \frac{\phi I_{a,max}}{k_p}. \tag{3.24}$$

However, this large stroke cannot usually be implemented in practice. For example, using the values given in table 3.1 for the Micromega Dynamics IA-01 actuator, the

redesigned actuator would have a stroke that is almost 13 times larger than the original. One can replicate the same analysis for a voltage driven actuator, setting the limitation of the power electronic on the voltage instead of the current. Hence, considering eq. (3.7) instead of eq. (3.18a), the maximum blocked force becomes,

$$F_{b,max}(j\omega) = \begin{cases} E_{a,max} \left(\dfrac{-j\omega m_p \phi}{(R_e + j\omega L_e)\left(j\omega m_p + c_p + \frac{k_p}{j\omega} + \frac{\phi^2}{R_e + j\omega L_e}\right)} \right), & \text{(3.25a)} \\ \omega^2 m_p x_0 & \text{(3.25b)} \end{cases}$$

where $E_{a,max}$ is the maximum voltage that can be applied to the actuator voice coil. The limits given by eq. (3.25) are shown in figure 3.11(b), where the maximum voltage has been set to 3 V. Stroke saturation can happen to every inertial actuator if excited below its saturation cut-off frequency. In fact, even if the stroke is large and the blocked force is limited only by the maximum input power, in a real application the inertial actuator is subject to shocks, rigid body motions or other low frequency base excitation that can lead to displacement saturation. Designing an actuator that is able to deliver the requested force even below the saturation cut-off frequency would mean that it is overdesigned in terms of volume and weight. This would negate its favourable force-to-weight ratio for controlling vibrations of lightweight structures.

3.4 Nonlinear parameter identification

The linear model used in section 3.3 to derive the actuator force limit over the entire frequency range gives a wrong physical interpretation of the consequences of stroke saturation. In fact, eq. (3.18b) tells that a saturation on the proof mass displacement corresponds to a saturation on the force delivered by the actuator, as if the proof mass was connected to a negative stiffness of the same value of the suspension stiffness, for displacements exceeding the stroke. What happens, instead, is that as the proof mass saturates in stroke it collides with the actuator's end-stops experiencing a much larger stiffness and generating impact forces that sums up to the total force delivered by the actuator. Hence, in general, the assumption of linearity in the model, as used in sections 3.2 and 3.3, holds only for small amplitude signals. For large amplitude signals, instead, a nonlinear model of the inertial actuator is required to reliably predict its dynamic behaviour, and this is crucial in case of instabilities or large amplitude vibrations. A general nonlinear lumped parameter model of the actuator is shown in figure 3.12, where the linear parameters associated with the suspension have been replaced by a nonlinear restoring force $f_{RF}(\dot{x}_r, x_r)$. Also, the transduction coefficient $\phi(x_r)$ is in general a nonlinear function of the displacement. Only mechanical nonlinearities have been considered in this study, which are functions of displacements or velocities. The electrical nonlinearities, which depend on current or voltage, have been neglected since they

affect the behaviour only at high frequency. The governing equations of the system in figure 3.12 can be written as,

$$\begin{cases} m_p\ddot{x}_p(t) = \phi(x_r(t))i_a(t) - f_{RF}(\dot{x}_r(t), x_r(t)) & \text{(3.26a)} \\ f(t) = \phi(x_r(t))i_a(t) - f_{RF}(\dot{x}_r(t), x_r(t)) + m_b\ddot{x}_b(t), & \text{(3.26b)} \\ e_a(t) = \phi(x_r(t))\dot{x}_r(t) + R_e i_a(t) + L_e\dfrac{\mathrm{d}}{\mathrm{d}t}i_a(t) & \text{(3.26c)} \end{cases}$$

where the transformation to the frequency domain is not possible in general, due to the nonlinear nature of these equations. The nonlinearity of the inertial actuator is identified following three steps, namely detection, characterisation and parameter identification, as proposed in [100; 101]. The inertial actuator is tested again using the base excitation experiment described in section 3.1. The first test is a harmonic excitation at different frequencies and amplitudes. This is useful to detect the nonlinearities by comparing the excitation and response waveforms looking for any distortions. If a nonlinear behaviour is detected, the next step is to apply a sine-sweep excitation in both directions in order to characterise the nonlinearity. Looking at the time history of the response and at the istantaneous frequencies, a formulation can be chosen for the nonlinear model of the actuator. Finally, the nonlinear parameters can be identified using the restoring force surface method and fitting the nonlinear model to the experimental data [99–101; 103–105].

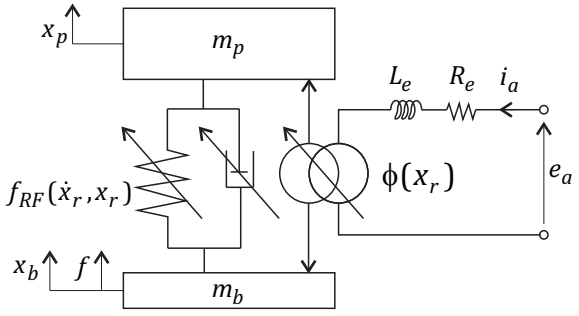

FIGURE 3.12: Electromechanical lumped parameter model of the inertial actuator considering a general nonlinear connection between the proof and base mass and a nonlinear transduction.

3.4.1 Detection

In this section the detection of the nonlinearity is investigated. Several experiments have been done using a harmonic base excitation varying frequency and amplitude. The most representative is shown in figure 3.13 for a harmonic base excitation at 8 Hz and 2.5 mm. In particular, figure 3.13(a) shows the waveforms of the base force, the relative proof mass velocity and displacement with a black solid line and the input base displacement with a dash-dotted red line. The waveform of the base force present periodic spikes,

which are due to the impacts between the proof mass and the end-stops. In fact, at the same timing of the spikes, the velocity plummets changing sign and the displacement waveform is clipped resulting in a highly distorted signal. This results in a nonlinear trajectory of the proof mass in the phase-space, as can be observed in figure 3.13(b). If the system were linear, the trajectory would have been elliptical, in this case, instead, it follows a distorted loop constrained within a certain displacement range. The back-emf signal has been measured considering that it is equal to the voltage across the actuator leads for an open-circuit electrical port. Hence, in this case eq. (3.26c) becomes,

$$e_a(t) = \phi(x_r(t))\dot{x}_r(t), \tag{3.27}$$

which is shown in figure 3.13(c) and presents a waveform that is similar to the one of the proof mass velocity in figure 3.13(a). The spectrum of the proof mass displacement and the back-emf are shown in figure 3.13(d) where many harmonics are observed in the response signals and their magnitudes are comparable to the fundamental one. The relevance of the harmonics generated by the nonlinearity, or the magnitude of waveform distortion is analysed considering the total harmonic distortion (THD) of the signals [102], which is defined as,

$$\text{THD} = \frac{\sqrt{\sum_{n=2}^{\infty} I_n^2}}{I_1}, \tag{3.28}$$

where I_1 is the magnitude of the fundamental component in the response, and I_n are the magnitude of the harmonics. The THD values of the signals in figure 3.13(d) are given in table 3.2 considering the response harmonics up to the 5^{th}. The THD is usually given in dBc (dB relative to the carrier), but it can easily translated in percentage. The results shown in figure 3.13 and table 3.2 motivate for a deeper understanding of the causes of the nonlinearity as well as the identification of the nonlinear actuator model.

TABLE 3.2: Total harmonic distortion (THD) of displacement, force and back-emf signals at 8 Hz harmonic excitation considering the response harmonics up to the 5^{th}.

Parameter	Value	Units
THD x_r	-6	dBc
THD x_r	50	%
THD f	-2.8	dBc
THD f	72.2	%
THD e_a	-2.2	dBc
THD e_a	77.2	%

3.4.2 Characterisation

This section focuses on choosing an appropriate nonlinear model that is representative of the dynamic behaviour of the inertial actuator. Several experiments have been carried

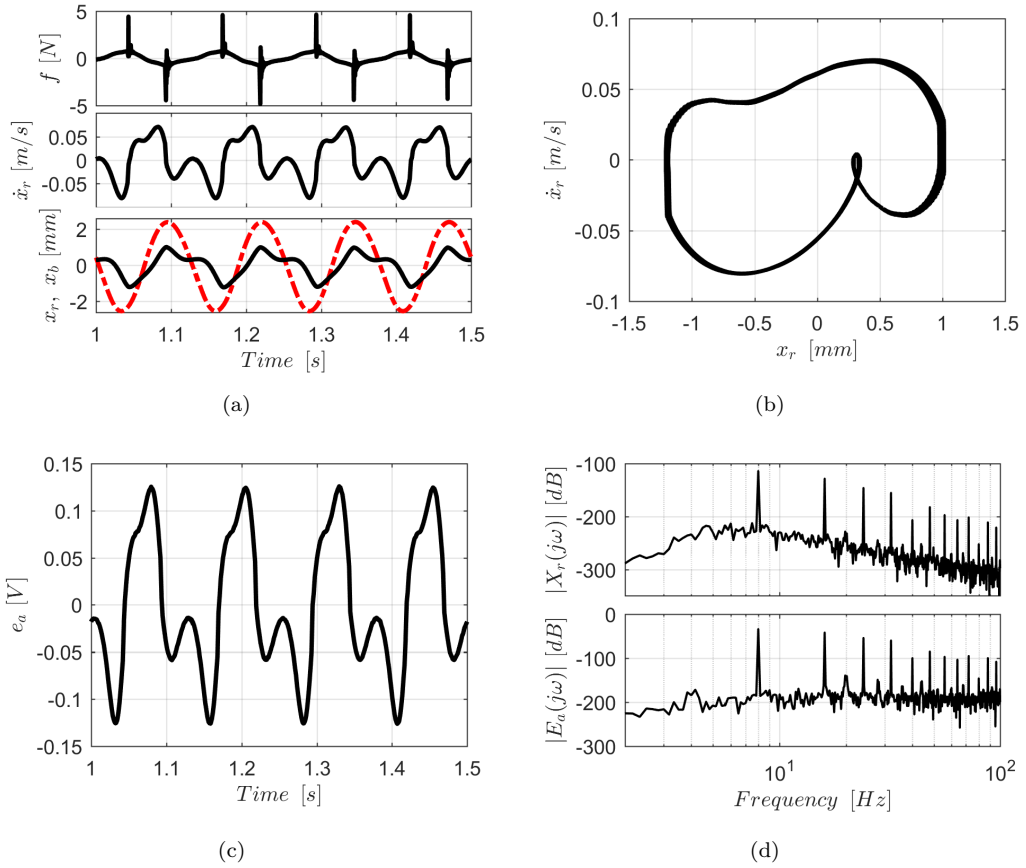

FIGURE 3.13: Detection of the nonlinearity with a harmonic excitation at 8 Hz. (a) Waveforms of the force at the base, relative proof mass velocity and displacement (solid black line) and input base displacement (dash-dotted red line); (b) Phase-space trajectory of the proof mass; (c) Waveform of the back-emf; (d) Spectrum of the relative displacement and back-emf.

out using a sine-sweep excitation with different amplitudes. The first test was to compare the sweep-up and the sweep-down excitations looking for hardening or softening behaviour of the suspension. The results for an input base excitation of 0.65 mm are presented in figure 3.14. The sweep-up and sweep-down time histories are shown with the black and the grey lines, respectively. The response to the sweep-up excitation from 5 Hz to 25 Hz at 40 Hz/min is characterised at low frequency by a displacement limit that flattens the response over a range of frequencies. The amplitude of the response remains bounded within these limits until the excitation frequency reaches 20 Hz, when a sudden jump down to a lower level can be observed. This nonlinear effect is referred to as the jump phenomenon and is peculiar of systems with hardening stiffness nonlinearities [99–101]. For frequencies higher than the jump, the response amplitude decreases proportionally to the inverse of the frequency. The sweep-down response in figure 3.14 presents a similar behaviour, but the amplitude jump occurs at a lower frequency than the one during the sweep-up. In this case the jump is from a lower to a higher amplitude, as the plot of the sweep-down response should be read from right to left. This confirms

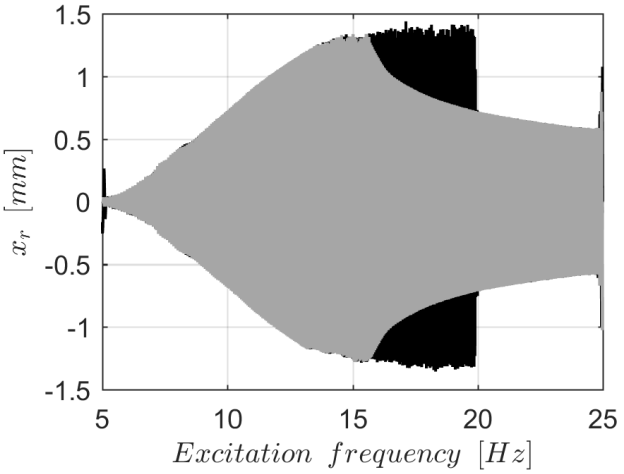

FIGURE 3.14: Time history of the relative proof mass displacement due to a sine sweep excitation with a base displacement input of 0.65 mm. Solid black (solid grey) line for the sweep-up (down) response from 5 Hz (25 Hz) to 25 Hz (5 Hz) at 40 Hz/min (-40 Hz/min).

that the actuator being investigated is characterised by a hardening stiffness behaviour. Another analysis has been done to compare the responses to a sweep-up excitation at different amplitude levels. The response to the highest level of excitation (x_b =0.65 mm) has been compared to the response at a lower level of excitation (x_b =0.10 mm) and the result is shown in figure 3.15. It is noted that the two responses are entirely different, being the response to a high amplitude excitation nonlinear and characterised by the jump phenomenon described before. The response to the low amplitude excitation, instead, presents an envelope that is a typical linear FRF for a SDoF system. This shows that the resonance frequency of the inertial actuator shifts to higher frequencies as the excitation level increases. The sine sweep signals can be further analysed in frequency domain. Classical Fourier transform cannot be applied for this analysis, as the excitation is non-stationary and the response is nonlinear, hence the Fourier transform would not be able to capture the time-varying frequencies. The wavelet transform, instead, highlights the harmonic components generated by the nonlinearity by mapping the time series into a time-frequency representation [148]. The wavelet transform of a signal is defined as [149–151],

$$X_r(a,b) = \frac{1}{\sqrt{a}} \int_{-\infty}^{+\infty} x_r(t) \psi \left(\frac{t-b}{a} \right) \mathrm{d}t, \tag{3.29}$$

where $X_r(a,b)$ is the time-frequency representation of the signal, in which the time lies along the x-axis and the instantaneous frequency along the y-axis. Hence, the variable b locates the observation window of the wavelet transform in the time domain, whereas a defines the frequency resolution by expanding or contracting the window. The function $\psi(\cdot)$, namely the mother wavelet, is the windowing function. The wavelet analysis in this thesis is performed using the NI2D software toolbox developed by NOLISYS at the

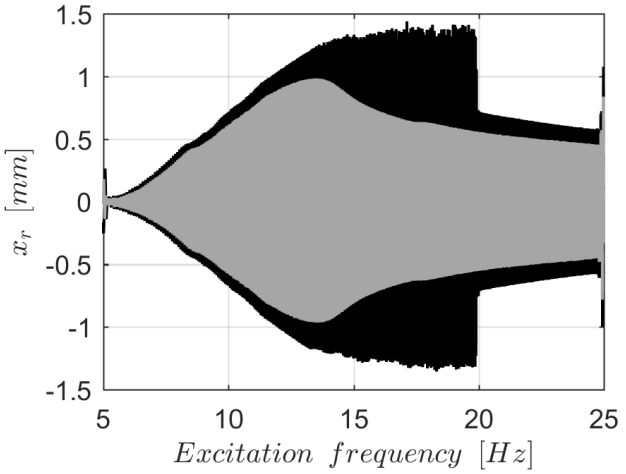

FIGURE 3.15: Time history of the relative proof mass displacement due to a sine sweep-up from 5 Hz to 25 Hz at 40 Hz/min for different levels of base excitation. Solid black line for the response to the highest level (x_b =0.65 mm); solid grey line for the response to a lower level (x_b =0.10 mm).

University of Liège (Belgium) [152], which involves a Morlet mother wavelet of the type,

$$\psi(t) = e^{\frac{t^2}{2}}\ e^{j\omega t}, \tag{3.30}$$

which is a Gaussian-windowed complex sinusoid. The amplitude of the wavelet transform of the time-series shown in figure 3.15 for the response to a sweep-up excitation at both low and high amplitude level is shown in figure 3.16. These plots are the amplitude of the instantaneous frequency of the response (y-axis) versus the duration of the sine sweep excitation (x-axis). Since there is a linear relationship between the time and frequency of the excitation, the x-axis has been conveniently converted to show the excitation frequency. Figure 3.16(a) shows the amplitude of the wavelet transform at low excitation level. The response is characterised by a strong presence of the fundamental frequency, but also there are contributions from the second and third harmonics. This is particularly true at frequencies between 8 Hz and 15 Hz, where the system is close to resonance and experiences larger amplitude of motion. Thus, the model of the suspension could be chosen to be a polynomial function of the 3^{rd} order. Increasing the level of excitation drives the actuator into stroke saturation, hence experiencing a stronger nonlinearity. The amplitude of the wavelet transform at high excitation level is shown in figure 3.16(b). The response is characterised by a wideband frequency components, which indicates the presence of impacts, hence a non-smooth nonlinearity. This harsh nonlinearity can be modelled using a piecewise function. Figure 3.16(b) also shows that the response is dominated by the fundamental frequency component for frequencies above the jump phenomenon at 20 Hz, where a linear model would be a good representation of the dynamic behaviour of the actuator.

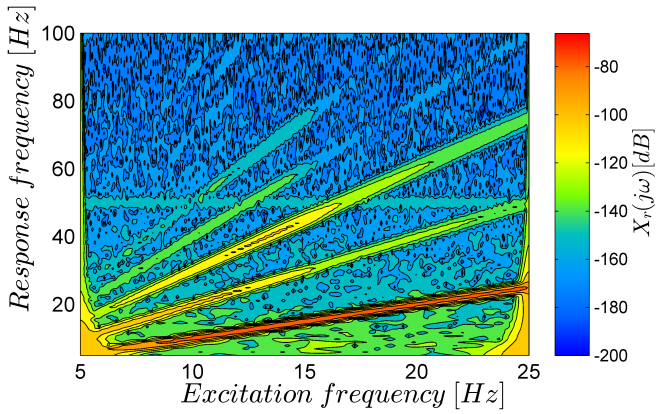

(a)

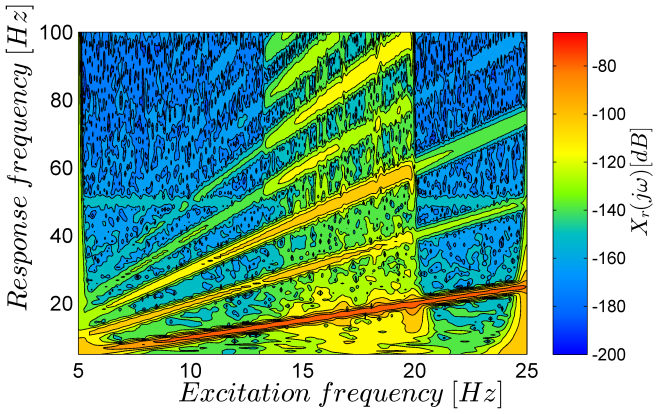

(b)

FIGURE 3.16: Amplitude of the wavelet transform of the relative proof mass displacement due to a sine sweep-up from from 5 Hz to 25 Hz at 40 Hz/min for different levels of base excitation. (a) For an excitation amplitude x_b =0.10 mm; (b) for an excitation amplitude x_b =0.65 mm.

3.4.3 Identification

In this section, the identification of the nonlinear parameters of the model is carried out. For this purpose the sine-sweep experiments are used and the data is processed using the restoring force method [99–101]. Since the actuator is open-circuit, from eq. (3.26b)

it follows that the restoring force of the actuator in figure 3.12 can be written as,

$$f_{RF}(\dot{x}_r, x_r) = m_b \ddot{x}_b(t) - f(t), \tag{3.31}$$

which can be easily calculated at each time step since m_b is already known from the underlying linear identification analysis and $\ddot{x}_b(t)$ and $f(t)$ are measured using an accelerometer and a force gauge as discussed in section 3.1. Considering eq. (3.26a) and remembering that the actuator is open-circuit, the restoring force can also be written as,

$$f_{RF}(\dot{x}_r, x_r) = -m_p \ddot{x}_p(t), \tag{3.32}$$

hence, equating the right-hand sides of eqs. (3.31) and (3.32) results,

$$\ddot{x}_r(t) = \ddot{x}_p(t) - \ddot{x}_b(t) = \frac{f - (m_b + m_p)\,\ddot{x}_b(t)}{m_p}. \tag{3.33}$$

In this way the relative proof mass acceleration can be calculated at each time step and the velocity and displacement can also be computed by high-pass filtering and integrating the acceleration signal. Using eqs. (3.31) and (3.33) the experimental data points of the restoring force can be plotted in the phase-space, as shown in figure 3.17 for the largest amplitude of excitation. In particular, figure 3.17(a) shows the data for the entire sine-sweep experiment, figure 3.17(b), instead, shows the restoring force of a few cycles of the proof mass when the excitation frequency is close to the actuator's resonance. If the actuator had a linear dynamic behaviour, all the data points in figure 3.17 would have lied on a plane tilted of a constant k_p slope with respect to one axis and a constant slope c_p with respect to the other axis. Although the restoring force measurements in figure 3.17(a) show that the actuator behaves in a linear manner when the proof mass is clear from the end-stops, it can be observed that the restoring force suddenly steepens as the proof mass collides with the end-stops. Moreover, the velocity quickly changes sign during stroke saturation and the proof mass can also experience multiple impacts as shown in figure 3.17(b) (double impact). In order to identify the parameters of the nonlinear model of the inertial actuator, an assumption needs to be made, that is,

$$f_{RF}(\dot{x}_r, x_r) = f_{RF,v}(\dot{x}_r) + f_{RF,d}(x_r) \tag{3.34}$$

hence, the contribution of the damping and elastic restoring forces can be separated. Assuming eq. (3.34) means that the elastic restoring force can be represented as a section of figure 3.17(a) at velocities that are close to zero. Similarly, the damping restoring force can be displayed by taking a section of figure 3.17(a) at displacements close to zero. The scattered data plot of the measured elastic restoring force is shown in figure 3.18 with the black dots and two different models are proposed for it. The fitted model shown in figure 3.18(a) with the dash-dotted cyan line is polynomial of the third order for displacements smaller than the maximum stroke and a non-smooth function with a very large stiffness for displacements exceeding the stroke. A simpler model can also

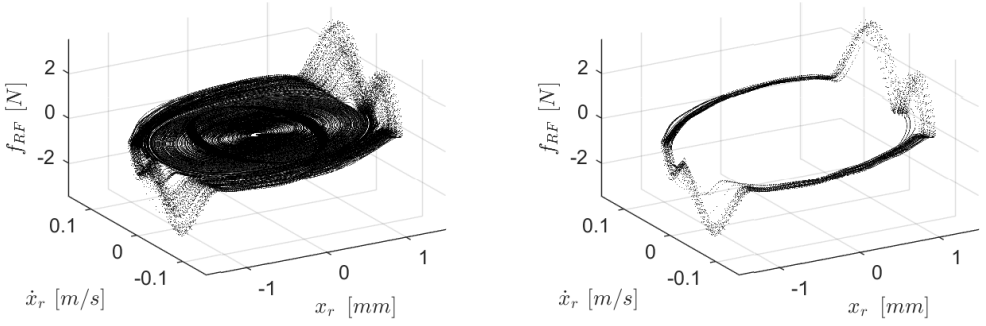

(a) (b)

FIGURE 3.17: 3D restoring force data points in the phase-space for a sine sweep excitation. (a) Entire sweep-up experiment from 5 Hz to 25 Hz at 40 Hz/min; (b) Only a few cycles close to the actuator resonance.

be fitted to the measurements, which is a piecewise linear function and is shown in figure 3.18(b) with the solid red line. The piecewise linear model will be considered for the rest of the study as it is simpler than the polynomial one and can still consider the stroke saturation nonlinearity, which is a major source of nonlinearity for the elastic restoring force compared to the weak polynomial nonlinearity of the suspension. The elastic restoring force of the fitted piecewise linear model shown in figure 3.18(b) with the solid red line can be written as,

$$f_{RF,d}(x_r) = \begin{cases} k_{sat}(x_r - x_0) + p_1 x_0 + p_2 & x_r \geq x_0 \quad (3.35a) \\ p_1 x_r + p_2 & |x_r| < x_0 \,, \quad (3.35b) \\ k_{sat}(x_r + x_0) - p_1 x_0 + p_2 & x_r \leq -x_0 \quad (3.35c) \end{cases}$$

where the parameters appearing in eq. (3.35) are p_1 =230 N/m, p_2 =0 N, k_{sat} =$2{\cdot}10^4$ N/m and x_0 =1.25 mm. It should be noticed that the end-stops in figure 3.18 are represented by tilted lines instead of vertical lines and this is because the experimental data describes the end-stops with a finite stiffness. The two end-stops have been found to have slightly different stiffness coefficients. For the sake of simplicity, the mean value of the two has been considered for both end-stops.

The scattered data plot of the damping restoring force is shown in figure 3.19. It can be observed that the experimental data points of the damping restoring force are well fitted by a linear model, which is shown with a solid red line and can be written as,

$$f_{RF,v}(\dot{x}_r) = p_1 \dot{x}_r + p_2, \quad (3.36)$$

where the parameters appearing in eq. (3.36) are p_1 =1.4 N/ms^{-1} and p_2 =0 N.

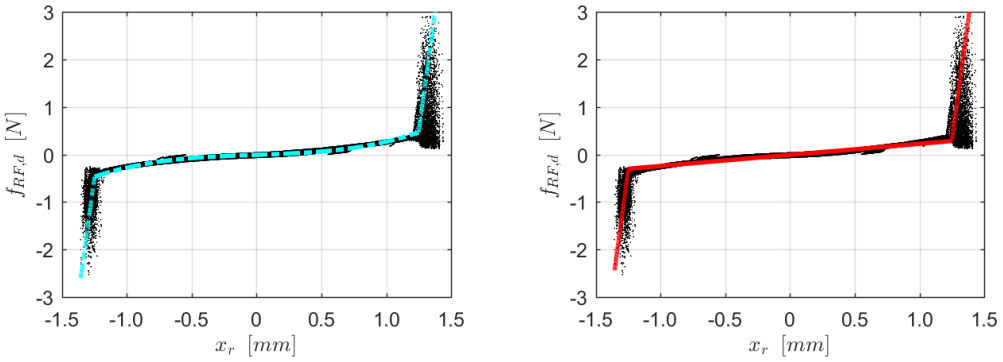

FIGURE 3.18: Model identification of the elastic restoring force experimental data (black dots). (a) Fitted cubic stiffness model with saturation (dash-dotted cyan line); (b) Fitted piecewise linear model (solid red line).

Since the actuator is open-circuit, from eq. (3.27) it follows that the transduction factor can be calculated as,

$$\phi(x_r(t)) = \frac{e_a(t)}{\dot{x}_r(t)}, \tag{3.37}$$

which can be easily calculated at each time step since both $e_a(t)$ and $\dot{x}_r(t)$ are measured. However, the values of the transduction coefficient for very small velocities should be neglected as they tend to infinity due to the division by zero in eq. (3.37). The scattered data plot of the transduction coefficient versus the proof mass displacement in shown in figure 3.20. It can be seen that the behaviour of the transduction coupling is polynomial and symmetric. The peak value is reached for the proof mass in centred position, whereas moving towards the end-stops leads to a slight decrease of the transduction coupling factor. From this scattered data plot a nonlinear model can be fitted, which is polynomial of the second order. The fitted model is shown in figure 3.20 with a solid red line and can be written as,

$$\phi(x_r) = p_1 x_r^2 + p_2 x_r + p_3, \tag{3.38}$$

where the parameters appearing in eq. (3.37) are p_1 =-300 kN/Am^2, p_2 =-6.5 N/Am and p_3 =1.8 N/A.

3.5 Summary

In this chapter an experimental investigation on the nonlinear behaviour of an inertial actuator has been presented. Firstly, the experimental set-up has been described, which consists of the base excitation and direct excitation experiments. Secondly, the underlying linear model parameters have been identified by comparing the measured

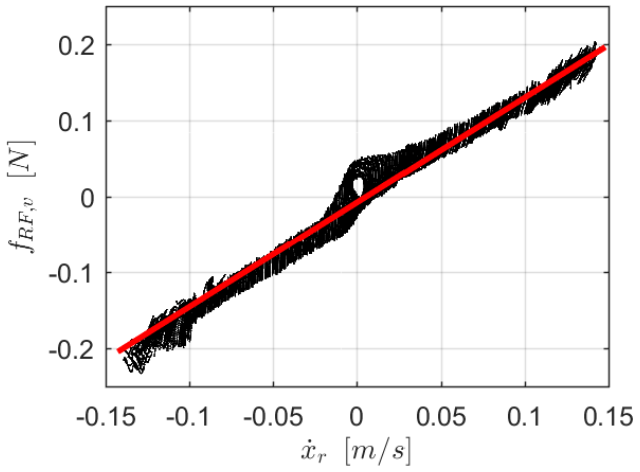

FIGURE 3.19: Model identification of the damping restoring force experimental data (black dots). The fitted model is shown with the solid red line.

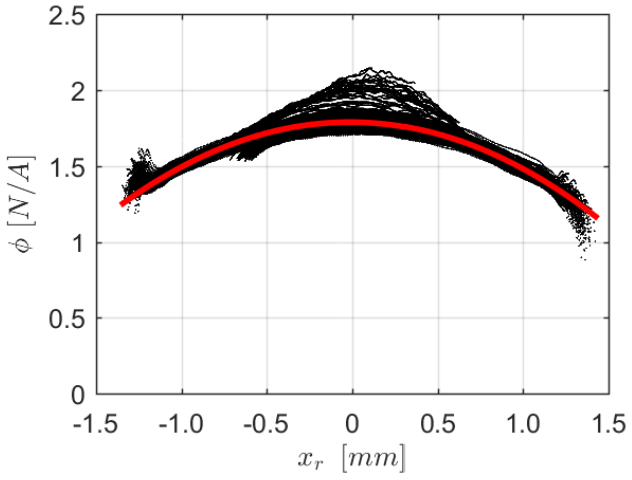

FIGURE 3.20: Model identification of the transduction coefficient. Experimental data (black dots) and fitted model (solid red line).

and analytical transmissibilities, mechanical and electrical impedances of the inertial actuator applying small excitation signals that do not activate the nonlinearity. The inductance losses due to the eddy currents in the magnetic pole have also been investigated due to the discrepancy of the measured and modelled electrical impedance at high frequency, resulting in a lossy inductor model that gives a better agreement. The operating range of the inertial actuator in terms of maximum force delivered in the frequency range of interest has been discussed. It is shown that the maximum force at relatively low frequency is limited by the actuator stroke constraints and above the saturation cut-off frequency is limited by the maximum electrical power that can be fed to the device or by the maximum temperature. Consequently, the nonlinear behaviour of the inertial actuator has been investigated, starting from the detection of the nonlinearity, through its characterisation, and then to the identification of the nonlinear parameters. The nonlinear characterisation analysis showed a wide band of high frequency content in the

instantaneous frequency response to a sine-sweep excitation that is caused by the impacts between the proof mass and the end-stops. This led to a non-smooth model of the nonlinearity, which is a piecewise linear function fitted to the elastic restoring force experimental data. The damping restoring force and the transduction coefficient, instead, have been fitted to the experimental data with a linear and a polynomial quadratic models, respectively. The nonlinear parameters have been identified using the restoring force method and the back-emf signal. In particular, the clearance between the end-stops and the saturation stiffness have been determined.

Chapter 4

Simulation analysis of nonlinear dynamics of inertial actuators

The experimental study presented in chapter 3 was aimed at providing an accurate nonlinear lumped parameter model of the inertial actuator under investigation. This chapter compares the dynamic behaviour of the nonlinear inertial actuator model with its underlying linear one, via numerical simulations in both time and frequency domains. Although several sources of nonlinearity in the actuator have been identified, only stroke saturation nonlinearity is considered in this study. A time domain model of the inertial actuator is derived and solved via numerical integration in section 4.1, where stroke saturation has been modelled as a piecewise linear function accordingly to the study in section 3.4. Many researchers have explored SDoF systems with piecewise linear characteristics in the past and in recent years [84–87; 112–116; 153] focusing mainly on multi-stability of the coexisting periodic solutions. However, the main objective of this study is to compare the blocked response of the inertial actuator using linear and nonlinear models under the same excitation conditions and to derive some general conclusions on how stroke saturation can affect the dynamic behaviour of the actuator. The results of the time domain analysis are then compared with the frequency domain solution using the harmonic balance method (HBM) in section 4.2, where the nonlinear effects, such as the jump response, are explained. The nonlinear frequency response curves and the frequency-amplitude diagrams are also investigated.

4.1 Numerical integration of the equation of motion

A lumped parameter model of the inertial actuator with stroke limits is shown in figure 4.1, where the device is mounted on a rigid frame. The parameters of the actuator appearing in the figure have already been introduced in section 3.2. The stroke limits are modelled as elastic end-stops of stiffness k_c and positioned at half of the stroke length

x_0 away from the resting position of the proof mass, in accordance with the study of section 3.4. The equation of motion of the proof mass displayed in figure 4.1 can be

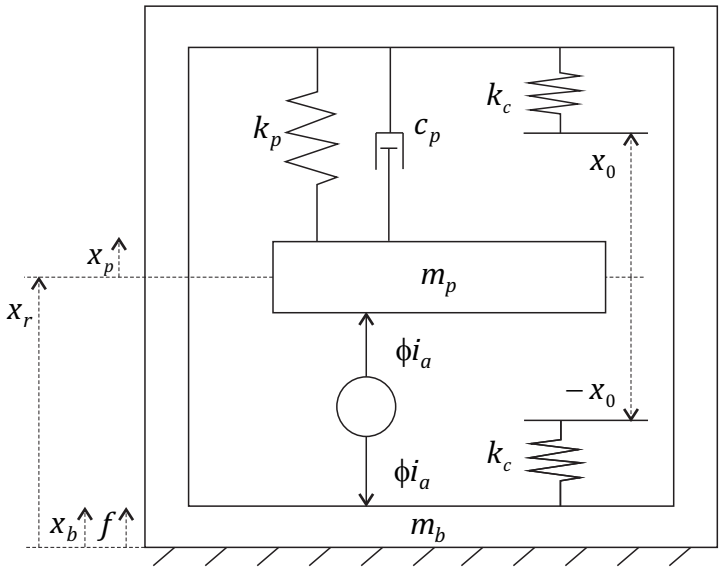

FIGURE 4.1: Lumped parameter model of the inertial actuator with elastic end-stops.

written as,

$$m_p\ddot{x}_p(t) + c_p\dot{x}_r(t) + f_{RF,d}(x_r(t)) = \phi i_a, \tag{4.1}$$

which is derived from eq. (3.26a) with the assumptions of a linear transduction coefficient, a linear damping and a nonlinear elastic restoring force $f_{RF,d}(x_r(t))$. The piecewise linear stiffness model has been identified in section 3.4 and is given by eq. (3.35), which can be rewritten as,

$$f_{RF,d}(x_r(t)) = \begin{cases} k_{sat}(x_r(t) - x_0) + k_p x_0 & x_r(t) \geq x_0 & \text{(4.2a)} \\ k_p x_r(t) & |x_r(t)| < x_0\,. & \text{(4.2b)} \\ k_{sat}(x_r(t) + x_0) - k_p x_0 & x_r(t) \leq -x_0 & \text{(4.2c)} \end{cases}$$

where k_p is the linear suspension stiffness and k_{sat} is the saturation stiffness experienced by the proof mass when exceeding the stroke length, which is given by,

$$k_{sat} = k_c + k_p, \tag{4.3}$$

in accordance with the model in figure 4.1. Equation (4.2) is also represented in figure 4.2 with the solid black line and is compared to the underlying linear model in figure 4.2 with the dashed blue line. It should be noted that if the end-stop stiffness is zero ($k_c = 0$), the nonlinear stiffness model given by eq. (4.2) becomes equivalent to the underlying linear model. Dividing eq. (4.2) by the proof mass relative displacement results in,

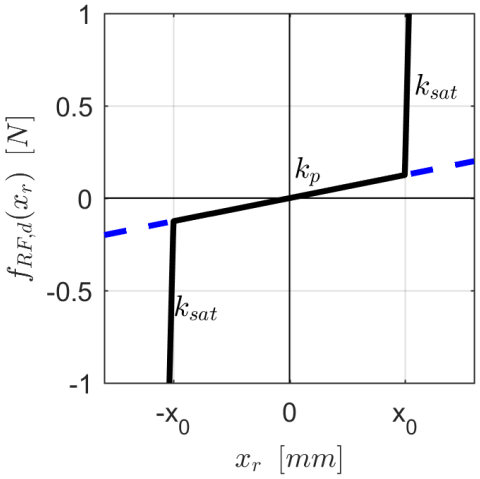

FIGURE 4.2: Elastic restoring force of the stroke limited inertial actuator (solid black line) and the underlying linear actuator (dashed blue line).

$$\kappa(x_r(t)) = f_{RF,d}(x_r(t))/x_r(t) = \begin{cases} k_{sat} + \dfrac{k_p x_0 - k_{sat} x_0}{x_r(t)} & x_r(t) \geq x_0 \quad (4.4a) \\ k_p & |x_r(t)| < x_0\,, \quad (4.4b) \\ k_{sat} + \dfrac{k_{sat} x_0 - k_p x_0}{x_r(t)} & x_r(t) \leq -x_0 \quad (4.4c) \end{cases}$$

where $\kappa(x_r(t))$ is a nonlinear parameter, which is conveniently introduced to further analyse the nonlinear eq. (4.1). Substituting eq. (4.3) into eq. (4.4) gives,

$$\kappa(x_r(t)) = \begin{cases} k_{sat} - k_c \dfrac{x_0}{x_r(t)} & x_r(t) \geq x_0 \quad (4.5a) \\ k_p & |x_r(t)| < x_0\,. \quad (4.5b) \\ k_{sat} + k_c \dfrac{x_0}{x_r(t)} & x_r(t) \leq -x_0 \quad (4.5c) \end{cases}$$

Using again eq. (4.3), eq. (4.5) can be finally written as,

$$\kappa(x_r(t)) = \begin{cases} k_p & |x_r(t)| < x_0 \quad (4.6a) \\ k_p + k_c(1 - \dfrac{x_0}{|x_r(t)|}) & |x_r(t)| \geq x_0\text{,} \quad (4.6b) \end{cases}$$

and the equation of motion given by eq. (4.1) becomes,

$$m_p \ddot{x}_p(t) + c_p \dot{x}_r(t) + \kappa(x_r(t)) x_r(t) = \phi i_a. \quad (4.7)$$

Since the actuator is blocked $\ddot{x}_r = \ddot{x}_p$ and eq. (4.7) can be cast in a state space form as follows,

$$\begin{cases} \dot{\mathbf{x}} = \mathbf{A}(\mathbf{x})\mathbf{x} + \mathbf{B}u & (4.8a) \\ y = \mathbf{C}\mathbf{x} & (4.8b) \end{cases},$$

in which the state vector is defined as,

$$\mathbf{x} = \{x_r \ \dot{x}_r\}^T, \tag{4.9}$$

where the superscript T denotes the transpose of the vector. The system matrix $\mathbf{A}$ can be written as,

$$\mathbf{A} = \begin{bmatrix} 0 & 1 \\ -\frac{\kappa(x_r)}{m_p} & -\frac{c_p}{m_p} \end{bmatrix}, \tag{4.10}$$

where the nonlinear stiffness $\kappa(x_r)$ is given by eq. (4.6). The input is given by,

$$u = i_a, \tag{4.11}$$

and the input matrix $\mathbf{B}$ results in,

$$\mathbf{B} = \begin{bmatrix} 0 \\ \frac{\phi}{m_p} \end{bmatrix}. \tag{4.12}$$

The system output is defined as,

$$y = x_r, \tag{4.13}$$

hence the output matrix becomes,

$$\mathbf{C} = [1 \ 0]. \tag{4.14}$$

The state space eq. (4.8) has been solved numerically using the Nonlinear Identification to Design software (NI2D®), which is a MatLab toolbox developed by NOLISYS [152] that uses a Newmark method for the numerical integration of the equations of motion. A comparison among different methods of numerical integration can be found in [107] and in appendix C. The parameters used in the numerical simulations are the piecewise linear model parameters of eq. (3.35) for the nonlinear stiffness and the underlying linear model parameters given in table 3.1. The numerical analysis is performed considering a sine-sweep-up (-down) current excitation from 5 Hz (25 Hz) to 25 Hz (5 Hz) with a sweep rate of 1 Hz/min (-1 Hz/min) and zero initial conditions, using a sampling frequency $f_s = 10$ kHz and a constant amplitude excitation over the whole frequency range. It should be noted that the linear relationship between time and frequency of the sine sweep excitation allows us to display the results of the numerical analysis using either frequency or time as the x-axis dimension. Figure 4.3 shows the response of the proof mass to a sine sweep excitation using an input current $i_a = 62.5$ mA for the underlying linear actuator (solid blue line), the nonlinear actuator during a sweep-up (solid black line) and the nonlinear actuator during a sweep-down (solid grey line). Figure 4.3 shows that the envelope of the linear response is comparable to the underlying linear FRF of the system, with a resonance at around 9 Hz, but it overshoots the stroke length of the actuator using this level of excitation. The nonlinear response of the system

presents a different behaviour, in fact, the response at low frequency is bounded by the displacement saturation, hence it is lower in amplitude when compared with the linear response for both the sweep-up and sweep-down excitations. There is a small frequency

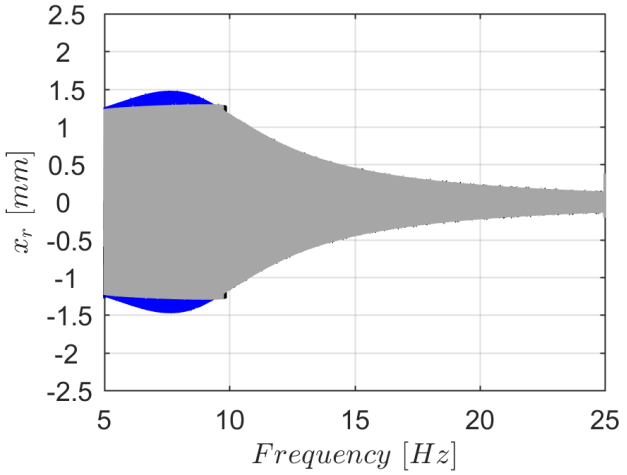

FIGURE 4.3: Time histories of the proof mass response to a sine sweep excitation with a current $i_a = 62.5$ mA. The solid blue line displays the response of the underlying linear system; the solid black line shows the response of the nonlinear system during the sweep-up; and the solid grey line shows the response of the nonlinear system during the sweep-down.

range between 9 Hz and 10 Hz in which the amplitude of the nonlinear response becomes higher than the linear response. This is more evident in figure 4.4 where the response of the proof mass to a sine sweep excitation using an higher input current $i_a = 100$ mA is shown. In this case, the frequency band in which the amplitude of the nonlinear response is higher than the linear response ranges from 12 Hz to 14.5 Hz for the sweep-up excitation and from 12 Hz to 12.5 Hz for the sweep-down excitation. What happens is that at low frequency the nonlinear system during each cycle experiences a mean stiffness that is higher than the one experienced by the linear system because of the piecewise linear stroke saturation model, moreover, every next cycle is the response to an increased excitation frequency in which the initial conditions are not zero, but the final conditions of the previous cycle. If these initial conditions at each cycle give to the system a sufficient amount of energy, the sweep-up response keeps the nonlinear system on saturating in stroke until the nonlinear resonance frequency for that particular excitation level is reached. A slight increment in frequency above the nonlinear resonance causes the response to jump down to a lower amplitude level that coincides with the linear response, because the initial conditions at this frequency of the sine sweep are no longer sufficient to maintain the system at higher stiffness. This is referred to as the jump phenomenon [99]. The sweep-down response presents a similar behaviour, but the jump occurs at a lower frequency and it is indeed a jump up to a higher amplitude as in this case the plot should be read from right to left and the system experienced a linear response before the jump. Comparing figure 4.4 with figure 4.3 shows that increasing the excitation level increases the jump frequency and widens the range between the jump up

and jump down frequencies. Figure 4.5 shows the waveforms of the response illustrated

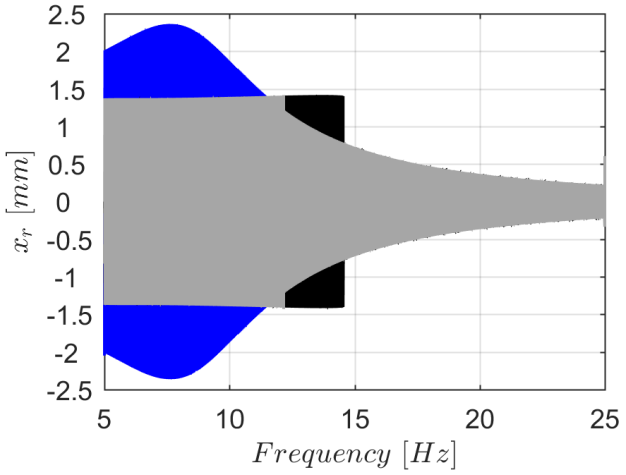

FIGURE 4.4: Time histories of the proof mass response to a sine sweep excitation with a current $i_a = 100$ mA. The solid blue line displays the response of the underlying linear system; the solid black line shows the response of the nonlinear system during the sweep-up; and the solid grey line shows the response of the nonlinear system during the sweep-down.

in figure 4.4 by zooming in three narrow frequency bands. In particular, figure 4.5(a) shows the waveforms of the linear response (solid blue line), nonlinear sweep-up (solid black line) and nonlinear sweep-down (solid grey line) for an excitation around 5 Hz. The nonlinear response is characterised by high frequency contents when the end-stops are hit and by the fundamental frequency when moving from one stroke end to the other. Moreover, a single collision each time the end-stops are reached can be observed. The sweep-up and sweep-down responses are identical apart for a 180° phase shift due to zero initial conditions given to the sweep-down response. Figure 4.5(b) shows the waveforms of the three responses when the excitation is around the jump down frequency. In fact, the figure shows identical sweep-down nonlinear response and linear response, whereas the sweep-up nonlinear response is characterised by a higher oscillation amplitude such that the response quickly reduces at around 14.55 Hz to match the linear response. The waveforms of the response for frequencies higher than the jump down frequency are all harmonic at the fundamental excitation frequency, as shown in figure 4.5(c).

A better insight of the nonlinear behaviour can be obtained by applying the wavelet transform to the sweep-up response of figure 4.4 as it has been done in section 3.4 for the experimental investigation. The amplitude of the wavelet transform is calculated using the simulated time signal shown in figure 4.4 and eqs. (3.29) and (3.30), where the calculation has been performed using the NI2D® software. The result is shown in figure 4.6, where the plot can be divided into two regions of different behaviour. Below 15 Hz the response is characterised by a high frequency content due to the non-smooth nonlinearity introduced by the piecewise linear model and the activation of many odd harmonics due to the symmetry of the nonlinear model. In particular, the 3^{rd} and 5^{th}

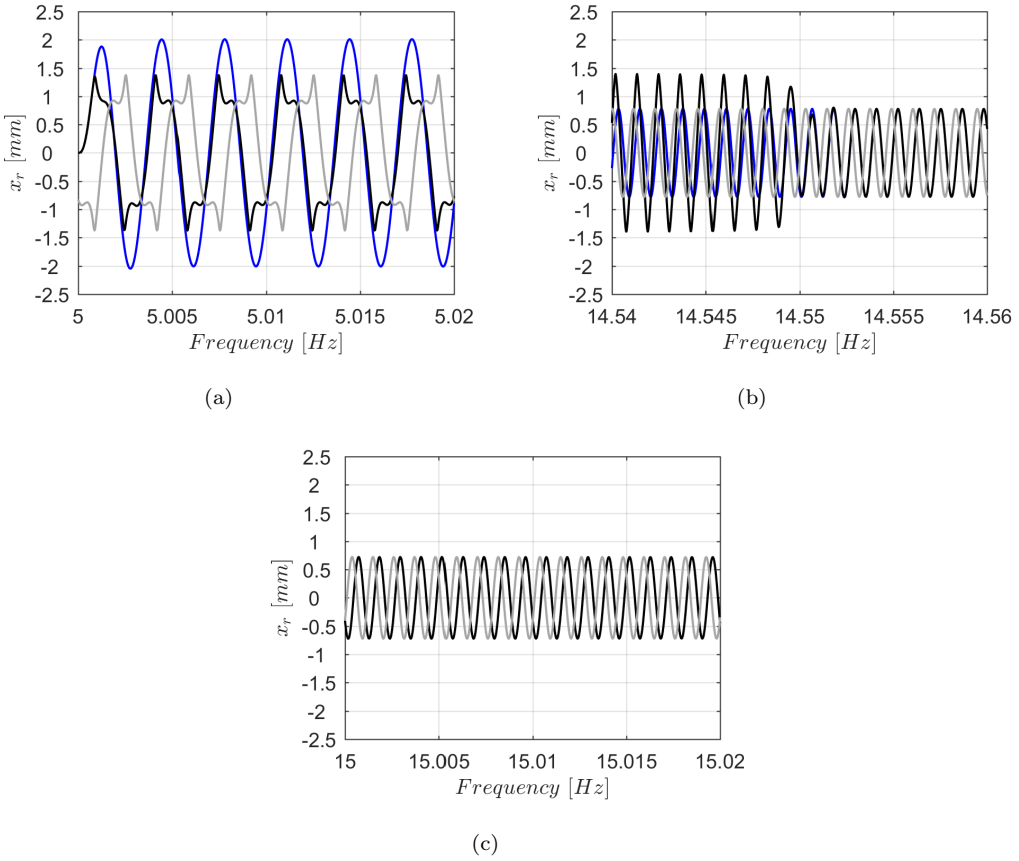

FIGURE 4.5: Waveforms of the simulated response during the sine sweep excitation shown in figure 4.4. The solid blue line displays the response of the underlying linear system; the solid black line shows the response of the nonlinear system during the sweep-up; and the solid grey line shows the response of the nonlinear system during the sweep-down. (a) excitation frequency around 5 Hz; (b) excitation frequency around 14.55 Hz (when the jump phenomenon occurs); (c) excitation frequency around 15 Hz.

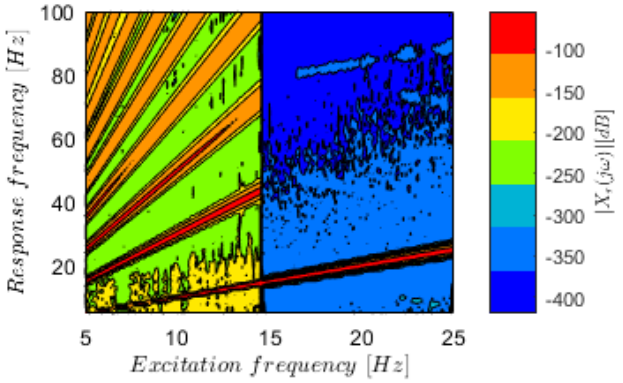

FIGURE 4.6: Amplitude of the wavelet transform of the proof mass response to the sine sweep-up excitation shown in figure 4.4. The sweep-down response produces the same graph, but with a lower jump frequency.

harmonics have an amplitude comparable to the fundamental component. The second region starts above the jump down frequency that is around 15 Hz. For frequencies

higher than the jump, the response is dominated by the fundamental component, hence indicating a linear regime of motion.

4.2 Harmonic balance method

A different approach to solve the nonlinear equation of motion given by eq. (4.7) is using the HBM for analysing the periodic solutions and comparing the nonlinear response with the underlying linear response in frequency domain. The method is explained in detail by Detroux et al. in [109], and it consists of calculating the periodic (steady state) solution of the system at each excitation frequency point. As it has been pointed out in the previous section, the non-smooth nonlinearity activates several harmonics, which need to be taken into account in the computation of the periodic solution. Hence, the frequency domain response of the nonlinear system cannot be a FRF, but instead a nonlinear frequency response curve (NFRC) that shows the maximum amplitude of the periodic solution at each frequency point. Simulation analysis involving the computation of periodic solutions are performed using the NI2D® software for this study, where the mathematical derivation of this approach can be found in [99; 109; 154]. Figure 4.7 shows the comparison between the NFRC shown with the solid red line and computed considering the harmonics up to the 5^{th}, and the time domain simulation of a sine sweep (solid black line for sweep-up and solid grey line for sweep-down) using an excitation level of $i_a = 100$ mA.

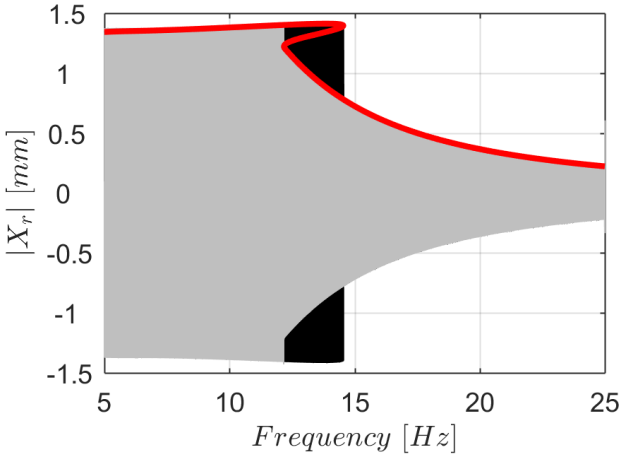

FIGURE 4.7: Comparison of the Newmark solution via integration of the equation of motion and the HBM. Solid black line for the Newmark sweep-up response; solid grey line for the Newmark sweep-down response; and solid red line for the HBM solution considering up to 5 harmonics.

Assuming that the time domain simulation is correct, it can be observed that the HBM is capable to fully predict the amplitude of the nonlinear response. Moreover, the fold bifurcation points [109] predicted by the HBM correspond to the jump frequencies of

the time domain analysis. It should be noted that for frequencies between 12.5 HZ and 14.5 Hz the HBM gives three coexisting solutions. The middle branch that lies between the two bifurcation points is an unstable solution for the proof mass motion and cannot be experienced in practice. The other two branches are stable periodic solutions, and the system can stabilise either to the upper or lower branch depending on the initial conditions for a given level of excitation (level of the input current).

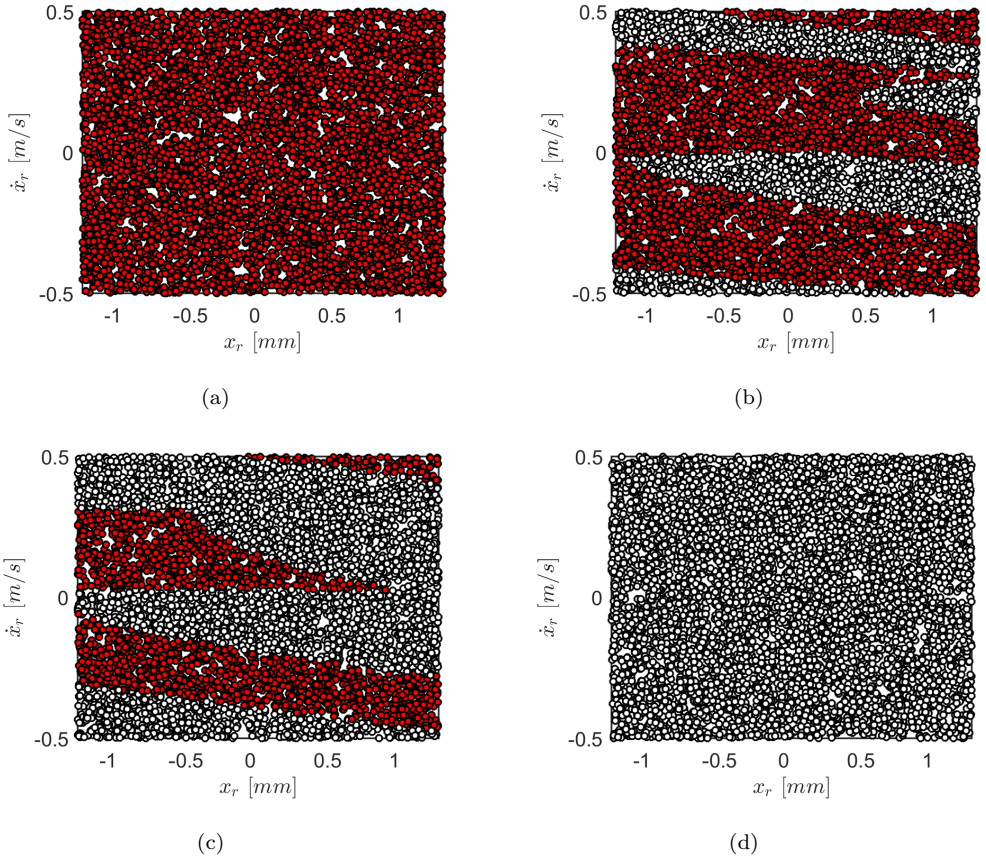

FIGURE 4.8: Basins of attraction for the NFRC of figure 4.7: (a) 12 Hz; (b) 13 Hz; (c) 14 Hz; (d) 15 Hz; initial conditions that stabilise the response on the upper branch are displayed with red circles, initial conditions that stabilise the response on the lower branch are displayed with white circles.

The basins of attraction for the NFRC of figure 4.7 at for different frequencies are shown in figure 4.8 and are computed using the global analysis method [101] using an excitation level of $i_a = 100$ mA for all of them. The figure represents the state space mapping of the initial conditions that lead the system to stabilise on each branch of the NFRC, when the system is harmonically excited. In particular, the red circles represent the initial conditions that lead the periodic solution of the equation of motion to stabilise on the upper branch, whereas the white circles represent the initial conditions that lead the system to stabilise on the lower branch. Figure 4.8(a) shows the basins of attraction at 12 Hz, where the solution is unique and lies on the upper branch. Increasing the frequency to 13 Hz causes both the attractors competing for the solution,

as shown in figure 4.8(b), where the solution is more likely to stabilise on the upper branch. Moreover, it can be noted that the initial condition on the velocity has a major influence on selecting which branch the solution will stabilise, regarding the initial displacement. At 14 Hz the basins of attraction of the upper branch becomes less dominant, as shown in figure 4.8(c), and ultimately, at 15 Hz all the initial conditions on the displacement and velocity lead to the unique solution on the lower branch, as shown in figure 4.8(d). As mentioned previously, the NFRC of figure 4.7 has been constructed considering 5 harmonics when calculating the periodic solutions. The participation factor of each harmonic component to the final periodic solution at each frequency point is shown in figure 4.9, where the fundamental component, the 3^{rd} harmonic and the 5^{th} harmonic are illustrated with the solid, dash-dotted and dashed red lines, respectively. The component participation is calculated as the ratio of the square of the component amplitudes divided by the sum of the square amplitudes, which corresponds to an energy ratio of each harmonic. Since the nonlinearity is symmetric, only the odd harmonics are present. Although the fundamental component is the one that contributes the most to the periodic solution and is the only one for frequencies above 14.5 Hz, the 3^{rd} and 5^{th} harmonics have a significant contribution when the system behaves nonlinearly. In particular, at 5 Hz the 3^{rd} harmonic contributes to the 6% and the 5^{th} harmonic to the 1% of the final periodic solution.

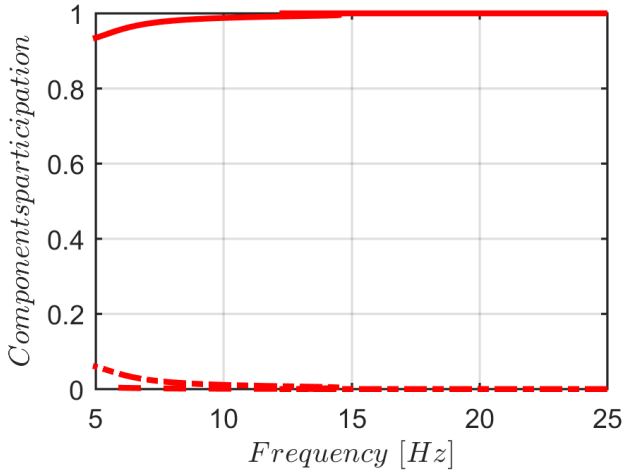

FIGURE 4.9: Energy ratio of components participation to the periodic solution for each frequency of the NFRC shown in figure 4.7. The components participation is calculated as the ratio of the square of the component amplitudes divided by the sum of the square amplitudes (from the fundamental up to the 5th). The fundamental, the third and fifth harmonics are shown with red solid, dash-dotted and dashed lines, respectively.

The numerical analysis enables one to test the actuator from low to very high level of excitation without destroying the actuator itself. Figure 4.10 shows a comparison between the NFRCs (black solid line) at increasing level of excitation, from 25 mA to 162.5mA with an increment of 12.5 mA for each simulation. It can be observed that for the three lowest level of excitation the proof mass displacement does not exceed

the stroke limits, hence the system is within its linear range and the NFRCs are effectively linear FRFs. The resonant frequency of the inertial actuator is invariant until the actuator encounters the nonlinearity. An increment in the input current causes the response to become nonlinear and the nonlinear resonant frequency shifts monotonically towards higher frequencies, as shown in figure 4.10 by the backbone curve that connects the resonant frequencies at increasing excitation levels (red circles connected by the red dash-dotted line). The amplitude of the resonance peaks for the nonlinear response, however, are proportionally lower than the resonance peak of the underlying linear response. This results in the NFRCs becoming particularly skewed towards higher frequency with respect to the linear FRFs. The values of the response are seen to be larger than the stroke length for certain values of the excitation. This is due to the finite stiffness of the end-stops as well as the excitation level being larger than the one used in the experimental investigation. A comparison between the linear and nonlin-

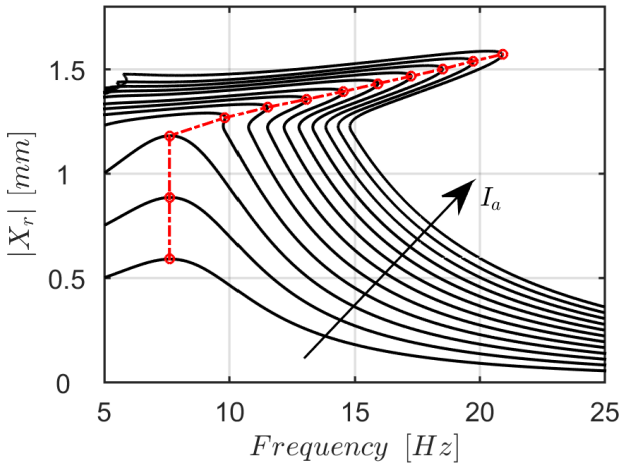

FIGURE 4.10: Linear FRFs and NFRCs for increasing excitation levels (solid black line); the actuator resonance frequency and its modification (backbone curve) with the amplitude level are shown with the red circles and the dash-dotted red line.

ear resonant frequency can be done in terms of either the response amplitude or the excitation amplitude. An interesting study is to apply the HBM to eq. (4.1) with a single harmonic approximation [99], hence, considering a harmonic excitation of a given amplitude, eq. (4.1) is linearised and in particular the elastic restoring force eq. (4.2) is written as,

$$f_{RF,d}(x_r) \simeq K_{eq}(\omega, X_r)x_r, \tag{4.15}$$

where $K_{eq}(\omega, X_r)$ is the equivalent stiffness for a given operating condition. Hence, eq. (4.1) can be transformed in frequency domain and results in,

$$\left[-m_p\omega^2 + j\omega c_p + K_{eq}(\omega, X_r)\right] X_r(j\omega) = \phi I_a(j\omega). \tag{4.16}$$

With this approximation a first-order FRF between the input phase-shifted excitation $\phi i_a(t) = \phi I_a \sin(\omega t - \varphi)$ and the trial solution $x_p(t) = X_p \sin(\omega t)$ can be obtained as,

$$\Lambda(\omega, X_r) = \frac{X_r(j\omega)}{\phi I_a(j\omega)} = \frac{1}{-m_p\omega^2 + j\omega c_p + K_{eq}(\omega, X_r)}, \tag{4.17}$$

where $\Lambda(\omega, X_r)$ denotes the amplitude dependent first-order FRF of the nonlinear system. HBM is applied by expanding a Fourier series of eq. (4.2) and imposing a harmonic solution for the proof mass displacement. The equivalent stiffness can be calculated considering only the fundamental term of the Fourier expansion and neglecting the higher harmonics generated by the nonlinearity. This can be written as,

$$K_{eq}(\omega, X_r) = g_1(\omega, X_r) + jb_1(\omega, X_r), \tag{4.18}$$

where $g_1(\omega, X_r)$ and $b_1(\omega, X_r)$ are the fundamental terms of the Fourier expansion. Noting that the restoring force is and odd function, thus only one Fourier term is not zero, results in,

$$K_{eq}(\omega, X_r) = g_1(\omega, X_r) = \frac{1}{\pi X_r} \int_0^{2\pi} f_{RF,d}\left(X_r \sin(\theta)\right) \sin(\theta) \mathrm{d}\theta, \tag{4.19}$$

where ωt has been replaced by,

$$\theta = \omega t, \tag{4.20}$$

It should be noted that the integrand of eq. (4.19) changes two times during one cycle of oscillation if $|X_p \sin(\omega t)|$ exceeds x_0, due to the piecewise linear model of eq. (4.2). This can be considered in the integral of eq. (4.19) by introducing an angle $\theta_0 = \omega t_0$, where

$$\theta_0 = \arcsin\left(\frac{x_0}{X_r}\right), \tag{4.21}$$

Hence, for $\theta_0 < \theta < \pi - \theta_0$ the integrand switches to the larger restoring force because the proof mass is saturating in stroke. This happens for the first half of the proof mass periodic cycle and due to the symmetry of the restoring force, the same switching in the integrand happens to the second half of the cycle. Equation (4.19) can thus be rewritten as,

$$\begin{aligned} K_{eq}(\omega, X_r) = \; k_p + \frac{k_{sat} - k_p}{\pi} \quad & \left[\int_{\theta_0}^{\pi-\theta_0} \left(\sin(\theta) - \frac{x_0}{X_r}\right) \sin(\theta) \mathrm{d}\theta + \right. \\ & \left. + \int_{\pi+\theta_0}^{2\pi-\theta_0} \left(\sin(\theta) + \frac{x_0}{X_r}\right) \sin(\theta) \mathrm{d}\theta \right], \end{aligned} \tag{4.22}$$

which gives the linearised or mean value of the stiffness experienced by the nonlinear system over one cycle. Equation (4.22) can be divided into two integrals that can be

calculated separately as,

$$I_1 = \alpha \int_{\theta_0}^{\pi-\theta_0} (\sin(\theta) - \gamma)\sin(\theta)\mathrm{d}\theta \tag{4.23a}$$

$$I_2 = \alpha \int_{\pi+\theta_0}^{2\pi-\theta_0} (\sin(\theta) + \gamma)\sin(\theta)\mathrm{d}\theta \tag{4.23b}$$

,

where the coefficient α is given by,

$$\alpha = \frac{k_{sat} - k_p}{\pi}, \tag{4.24}$$

and γ is,

$$\gamma = \frac{x_0}{X_r}. \tag{4.25}$$

The integral I_1 given by eq. (4.23a) can be rewritten as,

$$I_1 = \alpha \int_{\theta_0}^{\pi-\theta_0} \sin^2(\theta) - \alpha \int_{\theta_0}^{\pi-\theta_0} \gamma \sin(\theta)\mathrm{d}\theta, \tag{4.26}$$

and considering that $\sin^2(\theta) = [1 - \cos(2\theta)]/2$ it becomes,

$$I_1 = \alpha \int_{\theta_0}^{\pi-\theta_0} \left(\frac{1-\cos(2\theta)}{2}\right) - \alpha\gamma \int_{\theta_0}^{\pi-\theta_0} \sin(\theta)\mathrm{d}\theta, \tag{4.27}$$

which results in,

$$\begin{aligned} I_1 =& \frac{\alpha}{2}(\pi - 2\theta_0) - \frac{\alpha}{2}\left(\frac{\sin(2\pi - 2\theta_0)}{2} - \frac{\sin(2\theta_0)}{2}\right) + \\ &+ \alpha\gamma\left(\cos(\pi - \theta_0) - \cos(\theta_0)\right). \end{aligned} \tag{4.28}$$

Equation (4.28) can be simplified using the angle transformation formulas and can be written as,

$$I_1 = \frac{\alpha}{2}\left[\pi - 2\theta_0 + \sin(2\theta_0) - 4\gamma\cos(\theta_0)\right]. \tag{4.29}$$

In the same way the integral of eq. (4.23b) can be calculated and it is shown that $I_2 = I_1$. Hence, using eqs. (4.24), (4.25) and (4.29) the equivalent stiffness given by eq. (4.22) becomes,

$$K_{eq}(X_r) = k_p + \frac{k_{sat} - k_p}{\pi}\left[\pi - 2\theta_0 + \sin(2\theta_0) - 4\frac{x_0}{X_r}\cos(\theta_0)\right], \tag{4.30}$$

and substituting eq. (4.21) into eq. (4.30) the term $\sin(2\theta_0)$ results in,

$$\sin\left(2\arcsin\left(\frac{x_0}{X_r}\right)\right) = 2\frac{x_0}{X_r}\cos\left(\arcsin\left(\frac{x_0}{X_r}\right)\right), \tag{4.31}$$

which can be further simplified by noting that,

$$\cos\left(\arcsin\left(\frac{x_0}{X_r}\right)\right) = \frac{\sqrt{X_r^2 - x_0^2}}{X_r}. \tag{4.32}$$

Substituting eqs. (4.3), (4.21), (4.31) and (4.32) into eq. (4.30) gives the final form of the equivalent stiffness as,

$$K_{eq}(X_r) = k_p + \frac{k_c}{\pi}\left[\pi - 2\arcsin\left(\frac{x_0}{X_r}\right) - 2\frac{x_0}{X_r^2}\sqrt{X_r^2 - x_0^2}\right], \tag{4.33}$$

which is also known as the describing function of the nonlinearity [99; 118]. Combining eq. (4.33) with eq. (4.17), the first-order FRF for the nonlinear system becomes,

$$\Lambda(\omega, X_r) = \frac{1}{-m_p\omega^2 + j\omega c_p + k_p + \frac{k_c}{\pi}\left[\pi - 2\arcsin\left(\frac{x_0}{X_r}\right) - 2\frac{x_0}{X_r^2}\sqrt{X_r^2 - x_0^2}\right]}. \tag{4.34}$$

The change of the nonlinear resonant frequency with the amplitude of oscillation can be normalised with respect to the resonant frequency of the underlying linear system [99]. Hence, a non-dimensional parameter can be introduced as,

$$\beta^2 = \frac{\omega_{res,NL}^2}{\omega_p^2} = \frac{K_{eq}(X_r)}{k_p}, \tag{4.35}$$

where $\omega_{res,NL}$ is the resonant frequency of the nonlinear system.

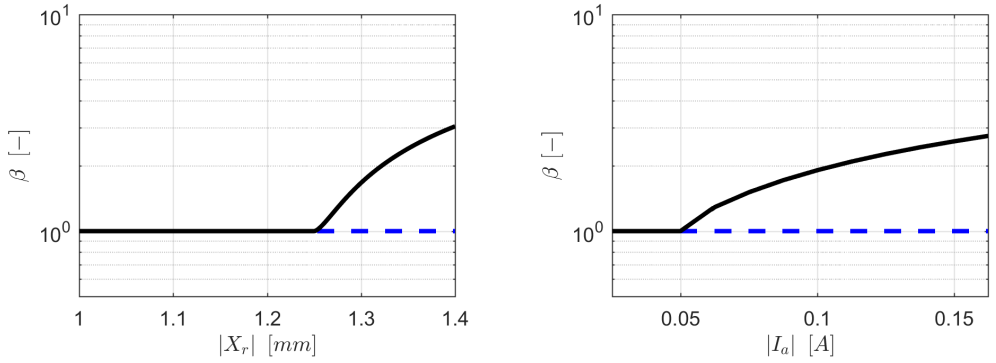

(a) (b)

FIGURE 4.11: Variation in the resonance frequency with: (a) amplitude of the oscillation; (b) amplitude of the excitation. Dashed blue line for the underlying linear model and solid black line for the nonlinear model.

Equation (4.35) is illustrated in figure 4.11(a) considering eq. (4.33) and the values in table 3.1. This figure shows a direct comparison between the nonlinear resonant frequency (solid black line) and the underlying linear resonant frequency (dashed blue line) with respect to the amplitude of the proof mass displacement. Figure 4.11(b) instead, shows the comparison between the linear and nonlinear resonant frequencies

with respect to the amplitude of excitation (level of the input current), which corresponds to the backbone curve of figure 4.10. In both figures 4.11(a) and 4.11(b), the nonlinear resonant frequency is invariant until the inertial actuator enters the nonlinear region, then it increases monotonically. This can pose a threat when the inertial actuator is used in a velocity feedback loop, since an increase in the actuator's resonant frequency can lead to a decrease of the stability margin of the controller.

4.3 Summary

In this chapter a numerical analysis on the nonlinear behaviour of a stroke limited inertial actuator has been presented. Simulation studies both in time and frequency domain have been carried out and the results have been compared. Firstly, a time domain model of the stroke limited inertial actuator has been derived, where the stroke limits have been modelled as a piecewise linear stiffness, consistently with the study of section 3.4. Secondly, the numerical integration of the nonlinear equation of motion allowed the comparison of the time history of the nonlinear response to a sine sweep excitation with the response of the underlying linear system. The nonlinear system is characterised by a mean stiffness at low frequency that is larger than the underlying linear stiffness. Also, if the initial conditions at every cycle provide the proof mass with a sufficient amount of energy, the proof mass itself continues to saturate until the nonlinear resonance is reached and a sudden jump in the response is observed. The waveforms of the nonlinear response have high frequency contents due to the non-smooth nonlinearity and the activation of many odd harmonics, in particular the third and the fifth are comparable to the fundamental component. Consequently, the nonlinear equation of motion has been analysed in frequency domain using the HBM for seeking the periodic solutions at each frequency. A comparison between the time domain simulation and the NFRC obtained using the HBM showed that the HBM can fully predict the amplitude of the nonlinear response and the bifurcation points corresponds to the frequencies of the amplitude jumps. A global analysis study has been carried out to study the initial conditions that lead the system to stabilise on the upper or lower branch of the NFRC. It has been observed that the velocity initial condition gives a major contribution in determining the solution branch, which is almost independent of the displacement initial condition. Finally, the frequency-amplitude diagrams have been investigated, concluding that the nonlinear resonant frequency of the stroke limited actuator increases as the amplitude of the excitation increases, due to the hardening behaviour of the nonlinearity.

Chapter 5

Nonlinear feedback control of a SDoF structure: theoretical analysis

The nonlinear behaviour of inertial actuators described in chapter 4 can be detrimental to the stability of VFCs, as observed in [12]. This chapter aims to develop a nonlinear strategy that accounts for the nonlinear dynamics of the actuator, enhancing the stability of the control system whilst maintaining the vibration attenuation performance provided by the VFC. Several attempts to address the issue of stroke saturation in inertial actuators have been reported in literature [37; 54; 83; 122; 127; 128], however, they focus mainly on on/off control strategies or in limiting the velocity feedback gain by means of gain scheduling techniques. The main objective of this study is to more fully understand the cause of stroke saturation instability and to develop a control strategy that can tackle this issue. A theoretical analysis of a stroke limited inertial actuator attached to a SDoF structure, driven by either a VFC or a combination of two feedback loops is presented. Firstly, the mathematical model of the nonlinear actuator, the structure and the feedback control system is derived in a state space form in section 5.1. Secondly, the stability of the closed-loop VFC system is addressed in section 5.2, comparing the results of the stability analysis of the underlying linear actuator model with the ones obtained from the nonlinear actuator model. Moreover, a comparison between the VFC and a relative velocity feedback controller (RFC) is made in section 5.2 in terms of stability and performance of the closed-loop system. The RFC also serves as an introduction to the nonlinear feedback control (NLFC), which is a nonlinear function of the proof mass relative velocity and displacement and is presented in section 5.3. Finally, the results of numerical simulations showing the effectiveness of the proposed control law are discussed and compared with those of the VFC in terms of stability of the closed-loop system for different sets of feedback gains and primary excitation.

5.1 Mathematical model

Figure 5.1 shows a lumped parameter model of a SDoF system connected to a stroke limited inertial actuator, where the SDoF may represent the first mode of a real structure. Conventionally, all the displacements and forces pointing upwards are considered to be positive. The parameters of the nonlinear actuator appearing in figure 5.1 have already

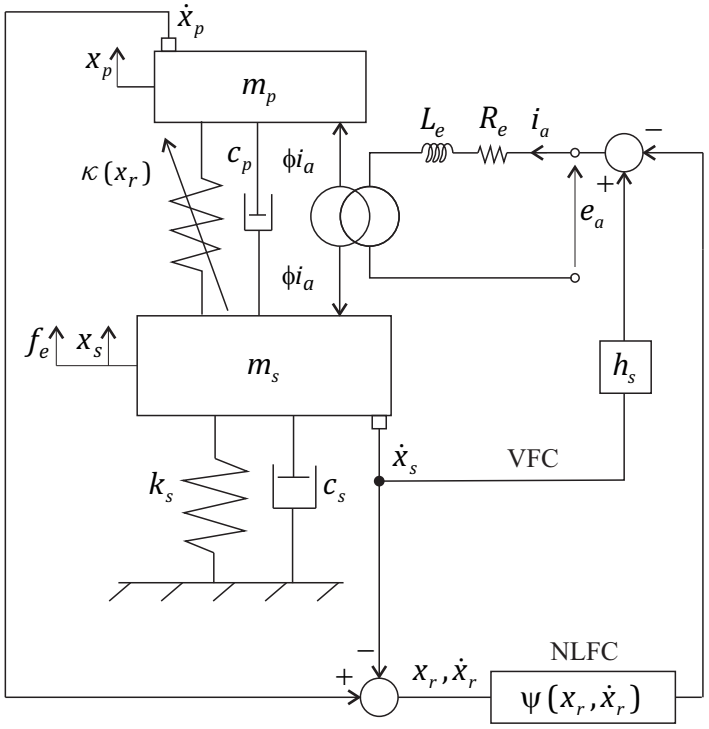

FIGURE 5.1: Lumped parameter model of the structure, nonlinear inertial actuator, velocity feedback controller (VFC) and nonlinear feedback controller (NLFC).

been introduced in chapter 4, where the actuator's base mass m_b is now included in the structural mass m_s and the base mass displacement $x_b(t)$ has been replaced by the structure's displacement $x_s(t)$. The structural mass m_s is connected to the ground via the stiffness and damping parameters k_s and c_s, respectively. The structure is subject to the external, or primary, force $f_e(t)$ and the control, or secondary, force $\phi i_a(t)$ that is generated by the actuator transducer. The VFC loop is assumed to be implemented by scaling the structure's velocity $\dot{x}_s(t)$ by a gain h_s and feeding this back to the actuator as the input current signal $i_a(t)$. A NLFC loop is added alongside the VFC loop in figure 5.1, and is defined as a nonlinear function of the relative proof mass velocity and displacement $\psi(x_r, \dot{x}_r)$. The equations of motion of the system in figure 5.1 can be expressed in a state space form as follows,

$$\begin{cases} \dot{\mathbf{x}}(t) = \mathbf{A}(\mathbf{x})\mathbf{x}(t) + \mathbf{B}_e f_e(t) + \mathbf{B}_a f_{a,s}(t) & \text{(5.1a)} \\ \mathbf{y}(t) = \mathbf{C}\mathbf{x}(t) & \text{(5.1b)} \end{cases},$$

where $\mathbf{x}$ is the state vector defined as,

$$\mathbf{x} = \{ \; x_s \quad x_p \quad \dot{x}_s \quad \dot{x}_p \; \}^T, \tag{5.2}$$

and $\mathbf{A}(\mathbf{x})$ is the state dependent system matrix defined as,

$$\mathbf{A}(\mathbf{x}) = \begin{bmatrix} \mathbf{0} & \mathbf{I} \\ -\mathbf{m}^{-1}\mathbf{k}(\mathbf{x}) & -\mathbf{m}^{-1}\mathbf{c} \end{bmatrix}, \tag{5.3}$$

where $\mathbf{0}$ and $\mathbf{I}$ are the 2-by-2 null matrix and identity matrix, respectively. The mass matrix $\mathbf{m}$ can be written as,

$$\mathbf{m} = \begin{bmatrix} m_s & 0 \\ 0 & m_p \end{bmatrix}, \tag{5.4}$$

whereas the nonlinear stiffness matrix of the system $\mathbf{k}(\mathbf{x})$ appearing in eq. (5.3) results in,

$$\mathbf{k}(\mathbf{x}) = \begin{bmatrix} k_s + \kappa(\mathbf{x}) & -\kappa(\mathbf{x}) \\ -\kappa(\mathbf{x}) & \kappa(\mathbf{x}) \end{bmatrix}, \tag{5.5}$$

where $\kappa(\mathbf{x}) = \kappa(x_p - x_s)$ is given by eq. (4.6). Also, the system's damping matrix $\mathbf{c}$ is defined as,

$$\mathbf{c} = \begin{bmatrix} c_s + c_p & -c_p \\ -c_p & c_p \end{bmatrix}. \tag{5.6}$$

The input vector of the primary excitation can be written as,

$$\mathbf{B}_e = \{ \; 0 \quad 0 \quad \tfrac{1}{m_s} \quad 0 \; \}^T, \tag{5.7}$$

whereas the input vector of the secondary force is given by,

$$\mathbf{B}_a = \{ \; 0 \quad 0 \quad \tfrac{1}{m_s} \quad -\tfrac{1}{m_p} \; \}^T, \tag{5.8}$$

and the control force acting on the structure is

$$f_{a,s} = -\phi i_a. \tag{5.9}$$

The output vector is defined as,

$$\mathbf{y} = \{ \; \dot{x}_s \quad \dot{x}_p \; \}^T, \tag{5.10}$$

hence, the output matrix can be written as,

$$\mathbf{C} = \{ \; \mathbf{0} \quad \mathbf{I} \; \}, \tag{5.11}$$

where $\mathbf{0}$ and $\mathbf{I}$ are the 2-by-2 zero matrix and identity matrix. The state space eq. (5.1) can also be represented with the block diagram illustrated in figure 5.2, which also

represents the open-loop control system since the input current is not directly related to the output variables.

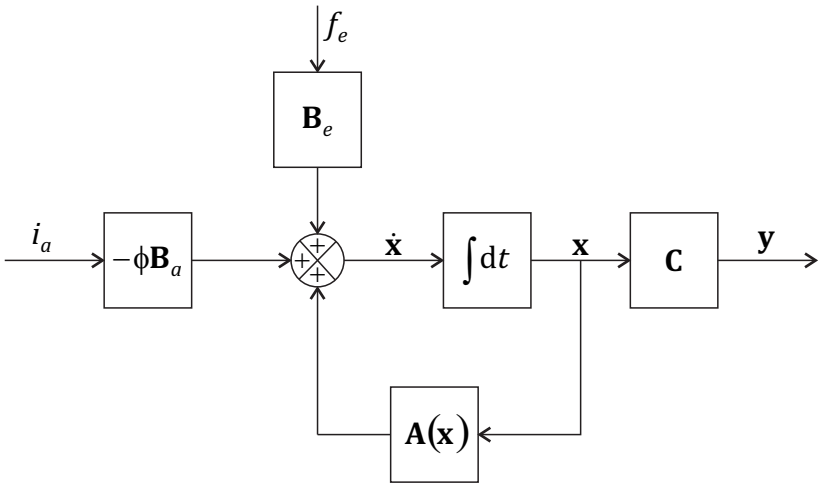

FIGURE 5.2: Block diagram of the open-loop system.

Hence, in general, the input current can be written as,

$$i_a = g_a \mathbf{H}\mathbf{r}, \tag{5.12}$$

where g_a is the amplifier gain, which is assumed to be unity throughout the thesis, $\mathbf{r} = [r_1\ r_2]^T$ is the vector of reference signals and $\mathbf{H}$ is the matrix of control gains. The feedback control system, as shown in the schematic of figure 5.1 is made by closing the loop around the output vector, and hence imposing,

$$\mathbf{r} = \mathbf{y}. \tag{5.13}$$

Using eqs. (5.12) and (5.13), the input current of the feedback control system becomes,

$$i_a = g_a \mathbf{H}\mathbf{y}, \tag{5.14}$$

where $\mathbf{H}$ is the matrix of feedback control gains. For a single VFC loop on the structure's velocity, the matrix of feedback gains $\mathbf{H}$ can be rewritten as,

$$\mathbf{H}_{vfc} = \{\ h_s \quad 0\ \}, \tag{5.15}$$

hence, substituting eq. (5.15) into eq. (5.14), the driving current of the inertial actuator becomes,

$$i_{a,vfc} = g_a \mathbf{H}_{vfc}\mathbf{y} = \{\ h_s \quad 0\ \} \left\{ \begin{array}{c} \dot{x}_s \\ \dot{x}_p \end{array} \right\} = h_s \dot{x}_s. \tag{5.16}$$

For a single NLFC loop on the proof mass relative velocity, the matrix of feedback gains $\mathbf{H}$ can be rewritten as,

$$\mathbf{H}_{nlfc} = \{ \ \eta_r(x_r) \quad -\eta_r(x_r) \ \}, \tag{5.17}$$

where $\eta(x_r)$ is a nonlinear gain that depends on the proof mass relative position. Thus, substituting eq. (5.17) into eq. (5.14), the driving current of the inertial actuator becomes,

$$\begin{aligned} i_{a,nlfc} =& g_a \mathbf{H}_{nlfc}\mathbf{y} = \{ \ \eta_r(x_r) \quad -\eta_r(x_r) \ \} \left\{ \begin{array}{c} \dot{x}_s \\ \dot{x}_p \end{array} \right\} = \\ =& \eta_r(x_r)\dot{x}_s - \eta_r(x_r)\dot{x}_p = -\eta_r(x_r)\dot{x}_r = -\psi(x_r, \dot{x}_r). \end{aligned} \tag{5.18}$$

For a double feedback loop, hence, combining the VFC loop on the structure's velocity with the NLFC loop on the proof mass relative velocity, the input current to the actuator's coil becomes,

$$\begin{aligned} i_{a,vfc+nlfc} =& i_{a,vfc} + i_{a,nlfc} = g_a \mathbf{H}_{vfc}\mathbf{y} + g_a \mathbf{H}_{nlfc}\mathbf{y} = \\ =& g_a \left(\mathbf{H}_{vfc} + \mathbf{H}_{nlfc} \right) \mathbf{y} = g_a \mathbf{H}_{vfc+nlfc}\mathbf{y} = \\ =& h_s \dot{x}_s - \psi(x_r, \dot{x}_r), \end{aligned} \tag{5.19}$$

where

$$\mathbf{H}_{vfc+nlfc} = \{ \ (h_s + \eta_r(x_r)) \quad -\eta_r(x_r) \ \}. \tag{5.20}$$

The closed-loop control system block diagram of the state space eq. (5.1) is illustrated in figure 5.3, where the driving current is given by the combination of both the VFC and the NLFC loops defined by eqs. (5.16) and (5.18).

Considering a general matrix of feedback gains $\mathbf{H}$, the control force applied to the structure by the closed-loop system can be written by substituting eq. (5.14) into eq. (5.9). That is,

$$f_{a,s} = -\phi g_a \mathbf{H}\mathbf{y} = -g_a \phi \mathbf{H}\mathbf{C}\mathbf{x}, \tag{5.21}$$

hence, the state eq. (5.1a) can be rewritten as,

$$\dot{\mathbf{x}}(t) = \mathbf{A}_0(\mathbf{x})\mathbf{x} + \mathbf{B}_e f_e(t), \tag{5.22}$$

where the closed-loop state dependent system matrix $\mathbf{A}_0(\mathbf{x})$ is derived as follows,

$$\mathbf{A}_0(\mathbf{x}) = \left[\mathbf{A}(\mathbf{x}) - g_a \phi \mathbf{B}_a \mathbf{H}\mathbf{C} \right]. \tag{5.23}$$

The compressed form of the state eq. (5.1a) given by eq. (5.22) is represented by the block diagram of figure 5.4. The parameters used in the numerical analysis af the system shown in figure 5.1 are provided in table 5.1.

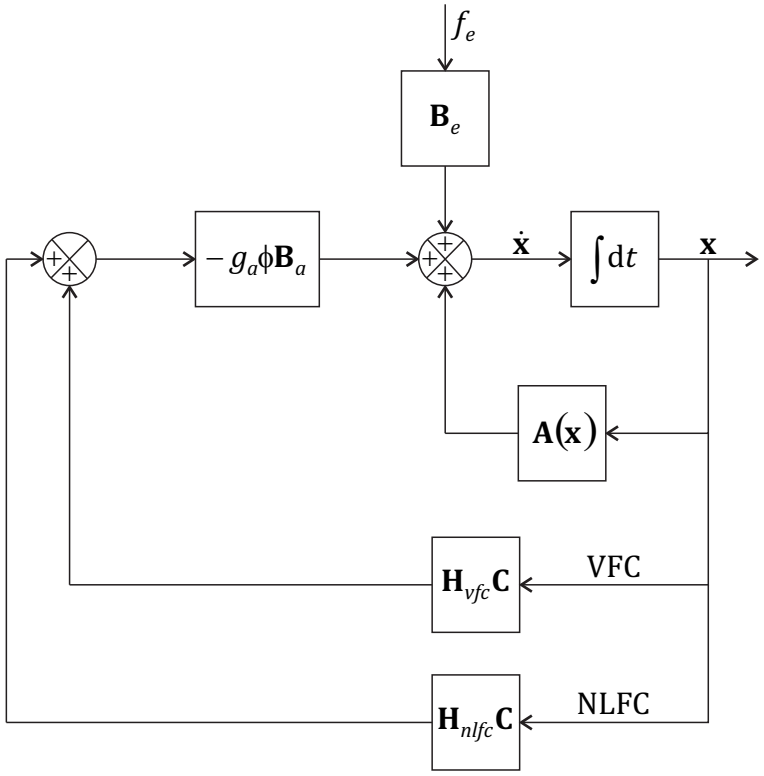

FIGURE 5.3: Block diagram of the closed-loop control system with both the VFC loop and the NLFC loop.

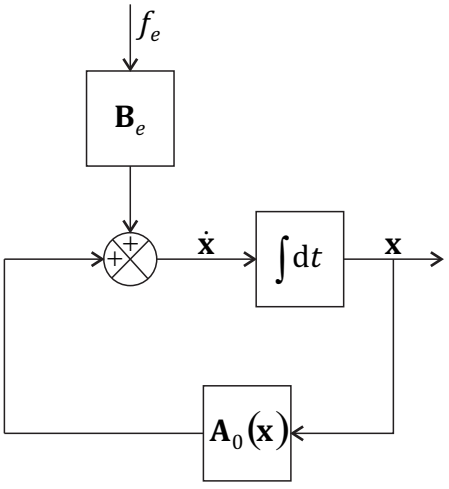

FIGURE 5.4: Block diagram of the closed-loop control system in a compressed form.

5.2 Absolute and relative linear velocity feedback control

In this section a preliminary numerical analysis is performed, which forms the basis for the development of the NLFC. VFCs, in which the velocity of the structure is fed back to a collocated inertial actuator are only conditionally stable [10], hence, there exists a maximum feedback gain, over which the system becomes unstable, due to inclusion of the actuator dynamics. Moreover, if the external excitation or the feedback gain is

TABLE 5.1: Table of model parameters.

Parameter	Value	Units
m_s	0.050	kg
k_s	5000	N/m
c_s	0.32	N/ms^{-1}
m_p	0.031	kg
k_p	115	N/m
k_{sat}	$2 \cdot 10^4$	N/m
c_p	1.4	N/ms^{-1}
x_0	1.25	mm
ϕ	1.55	N/A
g_a	1	A/ms^{-1}
ω_p (actuator)	$2\pi 9.7$	rad/s
ω_s (structure)	$2\pi 50.3$	rad/s

such that the inertial actuator saturates in stroke, then the control system may become unstable for even lower control gains than those predicted by a linear stability analysis [12; 13]. Firstly, the stability of the VFC is assessed for the underlying linear system. Secondly, a comparison is made in terms of stability and vibration attenuation performance between the VFC and when a second feedback loop on the relative velocity with constant feedback gain is added, namely the relative velocity feedback controller (RFC). Finally, the stability of the VFC is assessed considering the nonlinear dynamic behaviour of the stroke limited actuator.

5.2.1 Stability analysis and control performance using a linear actuator

The underlying linear model of the system in figure 5.1 is obtained by imposing a zero impact stiffness ($k_c = 0$), thus, the state dependent system matrix $\mathbf{A}(\mathbf{x})$ of eq. (5.3) becomes a constant state matrix

$$\bar{\mathbf{A}} = \mathbf{A}(\mathbf{x})\Big|_{k_c=0} \begin{bmatrix} \mathbf{0} & \mathbf{I} \\ -\mathbf{m}^{-1}\bar{\mathbf{k}} & -\mathbf{m}^{-1}\mathbf{c} \end{bmatrix}, \tag{5.24}$$

where the state dependent stiffness matrix $\mathbf{k}(\mathbf{x})$ given by eq. (5.5) results in,

$$\bar{\mathbf{k}} = \mathbf{k}(\mathbf{x})\Big|_{k_c=0} \begin{bmatrix} k_s + k_p & -k_p \\ -k_p & k_p \end{bmatrix}, \tag{5.25}$$

hence, the closed-loop state dependent system matrix $\mathbf{A}_0$ becomes,

$$\bar{\mathbf{A}}_0 = \left[\bar{\mathbf{A}} - g_a \phi \mathbf{B}_a \bar{\mathbf{H}} \mathbf{C}\right]. \tag{5.26}$$

where $\bar{\mathbf{H}} = [h_1 \; h_2]$ is a matrix of constant gains, which means that only linear feedback loops are considered. The first scenario is to analyse the stability of the controller for the underlying linear system when the actuator is driven by the VFC loop only. In such case, the output equation of the state space form given in eq. (5.1b) becomes,

$$y = \mathbf{C}_{vfc}\mathbf{x} = \dot{x}_s, \tag{5.27}$$

where the output matrix $\mathbf{C}_{vfc}$ is defined as,

$$\mathbf{C}_{vfc} = \begin{bmatrix} 0 & 0 & 1 & 0 \end{bmatrix}. \tag{5.28}$$

Setting $f_e = 0$ and assuming zero initial conditions $\mathbf{x}(0) = 0$, the Laplace transform of the the state eq. (4.8a) for the underlying linear system becomes,

$$\mathbf{X}(s) = \left[s\mathbf{I} - \bar{\mathbf{A}}\right]^{-1} \mathbf{B}_a F_{a,s}(s), \tag{5.29}$$

substituting the Laplace transform of eq. (5.9) into eq. (5.29) results in,

$$\mathbf{X}(s) = -\phi \left[s\mathbf{I} - \bar{\mathbf{A}}\right]^{-1} \mathbf{B}_a I_a(s), \tag{5.30}$$

and substituting eq. (5.30) into the Laplace transform of the output eq. (5.27) gives,

$$Y(s) = -\phi \mathbf{C}_{vfc} \left[s\mathbf{I} - \bar{\mathbf{A}}\right]^{-1} \mathbf{B}_a I_a(s). \tag{5.31}$$

Dividing eq. (5.31) by $-I_a(s)$ gives the plant transfer function $G_{sa}(s)$ as,

$$G_{sa}(s) = -\frac{Y(s)}{I_a(s)} = \phi \mathbf{C}_{vfc} \left[s\mathbf{I} - \bar{\mathbf{A}}\right]^{-1} \mathbf{B}_a. \tag{5.32}$$

In general, the input current can be written as,

$$I_a(s) = g_a h_s r(s), \tag{5.33}$$

where $r(s)$ is a reference signal. Substituting eq. (5.33) into eq. (5.32) gives the open-loop transfer function $L(s)$ as,

$$L(s) = g_a G_{sa}(s) h_s, \tag{5.34}$$

which is also illustrated in the block diagram of figure 5.5.

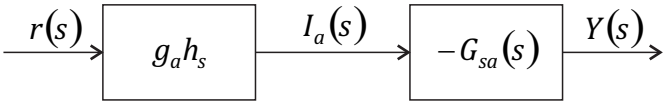

FIGURE 5.5: Block diagram of the open-loop VFC system.

Considering now the forced response, hence setting $f_e \neq 0$ and zero initial conditions $\mathbf{x}(0) = \mathbf{0}$, the Laplace transform of the state eq. (5.1a) for the underlying linear system

becomes,

$$\mathbf{X}(s) = \left[s\mathbf{I} - \bar{\mathbf{A}}\right]^{-1} \mathbf{B}_a F_{a,s}(s) + \left[s\mathbf{I} - \bar{\mathbf{A}}\right]^{-1} \mathbf{B}_e F_e(s). \tag{5.35}$$

Substituting eq. (5.35) into the Laplace transform of the output eq. (5.27) and considering eq. (5.9) gives,

$$Y(s) = -\phi \mathbf{C}_{vfc} \left[s\mathbf{I} - \bar{\mathbf{A}}\right]^{-1} \mathbf{B}_a I_a(s) + \mathbf{C}_{vfc} \left[s\mathbf{I} - \bar{\mathbf{A}}\right]^{-1} \mathbf{B}_e F_e(s), \tag{5.36}$$

which can be rewritten as,

$$Y(s) = -G_{sa}(s) I_a(s) + G_{se}(s) F_e(s), \tag{5.37}$$

where $G_{sa}(s)$ is given by eq. (5.32) and $G_{se}(s)$ is defined as follows,

$$G_{se}(s) = \mathbf{C}_{vfc} \left[s\mathbf{I} - \bar{\mathbf{A}}\right]^{-1} \mathbf{B}_e. \tag{5.38}$$

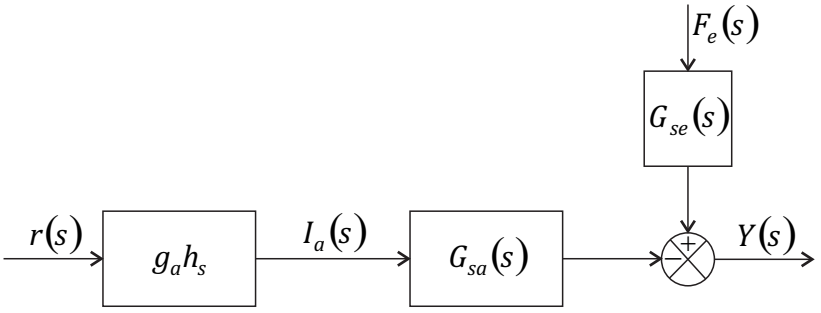

FIGURE 5.6: Block diagram of the open-loop VFC system including the disturbance of the external excitation.

The open-loop output eq. (5.37) that includes the disturbance given by the primary excitation is also displayed in figure 5.6. The closed-loop system is obtained by using the output signal as the reference signal, as shown in the block diagram of figure 5.7. The output equation of the closed-loop system can be written by substituting eqs. (5.33) and (5.34) into eq. (5.37) and imposing $r(s) = Y(s)$, which results in,

$$Y(s) = -L(s) Y(s) + G_{se}(s) F_e(s), \tag{5.39}$$

so that,

$$Y(s)(1 + L(s)) = G_{se}(s) F_e(s), \tag{5.40}$$

and dividing eq. (5.40) by $F_e(s)$ gives the closed-loop transfer function $T(s)$ between the output velocity of the structure and the input disturbance to the system as,

$$T(s) = \frac{Y(s)}{F_e(s)} = \frac{G_{se}(s)}{(1 + L(s))}, \tag{5.41}$$

which is defined for

$$1 + L(s) \neq 0. \tag{5.42}$$

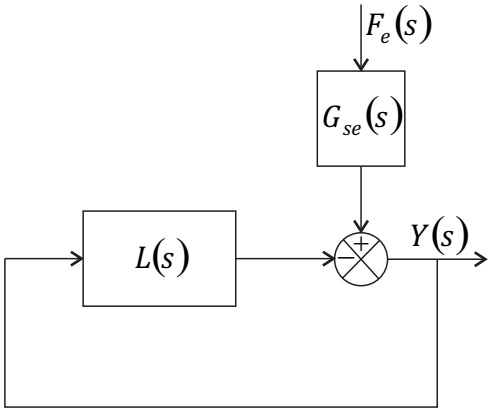

FIGURE 5.7: Block diagram of the closed-loop VFC system.

The stability of the closed-loop VFC for the underlying linear system can be studied using the Nyquist criterion. The Nyquist plot of the open-loop FRF $L(j\omega)$ given by eq. (5.34) for a velocity feedback gain $h_s = 21$ is shown in figure 5.8. The closed-loop VFC system is only conditionally stable as the polar plot crosses the real negative axis and a finite increase in gain would result in $L(j\omega)$ encircling the (-1,0) point.

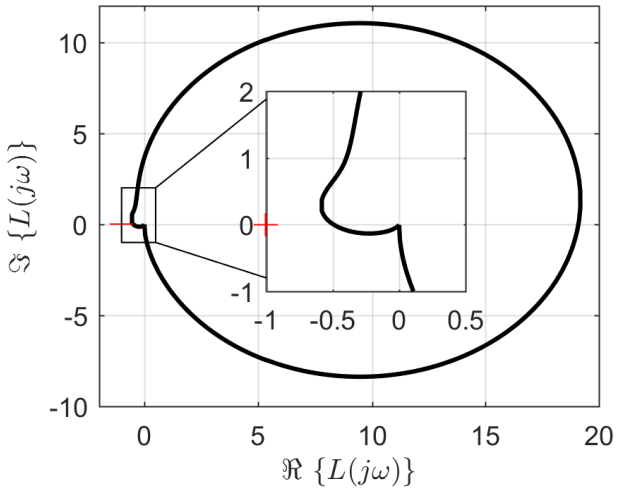

FIGURE 5.8: Nyquist plot of the open-loop FRF $L(j\omega)$ for a velocity feedback $h_s = 21$.

The gain margin is given by,

$$g_m = \frac{1}{L(\omega_c)}, \tag{5.43}$$

where $L(\omega_c)$ is the crossing point with the negative real axis and ω_c is the crossing frequency. For this system, the maximum feedback gain that can be used without causing instability ($g_m < 1$) is $h_{s,max} = 42$. The frequency of the crossing point in the Nyquist plot of figure 5.8, in which the system becomes unstable is $\omega_c = 2\pi 10$ rad/s, which is about the natural frequency of the inertial actuator. The amplitude and phase

of the closed-loop FRF given by eq. (5.41) are plotted in figure 5.9 for several values of the velocity feedback gain, starting from $h_s = 0$ for the uncontrolled system and then at increments of 25% $h_{s,max}$. It is clear that an increase in the control gain reduces the amplitude of the resonance associated with the structural mass, but also causes a spillover at the resonance of the inertial actuator. Increasing the gain to a value higher than the maximum will make the system unstable. In fact, as the feedback gain is increased over the maximum allowed, the overall damping of the system is reduced, which results in the instability. This effect can be clearly observed, for increasing control

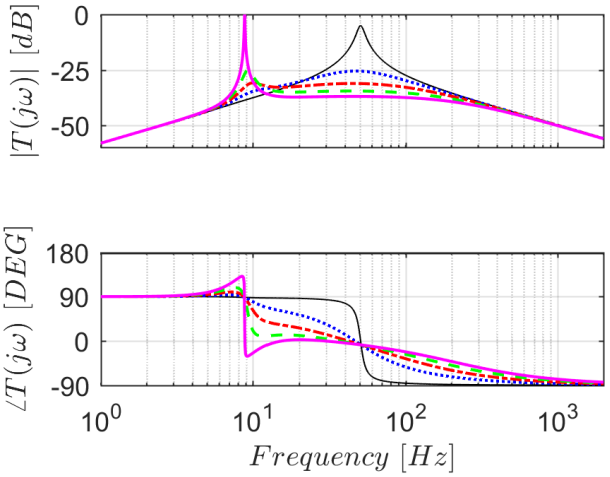

FIGURE 5.9: Bode plot of the closed-loop FRF $T(j\omega)$ for increasing control gains. The uncontrolled system $h_s = 0$ is shown with the solid black line, $h_s = 25\%h_{s,max}$ with the dotted blue line, $h_s = 50\%h_{s,max}$ with the dash-dotted red line, $h_s = 75\%h_{s,max}$ with the dashed green line, $h_s = h_{s,max}$ with the solid magenta line.

gains, in the response of the system to the external impulse excitation of the type,

$$f_e = Pe^{-\left(\frac{t}{\tau}\right)^2}, \tag{5.44}$$

where $P = 10$ N is the initial amplitude of the impulse and $\tau = 1$ ms is the decaying rate of the impulse excitation. The primary excitation given by eq. (5.44) is also shown in figure 5.10, where both its time history and spectrum are displayed. Figure 5.11 shows the response time history of the proof mass, structure and relative displacements due to the impulse excitation given by eq. (5.44). The time histories are simulated using MatLab's Simulink ODE4 solver with fixed time steps at a sampling frequency $f_s = 10$ kHz. The maximum stroke permitted x_0, $-x_0$ is also shown in figure 5.11 with the dashed red lines, however, only the underlying linear dynamics have been taken into account for this study, thus the proof mass is allowed to overshoot the stroke limit. The solid black line shows the response of the uncontrolled system, the feedback gain h_s is then increased of 25% $h_{s,max}$ each time until it reaches the maximum allowed by the linear stability analysis. The dotted blue line shows the response of the system when $h_s = 25\%h_{s,max}$, which results in a significant reduction of the vibration of the structural mass, whilst a slight increase of the proof mass response can be seen. Increasing further

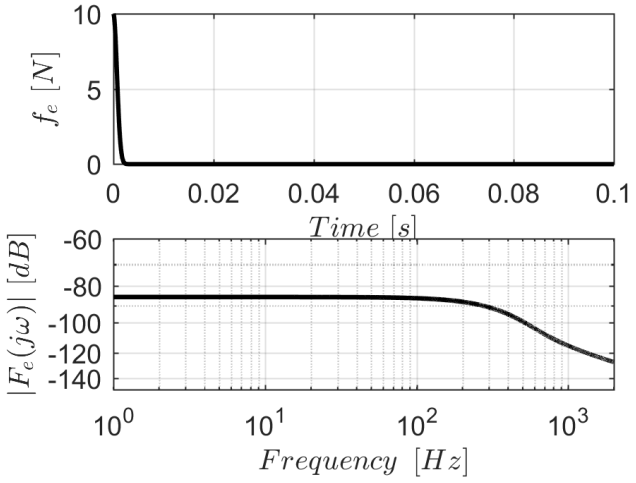

FIGURE 5.10: Time history and spectrum of the primary excitation on the structure.

the feedback gain results in a higher reduction of the structural vibration, but also the proof mass response overshoots the allowed stroke length. The solid magenta line shows the response of the system for the maximum stable gain scenario. In this case, the overall damping of the system goes to zero and the response to the initial impulse remains bounded and does not decay away. Before introducing the nonlinear controller,

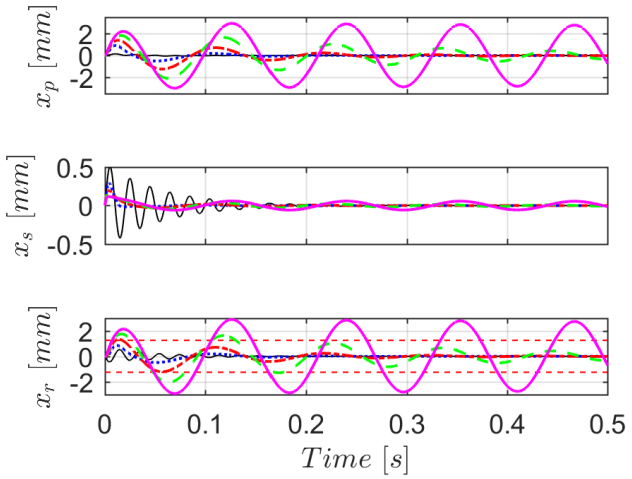

FIGURE 5.11: Response time histories of the closed-loop VFC system for increasing control gains using an impulse primary excitation on the structure and assuming a linear model of the actuator ($k_c = 0$). The uncontrolled system $h_s = 0$ is shown with the solid black line, $h_s = 25\%h_{s,max}$ with the dotted blue line, $h_s = 50\%h_{s,max}$ with the dash-dotted red line, $h_s = 75\%h_{s,max}$ with the dashed green line, $h_s = h_{s,max}$ with the solid magenta line. The horizontal dashed red lines indicate the position of the stroke limits, which are not considered in the underlying linear model of the actuator.

a simpler linear version is considered. The idea, firstly proposed in [9] and then studied in [29], is to use the second feedback loop to feed back the proof mass relative velocity amplified by a constant gain, in order to increase the effective damping of the actuator and to avoid the instability of the system. Hence, the nonlinear feedback gain $\eta_r(x_r)$ of

the second control loop can be linearised as,

$$\bar{\eta}_r(x_r) = h_r, \tag{5.45}$$

where h_r is defined as the feedback gain of the relative velocity feedback controller (RFC). The matrix of feedback gains $\mathbf{H}$ for the relative velocity feedback loop is given by,

$$\mathbf{H}_{rfc} = \bar{\mathbf{H}}_{nlfc} = \begin{bmatrix} h_r & -h_r \end{bmatrix}, \tag{5.46}$$

hence, the combined VFC loop and RFC loop results in the following matrix of feedback gains,

$$\mathbf{H}_{vfc+rfc} = \mathbf{H}_{vfc} + \mathbf{H}_{rfc} = \begin{bmatrix} h_s + h_r & -h_r \end{bmatrix}. \tag{5.47}$$

Setting $f_e = 0$ and assuming zero initial conditions $\mathbf{x}(0) = 0$, the Laplace transform of the the output eq. (4.8b) for the underlying linear system becomes,

$$\mathbf{Y}(s) = -\phi\mathbf{C}\left[s\mathbf{I} - \bar{\mathbf{A}}\right]^{-1}\mathbf{B}_a I_a(s), \tag{5.48}$$

which gives the plant matrix of transfer functions as follows,

$$\mathbf{G}_{sa}(s) = -\frac{\mathbf{Y}(s)}{I_a(s)} = \phi\mathbf{C}\left[s\mathbf{I} - \bar{\mathbf{A}}\right]^{-1}\mathbf{B}_a. \tag{5.49}$$

The open-loop driving current can be written as,

$$I_a(s) = g_a\mathbf{H}_{vfc+rfc}\mathbf{r}(s), \tag{5.50}$$

where $\mathbf{H}_{vfc+rfc}$ is given by eq. (5.47) and $\mathbf{r}(s) = [r_1 \; r_2]^T$ is the matrix of reference signals. Substituting eq. (5.50) into eq. (5.49) gives the open-loop matrix of transfer functions

$$\mathbf{L}(s) = g_a\mathbf{G}_{sa}(s)\mathbf{H}_{vfc+rfc}. \tag{5.51}$$

Considering now the forced response, hence setting $f_e \neq 0$ and zero initial conditions $\mathbf{x}(0) = \mathbf{0}$, the Laplace transform of the output eq. (4.8b) for the underlying linear system becomes,

$$\mathbf{Y}(s) = -\mathbf{G}_{sa}(s)I_a(s) + \mathbf{G}_{se}(s)F_e(s), \tag{5.52}$$

where $\mathbf{G}_{se}(s)$ is defined as follows,

$$\mathbf{G}_{se}(s) = \mathbf{C}\left[s\mathbf{I} - \bar{\mathbf{A}}\right]^{-1}\mathbf{B}_e. \tag{5.53}$$

The output equation of the closed-loop VFC+RFC system can be written by substituting eqs. (5.50) and (5.51) into eq. (5.52) and imposing $\mathbf{r}(s) = \mathbf{Y}(s)$, which results in,

$$\mathbf{Y}(s) = -\mathbf{L}(s)\mathbf{Y}(s) + \mathbf{G}_{se}(s)F_e(s), \tag{5.54}$$

thus,

$$\mathbf{Y}(s)(\mathbf{I}+\mathbf{L}(s)) = \mathbf{G}_{se}(s)F_e(s), \tag{5.55}$$

and the closed-loop matrix of transfer functions becomes,

$$\mathbf{T}(s) = \frac{\mathbf{Y}(s)}{F_e(s)} = [\mathbf{I}+\mathbf{L}(s)]^{-1}\,\mathbf{G}_{se}(s), \tag{5.56}$$

which is defined for

$$\det[\mathbf{I}+\mathbf{L}(s)] = \prod_{i=1}^{2}(1+\lambda_i) \neq 0, \tag{5.57}$$

where λ_i are the eigenvalues of the open-loop matrix $\mathbf{L}(s)$. It has to be made clear that using only the RFC would make the system asymptotically stable for arbitrarily large gains, as is well described in [9]. In practice, a single loop proportional to the relative velocity causes the inertial actuator to behave like a highly damped vibration absorber, hence, poor performance is achieved for the reduction of the structure's vibration. A more interesting controller is the one of eq. (5.47), where the two feedback gains can be adjusted to achieve better vibration reduction or to guarantee larger stability margins.Since this controller has two loops, the stability can be analysed using the generalised Nyquist criterion, which says that the closed-loop system is stable if the loci of the maximum $\lambda_i(j\omega)$ does not encircle the instability point (-1,0) [117]. Figure 5.12 compares the Nyquist plot of the open-loop FRFs of the system for three scenarios. The first one is for the single VFC loop with $h_s = 50\%h_{s,max}$ (solid black line); the second one is the single RFC loop with $h_r = 15$ (dash-dotted red line); and the third one is the combination of the VFC+RFC loops with feedback gains $h_s = 50\%h_{s,max}$ and $h_r = 0.25$. The added RFC loop shifts the crossing point between the polar plot and the negative real axis towards the origin, hence it increases the gain margin on the VFC with respect to the gain margin of the single VFC loop.

The effect of the RFC loop on the gain margin of the VFC can be studied using the sequential loop closing approach, which is shown in the block diagram of figure 5.13. The closed-loop state matrix of the RFC can be written as,

$$\bar{\mathbf{A}}_{0,rfc} = \left[\bar{\mathbf{A}} - g_a\phi\mathbf{B}_a\mathbf{H}_{rfc}\mathbf{C}\right]. \tag{5.58}$$

which then becomes the state matrix for the VFC loop, hence, the plant transfer function given by eq. (5.32) becomes,

$$G_{sa}(s) = \phi\mathbf{C}_{vfc}\left[s\mathbf{I} - \bar{\mathbf{A}}_{0,rfc}\right]^{-1}\mathbf{B}_a, \tag{5.59}$$

and the transfer function for the primary given by eq. (5.38) results in,

$$G_{se}(s) = \mathbf{C}_{vfc}\left[s\mathbf{I} - \bar{\mathbf{A}}_{0,rfc}\right]^{-1}\mathbf{B}_e. \tag{5.60}$$

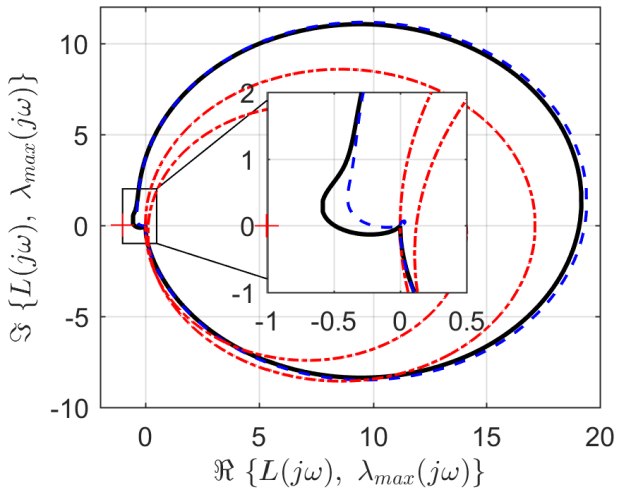

FIGURE 5.12: Comparison between the Nyquist diagram of the open-loop FRF $L(j\omega)$ of the VFC system for a velocity feedback gain $h_s = 21$ (solid black line) with the largest eigenvalue of the open-loop FRF $\mathbf{L}(j\omega)$ of the VFC+RFC system for $h_s = 21,\ h_r = 0.25$ (dashed blue line) and the RFC system for a relative feedback gain $h_r = 15$ (dash-dotted red line).

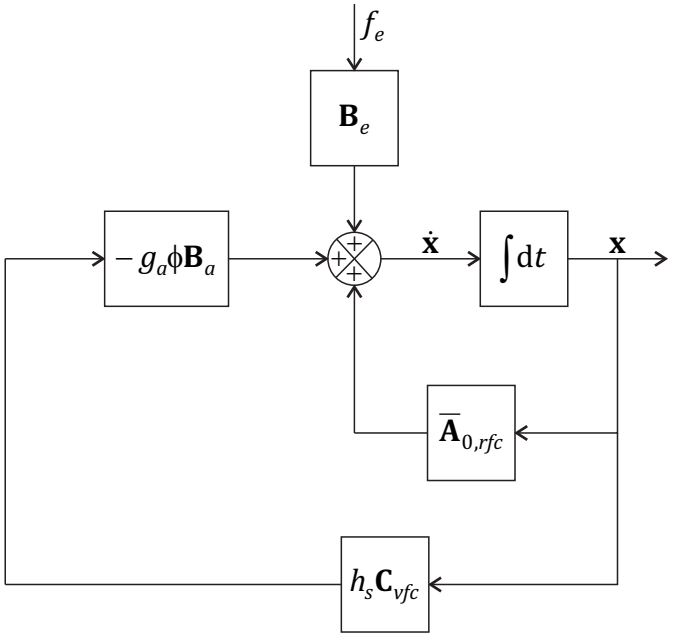

FIGURE 5.13: Block diagram of the sequential loop closing.

For each value of the relative feedback gain the gain margin of the outer VFC loop has been calculated, with respect to the nominal gain margin $g_{m,0}$ of the single VFC loop and the results are shown in figure 5.14. The y-axis of the plot represents the ratio of the gain margin with respect to its nominal value, whilst the x-axis represents increasing relative feedback gains. It can be observed that increasing h_r monotonically increases the gain margin of the VFC. On the other hand, increasing h_r may lead to a reduction in the performance in terms of vibration attenuation. This can be analysed by considering the kinetic energy of the structural mass as the index of performance [6]. Assuming

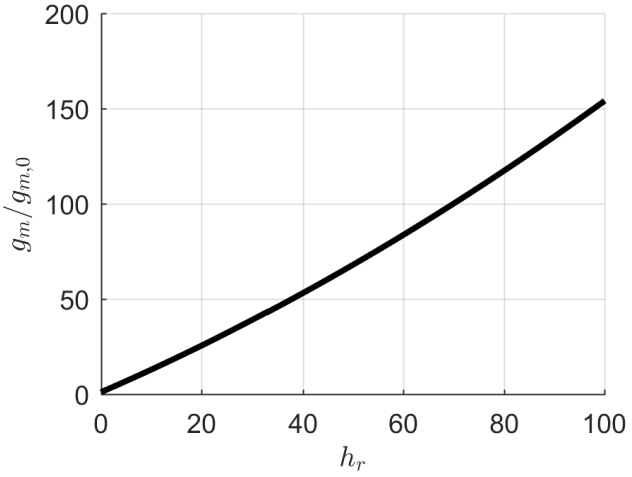

FIGURE 5.14: Variation of the gain margin with respect to the relative feedback gain.

harmonic vibrations, the time averaged kinetic energy of the SDoF structure is given by [6],

$$KE = \lim_{t\to\infty} \frac{1}{2t} m_s \int_0^t \dot{x}_s^2(t')\mathrm{d}t', \tag{5.61}$$

since

$$\dot{x}_s = \Re\left[\dot{X}_s(\omega)e^{j\omega t}\right] = \left|\dot{X}_s(\omega)\right| \cos\left(\omega t\right), \tag{5.62}$$

the time average kinetic energy becomes,

$$KE = \frac{1}{2} m_s \left|\dot{X}_s(\omega)\right|^2 \left[\lim_{t\to\infty} \frac{1}{t} \int_0^t \cos^2\left(\omega t'\right) \mathrm{d}t'\right], \tag{5.63}$$

which results in,

$$KE = \frac{1}{4} m_s \left|\dot{X}_s(\omega)\right|^2, \tag{5.64}$$

where the structural velocity $\dot{X}_s(\omega)$ is can be calculated by,

$$\dot{X}_s(j\omega) = \begin{bmatrix} 1 & 0 \end{bmatrix} \mathbf{T}(j\omega) F_e(j\omega), \tag{5.65}$$

with $\mathbf{T}(j\omega)$ the closed-loop matrix of transfer functions given by eq. (5.56). Figure 5.15 shows the PSD of the kinetic energy for several values of h_s and four increasing values of h_r when the external disturbance is set to unity at all frequencies. It can be noticed that an increase in h_r results in a reduction of the spillover effect, however, for same values of h_s and increasing values of h_r the kinetic energy increases. This effect can be clearly observed in figure 5.16, where the integral of the kinetic energy PSD is shown against the feedback gains h_s amd h_r. For $h_r = 0$ the kinetic energy of the structure monotonically decreases with respect to h_s, until it reaches a minimum and it suddenly rises, due to the proximity to instability. For small values of h_r, an optimal point is found, which minimises the kinetic energy, as demonstrated in [29]. However, for higher

values of h_r the kinetic energy of the structure significantly increases, hence a poorer performance is obtained.

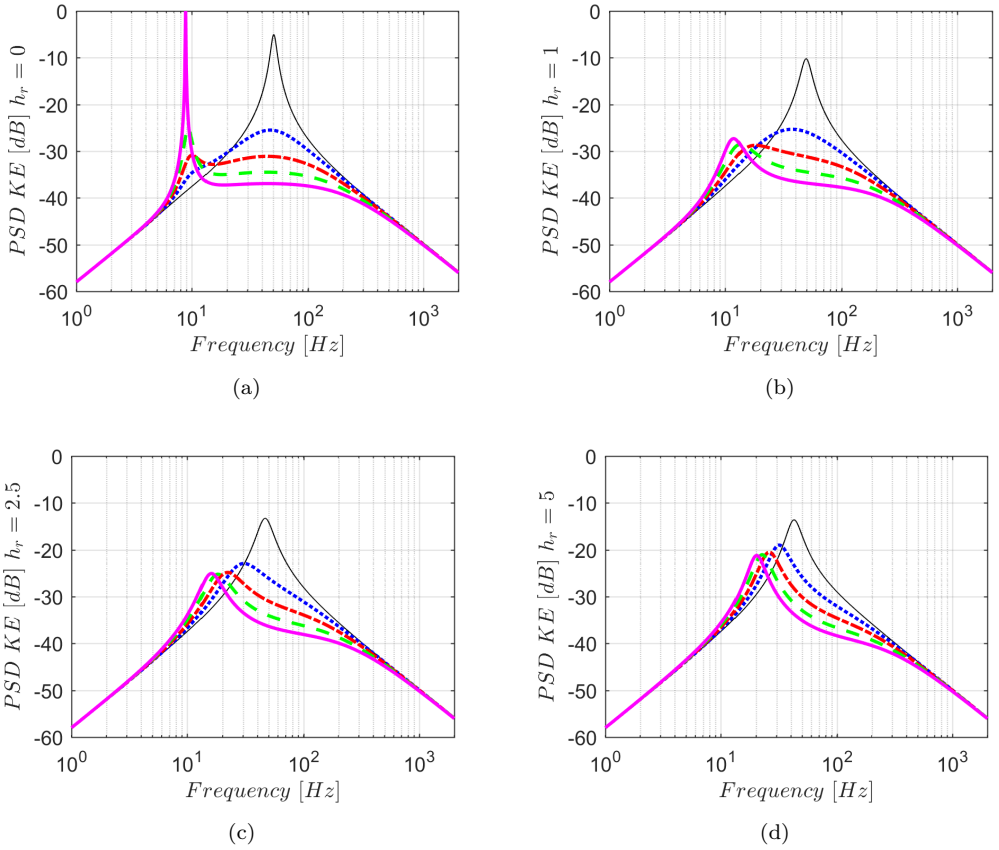

FIGURE 5.15: PSD of the kinetic energy for different values of h_r and h_s. (a) $h_r = 0$; (b) $h_r = 1$; (c) $h_r = 2.5$; (d) $h_r = 5$.The VFC gains are $h_s = 0$ shown with the solid black line, $h_s = 25\%h_{s,max}$ with the dotted blue line, $h_s = 50\%h_{s,max}$ with the dash-dotted red line, $h_s = 75\%h_{s,max}$ with the dashed green line, $h_s = h_{s,max}$ with the solid magenta line.

5.2.2 Stability analysis using a nonlinear actuator

In this section the nonlinear dynamic behaviour of the inertial actuator due to the limited stroke is taken into account for evaluating the stability of the VFC. By introducing the actuator nonlinearity, the stability of the closed-loop VFC becomes dependent on both the relative proof mass displacement and the velocity feedback gains. This dependency can be analysed through the Lyapunov linearisation stability method [119; 155].

Lyapunov indirect and direct method are often used to assess the local and global stability of a nonlinear system, respectively [119]. The indirect method analyses the local stability of a nonlinear system around its equilibrium points by evaluating the eigenvalues of the Jacobian matrix of the nonlinear state space equation. If the real part of the

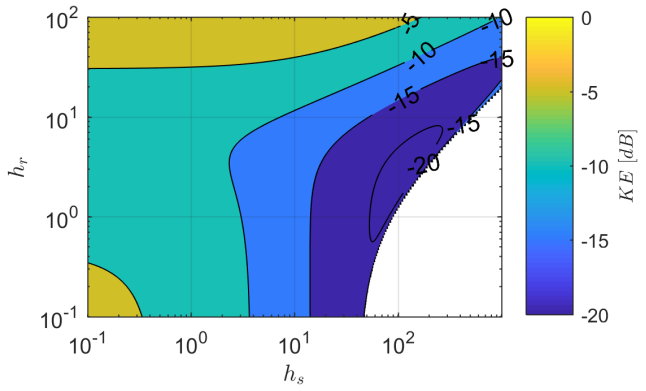

FIGURE 5.16: Average kinetic energy across a wide frequency band with respect to the feedback gains h_s and h_r: the region of instability is shown in white.

eigenvalues is negative for all eigenvalues, then the system is locally stable. Vice-versa, if the real part of the eigenvalues is positive for any eigenvalue, then the system is locally unstable. The main drawback of this method is that it gives information only about the local stability. Lyapunov direct method, instead, analyses the global stability of a nonlinear system by searching an energy-like function of the states that satisfies a set of conditions [119]. However, it is usually difficult to find a suitable Lyapunov function that satisfies all the conditions. Additionally, it is even more difficult to demonstrate instability, because the non-existence of suitable Lyapunov functions has to be proved. An interesting analysis is given by the Lyapunov exponents of the nonlinear system, which allows one to investigate the behaviour of the system around the initial condition $\tilde{\mathbf{x}}$ [155]. This case is similar to the direct method of Lyapunov, but the Jacobian matrix of the nonlinear state space equation is calculated at the initial condition $\tilde{\mathbf{x}}$ instead of the equilibrium point. If the eigenvalues of the Jacobian matrix have negative real part, then the nonlinear system is locally stable, if, instead, the largest eigenvalue of the Jacobian matrix has positive real part, then the nonlinear system is locally unstable [155].

The Jacobian matrix of the nonlinear state space equation is given by eq. (5.23). The VFC closed-loop state dependent system matrix can be derived from eq. (5.23) as,

$$\mathbf{A}_{0,vfc}(\mathbf{x}) = [\mathbf{A}(\mathbf{x}) - g_a \phi \mathbf{B}_a \mathbf{H}_{vfc} \mathbf{C}] \,. \tag{5.66}$$

and the stability of the closed-loop VFC system can be studied using the Lyapunov linearisation method, or Lyapunov exponent method, by calculating eigenvalues of eq. (5.66) for several proof mass relative displacements. If the real part of the largest eigenvalue is lower than zero, the system is stable, vice-versa if is greater than zero, then the system is unstable. The real part of the maximum eigenvalue of $\mathbf{A}_{0,vfc}$ for several proof mass displacements and velocity feedback gains is displayed in figure 5.17(a) and a detailed image around the stroke limit region is shown in figure 5.17(b), where the stroke limits are represented with dashed red lines. Figure 5.17 shows that the nonlinear system is

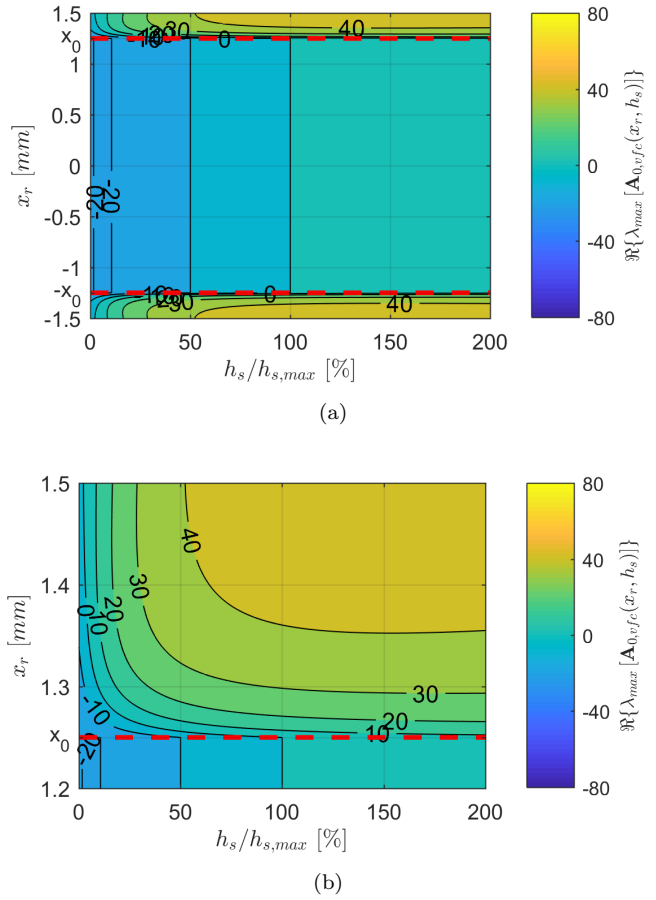

FIGURE 5.17: Real part of the maximum eigenvalue of the closed-loop matrix $\mathbf{A}_{0,vfc}(\mathbf{x})$ for several values of the relative proof mass displacement x_r and velocity feedback gain h_s. (a) full range; (b) zoom into the stroke limit.

stable for displacements within the stroke limits and feedback gains below $h_{s,max}$, as expected. Also, the system becomes unstable for $h_s > h_{s,max}$ regardless of the relative displacement. The delimiter of instability $\Re\{\lambda_{max}[\mathbf{A}_{0,vfc}(x_r, h_s)]\} = 0$ shows that for a particular feedback gain $h_s < h_{s,max}$ there exists a relative displacement $|x_r| > x_0$ above which the system becomes unstable, and the higher is the feedback gain, the lower is the relative displacement required to make the system unstable.

The stability of the nonlinear system of figure 5.1 subject to a single VFC loop can also be evaluated using the describing function method [108; 119]. The nonlinear system can be represented using a feedback connection with the nonlinear element, as shown in figure 5.18, where $K_{eq}(X_r)$ is the describing function of the nonlinearity and $G(j\omega)$ groups the underlying linear dynamic behaviour of the system including also the VFC loop. The characteristic equation of the system in figure 5.18 is,

$$G(j\omega)K_{eq}(X_r) + 1 = 0, \tag{5.67}$$

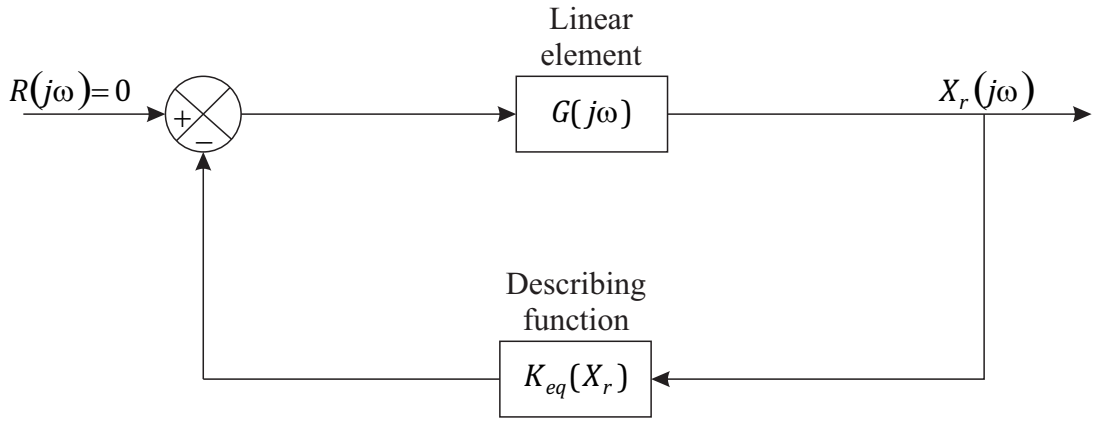

FIGURE 5.18: Block diagram of the describing function analysis for the existence of limit cycles.

which can be rewritten as,

$$G(j\omega) = -\frac{1}{K_{eq}(X_r)}, \tag{5.68}$$

where the describing function $K_{eq}(X_r)$ is given by eq. (4.33), and the linear FRF $G(j\omega)$ is given by,

$$G(j\omega) = \mathbf{C}_{DF}\left[s\mathbf{I} - \bar{\mathbf{A}}_{0,vfc}\right]^{-1}\mathbf{B}_a, \tag{5.69}$$

where the output matrix is defined as,

$$\mathbf{C}_{DF} = \begin{bmatrix} -1 & 1 & 0 & 0 \end{bmatrix}, \tag{5.70}$$

and the state matrix as,

$$\bar{\mathbf{A}}_{0,vfc} = \bar{\mathbf{A}} - g_a\phi\mathbf{B}_a h_s \mathbf{C}_{vfc}. \tag{5.71}$$

Figure 5.19 shows the polar plot of $G(j\omega)$ with the solid black line for a feedback gain $h_s = 75\%h_{s,max}$ and the loci of the describing function term with the dash-dotted red line. Since the nonlinearity considered here is an odd function, its describing function takes only real values, hence the term $-1/K_{eq}(X_r)$ lies on the negative real axis. It should be noted that this term starts from $-1/k_p$ for $|X_r| < x_0$, then it goes towards the origin as $|X_r|$ increases. The intersection between the polar plot with the negative inverse of the describing function, hence the solution of eq. (5.68), gives the condition for the existence of limit cycles in the nonlinear system [108; 119]. The amplitude of the limit cycle is given by the value of X_r corresponding to the negative inverse of the describing function at the point of intersection. Similarly, the frequency of the limit cycle ω_{lc} corresponds to the value of the frequency of the polar plot at the point of intersection. This procedure only gives a prediction of the existence of limit cycles, and due to its approximation nature, the results should be confirmed by time domain simulations. Higher feedback control gains h_s cause the polar plot to intersect with the negative inverse of the describing function at lower values. Hence a parametric study has been carried out to understand how the feedback gain h_s affects the point of intersection.

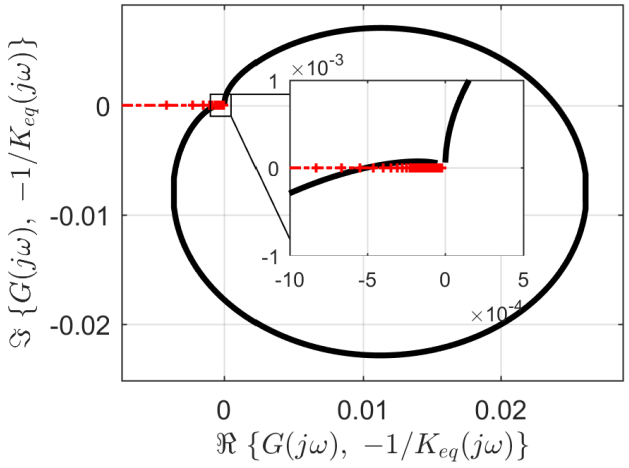

FIGURE 5.19: Polar plot of the underlying linear system FRF $G(j\omega)$ including VFC loop, and the negative inverse describing function $-1/K_{eq}(X_r)$ for the detection of limit cycles.

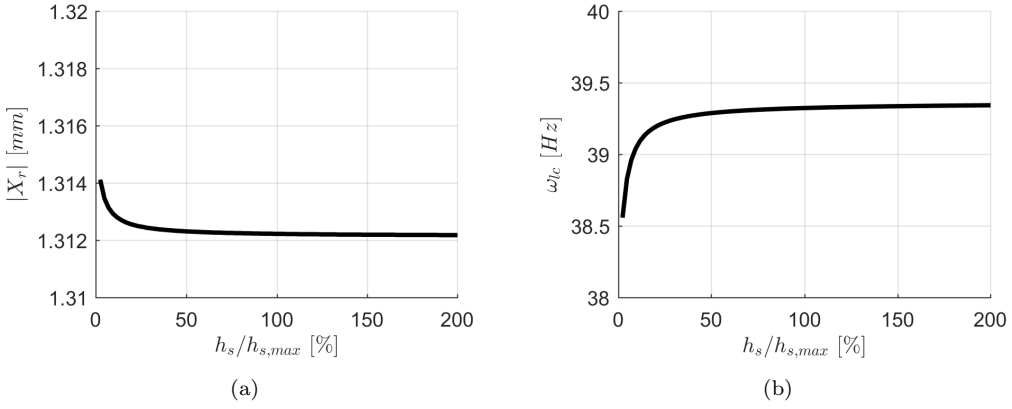

FIGURE 5.20: Amplitude and frequency of the limit cycle oscillation for several values of the VFC gain h_s. (a) Amplitude; (b) Frequency.

The amplitude of the limit cycle is shown in figure 5.20(a), which represents the maximum relative displacement reached by the proof mass. For low values of h_s, a higher relative displacement is needed to 'activate' the limit cycle when compared to higher values of h_s. For high values of the feedback gain, the curve is almost flat and settled around 1.31 mm. Figure 5.20(b) shows the frequency of the limit cycle oscillations versus the feedback gain. The frequency of the limit cycle increases as the feedback gain increases, but also in this case for high values of h_s the curve is almost flat at around 39.3 Hz. These results can be verified by analysing time domain impulse response of the system for increasing feedback gains.

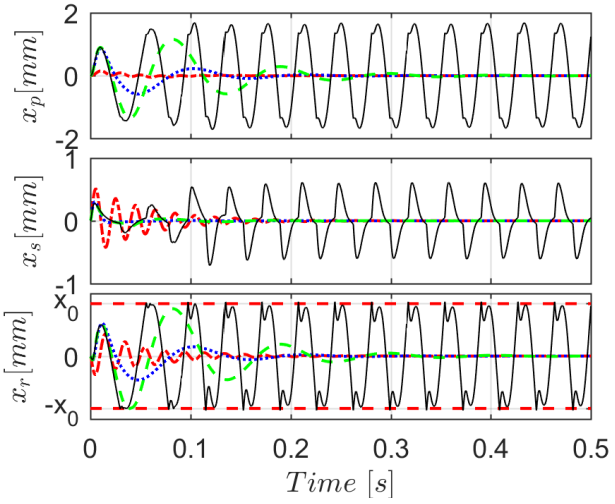

FIGURE 5.21: Response time histories of the closed-loop VFC system for increasing control gains using an impulse primary excitation on the structure and assuming a nonlinear model of the actuator. The uncontrolled system $h_s = 0$ is shown with the dash-dotted red line, $h_s = 25\%h_{s,max}$ with the dotted blue line, $h_s = 40\%h_{s,max}$ with the dashed green line, $h_s = 50\%h_{s,max}$ with the solid black line. The horizontal dashed red lines indicate the position of the stroke limits, which are considered in the nonlinear model of the actuator.

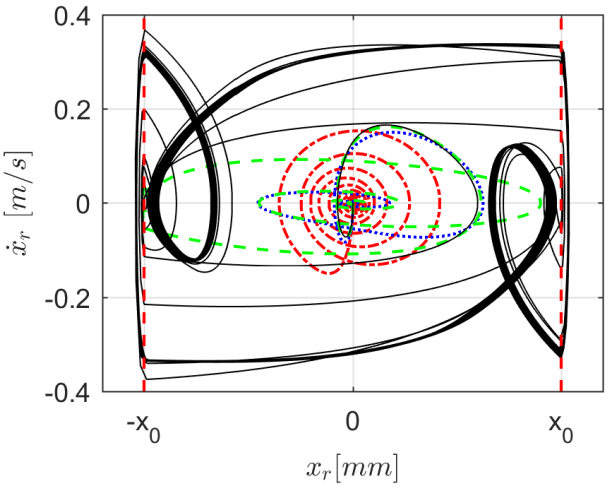

FIGURE 5.22: Response trajectories in the phase-space of the closed-loop VFC system for increasing control gains using an impulse primary excitation on the structure and assuming a nonlinear model of the actuator. The uncontrolled system $h_s = 0$ is shown with the dash-dotted red line, $h_s = 25\%h_{s,max}$ with the dotted blue line, $h_s = 40\%h_{s,max}$ with the dashed green line, $h_s = 50\%h_{s,max}$ with the solid black line. The vertical dashed red lines indicate the position of the stroke limits, which are considered in the nonlinear model of the actuator.

Figure 5.21 shows the time series of the proof mass, structure and relative displacements, respectively, due to the same impulse described in figure 5.10 and given by eq. (5.44). The dash-dotted red line shows the response of the uncontrolled system. As the feedback gain is increased to $25\%h_{s,max}$ (dotted blue line), the response of the structure to the same impulse is significantly reduced at the expense of the response of the proof mass. A further increase of the feedback gain to $40\%h_{s,max}$ (dashed green line) causes the relative

displacement to overshoot the allowed stroke length, hence an impulse-like excitation is imparted to the structure, however, after one impact the response decays away. Applying a slightly higher feedback gain $h_s = 50\%h_{s,max}$ (solid black line) results in an unstable system. It should be noted that the feedback gain causing the nonlinear system to become unstable is much lower than the one predicted by the linear Nyquist analysis for the underlying linear model of the system. The cause of this instability can be sought in the trajectories of the relative proof mass displacement in the phase-space for several feedback gains, which are shown in figure 5.22. It can be observed that an increase in the feedback gain rises the possibility of collisions with the end-stops, and for $h_s = 50\%h_{s,max}$ the proof mass experiences limit cycle oscillations. From the time simulation shown in figures 5.21 and 5.22 the amplitude and frequency of the limit cycle oscillation can be derived. In fact, the maximum amplitude of the relative displacement results to be 1.29 mm, which is slightly lower than the one predicted by the describing function analysis. The frequency of the limit cycle can be calculated from the time series of figure 5.21 considering the zero crossing of the signal. It follows that the frequency of the limit cycle is 27.6 Hz, which is also lower than the one predicted by the describing function analysis. These discrepancies in the outcomes have to be attributed to the contribution of the higher harmonics in the response that the describing function tool does not take into account. However, the frequency of the limit cycle, hence, the frequency of the instability of the nonlinear system is higher than the frequency of the instability of the underlying linear system, which is about the resonance frequency of the actuator.

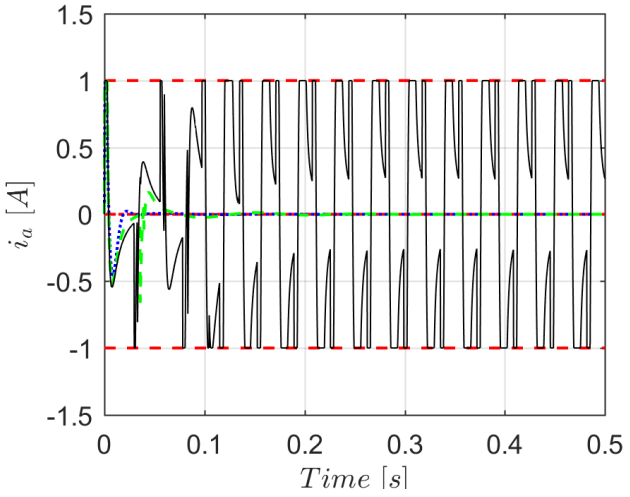

FIGURE 5.23: Actuator's input current of the closed-loop VFC system for increasing control gains using an impulse primary excitation on the structure and assuming a nonlinear model of the actuator. The uncontrolled system $h_s = 0$ is shown with the dash-dotted red line, $h_s = 25\%h_{s,max}$ with the dotted blue line, $h_s = 40\%h_{s,max}$ with the dashed green line, $h_s = 50\%h_{s,max}$ with the solid black line. The horizontal dashed red lines indicate the saturation of the power amplifier.

The control effort for each of the VFC closed-loop simulations at different gains is shown in figure 5.23, where the horizontal dashed red lines represent the saturation level of the

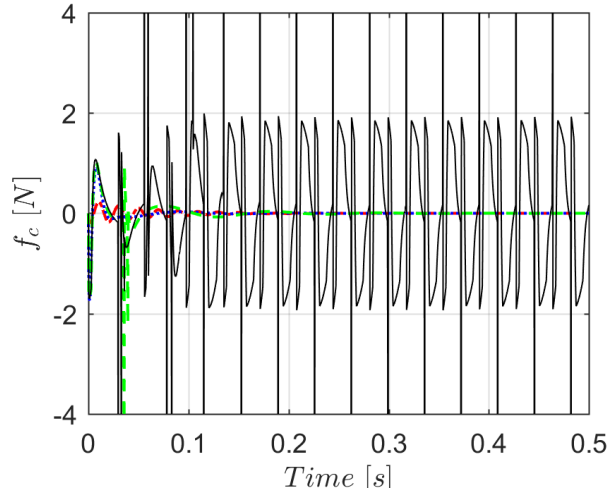

FIGURE 5.24: Control force delivered by the actuator in closed-loop VFC for increasing control gains using an impulse primary excitation on the structure and assuming a nonlinear model of the actuator. The uncontrolled system $h_s = 0$ is shown with the dash-dotted red line, $h_s = 25\%h_{s,max}$ with the dotted blue line, $h_s = 40\%h_{s,max}$ with the dashed green line, $h_s = 50\%h_{s,max}$ with the solid black line.

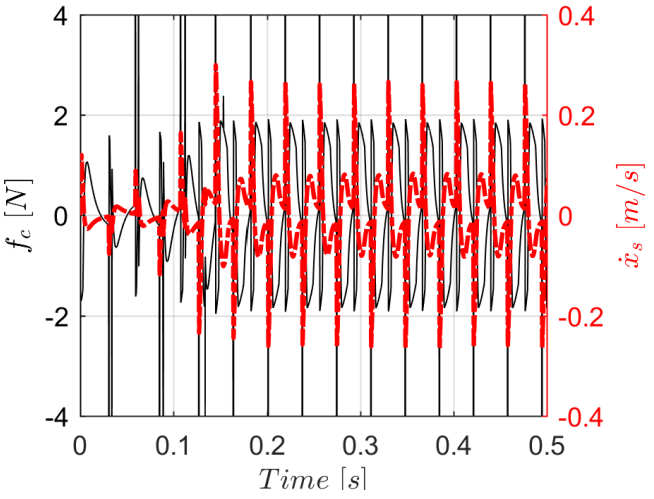

FIGURE 5.25: Control force delivered by the actuator and structural velocity in closed-loop VFC for $h_s = 40\%h_{s,max}$ using an impulse primary excitation on the structure and assuming a nonlinear model of the actuator. The control force is shown with the solid black line, the velocity of the structure is shown with the dash-dotted red line.

power amplifier. The dash-dotted red line shows the control effort for the uncontrolled scenario, which results to be zero, as expected. The dotted blue line and the dashed green line show the current flowing in the actuator coil for $h_s = 25\%h_{s,max}$ and $h_s = 40\%h_{s,max}$, respectively. The control effort for $h_s = 50\%h_{s,max}$, which is associated with the instability, is shown with the solid black line. It can be observed that the VFC generates an input current that changes sign quickly at every cycle and has a high amplitude, which is close to the saturation limit that sustains the limit cycle oscillation of the proof mass. The control force $f_c(t)$ delivered by the nonlinear actuator on the structure due to both the electro-mechanical transducer and the nonlinear mechanical

connection between the proof mass and the structure is shown in figure 5.24 for the same velocity feedback gains of figure 5.23. The control force for $h_s = 50\% h_{s,max}$ shown with the solid black line presents periodic spikes of large amplitude that are the impacts between the proof mass and the end-stops. These impacts cause the structure to respond with a high amplitude and with an in-phase velocity, as shown in figure 5.25 marked with the dash-dotted red line and hence, the overall damping of the system is reduced, eventually becoming negative and causing the instability.

5.3 Nonlinear feedback control

The study of the previous section motivates for the development of a nonlinear controller, whose aim is to prevent the destabilisation of the VFC loop due to stroke saturation and to maintain the vibration attenuation performance provided by the VFC. There have been several studies with different approaches that attempted to solve this problem. In fact, a first and crude solution is to switch off the VFC when stroke saturation is detected [83]. The system then becomes passive, as no more power is supplied to the actuator, and it stabilises. Eventually, after a certain period of time, one can trigger the VFC on again, until the next stroke saturation is detected. Another idea is to use a gain scheduling approach, which acts as a penalty function on the velocity feedback gain [127] and many studies have successfully implemented this [36; 54; 128; 156]. Basically, the controller decreases the velocity feedback gain of a certain amount if the proof mass is approaching the end stops. The author of [9] proposed to use a combination of RFC and VFC, where the tuning of the two feedback gains is a trade off between the stability and performance of the control system, as analysed in the previous section. Later on, other researchers dealt with the stroke saturation phenomenon using a NLFC, which is a function of the relative proof mass displacement [122]. This NLFC acts as a second loop alongside the VFC as shown in figure 5.1. In this thesis, the latter two strategies are merged together to form a NLFC loop, whose control law is,

$$\psi(x_r, \dot{x}_r) = \frac{n_r \dot{x}_r}{(x_0 - |x_r|)^{2p} + b}, \tag{5.72}$$

hence a relative velocity feedback controller with a state dependent relative feedback gain that is given by,

$$\eta(x_r) = \frac{n_r}{(x_0 - |x_r|)^{2p} + b}, \tag{5.73}$$

where n_r is the feedback gain of the nonlinear controller, b is a limitation parameter and p is an exponent parameter. The control law of eq. (5.72) increases the active internal damping of the inertial actuator as the proof mass approaches the end-stops without adding any damping when the proof mass is close to the resting position. In fact, as the relative displacement of the proof mass gets close to the stroke limit, the denominator term of equation eq. (5.72) reduces, hence the current proportional to the

relative velocity increases. The force applied to the structure by the NLFC can be written as,

$$f_{a,s,nlfc} = \phi\psi(x_r, \dot{x}_r), \tag{5.74}$$

thus, the active internal damping added to the actuator can be derived from eqs. (5.72) and (5.74) as,

$$c_{a,nlfc}(x_r) = \frac{\phi\psi(x_r, \dot{x}_r)}{\dot{x}_r} = \frac{\phi n_r}{(x_0 - |x_r|)^{2p} + b}. \tag{5.75}$$

The control action can be bounded between a minimum active damping $c_{a,nlfc}(0) = c_{a,min}$, that is reached when the proof mass is centred within the casing, and a maximum active damping $c_{a,nlfc}(x_0) = c_{a,max}$ that is reached when the proof mass saturates in stroke. From this consideration, the parameters b and n_r can be calculated. Assuming $x_r = 0$ and $b \ll x_0$, the corresponding value of n_r can be calculated from eq. (5.75) as,

$$c_{a,min} = \frac{\phi n_r}{x_0^{2p}} \Rightarrow n_r = \frac{c_{a,min} x_0^{2p}}{\phi}. \tag{5.76}$$

Similarly, assuming $x_r = x_0$, the parameter b results,

$$c_{a,max} = \frac{\phi n_r}{b} \Rightarrow b = \frac{\phi n_r}{c_{a,max}}. \tag{5.77}$$

A graphical representation of the NLFC is shown in figure 5.26, where the dotted, dash-dotted and solid black lines represent the control action for the exponent parameters $p = 1, 2, 3$, respectively. The vertical dashed red lines, instead, represent the position of the stroke limits. It can be observed that increasing the exponent parameter p increases the active internal damping of the actuator on a bigger range of displacements. On one hand this can be beneficial for the stability of the system, but on the other hand it can be detrimental for the vibration attenuation performance when used in combination with the VFC.

The stability of the closed-loop system using the combination of VFC and NLFC can be analysed through the Lyapunov linearisation stability method [119] as shown for the single VFC loop. In fact, the VFC+NLFC closed-loop state dependent system matrix can be derived from eq. (5.23) as,

$$\mathbf{A}_{0,vfc+nlfc}(\mathbf{x}) = \left[\mathbf{A}(\mathbf{x}) - g_a \phi \mathbf{B}_a \mathbf{H}_{vfc+nlfc} \mathbf{C}\right]. \tag{5.78}$$

and the stability of the closed-loop VFC+NLFC system for several proof mass relative displacements and velocity feedback gains can be studied by analysing the real part of the largest eigenvalue of eq. (5.78). The real part of the maximum eigenvalue of $\mathbf{A}_{0,vfc+nlfc}$ for several proof mass displacements and velocity feedback gains is displayed in figure 5.27(a) and a detailed image around the stroke limit region is shown in figure 5.27(b), where the stroke limits are represented with dashed red lines and the minimum and maximum active internal damping chosen for the calculation of the NLFC

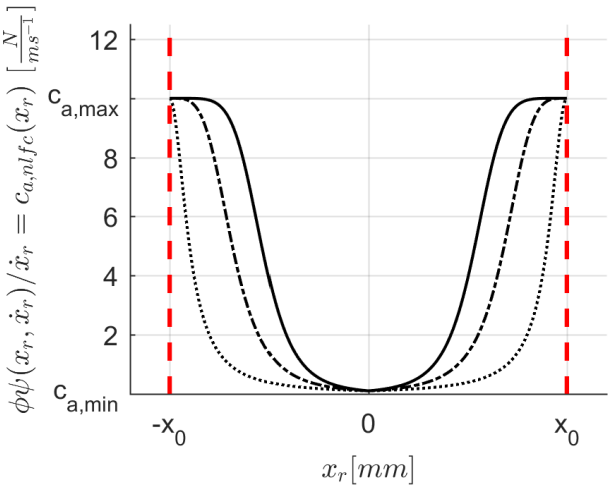

FIGURE 5.26: Nonlinear feedback control (NLFC) law for several exponent values. Dotted black line $p = 1$, dash-dotted black line $p = 2$, solid black line $p = 3$; where $c_{a,max} = 10$ N/ms^{-1} and $c_{a,min} = 0.1$ N/ms^{-1}. The dashed red lines indicate the stroke limits of the inertial actuator.

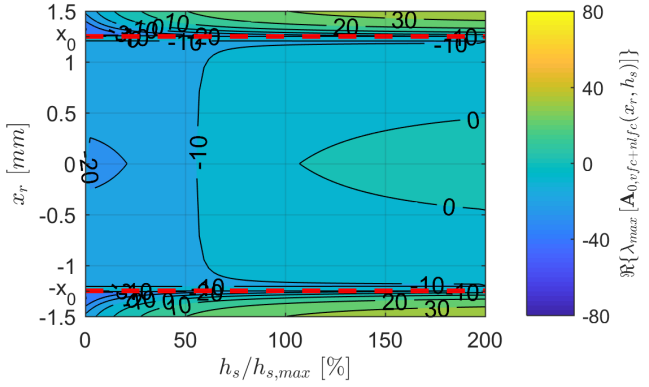

(a)

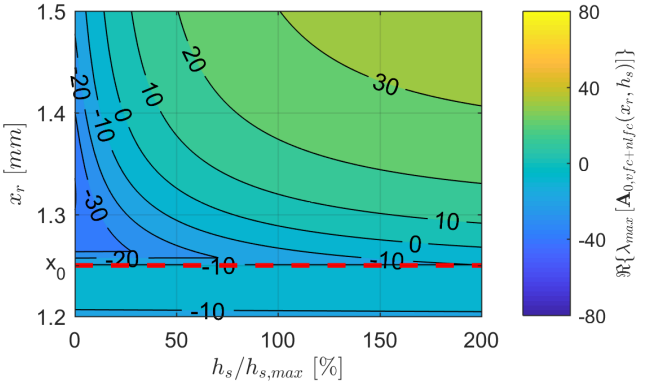

(b)

FIGURE 5.27: Real part of the maximum eigenvalue of the closed-loop matrix $\mathbf{A}_{0,vfc+nlfc}(\mathbf{x})$ for several values of the relative proof mass displacement x_r and velocity feedback gain h_s. (a) full range; (b) zoom into the stroke limit.

parameters are $c_{a,max} = 10$ N/ms^{-1} and $c_{a,min} = 0.1$ N/ms^{-1} and $p = 1$. A comparison between figure 5.27 and figure 5.17 shows that the NLFC enlarges the stability region of the system in terms of relative proof mass displacements. In fact, the delimiter of instability $\Re\{\lambda_{max}\,[\mathbf{A}_{0,vfc}(x_r, h_s)]\} = 0$ for the VFC+NLFC loop is shifted to larger relative displacements with respect to the one of single VFC loop. However, the dual loop controller becomes unstable if $h_s > h_{s,max}$ is chosen, because of the choice to use a small active internal damping for the proof mass around resting position.

Time simulation studies are carried out to assess the performance of the NLFC. In particular, a comparison is made between the control system with single VFC loop and VFC+NLFC loop. Figure 5.28 shows the time history and the phase-space trajectory of the system for a feedback gain $h_s = 25\%h_{s,max}$ excited by an impulse of the type given by eq. (5.44) when controlled by a single VFC loop (dashed green line) and when it is controlled by a VFC+NLFC loop (solid black line). It can be observe that for this scenario the proof mass does not collide with the end-stops and the presence of the NLFC loop is negligible as the system responds in the same way to the two controllers. Figure 5.29 shows the time history and the phase-space trajectory of the system for a feedback gain $h_s = 40\%h_{s,max}$ when controlled by a single VFC loop (dashed green line) and when it is controlled by a VFC+NLFC loop (solid black line). In this scenario the proof mass collides with one end-stop if the single VFC loop is used, after the collision the response decays away and the system does not get unstable. It can be seen from the phase-space trajectory of figure 5.29(b) that the configuration with both loops is able to avoid the contact with the end-stop, as the velocity approaches zero before the actuator saturates in stroke. Figure 5.30 shows the time history and the phase-space trajectory of the system for a feedback gain $h_s = 50\%h_{s,max}$ when controlled by a single VFC loop (dashed green line) and when it is controlled by a VFC+NLFC loop (solid black line). In this scenario the system goes unstable if the single VFC loop is used, whereas implementing the NLFC described by eq. (5.44) allows the proof mass to stand clear of the end-stops avoiding the limit cycle oscillation and hence the system remains stable. For the latter scenario, the control effort of the system controlled by a single VFC loop and by the VFC+NLFC loop can be compared. The comparison of the two control efforts for $h_s = 50\%h_{s,max}$ is shown in figure 5.31 where the input current of the single VFC loop is shown with the dashed green line and the input current of the VFC+NLFC loop is shown with the solid black line. It can be observed that during the first cycle the VFC current and the VFC+NLFC current overlap, but then the input current of the VFC+NLFC goes out-of-phase with respect to the one of the single VFC and the system quickly stabilises. Similarly, figure 5.32 shows that the control force delivered by the actuator using a VFC+NLFC loop (solid black line) is out-of-phase with respect to the velocity of the structure (dash-dotted red line) that quickly goes to zero. Of course, the stability of the nonlinear system does not depend only on the value of the VFC gain h_s, but also on the magnitude of the impulse excitation P. Therefore, a parametric study has been carried out in order to investigate the potential benefits of the NLFC

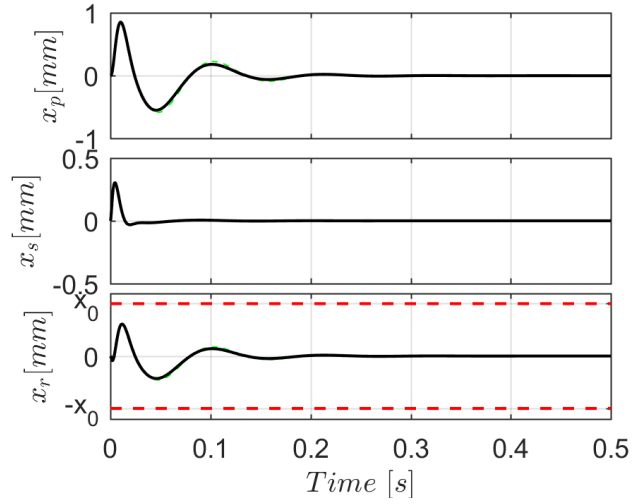

(a)

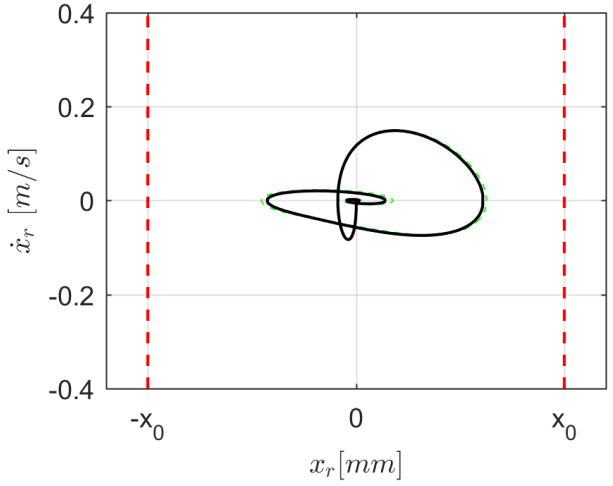

(b)

FIGURE 5.28: Response time histories and phase-space trajectories of the closed-loop VFC system (dashed green line) and the closed-loop VFC+NLFC system (solid black line) for a feedback gain $h_s = 25\% h_{s,max}$, using an impulse primary excitation on the structure and assuming a nonlinear model of the actuator. The dashed red lines indicate the position of the stroke limits. (a) Time history; (b) Phase-space trajectory.

over different scenarios. In particular, the stability of the system has been evaluated for each possible value of P and h_s, and for the two testing conditions of single VFC loop or the combination of VFC and NLFC loops. For each scenario, the operating region $\mathcal{OR}(P, h_s)$ of the inertial actuator is defined as,

$$\mathcal{OR}(P, h_s) = \{(P, h_s) | \max_{t \to \infty} |x_r(t)| < x_0\}, \tag{5.79}$$

where the sets of (P, h_s) inside the operating region are those in which the system is stable and the inertial actuator is adding active damping to the structure. The results of the parametric study are shown in figure 5.33. The dark grey area delimited by the dotted

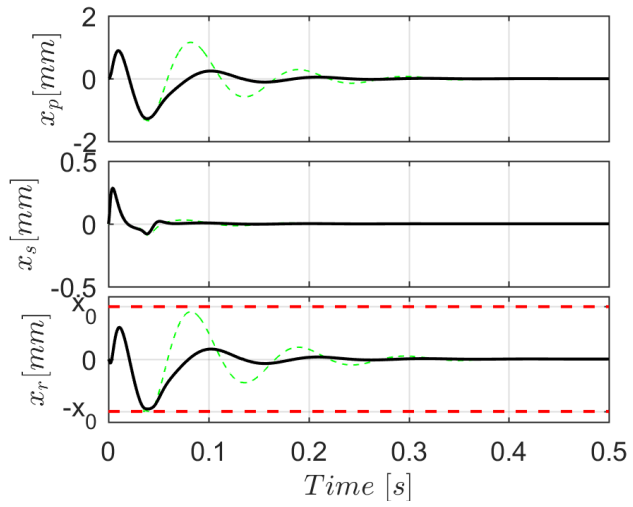

(a)

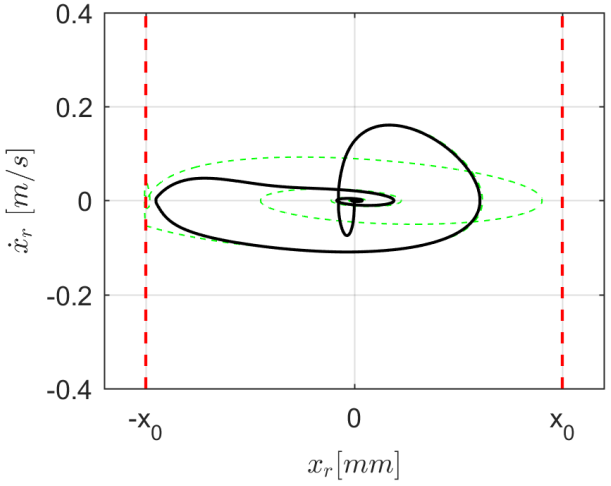

(b)

FIGURE 5.29: Response time histories and phase-space trajectories of the closed-loop VFC system (dashed green line) and the closed-loop VFC+NLFC system (solid black line) for a feedback gain $h_s = 40\% h_{s,max}$, using an impulse primary excitation on the structure and assuming a nonlinear model of the actuator. The dashed red lines indicate the position of the stroke limits. (a) Time history; (b) Phase-space trajectory.

black line shows the safe operating region when the single VFC loop is implemented. It can be seen that the nonlinearity in the inertial actuator severely reduces the stability of the system for large values of the excitation or the feedback gain. It should be noted that for very low values of excitation, the operating region reaches 100 % of $h_{s,max}$ because the proof mass does not reach the end-stops and the system behaves linearly. However, as soon as the excitation value is increased, the maximum gain that can be fed to the actuator without reaching the instability quickly drops down. Repeating the same parametric study, but using the combination of VFC+NLFC loops, produces a completely different result, which is shown in figure figure 5.33 with the light grey area delimited by the solid black line. In this case, the area covered by the operating region of

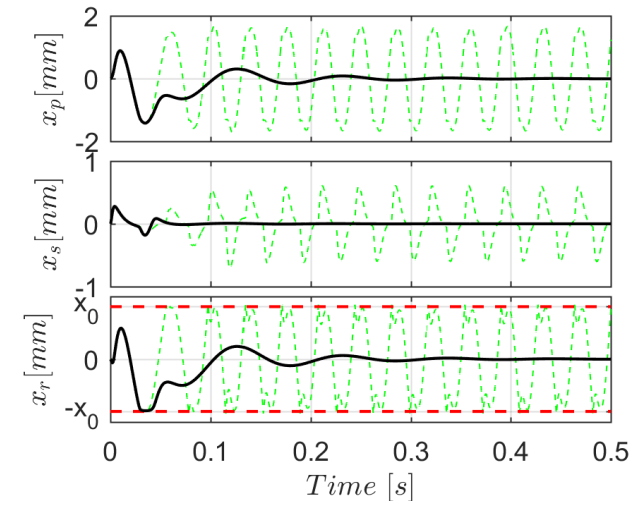

(a)

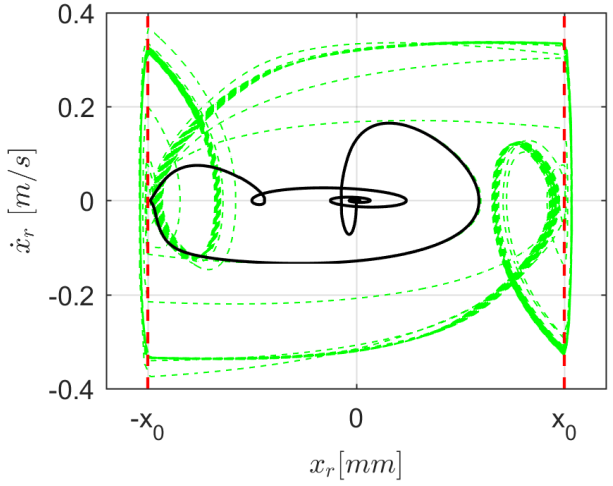

(b)

FIGURE 5.30: Response time histories and phase-space trajectories of the closed-loop VFC system (dashed green line) and the closed-loop VFC+NLFC system (solid black line) for a feedback gain $h_s = 50\%h_{s,max}$, using an impulse primary excitation on the structure and assuming a nonlinear model of the actuator. The dashed red lines indicate the position of the stroke limits. (a) Time history; (b) Phase-space trajectory.

the actuator using both VFC and NLFC loops is bigger than the area of the single VFC loop, hence, it increases the safe operating region of the inertial actuator. Moreover, the maximum gain that can be fed to the actuator slightly overshoots $h_{s,max}$, because, even for low excitations, the NLFC increases the effective internal damping of the actuator.

5.4 Summary

In this chapter a nonlinear feedback control strategy has been presented to avoid stroke saturation in inertial actuators enhancing their stability when driven in combination

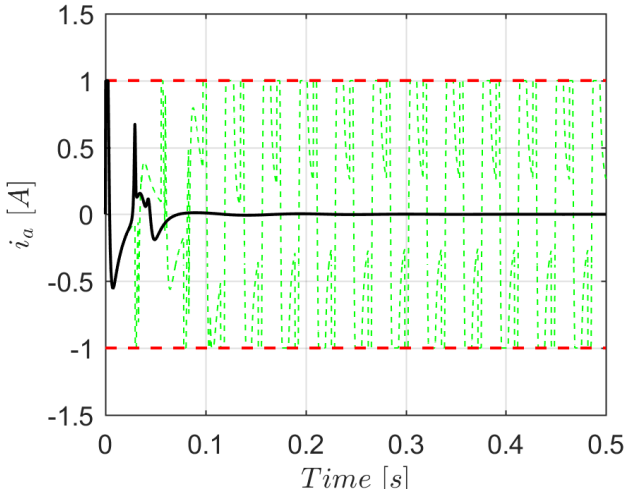

FIGURE 5.31: Actuator's input current for the closed-loop VFC system (dashed green line) and the closed-loop VFC+NLFC system (solid black line) for a feedback gain $h_s = 50\%h_{s,max}$, using an impulse primary excitation on the structure and assuming a nonlinear model of the actuator. The dashed red lines indicate the saturation of the power amplifier.

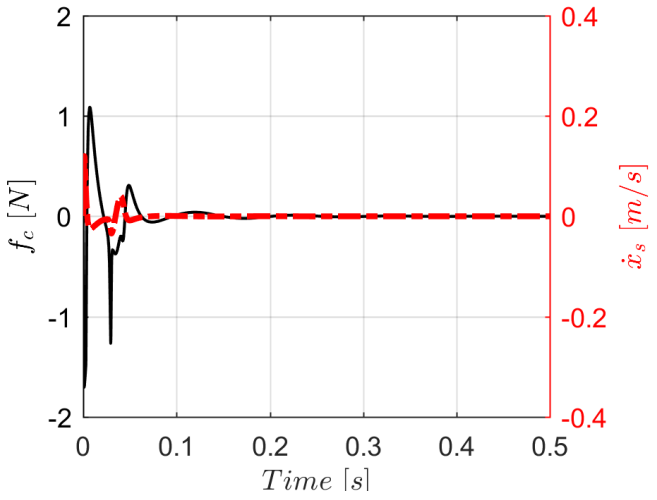

FIGURE 5.32: Control force delivered by the actuator and structural velocity in closed-loop VFC+NLFC system for a feedback gain $h_s = 50\%h_{s,max}$, using an impulse primary excitation on the structure and assuming a nonlinear model of the actuator. The control force is shown with the solid black line, the velocity of the structure is shown with the dash-dotted red line.

with VFCs. Firstly, the mathematical model of a nonlinear inertial actuator connected to a single degree of freedom structure has been derived, where the nonlinearity has been modelled as a piecewise linear stiffness, consistently with the study of chapters 3 and 4. Also, a general double loop controller on the system velocities has been added to the mathematical formulation. Secondly, a numerical analysis on the stability and performance of VFCs and RFCs has been carried out for both the underlying linear model and the nonlinear model of the inertial actuator. For the underlying linear system the stability has been assessed using the Nyquist criterion, whereas the control performance

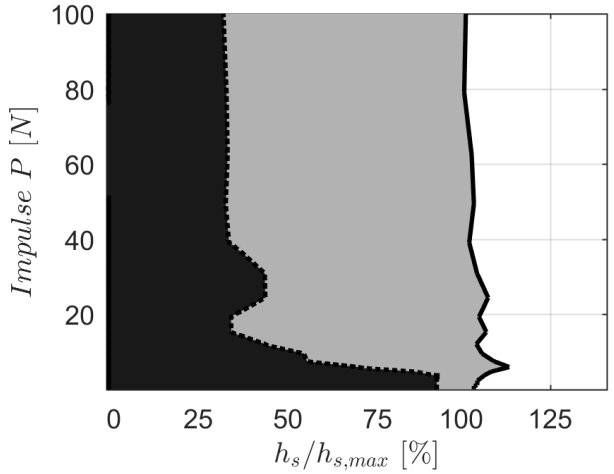

FIGURE 5.33: Operating regions of the inertial actuator for the closed-loop VFC system (dark grey area) and the closed-loop VFC+NLFC system (light grey area) for increasing values of the feedback gain, using an impulse primary excitation on the structure of amplitude P and assuming a nonlinear model of the actuator.

has been investigated in terms of time averaged kinetic energy of the structure. It has been shown that for a single VFC loop, the system is only conditionally stable, hence there exists a maximum feedback gain over which the system becomes unstable. Adding the RFC loop has shown to increase the stability of the system at the expense of the vibration reduction performance. The stability of the nonlinear system with a single VFC loop has been studied using the Lyapunov linearisation method for the local stability, the describing function method for the detection of limit cycle oscillations and the analysis of the time domain response to an impulse excitation. The numerical simulations have shown that VFCs are more liable to instability if the inertial actuator has stroke saturation nonlinearity. In fact, the impacts between the proof mass and the actuator's end-stops are in-phase with the velocity of the structure, thus they contribute to reducing the overall damping of the system, which results in the instability. Moreover, the feedback gain that causes the instability in the nonlinear system is much lower than the one predicted by the linear Nyquist analysis for the underlying linear system. Finally, this motivated the development of a NLFC that operates as a second loop in combination with the classical VFC. The proposed nonlinear controller actively increases the internal damping of the actuator as the proof mass approaches the end stops, taking negligible values when the proof mass is clear from the displacement constraints. The NLFC has been investigated using the Lyapunov linearisation method and the analysis of the time domain response to an impulse excitation and the results are compared in terms of stability of the control system with the single VFC loop scenario for several values of the feedback gain and amplitude of the impulse excitation. It has been shown that the NLFC is able to increase the safe operating region of the actuator with respect to the single VFC loop, hence, larger feedback gains can be used, or larger impulse excitations can be withstood, without the system becoming unstable.

Chapter 6

Nonlinear feedback control of a SDoF structure: experimental analysis

The nonlinear feedback controller (NLFC) presented and studied using numerical simulations in chapter 5 has been shown to increase the stability region of nonlinear inertial actuators. This chapter aims to investigate the experimental implementation of the NLFC and how it compares with the VFC in terms of stability of the closed-loop system under different scenarios. The author is not aware of experimental work on similar control strategies. In fact, the most similar nonlinear controller to the NLFC presented in this thesis can be found in [41; 122–125], which has been analysed only by theoretical studies. Experimental implementation of controllers that account for stroke saturation can be found in [54–56; 59; 83; 128; 156], however, these controllers focus mainly on strategies that limit or reduce the VFC gain. The main objective of this study is to implement the NLFC law developed in the previous chapter on a stroke limited inertial actuator that is used to control the first mode of a cantilever beam. Firstly, the modal analysis via impact testing of the cantilever beam is presented and the natural frequencies and mode shapes of the beam are measured in section 6.1. Secondly, the actuator is attached to the beam in a position where the structure's response is mainly given by its first mode. The open-loop FRF of the VFC system is measured for a unit feedback gain and the underlying linear gain margin is calculated in section 6.2. The closed-loop response of the VFC to an impulsive primary excitation for several values of the feedback gain and levels of excitation has also been measured. Finally, the NLFC implementation is discussed in section 6.3 and the closed-loop response of the combined VFC+NLFC loop is compared with that of the single VFC loop in terms of the stability of the control system.

6.1 Experimental set-up and modal analysis of a cantilever beam

The experimental set-up for the impact testing of the cantilever beam is displayed in figure 6.1. This analysis is conducted using a toolbox of the LMS Test.Lab® software employing a SCADAS data acquisition system. The cantilever beam is excited by a Dytran (Dynapulse 5800B3 S/N 6160) rowing hammer, which can be equipped with three different tips. A stiff aluminium tip (127-6250), a medium stiff Delrin tip (127-6250P) and a soft polyurethane tip (127-6250PS). Due to the light damping of the structure under testing, the Delrin plastic tip is used throughout the experiment. The response of the beam is measured by a B&K accelerometer (type 4375V) fixed on the free end. The acceleration signal passes through a B&K charge amplifier (type 2635) before being acquired by the SCADAS.

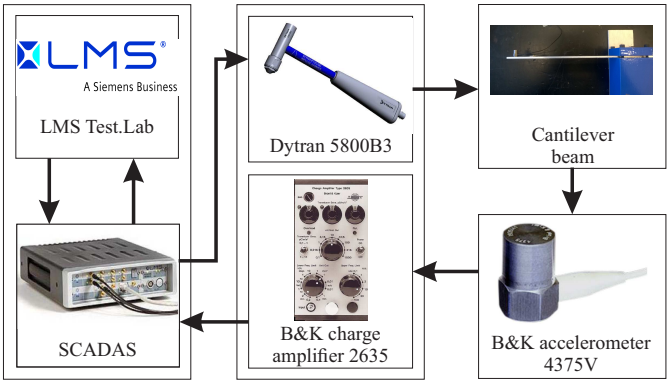

FIGURE 6.1: Block diagram of the modal analysis experimental set-up.

The test rig is shown in figure 6.2(a), which comprises of an aluminium bar with rectangular cross section, 25 mm width, 3 mm thick and 175 mm long and a a rigid connection to the ground at one end of the beam. The accelerometer is placed 7.5 mm away from the free end, which is shown in figure 6.2(b) as the point H_{11}. The hammering points are named with a progressive number starting from H_1 to H_{11} and they are spaced 15 mm apart, except for H_{10} and H_{11} that are 17.5 mm apart.

The experimental analysis is conducted hammering 5 times each point on the grid and taking the averaged FRF. The driving point FRF (H_{11}) between acceleration and input force is shown in figure 6.3 with the solid blue line and is compared with a theoretical model of the cantilever beam shown with the solid red line. For reference, the derivation of the theoretical model of the cantilever beam is reported in appendix D. The subscript c denotes the control point location, whereas the subscript p denotes the location of the primary excitation. In this case the two are collocated. The experimental results are in good agreement with the derived theoretical model, at least for the numeric value of the natural frequencies. In fact, the first and second experimentally identified resonances are

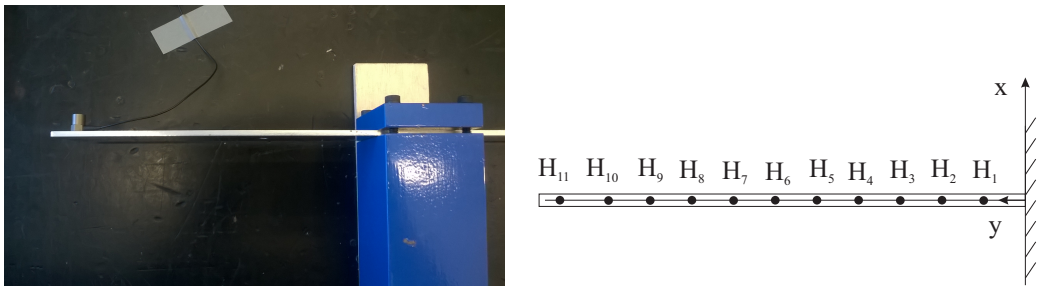

(a) (b)

FIGURE 6.2: Experimental test rig for the identification of the beam natural frequencies and mode shapes. (a) Picture of the test rig; (b) Sketch of the hammering point grid.

68.5 Hz and 443.2 Hz, while the theoretical ones are 68.9 Hz and 458.8 Hz, respectively.

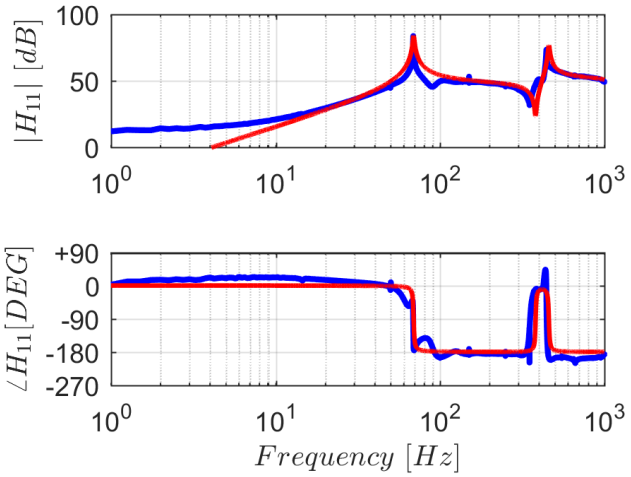

FIGURE 6.3: Comparison between the experimental and simulated FRFs of the beam at driving point H_{11}. The blue solid line shows the experimental FRF, whereas the red solid line displays the simulated FRF.

The fact that the first two resonances are well separated permits one to build an analogy between the response of the cantilever beam and of a SDoF system if the control position is on the node of the second mode of the beam. In fact, for low frequencies (below 1 kHz), the response of the beam is dominated by the first two modes. Using the toolbox provided by LMS Test.Lab® the mode shapes associated with the measured natural frequencies can be estimated. The first two mode shapes of the beam are shown in figure 6.4, where the grid is composed by the eleven hammering points displayed in figure 6.2(b). It can be seen in figure 6.4 that the first mode is characterised by an in phase motion of all the points along the beam. The second mode has both in phase and out of phase motion, instead. Hence, there is a point along the beam where the in phase and out of phase motion coincide and have zero amplitudes. Hence, any force applied

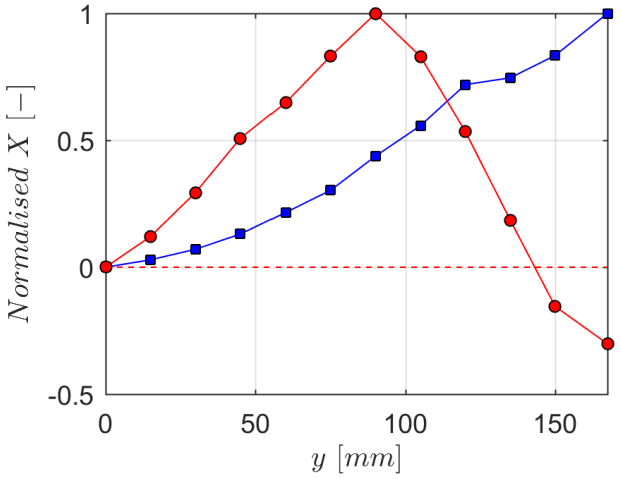

FIGURE 6.4: First and second mode shapes of the beam derived with LMS Test.Lab ® modal analysis software and normalise with respect to their maximum value. Mode one occurs at 68.5 Hz and is displayed by the blue squares. Mode two occurs at 443.2 Hz and is indicated by the red circles.

at this point would affect only the first mode of the beam. Consequently, it can be a good candidate for positioning the actuator.

6.2 Velocity feedback control of a cantilever beam using a nonlinear actuator

The inertial actuator is attached to the cantilever beam on the node of the second mode of the beam, as suggested by the analysis of the previous section. The test rig for the active vibration control of a beam using a stroke limited inertial actuator is shown in figure 6.5 consisting of the aluminium cantilever beam, the inertial actuator placed 38 mm away from the free end of the beam, a collocated accelerometer attached to the actuator casing and a force cell positioned between the beam and the proof mass actuator.

A simulation study has been conducted prior to the experimental investigation in order to understand the passive behaviour of the components attached to the beam. In particular, the response (velocity) of the beam at control position c due to a primary excitation at position p is investigated. The ratio between the velocity of the beam at the control position and the force at the primary position is called mobility $G_{cp}(j\omega)$ and its formulation is derived in appendix D and can be found in [157]. Figure 6.6 shows the Bode plot of the simulated mobilities $G_{cc}(j\omega)$ for the plain cantilever beam (solid red line) and for the beam with the actuator and the instrumentation attached (solid blue line), when the primary point p coincides with the control point c. In both cases the second resonance vanished, as the control point is on the node of the second mode shape,

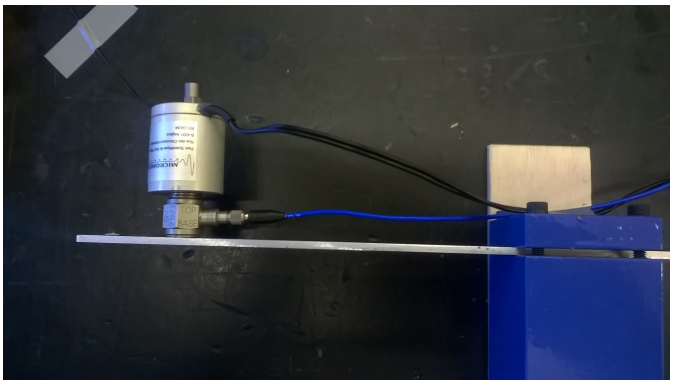

FIGURE 6.5: Experimental set-up for the VFC of a beam using a stroke limited inertial actuator. The set-up consists of an aluminium cantilever beam, a force gauge, a stroke limited actuator and a collocated accelerometer.

also, the first and third resonance are very well separated in frequency. Consequently, an excitation with a spectrum below 1 kHz produces a response that is mainly dominated by the first structural mode of the beam. A comparison between the FRFs of the driving point mobilities shows that adding the actuator and the instrumentation shifts the resonance frequencies towards lower values with respect to those of the plain beam, due to the added mass. In particular, the first natural frequency moves down to 40.3 Hz, which is still well above the natural frequency of the actuator and the amplitude of the first resonance is also reduced due to the added internal damping of the actuator.

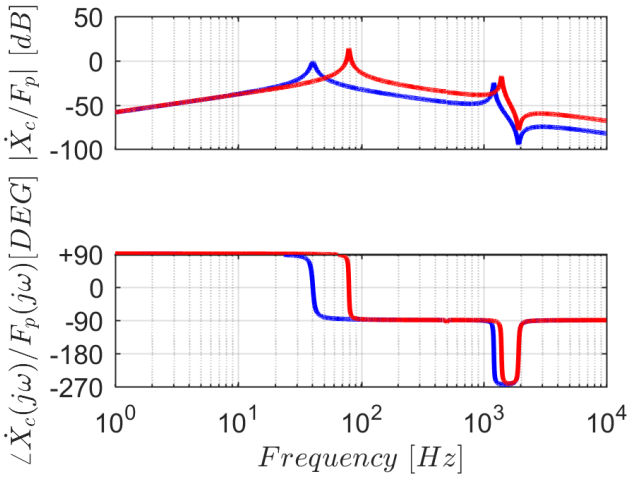

FIGURE 6.6: Comparison between the simulated FRFs of the beam response at the control position with and without the control unit attached. The solid blue line represents the beam response with the control unit, whereas the solid red line represents the beam response without the control unit.

The experimental set-up for the VFC of the cantilever beam using a stroke limited inertial actuator is displayed in figure 6.7. The cantilever beam is excited on its free end by a Dytran (Dynapulse 5800B3 S/N 6160) hammer with a medium stiff Delrin tip (127-6250P). The signal of the primary force is acquired by a dSPACE 1103 PPC

Controller Board, where the analogue-to digital conversion (ADC) is also performed with a sampling frequency f_s =10 kHz. The response of the beam at the control position is measured by a B&K accelerometer (type 4375V) fixed on the actuator casing connected to a B&K charge amplifier (type 2635), where the signal is integrated and high-pass filtered with a cut off frequency of 1 Hz. The force signal of the PCB Piezotronics 208C01 ICP force sensor is not used for the VFC scenario. All the measurements are then recorded by ControlDesk Next Generation software on a PC workstation. The structure's velocity signal is thus amplified in real time by a feedback gain h_s and then converted from digital to analogue by the dSPACE. The control signal from the dSPACE passes through a low pass analogue filter with a cut-off frequency at 4 kHz before entering the Micromega Dynamics voltage driven current amplifier PR-052-01-04-03 and then the inertial actuator.

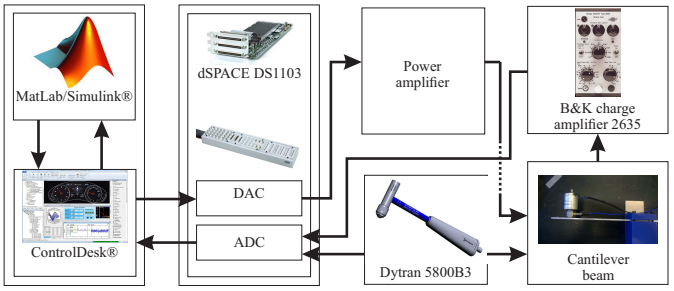

FIGURE 6.7: Block diagram of the experimental set-up including the active feedback control.

The same approach of the theoretical study of chapter 5 has been considered for the experimental study. Firstly, the open-loop FRF has been measured for small excitation signals in order to obtain the underlying linear gain margin of the VFC. Consequently, the VFC closed-loop response has been measured for several excitation levels and velocity feedback gains. The open-loop control diagram is the one represented in figure 5.5, where $Y(s) = \dot{X}_c(s)$ is the response of the beam at the control position, $r(s)$ is the input reference signal from the dSPACE and the mobility transfer function $G_{sa}(s) = G_{cc}(s)$. The stability of the system is analysed using the Nyquist criterion for the open loop FRF $L(j\omega) = g_a h_s G_{cc}(j\omega)$. The control gain h_s is set to unity and the actuator is driven by a broadband white noise current. This results in the polar plot shown in figure 6.8. It can be seen that the locus of the Nyquist intersects the negative real axis at a distance δ =0.068, which corresponds to a gain margin $g_m = 1/\delta = 14.7$. As a result, the maximum VFC gain calculated with a linear stability analysis that can be applied to the system without driving it unstable is $h_{s,max} = 14.7$. The other visible circles on the right half plane of figure figure 6.8 correspond to the upper natural frequencies of the system.

The open-loop FRF with $h_s = 1$ is also shown in amplitude and phase in figure 6.9, where the coherence of the measurement is also reported presenting values close to unity up to 7 Hz. This is an indication that the stiffness nonlinearity is not affecting the behaviour

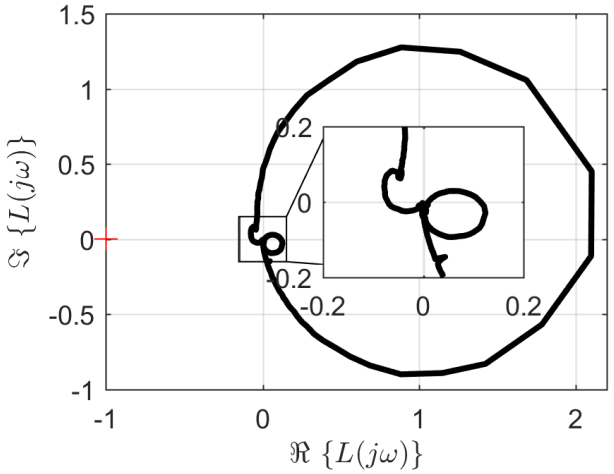

FIGURE 6.8: Nyquist plot of the measured open-loop FRF using a VFC gain $h_s = 1$.

of the system at this level of excitation [158]. The drop of the coherence that can be seen at 50 Hz is supposed to be caused by the frequency of the electrical network to which the accelerometer's charge amplifier is connected.

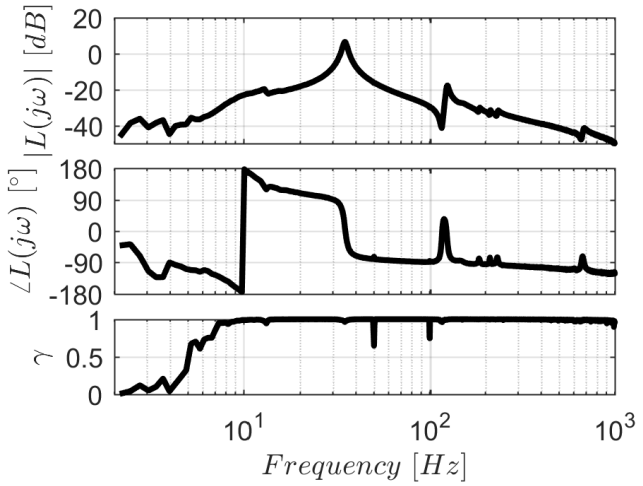

FIGURE 6.9: Bode plot of the measured open-loop FRF using a VFC gain $h_s = 1$.

After the stability has been assessed using the Nyquist criterion, the performance of the active control system is investigated evaluating the closed-loop FRFs. The closed-loop control diagram is the one represented in figure 5.7, where$F_e(s) = F_p(s)$ is the primary excitation at the tip of the beam, and $G_{se}(s) = G_{cp}(s)$ is the mobility at the control position due to a primary excitation at a different location. In this case the system is excited by an impulse at the free end of the beam using the instrumented hammer. A fixed control gain h_s is implemented for each test case, starting from the uncontrolled case and increasing its value until instability is reached. The data acquisition is performed using the ControlDesk software, where the trigger and pre-trigger settings are adjusted in order to record all the information of the signals and limiting the acquisition of the

noise. Each acquisition is 5 seconds long and 5 acquisitions are preformed for each test case (same h_s), then the mean FRF is plotted. Both the excitation and response signals are windowed using classical windows for hammer testing. An exponential window has been applied to both the signals to improve the signal to noise ratio since the noise can take over the signal towards the end of the acquisition time, where the response has decayed away. This window has been applied to both the signals to account for the damping correction. An additional force window is applied to the force signal to eliminate noise on the force channel after the impact. In fact, this noise is not an input energy that excites the system being tested. The windowing functions adopted in this study can be found also in [159; 160]. The FRFs of the closed-loop response are then estimated using the H_1 estimator defined as the ratio between the cross-spectrum of the input and output signals and the auto-spectrum of the input signal [140], and averaged between all the measurements.

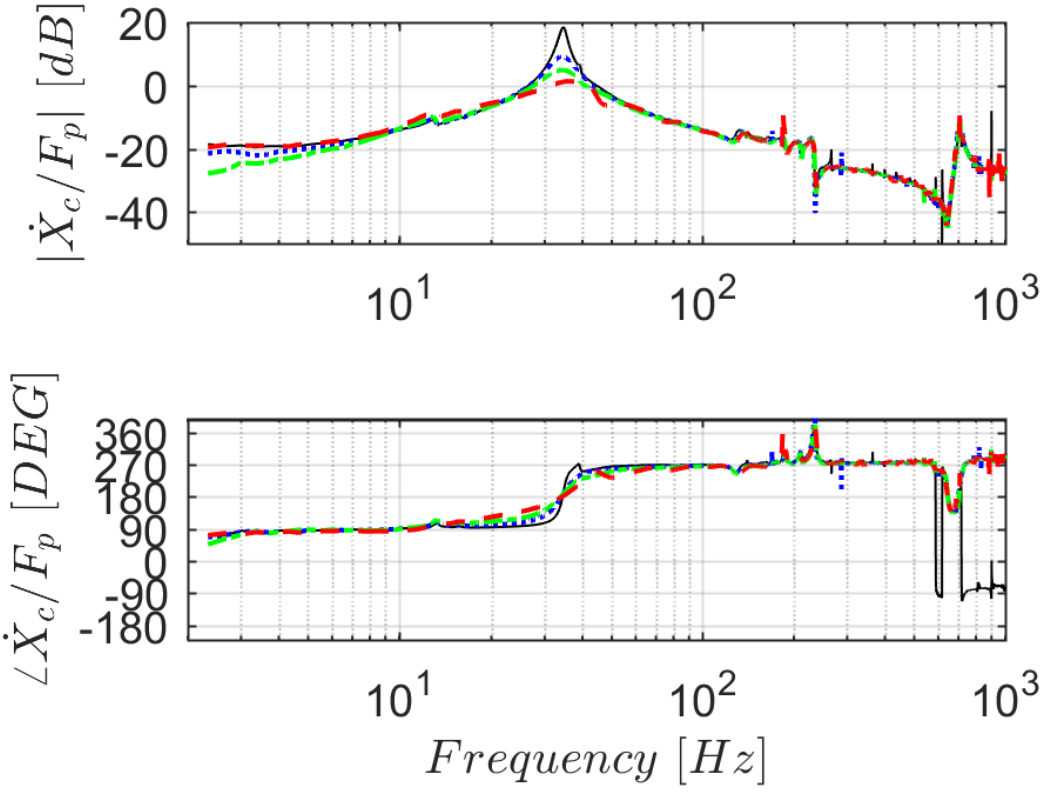

FIGURE 6.10: Bode plot of the measured closed-loop FRF with of the mobility at the control position for several VFC gains as follows. The solid black line shows the response of the uncontrolled beam, the dotted blue line shows the response for $h_s = 6\%h_{s,max}$, the dash-dotted green line shows the response for $h_s = 12\%h_{s,max}$ and the dashed red line shows the response for $h_s = 18\%h_{s,max}$. No stroke saturation has been observed for these cases.

The results are shown in figure 6.10 for feedback gains h_s from 0 (passive system) marked with the solid black line, $6\%h_{s,max}$ marked with the dotted blue line, $12\%h_{s,max}$ marked

with the dash-dotted green line, to 18%$h_{s,max}$ marked with the dashed red line. By increasing the control gain, the resonance peak of the first mode of the structure is effectively reduced, whereas the behaviour of the system at higher frequencies is not affected by the increase in the control gain. However, the vibration of the beam is significantly reduced as it is mainly determined by the first mode. A more detailed observation of figure 6.10 shows the presence of an increase of the response amplitude at a frequency around 12 Hz, which can be associated with the damping of the inertial actuator being reduced and consequently the resonance peak being increased.

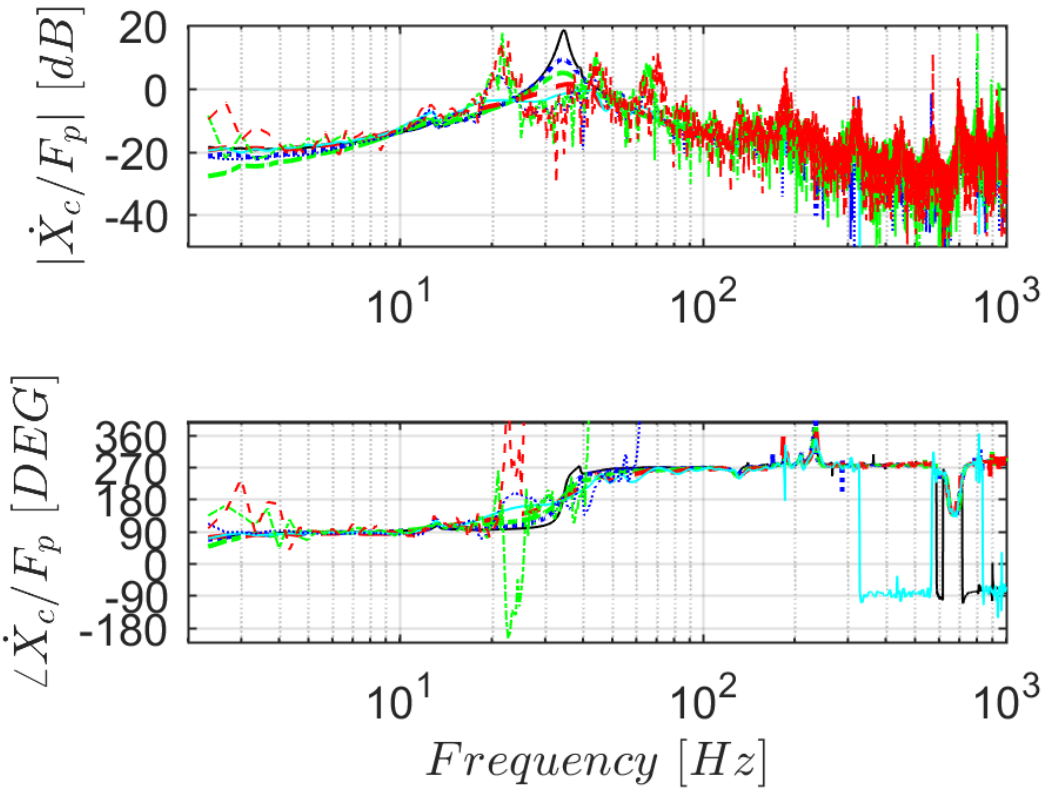

FIGURE 6.11: Bode plot of the measured closed-loop FRF with of the mobility at the control position for several VFC gains as indicated in the previous figure and as follows. The thin solid cyan line shows the response for $h_s = 24\%h_{s,max}$, the thin dotted blue line shows the response for $h_s = 30\%h_{s,max}$, the thin dash-dotted green line shows the response for $h_s = 36\%h_{s,max}$ and the thin dashed red line shows the response for $h_s = 42\%h_{s,max}$. Stroke saturation has been observed for $h_s > 24\%h_{s,max}$.

As the feedback gain is further increased, collisions between the proof mass and the actuator casing are observed and the system is susceptible to become unstable. The instability not only depends on the value of the feedback gain, but also on the amount of energy that the initial impulse releases into the system. The FRFs of the closed-loop response for feedback gains also from 24%$h_{s,max}$ to 42%$h_{s,max}$ are presented in figure 6.11. For $h_s = 24\%h_{s,max}$, shown with the thin solid cyan line, a significant increase of the response for frequencies below the structural resonance are observed. In

fact, the proof mass is subject to some impact after the initial excitation, but after a finite time the response decays away. Increasing the feedback gain to $h_s = 30\%h_{s,max}$, several collisions reported after the initial impulse and also in this case the response decays away after a certain time. The FRF of the response for $h_s = 30\%h_{s,max}$ is displayed with the thin dotted blue line and shows a more noticeable spillover effect and also the presence of another peak at around 21 Hz. A larger increase in the feedback gain for example $h_s = 36\%h_{s,max}$ (thin dash-dotted green line) and $h_s = 42\%h_{s,max}$ (thin dashed red line), eventually leads the system to instability even for small amplitudes of initial excitation. The vibration is thus self-sustained due to the fact that the response does not decay away and the control system continues to insert power into the system. It can be seen that for these last two cases the peak at 21 Hz shoots up and also the response at frequencies higher than the first structural resonance shows a significant increase.

A comparison between the uncontrolled beam and the VFC of the beam has also been made in time domain and the results are shown in figure 6.12. This figure compares the response of the system for $h_s = 0$ (dashed red line) and $h_s = 42\%h_{s,max}$ (dash-dotted black line) under equal excitation levels. Figure 6.12(a) shows the spectrum of the excitation force and the time history of the velocity of the beam at the control point. Figure 6.12(b) shows, instead, the phase-space trajectory of the proof mass relative displacement and velocity. In the uncontrolled scenario, the vibration of the structure dies out after a certain period of time. Also, the trajectory of the proof mass starts to orbit around the equilibrium point until it eventually decays to zero. If the VFC with a feedback gain $h_s = 42\%h_{s,max}$ is implemented, the response of the system changes dramatically. In fact, the trajectory of the proof mass experiences limit cycle oscillations that are self-sustained and lead the VFC system to instability for the same level of excitation of the uncontrolled scenario. In the next section the NLFC loop is implemented in order to tackle this instability issue.

6.3 Nonlinear feedback control of a cantilever beam using a nonlinear actuator

The combined VFC+NLFC controller is then implemented as illustrated in the schematic of figure 6.13. The signal of the accelerometer at the control position is acquired by the dSPACE, it is then digitally high-pass filtered with a cut-on frequency of 2 Hz and integrated using the trapezoidal rule in order to obtain the velocity signal at the control position. The velocity of the structure is then multiplied by a VFC gain h_s and the amplified signal is then fed into the actuator through the amplifier. This forms the VFC loop. The NLFC loop, instead, has been designed according to eq. (5.72) to add a minimum internal damping of $c_{min} = 0.5$ N/ms^{-1}, a maximum internal damping of $c_{max} = 100$ N/ms^{-1} and an exponential coefficient $p = 1$. Using these values, all

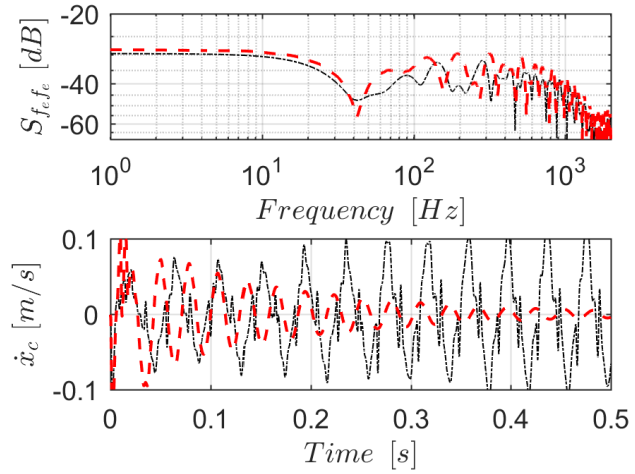

(a)

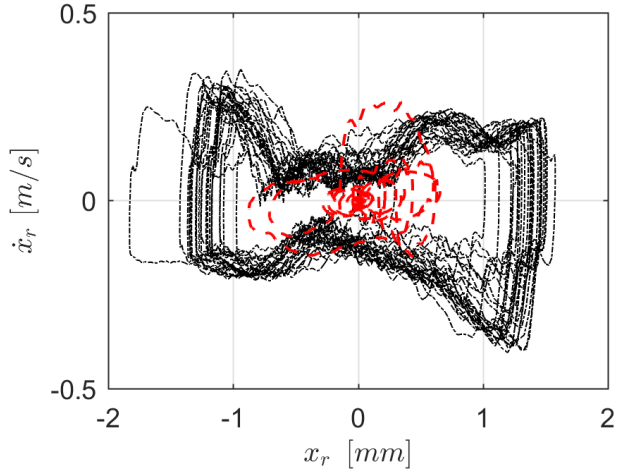

(b)

FIGURE 6.12: (a) Spectrum of the excitation force and time history of the velocity signal at the control point; (b) Phase-space trajectory of the relative proof mass displacement and velocity. Dashed red line for the uncontrolled scenario and dash-dotted black line for the single VFC scenario using $h_s = 42\% h_{s,max}$.

the parameters of the NLFC can be determined. For this control loop, both the force cell signal f_c and the acceleration signal $\ddot{x}_c$ have been filtered with a second order Butterworth high-pass filter with a cut-on frequency of 2 Hz.

The proof mass relative acceleration has been calculated as,

$$\ddot{x}_r = \frac{f_c - m_c \ddot{x}_c}{m_p}, \tag{6.1}$$

where,

$$m_c = m_{acc} + m_b + m_{gauge}, \tag{6.2}$$

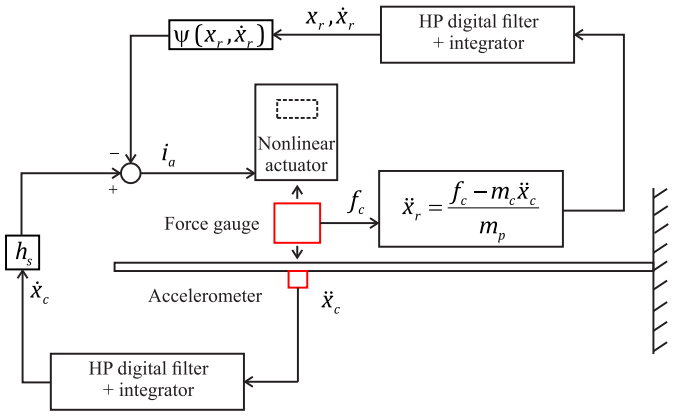

FIGURE 6.13: Schematic of the experimental implementation of the VFC and NLFC.

is the total mass attached to the beam at the control position, $m_{acc} = 0.005$ kg is the mass of the accelerometer and $m_{gauge} = 0.023$ kg is the mass of the force cell. The relative proof mass velocity and displacement are then estimated by high-pass filtering and integrating the acceleration signal, in the same way as it has been discussed for the structure's velocity signal. The NLFC control signal is then calculated in real time using equation eq. (5.72) before being fed back to the actuator. The Simulink model of the experimental implementation of the NLFC on the dSPACE is reported in appendix E.

Figure 6.14 shows a comparison of the response of the beam and proof mass among the uncontrolled scenario (dashed red line), the single VFC loop with $h_s = 42\%h_{s,max}$ (dash-dotted black line) and the combined VFC+NLFC loop with $h_s = 42\%h_{s,max}$ (blue solid line) under equal excitation levels. Figure 6.14(a) shows the spectrum of the excitation force and the time history of the velocity of the beam at the control point. Figure 6.14(b) shows, instead, the phase-space trajectory of the proof mass relative displacement and velocity. It can be observed that under the same excitation condition, the systems that implements the combined VFC+NLFC is able to avoid stroke saturation and hence the limit cycle oscillations of the proof mass so that the control system remains stable. In fact, the response of the beam quickly dies out and the trajectory of the proof mass goes to zero. The theoretical parametric study performed in section 5.3 has been repeated experimentally in order to test the robustness of the controller to increasing control gains and to increasing levels of excitation.

The beam has been excited with three different levels of excitation, namely: low (below 20 N peak amplitude, medium (between 20 N and 30 N) and high (above 30 N). For each level of excitation, the test has been repeated increasing the VFC gain from the uncontrolled scenario to $h_{s,max}$. The parametric study has been conducted in the first place for the single VFC loop and then for the combined VFC+NLFC loop in order to compare the operating regions of the stroke limited actuator for the two different control strategies. The results are shown in figure 6.15, where the red circles are the experimental data points in which the single VFC loop is stable and the black asterisks

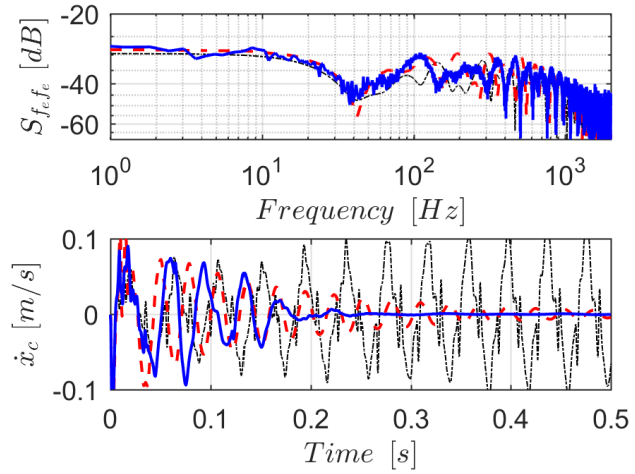

(a)

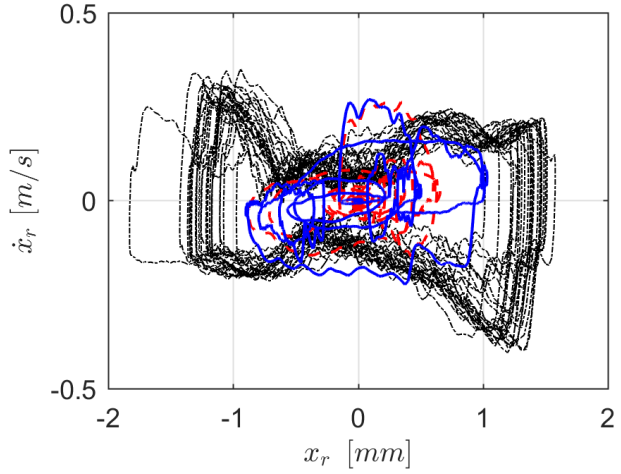

(b)

FIGURE 6.14: (a) Spectrum of the excitation force and time history of the velocity signal at the control point; (b) Phase-space trajectory of the relative proof mass displacement and velocity. Dashed red line for the uncontrolled scenario, dash-dotted black line for the single VFC scenario using $h_s = 42\%h_{s,max}$ and solid blue line for the VFC+NLFC scenario using $h_s = 42\%h_{s,max}$.

are the experimental data points in which the combined VFC+NLFC is stable. Each point in figure 6.15 corresponds to an experiment of the same type of the one presented in figure 6.14. In order to give more evidence, some of the time histories of the experimental data points shown in figure 6.15 are reported in appendix F. The data points of the two control strategies define the operating regions of the inertial actuator that are highlighted by the light grey area for the single VFC loop and by the dark grey area for the combined VFC+NLFC loop. It is clear that the added NLFC loop is able to extend the stability region of the inertial actuator to larger control gains and higher level of excitation compared to a single VFC loop.

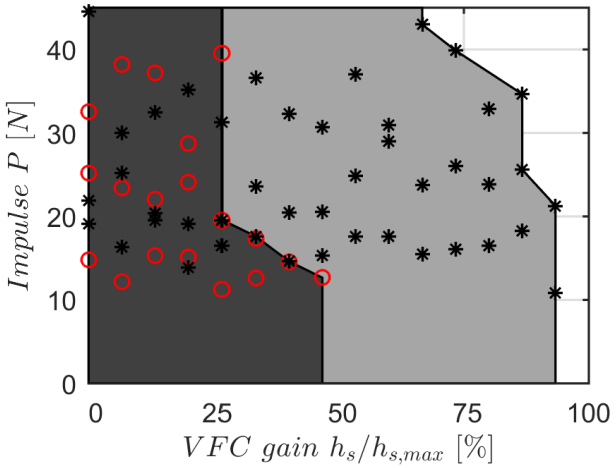

FIGURE 6.15: Comparison between the single VFC and VFC+NLFC in terms of stability range for the experimental investigation. The red circles in the dark grey area show the experimental data points in which the VFC is stable; the black asterisks in the light grey area show the experimental data point in which the combined VFC+NLFC controller is stable.

6.4 Summary

In this chapter an experimental analysis on a NLFC for a stroke limited inertial actuator used in the active vibration control of a cantilever beam has been presented. Firstly, impact testing and modal analysis have been performed on the aluminium cantilever beam with the aid of LMS Test.Lab® software. The structure under investigation presents well separated resonances, hence the response at low frequencies is dominated by the first mode. Secondly, the stroke limited inertial actuator has been attached to the free end of the cantilever beam and both the open-loop and closed-loop FRFs have been measured for the VFC using small excitation signals. The open-loop analysis, conducted for the actuator operating within its linear range, suggests a maximum feedback gain $h_{s,max} = 14.70$ guaranteeing closed-loop stability. The VFC performance has been analysed comparing the closed-loop FRFs for increasing feedback control gains. It has been shown that the VFC effectively reduces the amplitude of the structure's resonance peak up until a certain feedback gain. Further increase of the feedback gain results in stroke saturation and an enhanced level of vibration. For a feedback gain $h_s = 42\%h_{s,max}$, the system has become unstable under the same excitation conditions of the uncontrolled scenario. The real time implementation of the nonlinear control law has been discussed, where the control signal is dependent of the excitation level, the proof mass relative displacement and velocity. The relative displacement and velocity signals have been measured with the aid of a force gauge placed between the actuator and the beam, and a collocated accelerometer. The response of the beam and the phase-space trajectory of the proof mass have been analysed for both the single VFC loop and the combined VFC+NLFC loop, for several levels of excitation and increasing velocity

feedback gains. In each test the stability of the control system has been assessed. It has been shown that the NLFC is able to avoid stroke saturation and the associated limit cycle oscillations of the proof mass, hence, increasing the stability region of the inertial actuator with respect to the single VFC loop. This means that larger feedback gains can be used or, or higher levels of excitation can be withstood, without the system becoming unstable when this NLFC is in place. The NLFC has increased the operating range of the nonlinear inertial actuator.

Chapter 7

Proof mass state estimation

The NLFC, which has been developed in chapter 5 and experimentally investigated in chapter 6, relies on the real-time measurements of the proof mass relative displacement and velocity. Unfortunately, many actuators, including that under investigation in chapter 6 are not provided with a sensor that can measure either of these, which was why an additional force gauge was introduced in section 6.3 between the structure and the actuator base to measure the control force. The proof mass velocity was then estimated by considering the dynamic eq. (6.1). The proof mass of this device cannot be instrumented with an accelerometer or a strain gauge, since the actuator casing has been welded in place. However, the additional force gauge adds mass to the structure and is an expensive device. This motivates the development of a self-sensing algorithm that makes use of the available measurements and the identified mathematical model to give the best estimate of the proof mass states relatively to the structure. This approach is often referred as virtual sensing [161; 162] and can be beneficial as it reduces the cost and weight of fitting inertial actuators with an additional physical sensor. Several studies can be found on self-sensing electrodynamic actuators [70; 163–165], however, they consider either the base of the actuator to be blocked, or to modify the actuator with an additional magnet-coil in open-circuit that measures the relative velocity from the back-emf. Moreover, the dynamic behaviour of the actuator is assumed to be linear. This chapter investigates the estimation of the relative proof mass velocity from the available measurements, input signals and from the identified nonlinear model of the actuator, without having to rely on any additional physical sensors. Firstly, an open-loop algorithm is derived in section 7.1, which calculates the proof mass relative velocity by applying a digital filter to the input current and base velocity signals, where the digital filter coefficients are calculated from the actuator underlying linear identified model. Secondly, an extended Kalman filter (EKF) algorithm [133] is presented in section 7.2, which calculates the optimal estimate of the proof mass relative velocity using the nonlinear identified model of the actuator, the input current, the base acceleration

signals and the voltage measurement across the coil terminals. Finally, a comparison and a summary of the two approaches are given in section 7.3.

7.1 Linear digital filter approach

Considering the underlying linear model of the inertial actuator in figure 3.4 and that the control force applied by the actuator on the structure is $f_c = -f$, the equation of motion of the proof mass and the control force can be written as,

$$\begin{cases} m_p\ddot{x}_p(t) = \phi i_a(t) - c_p\dot{x}_r(t) + k_p\dot{x}_r(t) & \text{(7.1a)} \\ f_c(t) = -m_p\ddot{x}_p(t) - m_b\ddot{x}_b(t) & \text{(7.1b)} \end{cases}.$$

Considering zero initial conditions, the Laplace transform of eq. (7.1) results in,

$$\begin{cases} sm_p\dot{X}_p(s) = \phi I_a(s) - \left[c_p + \dfrac{k_p}{s}\right]\dot{X}_r(s) & \text{(7.2a)} \\ F_c(s) = -sm_p\dot{X}_p(s) - sm_b\dot{X}_b(s) & \text{(7.2b)} \end{cases}.$$

From the set of eq. (7.2) the control force can be written as,

$$\begin{cases} F_c(s) = -\phi I_a(s) + [c_p + \dfrac{k_p}{s}]\dot{X}_r(s) - sm_b\dot{X}_b(s) & \text{(7.3a)} \\ F_c(s) = -sm_p\dot{X}_r(s) - s(m_p + m_b)\dot{X}_b(s) & \text{(7.3b)} \end{cases},$$

where $x_r = x_p - x_b$ has been used. Equalling the right hand side terms of eqs. (7.3a) and (7.3b) leads to an algebraic equation that can be solved for the relative velocity as,

$$\dot{X}_r(s) = \frac{\phi I_a(s)}{sm_p + c_p + \frac{k_p}{s}} - \frac{sm_p\dot{X}_b(s)}{sm_p + c_p + \frac{k_p}{s}}, \tag{7.4}$$

hence, the proof mass relative velocity is given by the summation of two components, where the first one is a transfer function with respect to the input current, which can be written as,

$$H_{1a}(s) = \left.\frac{\dot{X}_r(s)}{I_a(s)}\right|_{\dot{X}_b(s)=0} = \frac{\phi s}{s^2m_p + sc_p + k_p}, \tag{7.5}$$

and the second one is a transfer function with respect to the base velocity, which can be written as,

$$H_{2a}(s) = \left.\frac{\dot{X}_r(s)}{\dot{X}_b(s)}\right|_{I_a(s)=0} = \frac{m_ps^2}{s^2m_p + sc_p + k_p}. \tag{7.6}$$

These transfer functions of eqs. (7.5) and (7.6) are then translated in the digital domain using the bilinear transformation [140; 166], thus substituting,

$$s \to \mu\frac{1 - z^{-1}}{1 + z^{-1}}, \tag{7.7}$$

where z is the complex variable for the discrete system and μ is a pre-warping coefficient calculated as follows,

$$\mu = \frac{\omega_p}{\tan(\frac{\omega_p}{2f_s})}, \tag{7.8}$$

where f_s is the sampling rate and ω_p is the natural frequency of the inertial actuator. Thus, the digital filter applied to the input current becomes,

$$\begin{aligned} H_{1d}(z) &= \left.\frac{\dot{X}_r(z)}{I_a(z)}\right|_{\dot{X}_b(z)=0} = \\ &= \frac{\phi\mu - \phi\mu z^{-2}}{(m_p\mu^2 + c_p\mu + k_p) + (2k_p - 2m_p\mu^2)z^{-1} + (m_p\mu^2 - c_p\mu + k_p)z^{-2}}, \end{aligned} \tag{7.9}$$

and the digital filter applied to the base velocity results in,

$$\begin{aligned} H_{2d}(z) &= \left.\frac{\dot{X}_r(z)}{\dot{X}_b(z)}\right|_{I_a(z)=0} = \\ &= \frac{m_p\mu^2 + 2m_p\mu^2 z^{-1} + m_p\mu^2 z^{-2}}{(m_p\mu^2 + c_p\mu + k_p) + (2k_p - 2m_p\mu^2)z^{-1} + (m_p\mu^2 - c_p\mu + k_p)z^{-2}}. \end{aligned} \tag{7.10}$$

Finally, combining the filtered measured signals using eqs. (7.9) and (7.10) gives the real-time estimation of the proof mass relative velocity, as shown by the block diagram in figure 7.1.

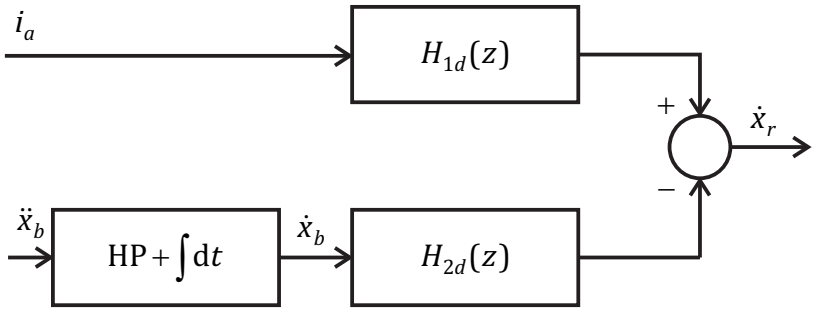

FIGURE 7.1: Block diagram of the proof mass relative velocity estimation using linear digital filters, the measured input current and the base acceleration signal.

The estimation of the proof mass relative velocity using the linear digital filter shown in figure 7.1 can be compared with the case in which it is calculated from the force gauge signal as presented in chapter 6 using the experimental data from the previous chapter. Figure 7.2 shows the time history of the proof mass relative velocity when the actuator is operating within its linear range of motion. The solid black line represents the proof mass velocity derived from the force gauge measurement using eq. (6.1), whereas the dash-dotted red line shows estimation of the velocity signal using the linear digital filter given by the combination of eqs. (7.9) and (7.10). Since the actuator is operating within its linear range of motion, the virtual sensing approach can reliably predict the proof mass relative velocity, however, this no longer applies when the actuator enters its nonlinear regime of motion. In fact, figure 7.3 shows the response of the proof mass

when it is subject to a limit cycle oscillation. In this scenario, the linear digital filter fails to match the reference signal given by the force gauge measurement, being out-of-phase and most importantly not predicting the sudden changes in the velocity signal from positive to negative values and vice-versa that are due to the proof mass colliding with the end-stops.

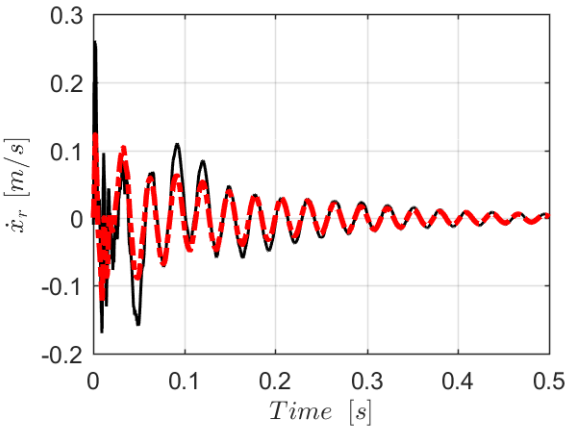

FIGURE 7.2: Time histories of the proof mass relative velocity measured by using the force gauge signal (solid black line) and estimated with a linear digital filter (dash-dotted red line) when the actuator is operating within its linear range of motion.

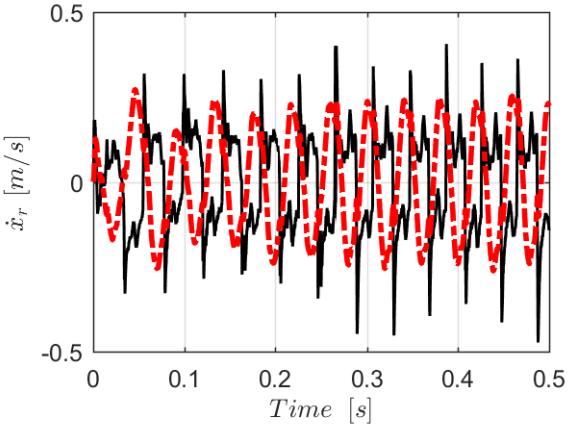

FIGURE 7.3: Time histories of the proof mass relative velocity measured by using the force gauge signal (solid black line) and estimated with a linear digital filter (dash-dotted red line) when the actuator is operating in nonlinear motion and the proof mass is experiencing limit cycle oscillations.

7.2 Extended Kalman filter approach

The results of the previous section motivate the development of a virtual sensor based on the nonlinear dynamic model of the stroke limited inertial actuator. The equation of

motion of the nonlinear inertial actuator model in figure 3.12 can be written as,

$$m_p\ddot{x}_r + c_p\dot{x}_r + \kappa(x_r)x_r = \phi i_a - m_p\ddot{x}_b, \tag{7.11}$$

where the nonlinear stiffness $\kappa(x_r)$ is given by,

$$\kappa(x_r) = \begin{cases} k_p & |x_r| < x_0 \quad (7.12a) \\ k_p + k_c(1 - \frac{x_0}{|x_r|}) & |x_r| \geq x_0 \text{,} \quad (7.12b) \end{cases}$$

according to eq. (4.6), where $k_c = k_{sat} - k_p$ is the impact stiffness. The equation of motion given by eq. (7.11) can be rewritten in a continuous time state-space form as,

$$\begin{cases} \dot{\mathbf{x}} = \mathbf{A}(\mathbf{x})\mathbf{x} + \mathbf{B}\mathbf{u} & (7.13a) \\ y = \mathbf{C}\mathbf{x} + \mathbf{D}\mathbf{u} & (7.13b) \end{cases},$$

where the state vector

$$\mathbf{x} = \{x_r \ \dot{x}_r\}^T, \tag{7.14}$$

the input vector

$$\mathbf{u} = \{i_a \ \ddot{x}_b\}^T, \tag{7.15}$$

the system matrix is given by,

$$\mathbf{A}(\mathbf{x}) = \begin{bmatrix} 0 & 1 \\ -\frac{\kappa(x_r)}{m_p} & -\frac{c_p}{m_p} \end{bmatrix}, \tag{7.16}$$

and the input matrix can be written as,

$$\mathbf{B} = \begin{bmatrix} 0 & 0 \\ \frac{\phi}{m_p} & -1 \end{bmatrix}. \tag{7.17}$$

The system output cannot be $y = \dot{x}_r$ as it would not be measurable. Instead, the voltage across the actuator coil terminals can be measured as,

$$e_a = \phi\dot{x}_r + R_e i_a, \tag{7.18}$$

where the inductive term $L_e\frac{\mathrm{d}}{\mathrm{d}t}i_a$ has been neglected. The output can thus be written as,

$$y = e_a, \tag{7.19}$$

and the output matrices are

$$\mathbf{C} = \{0 \ \phi\}, \tag{7.20}$$

and

$$\mathbf{D} = \{R_e \ 0\}. \tag{7.21}$$

In order to compare the estimation of the model with the measured data at each time step n, the discrete-time state-space form of eq. (7.13) can be obtained as,

$$\begin{cases} \dfrac{\mathbf{x}_{n+1}-\mathbf{x}_n}{\Delta t} = \mathbf{A}(\mathbf{x}_n)\mathbf{x}_n + \mathbf{B}\mathbf{u}_n & \text{(7.22a)} \\ y_{n+1} = \mathbf{C}\mathbf{x}_{n+1} + \mathbf{D}\mathbf{u}_{n+1} & \text{(7.22b)} \end{cases},$$

where n and $n+1$ represent the current and following time step, respectively, $\Delta t = 1/f_s$ is the fixed time step and the forward Euler method has been used to write eq. (7.22).

Both eq. (7.22a) and eq. (7.22b) are assumed to have stochastic disturbance contributions of zero mean uncorrelated Gaussian white noise $\mathbf{W}$ and v of known covariances $\mathbf{Q}$ and R, respectively. Thus, eq. (7.22) can be rewritten as,

$$\begin{cases} \dfrac{\mathbf{x}_{n+1}-\mathbf{x}_n}{\Delta t} = \mathbf{A}(\mathbf{x}_n)\mathbf{x}_n + \mathbf{B}\mathbf{u}_n + \mathbf{W}_n & \text{(7.23a)} \\ y_{n+1} = \mathbf{C}\mathbf{x}_{n+1} + \mathbf{D}\mathbf{u}_{n+1} + v_{n+1} & \text{(7.23b)} \end{cases},$$

In practice, the additional signals $\mathbf{W}$ and v take into account the process and measurement noise. The covariance matrix $\mathbf{Q}$ has been assumed to be diagonal and time-invariant as well as for the covariance R. Similarly, the states of the system are assumed to be Gaussian variables with covariance $\mathbf{P}$. The estimation of the system states is then performed using an extended Kalman filter (EKF) algorithm [133] due to its simple extension to nonlinear systems from the well-known linear Kalman filter [134; 135]. The aim of the EKF algorithm is to provide the mean value $\hat{\mathbf{x}}_n$ and the error covariance $\hat{\mathbf{P}}_n = \mathbf{E}\left[(\mathbf{x}_n - \hat{\mathbf{x}}_n)(\mathbf{x}_n - \hat{\mathbf{x}}_n)^T\right]$ of the estimate of the state vector given the sequence of inputs and measurements, where $\mathbf{E}[\cdot]$ represents the matrix expected value operator. At each time step n the EKF linearises the model around the current estimation point and propagates a linear approximation of the mean and the covariance of the states. Firstly, an a-priori estimate of the mean and covariance is obtained using the model of the system, then an a-posteriori estimate is calculated using the value of the measured signal. The estimation of the proof mass states can be derived using the EKF as follows,

- Initialise the estimation of the states mean and covariance: $\hat{\mathbf{x}}_0^+$, $\hat{\mathbf{P}}_0^+$;
- Calculate the a-priori estimate $\hat{\mathbf{x}}_{n+1}^- = \hat{\mathbf{x}}_n^+ + [\mathbf{A}(\hat{\mathbf{x}}_n^+)\hat{\mathbf{x}}_n^+ + \mathbf{B}\mathbf{u}_n]\,\Delta t + \mathbf{W}_n \Delta t$;
- Calculate the predicted output $y_{n+1} = \mathbf{C}\hat{\mathbf{x}}_{n+1}^- + \mathbf{D}\mathbf{u}_{n+1} + v_{n+1}$;
- Calculate the predicted covariance $\hat{\mathbf{P}}_{n+1}^- = \mathbf{F}_n \hat{\mathbf{P}}_n^+ \mathbf{F}_n^T + \mathbf{Q}$, where $\mathbf{F}_n = \frac{\partial\{[\mathbf{A}(\mathbf{x}_n)\mathbf{x}_n + \mathbf{B}\mathbf{u}_n]\Delta t\}}{\partial \mathbf{x}_n}$ is the state Jacobian matrix and $\mathbf{Q}$ is the covariance matrix of the process noise;
- Calculate the Kalman gain $\mathbf{K}_{n+1} = \hat{\mathbf{P}}_{n+1}^- \mathbf{C}^T \left(\mathbf{C}\hat{\mathbf{P}}_{n+1}^- \mathbf{C}^T + R\right)^{-1}$, where R is the covariance of the measurement noise;

- Calculate the a-posteriori mean estimate as $\hat{\mathbf{x}}_{n+1}^{+} = \hat{\mathbf{x}}_{n+1}^{-} + \mathbf{K}_{n+1}\left(y_{n+1} - \mathbf{C}\hat{\mathbf{x}}_{n+1}^{-}\right)$, where y_{n+1} is the measurement signal at step $n+1$;
- Calculate the a-posteriori covariance estimate as $\hat{\mathbf{P}}_{n+1}^{+} = \left(\mathbf{I} - \mathbf{K}_{n+1}\mathbf{C}\right)\hat{\mathbf{P}}_{n+1}^{-}$.

This EKF algorithm is then repeated at each time step n, apart for the initialisation step, which is computed only for $n = 0$.

The overall estimation procedure can be summarised by the block diagram shown in figure 7.4. The nonlinear actuator is excited by the input current and base acceleration $\mathbf{u}$ and is affected by some process noise $\mathbf{W}$ due to the uncertainties in the model. The electrical voltage across the actuator leads is measured and its time signal y, which is affected by some measurement noise v is given to the EKF algorithm together with the input signal $\mathbf{u}$. The EKF then computes the estimation of the proof mass states using the algorithm described above.

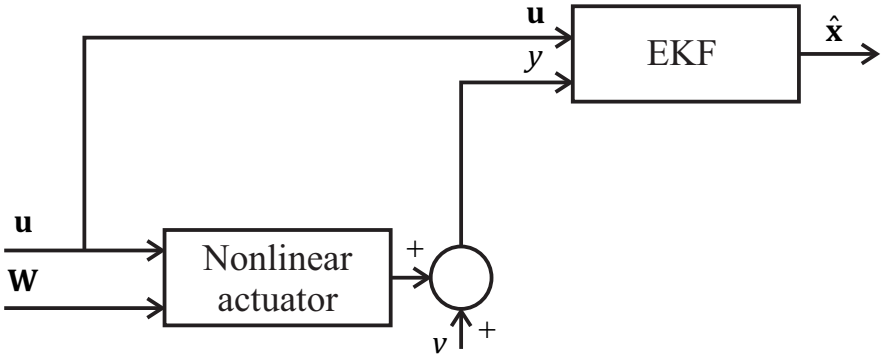

FIGURE 7.4: Block diagram of the proof mass relative velocity estimation using an extended Kalman Filter (EKF) with the measured input current and base acceleration signals and the voltage between the actuator coil terminals.

The state-space eq. (7.13) have to be observable for the virtual sensor to work, which means that the measurements have to contain enough information to be able to estimate the states of the model [133]. The observability matrix of the linearised state-space eq. (7.13) at the estimation point is given by,

$$\mathbf{Ob} = \begin{bmatrix} \mathbf{C} \\ \mathbf{CA}(\mathbf{x}) \end{bmatrix} = \begin{bmatrix} 0 & \phi \\ -\frac{\phi\kappa(x_r)}{m_p} & -\frac{\phi c_p}{m_p} \end{bmatrix}, \tag{7.24}$$

which has rank 2, hence the system is observable [133]. Another common method to asses the observability of the system is the Popov-Belevitch-Hautus (PBH) criterion [167], which states that the linearised state-space eq. (7.13) is observable if the **PBH** matrix given by,

$$\mathbf{PBH} = \begin{bmatrix} s\mathbf{I} - \mathbf{A}(\mathbf{x}) \\ \mathbf{C} \end{bmatrix} = \begin{bmatrix} s & -1 \\ \frac{\kappa(x_r)}{m_p} & s + \frac{c_p}{m_p} \\ 0 & \phi \end{bmatrix}, \tag{7.25}$$

is of the same rank as the number of states for each s. In this case the rank of the **PBH** matrix given by eq. (7.25) is 2, hence the system is observable.

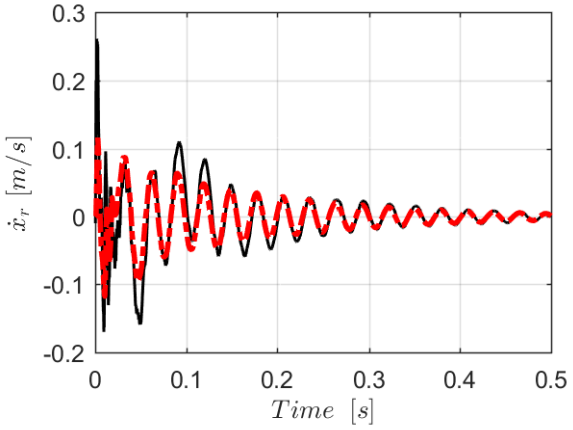

FIGURE 7.5: Time histories of the proof mass relative velocity measured by using the force gauge signal (solid black line) and estimated with an EKF (dash-dotted red line) when the actuator is operating within its linear range of motion.

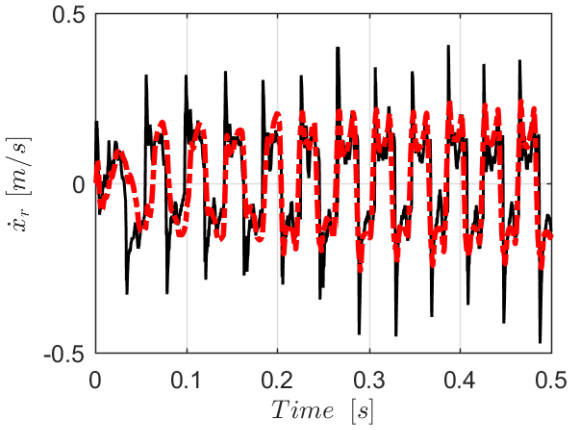

FIGURE 7.6: Time histories of the proof mass relative velocity measured by using the force gauge signal (solid black line) and estimated with an EKF (dash-dotted red line) when the actuator is operating in nonlinear motion and the proof mass is experiencing limit cycle oscillations.

The estimation of the proof mass relative velocity using the EKF algorithm shown in figure 7.4 can be compared with the case in which it is calculated from the force gauge signal as presented in chapter 6 using the experimental data from the previous chapter. Figure 7.5 shows the time history of the proof mass relative velocity when the actuator is operating within its linear range of motion. The solid black line represents the proof mass velocity derived from the force gauge measurement using eq. (6.1), whereas the dash-dotted red line shows estimation of the velocity signal using the EKF algorithm given above. In this case the actuator is operating within its linear range of motion and the virtual sensing approach can reliably predict the proof mass relative velocity and the results are similar to those obtained in section 7.1 using a linear digital filter. Figure 7.6, instead, shows the response of the proof mass when it is subject to a limit

cycle oscillation. In this scenario there is a good matching between the EKF estimation and the reference signal given by the force gauge measurement, contrarily to the estimation given by the linear digital filter shown in figure 7.3. The time history of the EKF estimation is subject to a small delay during the first few cycles, but then it is able to predict accurately the response of the proof mass relative velocity and the sudden changes in the velocity signal from positive to negative values and vice-versa that are due to the proof mass colliding with the end-stops. The initial delay of the estimate with respect to the reference signal could be attributed to the choice of the discrete integration scheme, a forward Euler method in this case, hence even better results might be obtained using more sophisticated numerical integration methods, which however could be more computationally expensive and not suitable for a real-time application. Also, the initial delay of the estimate with respect to the reference signal could be attributed to the choice of using an EKF, instead of an unscented Kalman filter (UKF) [168], since the inertial actuator is subject to a non-smooth harsh nonlinearity, which is more suited to UKF than EKF. However, the UKF is more computationally expensive and much more difficult to implement than an EKF algorithm.

7.3 Summary

In this chapter a virtual sensing approach for the estimation of the proof mass relative velocity has been investigated. The general idea is to estimate the proof mass states from the available measurement, the input signals and from the identified model of the actuator, without having to rely on additional physical sensors or the model of the structure on which the actuator is being used. Firstly, an open-loop algorithm with a linear digital filter has been derived. The transfer functions between the proof mass velocity and the input current as well as between the proof mass velocity and the input base velocity have been derived for the underlying linear model of the actuator. Secondly, the transfer functions have been obtained in digital domain and the digital filter coefficients have been calculated. Consequently, the real-time estimate of the proof mass velocity is given by combining the filtered input current and base velocity signals available from the measurements. It is shown that this virtual sensing approach performs well when the actuator is operating within its linear range of motion, however, it fails to predict the response of the proof mass when the latter is subject to stroke saturation. A second virtual sensing method has been derived using an EKF algorithm, hence, including the actuator nonlinear dynamic behaviour. The derivation of the virtual sensor has been explained in detail and also the EKF algorithm has been summarised. At each time step, the EKF linearises the state-space equation of the system and calculates the a-priori estimate of the mean of the states and the error covariance using the state estimation of the previous step and the inputs to the system. Then it calculates the Kalman gain, which is used to compute the a-posteriori estimate of the mean of the

states and the error covariance using the output measurement of the system. It is shown that this virtual sensing approach performs well both for the linear and nonlinear motion of the actuator. A small initial delay can be observed in the estimation with respect to the reference signal when the proof mass experiences limit cycle oscillations. Indications to possible solutions have been pointed out.

Chapter 8

Conclusions and suggestions for future work

This final chapter summarises the findings presented in the thesis, and also outlines suggestions for future work on active vibration control using stroke limited inertial actuators.

8.1 Conclusions

Electromechanical inertial, or proof mass, actuators are commonly used as forcing devices in active vibration controllers. The inertial actuator is attached to the structure to which one wishes to apply a force and is fed by a signal proportional to the velocity of the structure, which is measured by a collocated sensor of vibration. The current flowing through the actuator's coil generates the control force that acts between the proof mass and the structure. Since the control force is generated by accelerating the proof mass, controlling low frequency motions requires a very long stroke, however, among the main limitations of inertial actuators is that the stroke length is finite. Exceeding the stroke length, hence saturating in stroke, forces the proof mass to stop, resulting in impulse-like excitations that are transmitted to the structure, which is liable to damage. Additionally, the shocks produced by the impacts generate a control input opposite to that demanded, which reduces the overall damping of the system and eventually leads to limit cycle oscillations and the instability of the system.

The symptoms of stroke saturation on the stability of velocity feedback controllers (VFCs) have been investigated, after the nonlinearity has been identified experimentally. A novel nonlinear feedback control (NLFC) law has also been presented and both simulation and experimental studies under different scenarios were performed to test its

characteristics. The NLFC law requires the knowledge of the proof mass position and velocity, hence a virtual sensor that estimates these states has been researched.

The thesis began with an experimental investigation of the nonlinear dynamic behaviour of an inertial actuator. Base and direct excitation experiments have been used to identify both the underlying linear and the nonlinear actuator dynamics. The underlying linear model parameters have been identified by comparing the measured and analytical transmissibility, mechanical and electrical impedances of the inertial actuator applying small excitation signals that do not activate the nonlinearity. Larger amplitude signals have been used to identify the nonlinear behaviour of the inertial actuator, going from the detection of the nonlinearity, through its characterisation to the nonlinear parameters estimation. The nonlinear characterisation led to a non-smooth and strongly nonlinear piecewise linear model for the elastic restoring force, a linear model for the damping restoring force and a weakly nonlinear polynomial quadratic model for the transduction coefficient. The nonlinear parameters have been estimated by fitting a curve to the restoring force data points and the back-emf signal.

A numerical study has also been presented where both time and frequency domain analyses have been carried out using the Newmark method for the numerical integration of the equations of motion and the harmonic balance method (HBM) for seeking the periodic solutions of the equations of motion, respectively. The numerical analysis showed that the nonlinear system is characterised by a mean stiffness at low frequency that is larger than the underlying linear stiffness. Also, if the actuator is excited by a sine-sweep and the initial conditions at every cycle give the proof mass a sufficient amount of energy, the proof mass itself keeps on saturating in stroke until the nonlinear resonance is reached and for a further increase in frequency a sudden jump in the response is observed. A comparison between the time domain simulation and the frequency domain simulations obtained using the HBM showed that the bifurcation points corresponds to the frequencies and the amplitudes of the jumps. The frequency-amplitude diagrams have also been investigated, concluding that the nonlinear resonant frequency of the stroke limited actuator increases as the amplitude of the excitation increases, due to the hardening behaviour of the nonlinearity.

The mathematical model of the identified nonlinear inertial actuator was coupled with a single degree of freedom structure and a general double loop controller on the system velocities was also added to the mathematical formulation. A numerical analysis on the stability and the performance of VFCs and relative feedback controllers (RFCs) has been carried out for both the underlying linear model and the nonlinear model of the inertial actuator. It has been shown that for a single VFC loop, the system is only conditionally stable, whereas adding the RFC loop has shown to increase the stability of the system at the expenses of the vibration reduction performance. The numerical simulations have shown that VFCs are more liable to instability if the inertial actuator has stroke saturation nonlinearity. In fact, the impacts between the proof mass and the

actuator's end-stops are in-phase with the velocity of the structure, thus they contribute to reducing the overall damping of the system, which results in the instability. Moreover, the feedback gain that causes the instability in the nonlinear system is much lower than the one predicted by the linear Nyquist analysis for the underlying linear system. This motivated the development of a NLFC that operates as a second loop in combination with the classical VFC. The proposed nonlinear controller actively increases the internal damping of the actuator as the proof mass approaches the end stops, taking negligible values when the proof mass is clear from the displacement constraints. The combination of NLFC+VFC has been investigated and compared, in terms of stability of the control system, with the single VFC loop scenario for several values of the feedback gain and amplitude of the impulse excitation. It has been shown that the NLFC is able to increase the safe operating region of the actuator with respect to the single VFC loop, hence, larger feedback gains can be used, or larger impulse excitations can be withstood, without the system becoming unstable.

An experimental investigation on a cantilever beam controlled by a stroke limited inertial actuator using both VFC and NLFC was carried out. A modal analysis have been performed on the cantilever beam to assess that the response at low frequency is dominated by the first mode and the structure response can be approximated as of a SDoF system. A control unit composed by the stroke limited inertial actuator driven in VFC or NLFC+VFC, an accelerometer and a force gauge has been attached close to the free end of the cantilever beam. The stability of the VFC has been assessed using the open-loop analysis conducted for the actuator operating within its linear range, and resulted in a maximum feedback gain $h_{s,max} = 14.70$. The VFC performance has been analysed comparing the closed-loop FRFs for increasing feedback control gains and it has been shown that the VFC effectively reduces the amplitude of the structure's resonance peak up until a certain feedback gain. Further increases of the feedback gain lead the proof mass to hit the end stops and to increase the level of vibration. In particular for a feedback gain $h_s = 42\% h_{s,max}$ and above, the system has been seen to become unstable under the same excitation conditions of the uncontrolled scenario. The real-time implementation of the NLFC has been discussed, using the signals of the force gauge placed between the actuator and the beam, and the collocated accelerometer. The response of the beam and the phase-space trajectory of the proof mass have been analysed for both the single VFC loop and the combined VFC+NLFC loop, for several levels of excitation and increasing velocity feedback gains. In each test the stability of the control system has been assessed. It has been shown that the NLFC is able to avoid stroke saturation and the associated limit cycle oscillations of the proof mass, hence, increasing the stability region of the inertial actuator with respect to the single VFC loop.

A virtual sensing approach for the estimation of the proof mass states has also been investigated due to the fact that those are required by the NLFC law and the proof mass of the inertial actuator might not be available to be directly instrumented. The

proof mass states are estimated from the available measurement and input signals using the identified model of the actuator, without having the knowledge of the model of the structure on which the actuator is being used. An open-loop algorithm with a linear digital filter has been derived, however, it is shown that this virtual sensing approach performs well only when the actuator is operating within its linear range of motion. Hence, A second virtual sensing method has been investigated using an extended Kalman filter (EKF) algorithm, which includes the actuator nonlinear dynamic behaviour. At each time step, this virtual sensor linearises the state-space equation of the system and calculates an 'a-priori' estimate of the states using the state estimation of the previous step and the inputs to the system. After that it calculates the Kalman gain, which is used to update the estimate using the output measurement of the system. It is shown that the results of this virtual sensing approach are in good agreement with the reference signals both for the linear and nonlinear motion of the actuator.

8.2 Future work

The results and discussions presented in this thesis suggest that future work could progress in the directions listed below.

- Identification of the electrical nonlinearities of inertial actuators, for example the reduction of the transduction coefficient at increasing input currents, or the variation of resistance and inductance;
- Experimental implementation of the virtual sensor in a NLFC loop and comparison of the results with those obtained using a physical sensor to measure the proof mass states;
- Further investigation of the virtual sensing technique to reduce the initial delay given by the EKF. Since the type of nonlinearity is piecewise linear, it can cause numerical problems during the linearisation when using the EKF, hence, it might be interesting to use a smoothed model close to the angular points. Also, different type of estimators such as the unscented Kalman filter or the particle filter may be investigate and the results compared with those of the EKF;
- A comparison of the performance of the combined NLFC+VFC loop with the single VFC loop in terms of structural vibration reduction, when the structure is subject to a broadband excitation;
- A comparison of the NLFC strategy with other control strategies that tackles stroke saturation in inertial actuators, such as on/off control and gain scheduling;
- Implementation of the NLFC to a larger structure controlled by multiple decentralised control units.

Bibliography

[1] F. Fahy and D. J. Thompson, *Fundamentals of sound and vibration*, 2nd ed. CRC Press, 2016.

[2] L. Meirovitch, *Dynamics and control of structures.* New York: John Wiley & Sons, 1990.

[3] C. C. Fuller, S. J. Elliott, and P. A. Nelson, *Active control of vibration.* Academic Press, 1996.

[4] S. J. Elliott, *Signal processing for active control.* Academic press, 2001.

[5] D. J. Inman, *Vibration with control.* John Wiley & Sons, 2006.

[6] F. Fahy and P. Gardonio, *Sound and structural vibration: radiation, transmission and response*, 2nd ed. Elsevier Science, 2007.

[7] D. J. Wagg and S. A. Neild, *Nonlinear vibration with control: for flexible and adaptive structures.* the Netherlands: Springer, 2010.

[8] A. Preumont, *Vibration control of active structures: an introduction.* the Netherlands: Springer, 2011.

[9] D. J. Inman, "Control/structure interaction: effects of actuator dynamics," in *Dynamics Specialists Conference, Structures, Structural Dynamics, and Materials, Long Beach, CA, USA.* American Institute of Aeronautics and Astronautics, 05 - 06 April 1990, pp. 507–533.

[10] S. J. Elliott, M. Serrand, and P. Gardonio, "Feedback stability limits for active isolation systems with reactive and inertial actuators," *Journal of Vibration and Acoustics-Transactions of the Asme*, vol. 123, no. 2, pp. 250–261, 2001.

[11] P. Gardonio and C. G. Díaz, "Downscaling of proof mass electrodynamic actuators for decentralized velocity feedback control on a panel," *Smart Materials and Structures*, vol. 19, no. 2, 2010.

[12] O. N. Baumann and S. J. Elliott, "Destabilization of velocity feedback controllers with stroke limited inertial actuators," *The Journal of the Acoustical Society of America*, vol. 121, no. 5, pp. EL211–EL217, 2007.

[13] ——, "The stability of decentralized multichannel velocity feedback controllers using inertial actuators," *The Journal of the Acoustical Society of America*, vol. 121, no. 1, pp. 188–196, 2007.

[14] C. Hansen, S. Snyder, X. Qiu, L. Brooks, and D. Moreau, *Active control of noise and vibration*, 2nd ed. Boca Raton, FL, USA: CRC press, 2012.

[15] S. J. Elliott, "Distributed control of sound and vibration," *Noise Control Engineering Journal*, vol. 53, no. 5, pp. 165–180, 2005.

[16] W. P. Engels, O. N. Baumann, S. J. Elliott, and R. Fraanje, "Centralized and decentralized control of structural vibration and sound radiation," *Journal of the Acoustical Society of America*, vol. 119, pp. 1487–1495, 2006.

[17] K. D. Frampton, O. N. Baumann, and P. Gardonio, "A comparison of decentralized, distributed, and centralized vibro-acoustic control," *Journal of the Acoustical Society of America*, vol. 128, no. 5, pp. 2798–806, 2010.

[18] M. J. Balas, "Feedback control of flexible systems," *IEEE Transactions on Automatic Control*, vol. 23, no. 4, pp. 673–679, 1978.

[19] ——, "Direct velocity feedback control of large space structures," *Journal of Guidance, Control, and Dynamics*, vol. 2, no. 3, pp. 252–253, 1979.

[20] J. Pearson, R. Goodall, and I. Lyndon, "Active control of helicopter vibration," *Computing & Control Engineering Journal*, vol. 5, no. 6, pp. 277–284, 1994.

[21] L. Dal Bo, P. Gardonio, D. E. Casagrande, and S. Saggini, "Smart panel with sweeping and switching piezoelectric patch vibration absorbers: Experimental results," *Mechanical Systems and Signal Processing*, vol. 120, pp. 308–325, 2019.

[22] N. Choudhary and D. Kaur, "Shape memory alloy thin films and heterostructures for mems applications: A review," *Sensors and Actuators A: Physical*, vol. 242, pp. 162–181, 2016.

[23] S. J. Elliott, P. A. Nelson, I. M. Stothers, and C. C. Boucher, "In-flight experiments on the active control of propeller-induced cabin noise," *Journal of Sound and Vibration*, vol. 140, no. 2, pp. 219–238, 1990.

[24] P. Gardonio, "Review of active techniques for aerospace vibro-acoustic control," *Journal of aircraft*, vol. 39, no. 2, pp. 206–214, 2002.

[25] J. Rohlfing, P. Gardonio, and S. J. Elliott, "Base impedance of velocity feedback control units with proof-mass electrodynamic actuators," *Journal of Sound and Vibration*, vol. 330, no. 20, pp. 4661–4675, 2011.

[26] J. Rohlfing, S. J. Elliott, and P. Gardonio, "Feedback compensator for control units with proof-mass electrodynamic actuators," *Journal of Sound and Vibration*, vol. 331, no. 15, pp. 3437–3450, 2012.

[27] C. G. Díaz, C. Paulitsch, and P. Gardonio, "Smart panel with active damping units. implementation of decentralized control," *Journal of the Acoustical Society of America*, vol. 124, no. 2, pp. 898–910, 2008.

[28] ——, "Active damping control unit using a small scale proof mass electrodynamic actuator," *Journal of the Acoustical Society of America*, vol. 124, no. 2, pp. 886–897, 2008.

[29] C. Paulitsch, P. Gardonio, and S. J. Elliott, "Active vibration control using an inertial actuator with internal damping," *Journal of the Acoustical Society of America*, vol. 119, no. 4, pp. 2131–2140, 2006.

[30] W. L. Hallauer and S. E. Lamberson, "Experimental active vibration damping of a plane truss using hybrid actuation," in *30th Structures, Structural Dynamics and Materials Conference, Mobile, AL, U.S.A.* AIAA, 1989, pp. 80–90.

[31] F. M. Ham, S. W. Greeley, and B. L. Henniges, "Active vibration suppression for the mast flight system," *IEEE Control Systems Magazine*, vol. 9, no. 1, pp. 85–90, 1989.

[32] J. K. Haviland, T. W. Lim, W. D. Pilkey, and H. Politansky, "Control of linear dampers for large space structures," *Journal of Guidance Control and Dynamics*, vol. 13, no. 2, pp. 234–240, 1990.

[33] R. Hinchliffe, I. Scott, M. Purver, and I. Stothers, "Tonal active control in production on a large turbo-prop aircraft," in *Proceedings of ACTIVE 02, The International Symposium on Active Control of Sound and Vibration, Southampton, UK*, 15-17 July 2002.

[34] E. J. Hudson, P. Reynolds, and D. S. Nyawako, "Active vibration control of a multi-panel floor area," in *Structures Congress 2014, Boston, Massachussetts, U.S.A.*, 2014, pp. 2500–2511.

[35] D. W. Miller and E. F. Crawley, "Theoretical and experimental investigation of space-realizable inertial actuation for passive and active structural control," *Journal of Guidance Control and Dynamics*, vol. 11, no. 5, pp. 449–458, 1988.

[36] N. Noormohammadi and P. Reynolds, "Experimental investigation of dynamic performance of a prototype hybrid tuned mass damper under human excitation," in *Active and Passive Smart Structures and Integrated Systems 2013, San Diego, Califirnia, USA*, vol. 8688. Spie, 10-14 March 2013.

[37] H. Politansky and W. D. Pilkey, "Suboptimal feedback vibration control of a beam with a proof-mass actuator," *Journal of Guidance Control and Dynamics*, vol. 12, no. 5, pp. 691–697, 1989.

[38] D. C. Zimmerman, G. C. Horner, and D. J. Inman, "Microprocessor controlled force actuator," *Journal of Guidance Control and Dynamics*, vol. 11, no. 3, pp. 230–236, 1988.

[39] D. C. Zimmerman and D. J. Inman, "On the nature of the interaction between structures and proof-mass actuators," *Journal of Guidance Control and Dynamics*, vol. 13, no. 1, pp. 82–88, 1990.

[40] Micromega Dynamics. Active damping devices and inertial actuators. Last accessed: 2017-04-10. [Online]. Available: http://www.micromega-dynamics.com/download/category/4-active-damping-device.html

[41] D. K. Lindner, G. A. Zvonar, and D. Borojevic, "Performance and control of proof-mass actuators accounting for stroke saturation," *Journal of Guidance Control and Dynamics*, vol. 17, no. 5, pp. 1103–1108, 1994.

[42] F. V. Hunt, *Electroacoustics: the analysis of transduction, and its historical background*. Cambridge: Harvard University Press, 1954.

[43] S. H. Crandall, *Dynamics of mechanical and electromechanical systems*. New York: McGraw-Hill, 1968.

[44] H. A. Tilmans, "Equivalent circuit representation of electromechanical transducers: I. lumped-parameter systems," *Journal of Micromechanics and Microengineering*, vol. 6, no. 1, p. 157, 1996.

[45] S. J. Elliott and M. Zilletti, "Scaling of electromagnetic transducers for shunt damping and energy harvesting," *Journal of Sound and Vibration*, vol. 333, no. 8, pp. 2185 – 2195, 2014.

[46] L. Dal Bo and P. Gardonio, "Energy harvesting with electromagnetic and piezoelectric seismic transducers: Unified theory and experimental validation," *Journal of Sound and Vibration*, vol. 433, pp. 385–424, 2018.

[47] L. Benassi and S. J. Elliott, "Global control of a vibrating plate using a feedback-controlled inertial actuator," *Journal of Sound and Vibration*, vol. 283, no. 1-2, pp. 69–90, 2005.

[48] ——, "Active vibration isolation using an inertial actuator with local displacement feedback control," *Journal of Sound and Vibration*, vol. 278, no. 4-5, pp. 705–724, 2004.

[49] W. Clark, H. Robertshaw, and T. Warrington, "A planar comparison of actuators for vibration control of flexible structures," in *30th Structures, Structural Dynamics and Materials Conference*, 1989, pp. 1495–1503.

[50] N. W. Hagood and E. F. Crawley, "Experimental investigation of passive enhancement of damping for space structures," *Journal of Guidance Control and Dynamics*, vol. 14, no. 6, pp. 1100–1109, 1991.

[51] J. W. Umland and D. J. Inman, "Candidate proof mass actuator control laws for the vibration suppression of a frame," in *Fourth NASA workshop on Computational Control of Flexible Aerospace Systems, NASA, Langley Research Center*, March 1991, pp. 672–690.

[52] E. Garcia, S. Webb, and J. Duke, "Passive and active control of a complex flexible structure using reaction mass actuators," *Journal of Vibration and Acoustics-Transactions of the Asme*, vol. 117, no. 1, pp. 116–122, 1995.

[53] P. Reynolds, A. Pavic, and Z. Ibrahim, "A remote monitoring system for stadia dynamics," *Proceedings of the Institution of Civil Engineers-Structures and Buildings*, vol. 157, no. 6, pp. 385–393, 2004.

[54] D. Nyawako and P. Reynolds, "Response-dependent velocity feedback control for mitigation of human-induced floor vibrations," *Smart Materials and Structures*, vol. 18, no. 7, p. 14, 2009.

[55] I. M. Díaz and P. Reynolds, "Robust saturated control of human-induced floor vibrations via a proof-mass actuator," *Smart Materials and Structures*, vol. 18, no. 12, p. 125024, 2009.

[56] ——, "On-off nonlinear active control of floor vibrations," *Mechanical Systems and Signal Processing*, vol. 24, no. 6, pp. 1711–1726, 2010.

[57] ——, "Acceleration feedback control of human-induced floor vibrations," *Engineering Structures*, vol. 32, no. 1, pp. 163–173, 2010.

[58] C. A. Jones, A. Pavic, P. Reynolds, and R. E. Harrison, "Verification of equivalent mass–spring–damper models for crowd–structure vibration response prediction," *Canadian Journal of Civil Engineering*, vol. 38, no. 10, pp. 1122–1135, 2011.

[59] I. M. Díaz, E. Pereira, and P. Reynolds, "Integral resonant control scheme for cancelling human-induced vibrations in light-weight pedestrian structures," *Structural Control and Health Monitoring*, vol. 19, no. 1, pp. 55–69, 2012.

[60] I. M. Díaz, E. Pereira, M. J. Hudson, and P. Reynolds, "Enhancing active vibration control of pedestrian structures using inertial actuators with local feedback control," *Engineering Structures*, vol. 41, pp. 157–166, 2012.

[61] M. J. Hudson and P. Reynolds, "Implementation considerations for active vibration control in the design of floor structures," *Engineering Structures*, vol. 44, pp. 334–358, 2012.

[62] E. J. Hudson and P. Reynolds, "Implications of structural design on the effectiveness of active vibration control of floor structures," *Structural Control and Health Monitoring*, vol. 21, no. 5, pp. 685–704, 2014.

[63] D. Nyawako, P. Reynolds, and E. Hudson, "Incorporating a disturbance observer with direct velocity feedback for control of human-induced vibrations," in *Active and Passive Smart Structures and Integrated Systems 2016, Las Vegas, NV, USA*, vol. 9799, 20 - 24 March 2016.

[64] Y. Ikeda, "Active and semi-active vibration control of buildings in japan–practical applications and verification," *Structural Control and Health Monitoring*, vol. 16, pp. 703–723, 2009.

[65] P. Gardonio and S. J. Elliott, "Passive and active isolation of structural vibration transmission between two plates connected by a set of mounts," *Journal of Sound and Vibration*, vol. 237, no. 3, pp. 483–511, 2000.

[66] C. R. Fuller and J. D. Jones, "Experiments on reduction of propeller induced interior noise by active control of cylinder vibration," *Journal of Sound and Vibration*, vol. 112, no. 2, pp. 389–395, 1987.

[67] B. Petitjean, I. Legrain, F. Simon, and S. Pauzin, "Active control experiments for acoustic radiation reduction of a sandwich panel: feedback and feedforward investigations," *Journal of Sound and Vibration*, vol. 252, no. 1, pp. 19–36, 2002.

[68] E. Helffer, "From external to internal noise on Airbus A350," in *25th International Congress on Sound and Vibration (ICSV25), Hiroshima, Japan*, 8 - 12 July 2018, pp. 1–7.

[69] M. Misol, "Experiments on noise reduction in aircraft with active sidewall panels," in *25th International Congress on Sound and Vibration (ICSV25), Hiroshima, Japan*, 8 - 12 July 2018, pp. 1–7.

[70] S. Chesné, G. Inquieté, P. Cranga, F. Legrand, and B. Petitjean, "Innovative hybrid mass damper for dual-loop controller," *Mechanical Systems and Signal Processing*, vol. 115, pp. 514–523, 2019.

[71] S. Chesné, K. Billon, G. Zhao, and C. Collette, "On the passivity concept to design hybrid tuned mass damper," in *25th International Congress on Sound and Vibration (ICSV25), Hiroshima, Japan*, 8 - 12 July 2018, pp. 1–8.

[72] J. Scruggs and D. Lindner, "Optimal sizing of a proof-mass actuator," in *40th Structures, Structural Dynamics, and Materials Conference, St. Louis, MO, USA*. American Institute of Aeronautics and Astronautics, 12-15 April 1999.

[73] C. Paulitsch, "Vibration control with electrodynamic actuators," Ph.D. Thesis, Institute of Sound and Vibration Research, 2005.

[74] C. Paulitsch, P. Gardonio, S. J. Elliott, P. Sas, and R. Boonen, "Design of a lightweight, electrodynamic, inertial actuator with integrated velocity sensor for active vibration control of a thin lightly-damped panel," in *Proceedings of ISMA 2004: International Conference on Noise and Vibration Engineering, Leuven, Belgium*, 20-22 September 2004, pp. 239–253.

[75] L. I. Wilmshurst, "Analysis and control of nonlinear vibration in inertial actuators," PhD thesis, Institute of Sound and Vibration Research, 2015.

[76] W. J. Klippel, "Loudspeaker nonlinearities causes, parameters, symptoms," in *119th Audio Engineering Society Convention, New York, NY, USA*, 7 - 10 October 2005.

[77] ——, "Measurement of large-signal parameters of electrodynamic transducer," in *107th Audio Engineering Society Convention, New York, NY, USA*, 24 - 27 September 1999.

[78] IEC 62458:2010(E), "Sound system equipment – electroacoustical transducers – measurement of large signal parameters," International Electrotechnical Commission, Standard, 2010.

[79] M. Dodd, W. J. Klippel, and J. Oclee-Brown, "Voice coil impedance as a function of frequency and displacement," in *117th Audio Engineering Society Convention, San Francisco, CA, USA*, 28 - 31 October 2004.

[80] W. J. Klippel, "Assessment of voice-coil peak displacement xmax," *Journal of the Audio Engineering Society*, vol. 51, no. 5, pp. 307–324, 2003.

[81] L. I. Wilmshurst, M. Ghandchi Tehrani, and S. J. Elliott, "Nonlinear vibrations of a stroke-saturated intertial actuator," in *11th International Conference on Recent Advances in Structural Dynamics (RASD 2013), Pisa, Italy*, 01-03 July 2013.

[82] ——, "Nonlinear identification of proof-mass actuators accounting for stroke saturation," in *Proceedings of ISMA 2014: International Conference on Noise and Vibration Engineering, Leuven, Belgium*, 15-17 September 2014, pp. 209–223.

[83] ——, "Active control and stability analysis of flexible structures using nonlinear proof-mass actuators," in *IX International Conference on Structural Dynamics (Eurodyn 2014), Porto, Portugal*, 30th June - 2nd July 2014, pp. 1571–1578.

[84] J. Páez Chávez, Y. Liu, E. Pavlovskaia, and M. Wiercigroch, "Path-following analysis of the dynamical response of a piecewise-linear capsule system," *Communications in Nonlinear Science and Numerical Simulation*, vol. 37, pp. 102–114, 2016.

[85] Y. Liu and J. Páez Chávez, "Controlling coexisting attractors of an impacting system via linear augmentation," *Physica D: Nonlinear Phenomena*, vol. 348, pp. 1–11, 2017.

[86] ——, "Controlling multistability in a vibro-impact capsule system," *Nonlinear Dynamics*, vol. 88, no. 2, pp. 1289–1304, 2017.

[87] Y. Yan, Y. Liu, and M. Liao, "A comparative study of the vibro-impact capsule systems with one-sided and two-sided constraints," *Nonlinear Dynamics*, vol. 89, no. 2, pp. 1063–1087, 2017.

[88] L. Zhang, H. Jiang, and Y. Liu, "Bifurcation analysis of a rigid impact oscillator with bilinear damping," *Shock and Vibration*, vol. 2018, p. 10, 2018.

[89] U. von Wagner, "Nonlinear dynamic behaviour of a railway wheelset," *Vehicle System Dynamics*, vol. 47, no. 5, pp. 627–640, 2009.

[90] L. Renson, G. Kerschen, and B. Cochelin, "Numerical computation of nonlinear normal modes in mechanical engineering," *Journal of Sound and Vibration*, vol. 364, pp. 177–206, 2016.

[91] S. T. De la Cruz, F. Lopez-Almansa, and S. Oller, "Numerical simulation of the seismic behavior of building structures equipped with friction energy dissipators," *Computers and Structures*, vol. 85, no. 1-2, pp. 30–42, 2007.

[92] S. H. Strogatz, *Nonlinear dynamics and chaos: With applications to physics, biology, chemistry, and engineering*, ser. Studies in nonlinearity, Reading, Massachussets, USA, 1994.

[93] A. H. Nayfeh and B. Balachandran, *Applied nonlinear dynamics: analytical, computational, and experimental methods*. John Wiley & Sons, 1995.

[94] J. Guckenheimer and P. Holmes, *Nonlinear oscillations, dynamical systems, and bifurcations of vector fields*. Springer, 1983.

[95] G. Habib and G. Kerschen, "A principle of similarity for nonlinear vibration absorbers," *Physica D: Nonlinear Phenomena*, vol. 332, pp. 1–8, 2016.

[96] G. Habib, G. I. Cirillo, and G. Kerschen, "Uncovering detached resonance curves in single-degree-of-freedom systems," *Procedia Engineering*, vol. 199, pp. 649–656, 2017.

[97] G. Gatti, M. J. Brennan, and I. Kovacic, "On the interaction of the responses at the resonance frequencies of a nonlinear two degrees-of-freedom system," *Physica D: Nonlinear Phenomena*, vol. 239, no. 10, pp. 591–599, 2010.

[98] L. Renson, J.-P. Noël, and G. Kerschen, "Complex dynamics of a nonlinear aerospace structure: numerical continuation and normal modes," *Nonlinear Dynamics*, vol. 79, no. 2, pp. 1293–1309, 2014.

[99] K. Worden and G. R. Tomlinson, *Nonlinearity in structural dynamics: detection, identification and modelling.* Bristol, UK: Institute of Physics, 2000.

[100] G. Kerschen, K. Worden, A. F. Vakakis, and J.-C. Golinval, "Past, present and future of nonlinear system identification in structural dynamics," *Mechanical Systems and Signal Processing*, vol. 20, no. 3, pp. 505–592, 2006.

[101] J.-P. Noël and G. Kerschen, "Nonlinear system identification in structural dynamics: 10 more years of progress," *Mechanical Systems and Signal Processing*, vol. 83, pp. 2–35, 2017.

[102] D. Shmilovitz, "On the definition of total harmonic distortion and its effect on measurement interpretation," *Ieee Transactions on Power Delivery*, vol. 20, no. 1, pp. 526–528, 2005.

[103] K. Worden, "Data-processing and experiment design for the restoring force surface method, part 1: integration and differentiation of measured time data," *Mechanical Systems and Signal Processing*, vol. 4, no. 4, pp. 295–319, 1990.

[104] J.-P. Noël, L. Renson, G. Kerschen, B. Peeters, S. Manzato, and J. Debille, "Nonlinear dynamic analysis of an f-16 aircraft using gvt data," in *Proceedings of the international forum on aeroelasticity and structural dynamics, Bristol, UK*, 24-26 June 2013.

[105] J.-P. Noël, L. Renson, and G. Kerschen, "Complex dynamics of a nonlinear aerospace structure: experimental identification and modal interactions," *Journal of Sound and Vibration*, vol. 333, no. 12, pp. 2588–2607, 2014.

[106] J.-P. Noël, "A frequency-domain approach to subspace identification of nonlinear systems: application to aerospace structures," PhD thesis, 2014.

[107] M. M. I. Baig and T. Grätsch, "Recommendations for practical use of numerical methods in linear and nonlinear dynamics," Simpson Gumpertz and Heger, Inc, Report, 2005.

[108] H. K. Khalil, *Nonlinear systems*, 3rd ed. New Jersey, USA: Prentice-Hall, 2002.

[109] T. Detroux, L. Renson, L. Masset, and G. Kerschen, "The harmonic balance method for bifurcation analysis of large-scale nonlinear mechanical systems," *Computer Methods in Applied Mechanics and Engineering*, vol. 296, pp. 18–38, 2015.

[110] T. Detroux, "Performance and robustness of nonlinear systems using bifurcation analysis," PhD thesis, 2016.

[111] R. Genesio and A. Tesi, "Harmonic balance methods for the analysis of chaotic dynamics in nonlinear systems," *Automatica*, vol. 28, no. 3, pp. 531–548, 1992.

[112] S. L. Lau and W. S. Zhang, "Nonlinear vibrations of piecewise-linear systems by incremental harmonic balance method," *Journal of Applied Mechanics*, vol. 59, no. 1, pp. 153–160, 1992.

[113] S. Maezawa and S. Furukawa, "Superharmonic resonance in piecewise-linear system (effect of damping and stability problem)," *Bulletin of the Japan Society of Mechanical Engineers*, vol. 16, no. 96, pp. 931–941, 1973.

[114] S. Natsiavas, "On the dynamics of oscillators with bi-linear damping and stiffness," *International Journal of Non-Linear Mechanics*, vol. 25, no. 5, pp. 535 – 554, 1990.

[115] S. W. Shaw and P. J. Holmes, "A periodically forced piecewise linear oscillator," *Journal of Sound and Vibration*, vol. 90, no. 1, pp. 129 – 155, 1983.

[116] L. Xu, M. W. Lu, and Q. Cao, "Nonlinear vibrations of dynamical systems with a general form of piecewise-linear viscous damping by incremental harmonic balance method," *Physics Letters A*, vol. 301, no. 12, pp. 65–73, 2002.

[117] S. Skogestad and I. Postlethwaite, *Multivariable feedback control: analysis and design*, 2nd ed. New York, USA: John Wiley & Sons, 2007.

[118] J. E. Gibson, *Nonlinear automatic control*. McGraw-Hill, 1963.

[119] J.-J. E. Slotine and W. Li, *Applied nonlinear control*. Englewood Cliffs, NJ, USA: Prentice-Hall, 1991.

[120] S. S. Sastry, *Nonlinear systems: analysis, stability, and control*, 1st ed., ser. Interdisciplinary Applied Mathematics. New York, USA: Springer-Verlag New York, 1999.

[121] H.-D. Chiang, M. W. Hirsch, and F. F. Wu, "Stability regions of nonlinear autonomous dynamical systems," *IEEE Transactions on Automatic Control*, vol. 33, no. 1, pp. 16–27, 1988.

[122] G. A. Zvonar, D. K. Lindner, and D. Borojevic, "Nonlinear control of a proof-mass actuator to prevent stroke saturation," in *Dynamics and control of large structures; Proceedings of the 8th VPI & SU Symposium, Blacksburg, VA, USA*, 06 - 08 May 1991, pp. 37–48.

[123] D. K. Lindner, T. P. Celano, and E. N. Ide, "Vibration suppression using a proof-mass actuator operating in stroke/force saturation," *Journal of Vibration and Acoustics-Transactions of the Asme*, vol. 113, no. 4, pp. 423–433, 1991.

[124] D. K. Lindner, G. A. Zvonar, and D. Borojevic, "Limit cycle analysis of a nonlinear controller for a proof-mass actuator," in *AIAA Dynamics Specialists Conference, Dallas, TX, USA*. American Institute of Aeronautics and Astronautics, 16 - 17 April 1992, pp. 585–594.

[125] ——, "Nonlinear control of a proof-mass actuator," *Journal of Guidance, Control, and Dynamics*, vol. 20, no. 3, pp. 464–470, 1997.

[126] L. I. Wilmshurst, M. Ghandchi Tehrani, and S. J. Elliott, "Preventing of stroke saturation in inertial actuators using a detection scheme," in *The 21st International Congress on Sound and Vibration (ICSV21), Beijing, China*, 13-17 July 2014.

[127] E. G. Gilbert and K. T. Tan, "Linear systems with state and control constraints: the theory and application of maximal output admissible sets," *Ieee Transactions on Automatic Control*, vol. 36, no. 9, pp. 1008–1020, 1991.

[128] J. Rohlfing, T. May, L. Walter, and J. Millitzer, "Self-tuning velocity feedback control for a time varying structure using a voltage driven electrodynamic inertial mass actuator," in *27th International Conference on Noise and Vibration Engineering (ISMA2016), Leuven, Belgium*, 19 - 21 September 2016 2016.

[129] F. Naets, J. Croes, and W. Desmet, "An online coupled state/input/parameter estimation approach for structural dynamics," *Computer Methods in Applied Mechanics and Engineering*, vol. 283, pp. 1167–1188, 2015.

[130] E. Risaliti, T. Tamarozzi, B. Cornelis, and W. Desmet, "Virtual sensing of wheel center loads on a macpherson suspension," in *28th International Conference on Noise and Vibration Engineering (ISMA2018), Leuven, Belgium*, 17 -19 September 2018 2018.

[131] M. González, O. Salgado, X. Hernandez, J. Croes, B. Pluymers, and W. Desmet, "Model-based condition monitoring of guiding rails in electro-mechanical systems," *Mechanical Systems and Signal Processing*, vol. 120, pp. 630–641, 2019.

[132] D. G. Luenberger, "An introduction to observers," *IEEE Transactions on automatic control*, vol. 16, no. 6, pp. 596–602, 1971.

[133] D. Simon, *Optimal state estimation: Kalman, H infinity, and nonlinear approaches*. Hoboken, New Jersey, USA: John Wiley & Sons, 2006.

[134] R. E. Kalman, "A new approach to linear filtering and prediction problems," *Journal of Basic Engineering*, vol. 82, no. 1, pp. 35–45, 1960.

[135] R. E. Kalman and R. S. Bucy, "New results in linear filtering and prediction theory," *Journal of Basic Engineering*, vol. 83, no. 1, pp. 95–108, 1961.

[136] M. Dal Borgo, M. Ghandchi Tehrani, and S. J. Elliott, "Dynamic analysis of nonlinear behaviour in inertial actuators," in *13th International Conference on Motion and Vibration Control (MOVIC 2016) and the 12th International Conference on Recent Advances in Structural Dynamics (RASD 2016), Southampton, UK*, vol. 744. Journal of Physics Conference Series, 04 06 July 2016, p. 012027.

[137] ——, "Identification and analysis of nonlinear dynamics of inertial actuators," *Mechanical Systems and Signal Processing*, vol. 115, pp. 338 – 360, 2019.

[138] Micromega Dynamics, "Inertial actuator - operation and maintenance manual. prepared for institute of sound and vibration research," University of Southampton, Report, 2005.

[139] A. Preumont, *Mechatronics: dynamics of electromechanical and piezoelectric systems*. the Netherlands: Springer, 2006.

[140] K. Shin and J. Hammond, *Fundamentals of signal processing for sound and vibration engineers*. John Wiley & Sons, 2008.

[141] W. J. Klippel and U. Seidel, "Fast and accurate measurement of linear transducer parameters," in *110th Audio Engineering Society Convention, Amsterdam, The Netherlands*, 12 - 15 May 2001.

[142] J. Vanderkooy, "A model of loudspeaker driver impedance incorporating eddy currents in the pole structure," *Journal of the Audio Engineering Society*, vol. 37, no. 3, pp. 119–128, 1989.

[143] A. N. Thiele, "Loudspeakers in vented boxes: Part 1," *Journal of the Audio Engineering Society*, vol. 19, no. 5, pp. 382–392, 1971.

[144] ——, "Loudspeakers in vented boxes: Part 2," *Journal of the Audio Engineering Society*, vol. 19, no. 6, pp. 471–483, 1971.

[145] J. R. Wright, "An empirical model for loudspeaker motor impedance," *Journal of the Audio Engineering Society*, vol. 38, no. 10, pp. 749–754, 1990.

[146] W. M. Leach, "Loudspeaker voice-coil inductance losses: circuit models, parameter estimation, and effect on frequency response," *Journal of the Audio Engineering Society*, vol. 50, no. 6, pp. 442–450, 2002.

[147] ——, *Introduction to electroacoustics and audio amplifier design*. Kendall/Hunt Publishing Company, 2003.

[148] W. J. Staszewski, "Analysis of non-linear systems using wavelets," *Proceedings of the Institution of Mechanical Engineers*, vol. 214, no. 11, pp. 1339–1353, 2000.

[149] D. E. Newland, "Harmonic wavelet analysis," *Proceedings of the Royal Society of London Series a-Mathematical Physical and Engineering Sciences*, vol. 443, no. 1917, pp. 203–225, 1993.

[150] ——, "Wavelet analysis of vibration, part 1: theory," *Journal of Vibration and Acoustics-Transactions of the Asme*, vol. 116, no. 4, pp. 409–416, 1994.

[151] ——, "Wavelet analysis of vibration, part 2: wavelet maps," *Journal of Vibration and Acoustics-Transactions of the Asme*, vol. 116, no. 4, pp. 417–425, 1994.

[152] Nolisys. Nonlinear identification to design software (ni2d®). Last accessed: 2017-04-10. [Online]. Available: http://www.nolisys.com/en/products

[153] A. Thorin and M. Legrand, "Spectrum of an impact oscillator via nonsmooth modal analysis," in *9th European Nonlinear Dynamics Conference (ENOC2017), Budapest, Hungary*, 25 - 30 June 2017 2017.

[154] A. Pavlov, N. van de Wouw, and H. Nijmeijer, "Frequency response functions and bode plots for nonlinear convergent systems," in *Proceedings of the 45th IEEE Conference on Decision and Control, San Diego, CA, USA*. Ieee, 13-15 December 2006, pp. 3765–3770.

[155] L. Arnold and V. Wihstutz, *Lyapunov exponents: A survey*, ser. Lecture Notes in Mathematics. Springer Berlin, 1986, vol. 1186.

[156] I. M. Díaz, E. J. Hudson, E. Pereira, and P. Reynolds, "Experimental implementation of multi-actuator vibration control on an indoor walkway," in *6th World Conference on Structural Control and Monitoring, Barcelona, Spain*, 15 - 17 July 2014.

[157] P. Gardonio and M. J. Brennan, "Mobility and impedance methods in structural dynamics: an historical review," Institute of Sound and Vibration Research, ISVR Technical Report 289, October 2000.

[158] M. Zilletti, A. Marker, S. J. Elliott, and K. Holland, "Identifying the nonlinear mechanical behaviour of micro-speakers from their quasi-linear electrical response," *Mechanical Systems and Signal Processing*, vol. 88, pp. 212–223, 2017.

[159] D. L. Brown, R. J. Allemang, and A. W. Phillips, "Forty years of use and abuse of impact testing: a practical guide to making good frf measurements," in *Proceedings of the 33rd IMAC, A Conference and Exposition on Structural Dynamics*, 2015, pp. 221–241.

[160] W. G. Halvorsen and D. L. Brown, "Impulse technique for structural frequency response testing," *Sound and Vibration*, vol. 11, no. 11, pp. 8–21, 1977.

[161] C. D. Petersen, R. Fraanje, B. S. Cazzolato, A. C. Zander, and C. H. Hansen, "A kalman filter approach to virtual sensing for active noise control," *Mechanical Systems and Signal Processing*, vol. 22, no. 2, pp. 490–508, 2008.

[162] L. Liu, S. M. Kuo, and M. Zhou, "Virtual sensing techniques and their applications," in *International Conference on Networking, Sensing and Control (ICNSC2009), Okayama, Japan.* IEEE, 26 - 29 March 2009, pp. 31–36.

[163] Y. Okada, K. Matsuda, and H. Hashitani, "Self-sensing active vibration control using the moving-coil-type actuator," *Journal of Vibration and Acoustics-Transactions of the Asme*, vol. 117, no. 4, pp. 411–415, 1995.

[164] M. R. Bai and H. Wu, "Robust control of a sensorless bass-enhanced moving-coil loudspeaker system," *The Journal of the Acoustical Society of America*, vol. 105, no. 6, pp. 3283–3289, 1999.

[165] C. Paulitsch, P. Gardonio, and S. J. Elliott, "Active vibration damping using self-sensing, electrodynamic actuators," *Smart Materials and Structures*, vol. 15, no. 2, p. 499, 2006.

[166] A. V. Oppenheim and R. W. Schafer, *Discrete-time signal processing*, 3rd ed. Pearson Education, 2010.

[167] B. K. Ghosh and J. Rosenthal, "A generalized popov-belevitch-hautus test of observability," *IEEE transactions on automatic control*, vol. 40, no. 1, pp. 176–180, 1995.

[168] S. Julier, J. Uhlmann, and H. F. Durrant-Whyte, "A new method for the nonlinear transformation of means and covariances in filters and estimators," *IEEE Transactions on automatic control*, vol. 45, no. 3, pp. 477–482, 2000.

[169] T. J. Ypma, "Historical development of the newton–raphson method," *SIAM Review*, vol. 37, no. 4, pp. 531–551, 1995.

[170] N. M. Newmark, "A method of computation for structural dynamics," *ASCE Journal of the engineering mechanics division*, vol. 85, no. 3, pp. 67–94, 1959.

[171] K.-J. Bathe, *Finite element procedures.* Prentice-Hall, 1996.

[172] A. W. Leissa, "Vibration of plates," National Aeronautics and Space Administration, Technical Report NASA-SP-160, 1969.

Appendix A

Fraunhofer LBF actuator

The nonlinear identification methodology described in chapter 3 was also applied to a prototype inertial actuator developed by Fraunhofer LBF (Darmstadt, Germany), which is shown in figure A.1 and was characterised during a test campaign at their laboratories.

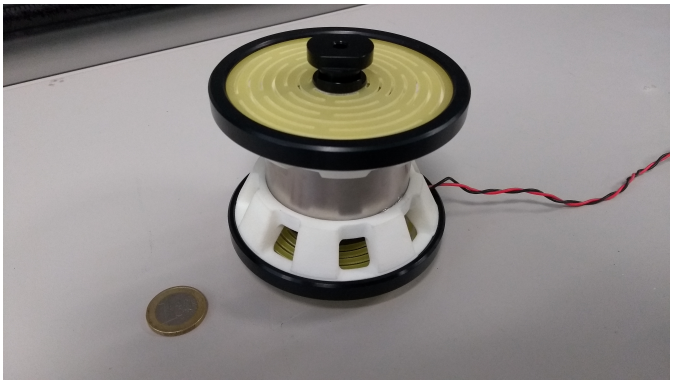

FIGURE A.1: Picture of the Fraunhofer LBF inertial actuator.

The measured and identified mechanical impedances in open- and closed-circuit are shown in figures A.2(a) and A.2(b), respectively. Figure A.3(a) shows the measured and identified transmissibility measured with the base excitation experiment, whereas figure A.3(b) shows the transmissibility with respect to the input current for the direct excitation experiment. Figure A.4(a) shows the measured and identified transmissibility with respect to the input voltage for the direct excitation experiment. The measured electrical impedance is shown figure A.4(b) with the solid black line. The ideal inductance model (blue dash-dotted line) and the LR-2 model (red dotted line) given by eq. (3.9) were fitted to the data. It can be noticed that the LR-2 model of the electrical port gives a much better agreement with the measured data.

The actuator was then tested using the same methodology outlined in section 3.4. The results of the nonlinear identification are shown in figure A.5. In particular, figure A.5(a)

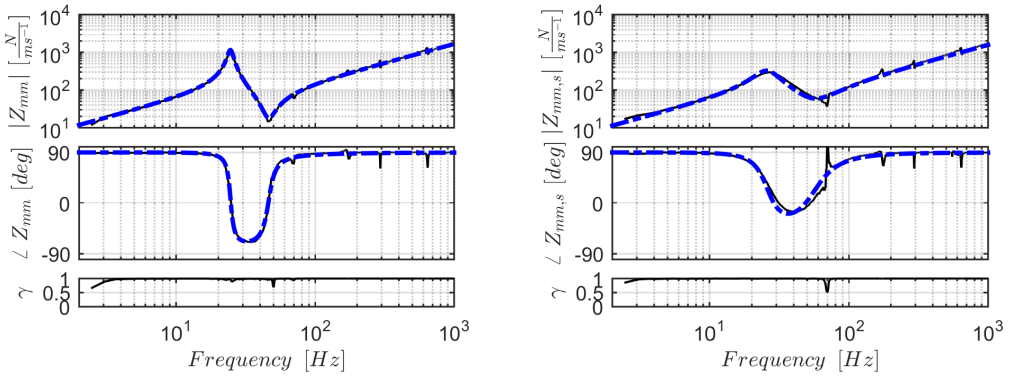

(a) (b)

FIGURE A.2: Magnitude, phase and coherence of the measured mechanical driving-point impedance (black solid line) and identified model (blue dash-dotted line). (a) Open-circuit mechanical impedance; (b) Short-circuit mechanical impedance.

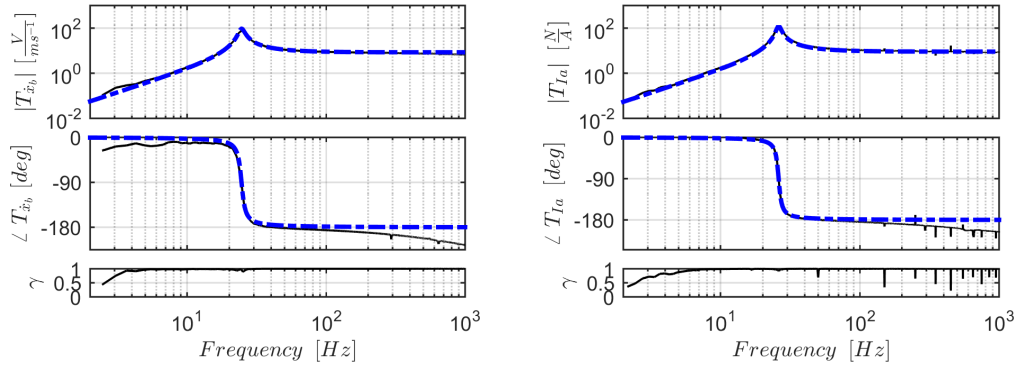

(a) (b)

FIGURE A.3: Magnitude, phase and coherence of the measured transmissibility (black solid line) and identified model (blue dash-dotted line). (a) Base excitation experiment; (b) Direct (current) excitation experiment.

displays the experimental data points of the restoring force versus the state-space plane. Figure A.5(b) shows the experimental data points of the elastic restoring force and the fitted model. It can be noticed that the stiffness characteristic of the actuator is linear even for high amplitude oscillations, until the proof mass reaches one end-stop. Hence, the fitted model is a piecewise linear function with a discontinuity point at the location of the stroke limit. Figure A.5(c) shows the scattered data points of the damping restoring force and the identified model. The behaviour is weakly nonlinear and it has been identified as polynomial of the third order. The scattered data plot of the transduction coefficient versus the displacement is shown in figure A.5(d). Its behaviour is given by a third order polynomial function, which is asymmetric with respect to the proof mass resting position. In fact, the peak in the transduction coefficient is reached for negative displacements, whereas for positive displacements it is significantly reduced.

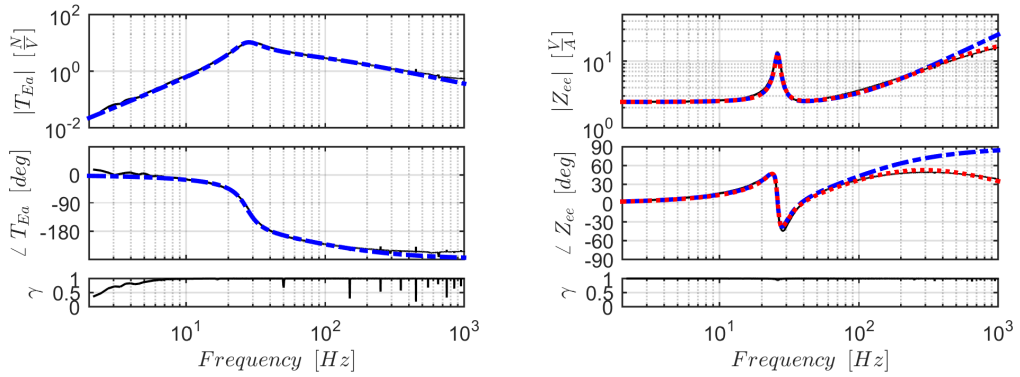

(a) (b)

FIGURE A.4: Magnitude, phase and coherence of the measured transmissibility and electrical impedance (black solid line) and identified model (blue dash-dotted line). (a) Transmissibility for the direct (voltage) excitation experiment; (b) Electrical impedance for the direct (current) excitation experiment considering an ideal inductance model (blue dash-dotted line) and considering an LR-2 model for the inductance losses (red dashed line).

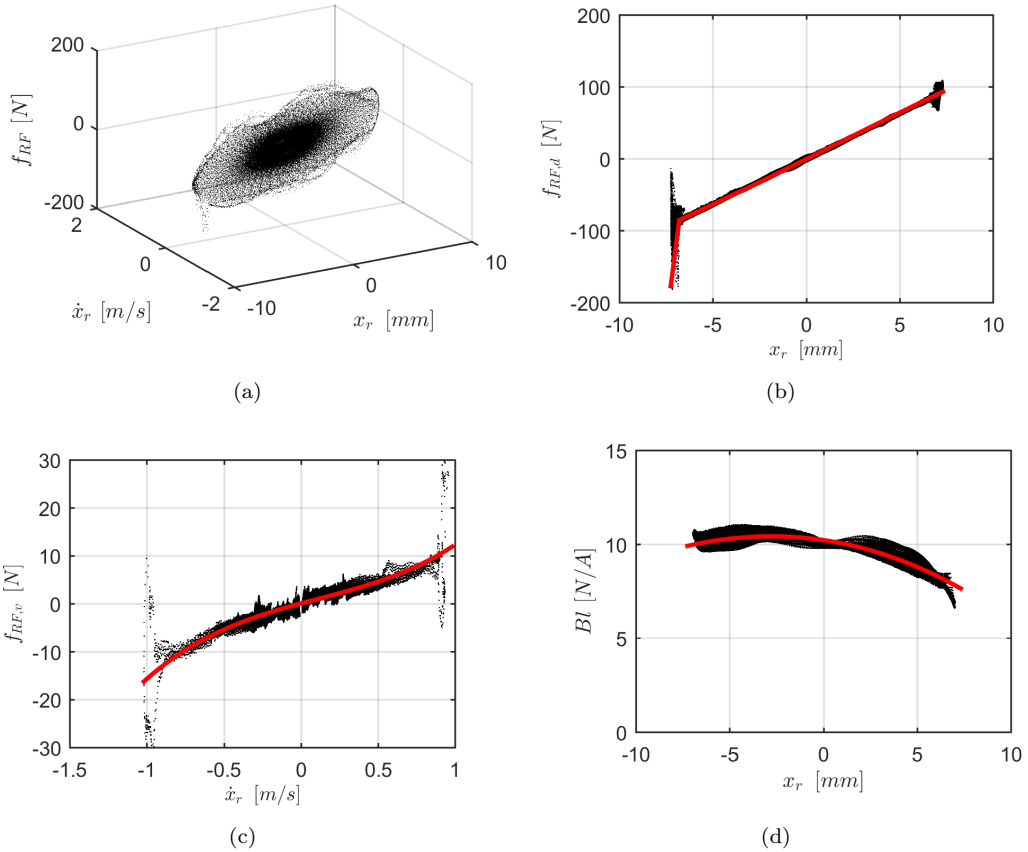

(a) (b)

(c) (d)

FIGURE A.5: Restoring force data points, the experimental data is shown with the black dots, whereas the curve fitting is shown with the solid red line. (a) 3D restoring force in the phase space; (b) elastic restoring force; (c) damping restoring force; (d) nonlinear transduction coefficient.

Appendix B

TECTONIC elements actuator

Another example of the identification methodology is given in this appendix on a Tectonic Elements TEBM46C20N-4B audio speaker, which can be used as inertial actuator and is shown in figure B.1.

The measured and identified mechanical impedances in open- and closed-circuit are shown in figures B.2(a) and B.2(b), respectively. Figure B.3(a) shows the measured and identified transmissibility measured with the base excitation experiment, whereas figure B.3(b) shows the transmissibility with respect to the input current for the direct excitation experiment. Figure B.4(a) shows the measured and identified transmissibility with respect to the input voltage for the direct excitation experiment. The measured electrical impedance is shown figure B.4(b) with the solid black line. The ideal inductance model (blue dash-dotted line) and the Leach model (red dotted line) given by eq. (3.12) were fitted to the data. It can be noticed that the Leach model of the electrical port gives a much better agreement with the measured data.

FIGURE B.1: Picture of the Tectonic Elements TEBM46C20N-4B audio speaker.

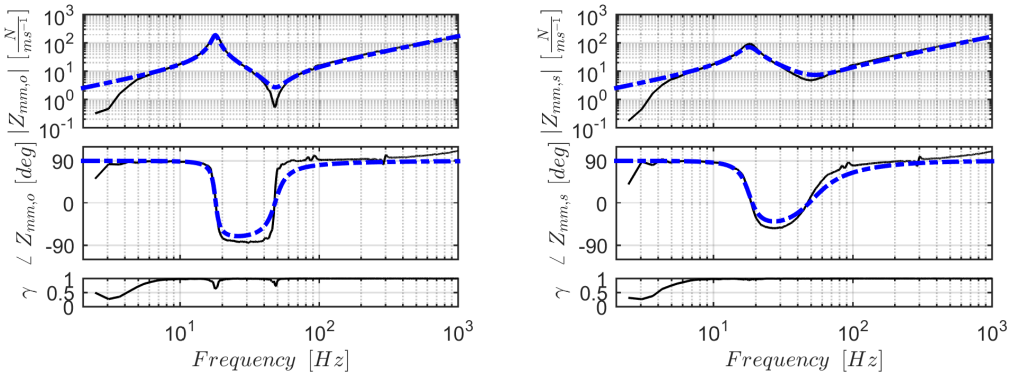

(a) (b)

FIGURE B.2: Magnitude, phase and coherence of the measured mechanical driving-point impedance (black solid line) and identified model (blue dash-dotted line). (a) Open-circuit mechanical impedance; (b) Short-circuit mechanical impedance.

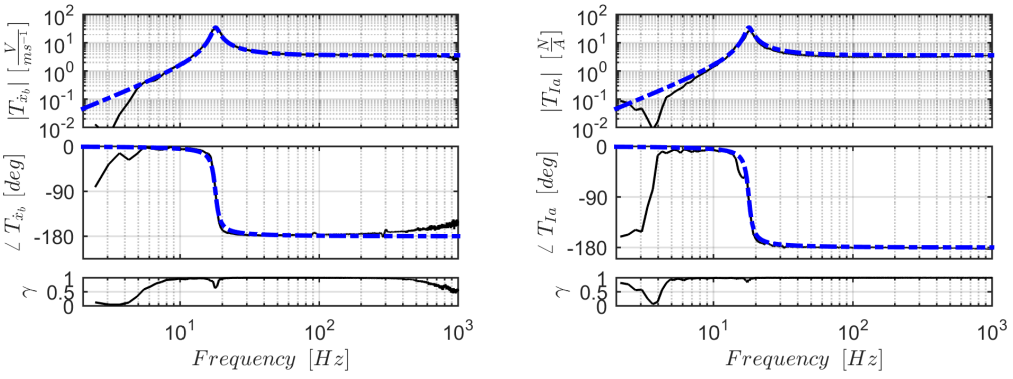

(a) (b)

FIGURE B.3: Magnitude, phase and coherence of the measured transmissibility (black solid line) and identified model (blue dash-dotted line). (a) Base excitation experiment; (b) Direct (current) excitation experiment.

The actuator was then tested using the same methodology outlined in section 3.4. The results of the nonlinear identification are shown in figure B.5. In particular, figure B.5(a) displays the experimental data points of the restoring force versus the state-space plane. Figure B.5(b) shows the experimental data points of the elastic restoring force and the fitted model. It can be noticed that the elastic restoring force behaves nonlinearly and asymmetrically with respect to the resting position of the proof mass. Hence, the fitted model is a piecewise linear function with a discontinuity point at the equilibrium position. Figure B.5(c) shows the scattered data points of the damping restoring force and the identified model. The behaviour is highly nonlinear and it has been identified as polynomial of the third order. In particular, for positive velocities the damping restoring force is almost constant, which can be associated with the friction between the coil support and the proof mass. The scattered data plot of the transduction coefficient versus

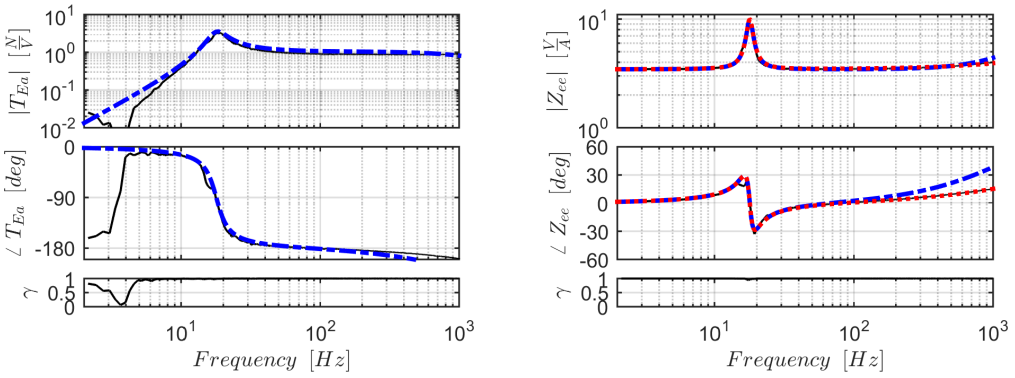

(a) (b)

FIGURE B.4: Magnitude, phase and coherence of the measured transmissibility and electrical impedance (black solid line) and identified model (blue dash-dotted line). (a) Transmissibility for the direct (voltage) excitation experiment; (b) Electrical impedance for the direct (current) excitation experiment considering an ideal inductance model (blue dash-dotted line) and considering an Leach model for the inductance losses (red dotted line).

the displacement is shown in figure B.5(d). Its behaviour is given by a linearly decreasing function. In fact, for negative displacements the transduction coefficient keeps increasing without reaching a peak, whereas for positive displacements the coil decouples from the magnet and the transduction coefficient decreases significantly.

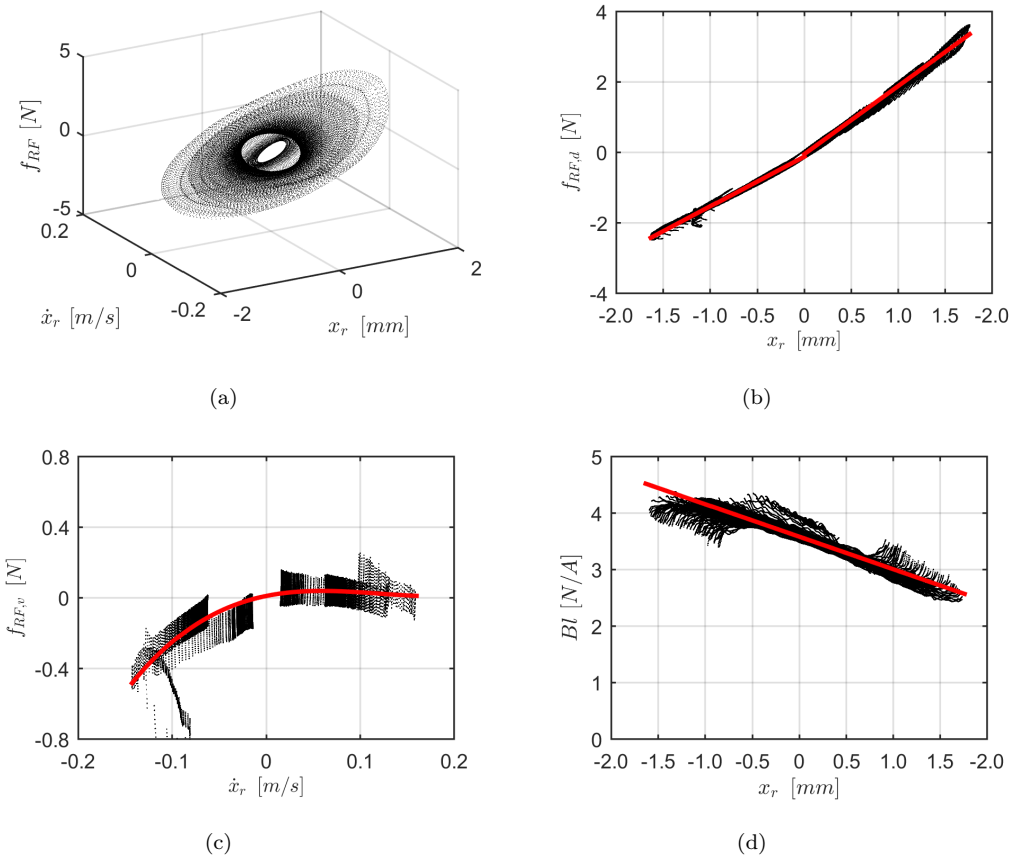

FIGURE B.5: Restoring force data points, the experimental data is shown with the black dots, whereas the curve fitting is shown with the solid red line. (a) 3D restoring force in the phase space; (b) elastic restoring force; (c) damping restoring force; (d) nonlinear transduction coefficient.

Appendix C

Numerical integration of ODEs

This appendix gives a brief overview of numerical methods for the solution of first and second order ordinary differential equations (ODEs) [107]. In general, the state-space equation of a nonlinear system can be written as,

$$\dot{\mathbf{x}} = \mathbf{f}\left(\mathbf{x}, u\right), \tag{C.1}$$

where $\mathbf{x}$ represents the state vector, u denotes the input and $\mathbf{f}$ is a nonlinear function of the input and the states.

- **Euler forward difference method**:

  Equation (C.1) is approximated using the forward difference equation,

  $$\dot{\mathbf{x}}_i = \frac{\mathbf{x}_{i+1} - \mathbf{x}_i}{\Delta t}, \tag{C.2}$$

  where i is an index of the current step in the solution and Δt is the time step size. Using eqs. (C.1) and (C.2) the solution of the states at the following time step can be written as,

  $$\mathbf{x}_{i+1} = \mathbf{x}_i + \mathbf{f}\left(\mathbf{x}_i, u_i\right) \Delta t, \tag{C.3}$$

- **Euler backward difference method**:

  Equation (C.1) is approximated using the backward difference equation,

  $$\dot{\mathbf{x}}_{i+1} = \frac{\mathbf{x}_{i+1} - \mathbf{x}_i}{\Delta t}, \tag{C.4}$$

  hence, substituting eq. (C.4) into eq. (C.1), the solution of the states at the following time step can be written as,

  $$\mathbf{x}_{i+1} = \mathbf{x}_i + \mathbf{f}\left(\mathbf{x}_{i+1}, u_{i+1}\right) \Delta t. \tag{C.5}$$

If a simple algebraic reordering of eq. (C.5) is not possible, then the Newton-Raphson method [169] may be adopted to calculate $\mathbf{f}(\mathbf{x}_{i+1}, u_{i+1})$.

- **4^{th} order Runge-Kutta method**:

  The derivatives of the states are calculated as,

$$\begin{cases} \mathbf{h}_1 = \mathbf{f}(\mathbf{x}_i, u_i) & \text{(C.6a)} \\ \mathbf{h}_2 = \mathbf{f}\left(\mathbf{x}_i + \frac{1}{2}\mathbf{h}_1, u_{i+\frac{1}{2}}\right) & \text{(C.6b)} \\ \mathbf{h}_3 = \mathbf{f}\left(\mathbf{x}_i + \frac{1}{2}\mathbf{h}_2, u_{i+\frac{1}{2}}\right), & \text{(C.6c)} \\ \mathbf{h}_4 = \mathbf{f}(\mathbf{x}_i + \mathbf{h}_3, u_{i+1}) & \text{(C.6d)} \end{cases}$$

  hence, the solution of the state-space eq. (C.1) at the following time step can be approximated as,

$$\mathbf{x}_{i+1} = \mathbf{x}_i + \frac{\Delta t}{6}(\mathbf{h}_1 + 2\mathbf{h}_2 + 2\mathbf{h}_3 + \mathbf{h}_4). \tag{C.7}$$

- **Newmark method**:

  This method is usually applied directly to second order ODEs of the type,

$$\mathbf{m}\ddot{\mathbf{x}} + \mathbf{c}\dot{\mathbf{x}} + \mathbf{f}(\mathbf{x}) = \mathbf{D}(t), \tag{C.8}$$

  where $\mathbf{m}$ is the mass, $\mathbf{c}\dot{\mathbf{x}}$ is the damping force, $\mathbf{f}(\mathbf{x})$ is the restoring force and $\mathbf{D}(t)$ is the external force. The Newmark method approximates the velocities and displacements as [170],

$$\begin{cases} \dot{\mathbf{x}}_{i+1} = \dot{\mathbf{x}}_i + [(1-\delta)\ddot{\mathbf{x}}_i + \delta\ddot{\mathbf{x}}_{i+1}]\Delta t & \text{(C.9a)} \\ \mathbf{x}_{i+1} = \mathbf{x}_i + \dot{\mathbf{x}}_i\Delta t + [(1/2-\alpha)\ddot{\mathbf{x}}_i + \alpha\ddot{\mathbf{x}}_{i+1}]\Delta t^2, & \text{(C.9b)} \end{cases}$$

  where α, δ are parameters which can be chosen to provide numerical stability or accuracy in the approximation. The Newmark method is unconditionally stable for [171],

$$\begin{cases} \delta \geq 0.5 & \text{(C.10a)} \\ \alpha \geq 0.25(0.5+\delta)^2. & \text{(C.10b)} \end{cases}$$

Substituting eq. (C.9) in eq. (C.8) gives the solution of the displacement vector at step $i+1$ as,

$$\begin{aligned}\left(\frac{\mathbf{m}}{\alpha\Delta t^2}+\mathbf{c}\frac{\delta}{\alpha\Delta t}\right)\mathbf{x}_{i+1} =&\mathbf{D}i+1-\mathbf{f}(\mathbf{x}_{i+1})+\\ &+\mathbf{m}\left[\left(\frac{1}{2\alpha}-1\right)\ddot{\mathbf{x}}_i+\frac{1}{\alpha\Delta t^2}\left(\mathbf{x}_i+\dot{\mathbf{x}}\Delta t\right)\right]+ \quad . \quad \text{(C.11)}\\ &+\mathbf{c}\left[\frac{\delta}{\alpha\Delta t}\left(\mathbf{x}_i+\dot{\mathbf{x}}_i\Delta t\right)-\dot{\mathbf{x}}_i-\ddot{\mathbf{x}}_i\Delta t\left(1-\frac{\delta}{2\alpha}\right)\right]\end{aligned}$$

If a simple algebraic reordering of eq. (C.11) is not possible, then the Newton-Raphson method [169] may be adopted to calculate $\mathbf{f}\left(\mathbf{x}_{i+1}\right)$.

Appendix D

Theoretical model cantilever beam

A schematic of a free vibrating cantilever beam is shown in figure D.1, where $w(x,t)$ is the transversal displacement of a point at any distance x at any time t. Assuming that

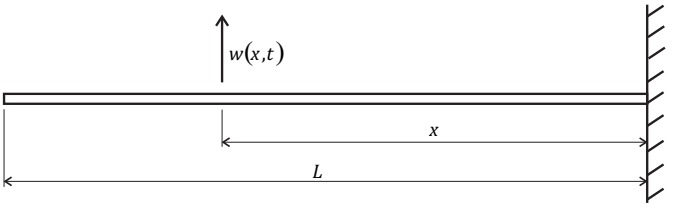

FIGURE D.1: A schematic representation of a cantilever beam. $w(x,t)$ is the displacement of a point at any distance x at any time t.

the material of the beam is homogeneous and isotropic and that plane sections remain plain and orthogonal to the neutral axis and the displacement of any point of the beam is due only to the bending moment, the flexural wave equation can be written as [172],

$$EI_z \frac{\partial^4 w(x,t)}{\partial x^4} + \rho A \frac{\partial^2 w(x,t)}{\partial t^2} = 0, \tag{D.1}$$

where E is the Young's modulus of the material, I_z the moment of inertia for the cross-section with respect to the transverse axis, ρ is the material density and A the cross-section area. Applying separation of variable, the displacement can be written as,

$$w(x,t) = \phi(x)q(t), \tag{D.2}$$

and substituting eq. (D.2) into eq. (D.1) gives,

$$EI_z \frac{\partial^4 \phi(x)}{\partial x^4} q(t) + \rho A \phi(x) \ddot{q}(t) = 0. \tag{D.3}$$

Taking the Laplace transform of eq. (D.3) and assuming zero initial conditions results in,

$$\left[EI_z \frac{\partial^4 \phi(x)}{\partial x^4} + \rho A s^2 \phi(x)\right] Q(s) = 0, \tag{D.4}$$

which is solved for,

$$\frac{\partial^4 \phi(x)}{\partial x^4} - \beta^4 \phi(x) = 0, \tag{D.5}$$

where

$$\beta^4 = -\frac{\rho A}{EI_z} s^2. \tag{D.6}$$

The characteristic equation of eq. (D.5) can be written as,

$$\alpha^4 - \beta^4 = 0, \tag{D.7}$$

which is true for,

$$\alpha = \pm\beta, \quad \alpha = \pm j\beta, \tag{D.8}$$

hence, the general solution of eq. (D.5) results in,

$$\phi(x) = Ce^{\beta x} + De^{-\beta x} + Ee^{j\beta x} + Fe^{-j\beta x}. \tag{D.9}$$

Considering that,

$$\begin{aligned} e^{\beta x} &= \frac{e^{\beta x} + e^{-\beta x}}{2} + \frac{e^{\beta x} - e^{-\beta x}}{2} = \cosh(\beta x) + \sinh(\beta x) && \text{(D.10a)} \\ e^{-\beta x} &= \cosh(\beta x) - \sinh(\beta x) && \text{(D.10b)} \\ e^{j\beta x} &= \cos(\beta x) + j\sin(\beta x) && \text{(D.10c)} \\ e^{-j\beta x} &= \cos(\beta x) - j\sin(\beta x) && \text{(D.10d)} \end{aligned} \quad ,$$

the general solution given by eq. (D.9) can be rewritten as,

$$\begin{aligned} \phi(x) =& A_1 \left(\cos(\beta x) + \cosh(\beta x)\right) + A_2 \left(\cos(\beta x) - \cosh(\beta x)\right) + \\ &+ A_3 \left(\sin(\beta x) + \sinh(\beta x)\right) + A_4 \left(\sin(\beta x) - \sinh(\beta x)\right). \end{aligned} \tag{D.11}$$

Considering the boundary conditions that are a clamped end and a free end,

$$\begin{aligned} &w(x=0) = 0, && \left.\frac{\partial w}{\partial x}\right|_{x=0} = 0 && \text{(D.12a)} \\ &M(x=L) = \left.\frac{\partial^2 w}{\partial x^2}\right|_{x=L} = 0, && V(x=L) = \left.\frac{\partial^3 w}{\partial x^3}\right|_{x=L} = 0 && \text{(D.12b)} \end{aligned} \quad .$$

Applying eq. (D.12a) to eq. (D.11) results in,

$$A_1 = 0, \quad A_3 = 0, \tag{D.13}$$

so that the general solution reduces to,

$$\phi(x) = A_2 \left(\cos(\beta x) - \cosh(\beta x)\right) + A_4 \left(\sin(\beta x) - \sinh(\beta x)\right). \tag{D.14}$$

Applying eq. (D.12b) to eq. (D.14) gives the following system of equations,

$$\begin{bmatrix} \cos(\beta L) + \cosh(\beta L) & sin(\beta L) + \sinh(\beta L) \\ -\sin(\beta L) + \sinh(\beta L) & \cos(\beta L) + \cosh(\beta L) \end{bmatrix} \begin{Bmatrix} A_2 \\ A_4 \end{Bmatrix} = \begin{Bmatrix} 0 \\ 0 \end{Bmatrix}, \tag{D.15}$$

which has non-trivial solutions when the determinant of the matrix is zero, which results in,

$$\cos(\beta L)\cosh(\beta L) = -1. \tag{D.16}$$

Equation (D.16) has infinite solutions, which are named $\beta_n L$ and can be found numerically using for example Newton-Raphson method. The general solution, or mode shape, associated with each $\beta_n L$ can be written as,

$$\phi_n(x) = A_2 \left[\left(\cos(\beta_n x) - \cosh(\beta_n x)\right) + \sigma_N \left(\sin(\beta_n x) - \sinh(\beta_n x)\right)\right], \tag{D.17}$$

where,

$$\sigma_N = \frac{A_2}{A_4} = \frac{\sin(\beta_n L) - \sinh(\beta_n L)}{\cos(\beta_n L) + \cosh(\beta_n L)}, \tag{D.18}$$

which has been taken from eq. (D.15). The mode shapes given by eq. (D.17) can be normalised with respect to the length of the beam, so that the coefficient A_2 results in,

$$A_2 = \sqrt{L}. \tag{D.19}$$

The analytical expression of the natural frequencies of the beam can be deduced from eq. (D.3) as,

$$\frac{\ddot{q}(t)}{q(t)} = -\frac{EI_z \phi(x)''''}{\rho A \phi(x)} = -\omega^2, \tag{D.20}$$

hence, the flexural wave equation can be split into two, one time-dependent,

$$\ddot{q}(t) - \omega^2 q(t) = 0, \tag{D.21}$$

and one spatial-dependent,

$$\phi(x)'''' - \frac{\rho A \omega^2}{EI_z}\phi(x) = 0. \tag{D.22}$$

Considering eqs. (D.6) and (D.16) it follows that,

$$(\beta_n L)^4 = \frac{\rho A L^4 \omega_n^2}{EI_z}, \tag{D.23}$$

so that the expression of the n-th natural frequency is given by,

$$\omega_n = (\beta_n L)^2 \sqrt{\frac{EI_z}{\rho A L^4}}. \tag{D.24}$$

The forced response of the cantilever beam subject to a primary excitation $F_p(x_p, t)$ is shown in figure D.2 and can be written as,

$$EI_z \frac{\partial^4 w(x,t)}{\partial x^4} + \rho A \frac{\partial^2 w(x,t)}{\partial t^2} = F_p(x_p, t). \tag{D.25}$$

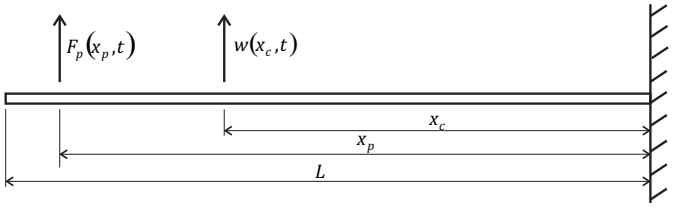

FIGURE D.2: Schematic of cantilever beam excited by a point force.

The forced response of the beam can be expressed as a linear superposition of the natural modes, also assuming harmonic excitation,

$$w(x_c, t) = \sum_{n=1}^{\infty} \phi_n(x_c) q_n(t) \tag{D.26a}$$

$$F_p(t) = \Re\{F_p e^{j\omega t}\} \tag{D.26b}$$

Considering the motion due to the n-th mode, the force wave eq. (D.25) becomes,

$$EI_z \phi_n(x)'''' q_n(t) + \rho A \phi_n(x) \ddot{q}_n(t) = F_p(x_p, t), \tag{D.27}$$

multiplying eq. (D.27) by the m-th mode and integrating along the length of the beam gives,

$$EI_z \int_0^L \phi_n(x)'''' \phi_m(x) q_n(t) \mathrm{d}x + \rho A \int_0^L \phi_n(x) \phi_m(x) \ddot{q}_n(t) \mathrm{d}x = \int_0^L \phi_m(x) F_p(x_p, t) \mathrm{d}x, \tag{D.28}$$

using orthogonality and normalisation conditions the following equation is obtained for $n = m$,

$$\ddot{q}_n(t) + \frac{K_n}{M_n} q_n(t) = \frac{1}{M_n} \int_0^L \phi_n(x) F_p(x_p, t) \mathrm{d}x, \tag{D.29}$$

where,

$$M_n = \rho A \int_0^L \phi_n(x)^2 \mathrm{d}x = \rho A L = m_{beam}, \tag{D.30}$$

is the modal mass (and the total mass of the beam) and,

$$K_n = EI_z \int_0^L \phi_n(x)''''\phi_n(x)\mathrm{d}x = EI_z\beta_n L. \tag{D.31}$$

is the modal stiffness. Since the excitation is a point force it follows that,

$$\int_0^L \phi_n(x)F_p(x_p,t)\mathrm{d}x = \phi_n(x_p)F_p(t). \tag{D.32}$$

hence eq. (D.29) can be rewritten as,

$$\ddot{q}_n(t) + \omega_n^2 q_n(t) = \frac{1}{M_n}\phi_n(x_p)F_p(t). \tag{D.33}$$

Assuming zero initial conditions, the Laplace transform of eq. (D.33) results in,

$$s^2 Q_n(s) + \omega_n^2 Q_n(s) = \frac{1}{M_n}\phi_n(x_p)F_p(s), \tag{D.34}$$

which gives the modal response as,

$$Q_n(j\omega) = \frac{\phi_n(x_p)F_p(j\omega)}{m_{beam}(\omega_n^2 + 2j\omega\xi\omega_n - \omega^2)}, \tag{D.35}$$

where eq. (D.30) has been used, $s = j\omega$ has been set and a modal damping has been considered with equal damping ratio for all modes. Combining eq. (D.26a) with eq. (D.35), the velocity at the control position can be expressed as,

$$\dot{w}_c(j\omega) = j\omega \sum_{n=1}^{\infty} \frac{\phi_n(x_c)\phi_n(x_p)}{m_{beam}(\omega_n^2 + 2j\omega\xi\omega_n - \omega^2)} F_p(j\omega). \tag{D.36}$$

The ratio between velocity and force both at location c, namely point mobility, is given by,

$$Y_{cc} = \frac{\dot{w}_c(j\omega)}{F_c(j\omega)}, \tag{D.37}$$

whereas the ratio between velocity at location c and force at location p, namely cross mobility, can be written as,

$$Y_{cc} = \frac{\dot{w}_c(j\omega)}{F_p(j\omega)}. \tag{D.38}$$

Equation (D.36) can be expressed as,

$$\dot{w}_c(j\omega) = \mathbf{\Phi}_c^T \mathbf{\Omega} \mathbf{\Phi}_p F_p(j\omega). \tag{D.39}$$

where,

$$\mathbf{\Phi}_c = \begin{Bmatrix} \phi_1(x_c) \\ \phi_2(x_c) \\ \vdots \end{Bmatrix}, \quad \mathbf{\Phi}_p = \begin{Bmatrix} \phi_1(x_p) \\ \phi_2(x_p) \\ \vdots \end{Bmatrix}, \tag{D.40}$$

and,

$$\mathbf{\Omega} = \begin{bmatrix} \frac{j\omega}{m_{beam}\left(\omega_{b1}^2+2j\omega\xi\omega_{b1}-\omega^2\right)} & 0 & 0 & \cdots \\ 0 & \frac{j\omega}{m_{beam}\left(\omega_{b2}^2+2j\omega\xi\omega_{b2}-\omega^2\right)} & & \\ 0 & & \ddots & \\ \vdots & & & \ddots \end{bmatrix}. \tag{D.41}$$

Calling $\mathbf{a}_p = \mathbf{\Omega}\mathbf{\Phi}_p$ and $\mathbf{a}_c = \mathbf{\Omega}\mathbf{\Phi}_c$, eq. (D.39) can be rewritten as,

$$\dot{w}_c(j\omega) = \mathbf{\Phi}_c^T \mathbf{a}_p F_p(j\omega). \tag{D.42}$$

Figure D.3 shows a schematic of a cantilever beam where and inertial actuator is attached and left open-circuit so that it behaves as a passive device. The mathematical model

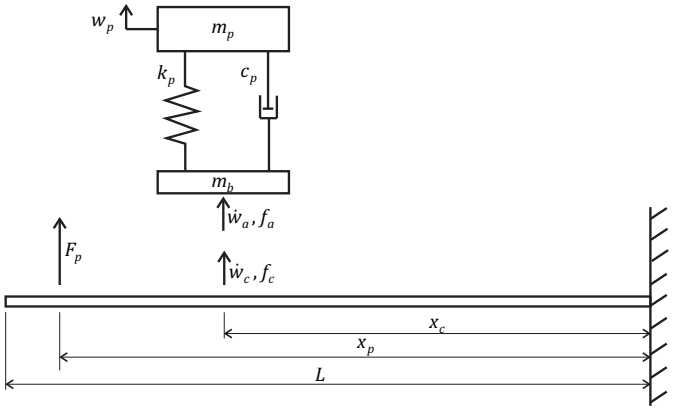

FIGURE D.3: Schematic of a beam with a passive inertial actuator attached at the control point. The beam is excited by a point force.

of the cantilever beam with the inertial actuator attached is derived using the notion of impedance ($Z = f/\dot{w}$). The equivalent impedance of the inertial actuator is given by the sum of the impedances of the proof mass and base mass, which can be written as,

$$Z_a = Z_{a,PM} + Z_{a,BM}. \tag{D.43}$$

where,

$$Z_{a,BM} = j\omega m_b. \tag{D.44}$$

and,

$$Z_{a,PM} = \frac{k_p}{j\omega} + c_p - \frac{\left(\frac{k_p}{j\omega} + c_p\right)^2}{j\omega m_p + c_p + \frac{k_p}{j\omega}}. \tag{D.45}$$

The response of the beam at the control point with the passive actuator can be calculated as follows,

$$\dot{w}_c = Y_{cp}F_p + Y_{cc}F_c, \tag{D.46}$$

where F_c is the force produced by the actuator on the beam, hence, eq. (D.46) results in,

$$\dot{w}_c = Y_{cp}F_p - Y_{cc}Z_a\dot{w}_c. \tag{D.47}$$

Rearranging the terms of eq. (D.47) gives,

$$\dot{w}_c = \frac{Y_{cp}F_p}{1 + Y_{cc}Z_a}. \tag{D.48}$$

Remembering that $\mathbf{a}_p = \mathbf{\Omega\Phi}_p$ and $\mathbf{a}_c = \mathbf{\Omega\Phi}_c$, eq. (D.48) can be rewritten as,

$$\dot{w}_c = \mathbf{\Phi}_c^T \mathbf{a} F_p, \tag{D.49}$$

where,

$$\mathbf{a} = \mathbf{a}_p - \mathbf{a}_c \frac{Z_a Y_{cp}}{1 + Z_a Y_{cc}}. \tag{D.50}$$

Appendix E

Simulink model of VFC+NLFC implementation

This appendix shows the Simulink models used in the experiments for the VFC and the NLFC.

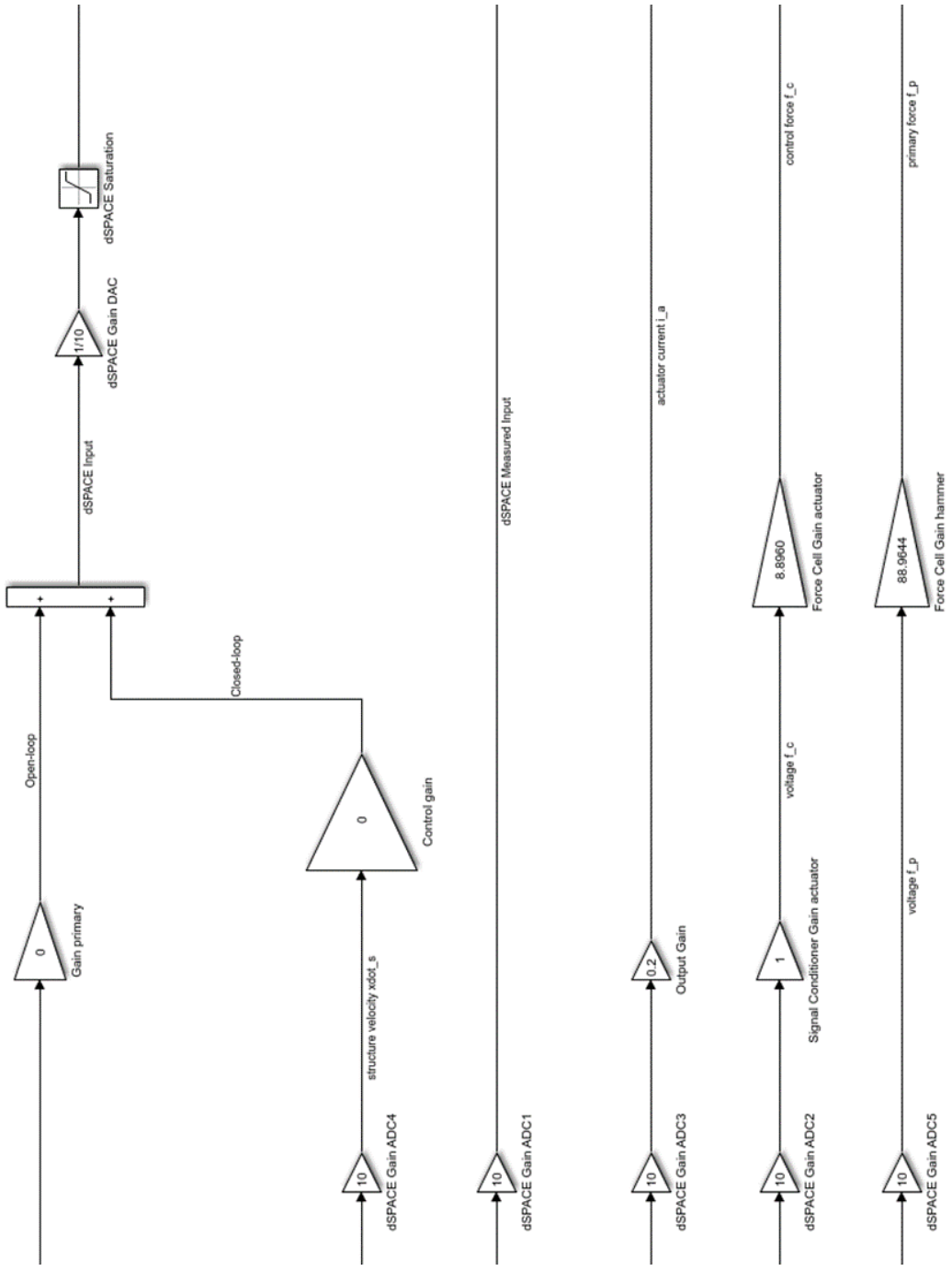

FIGURE E.1: Schematic of the Simulink model used in the VFC experiments.

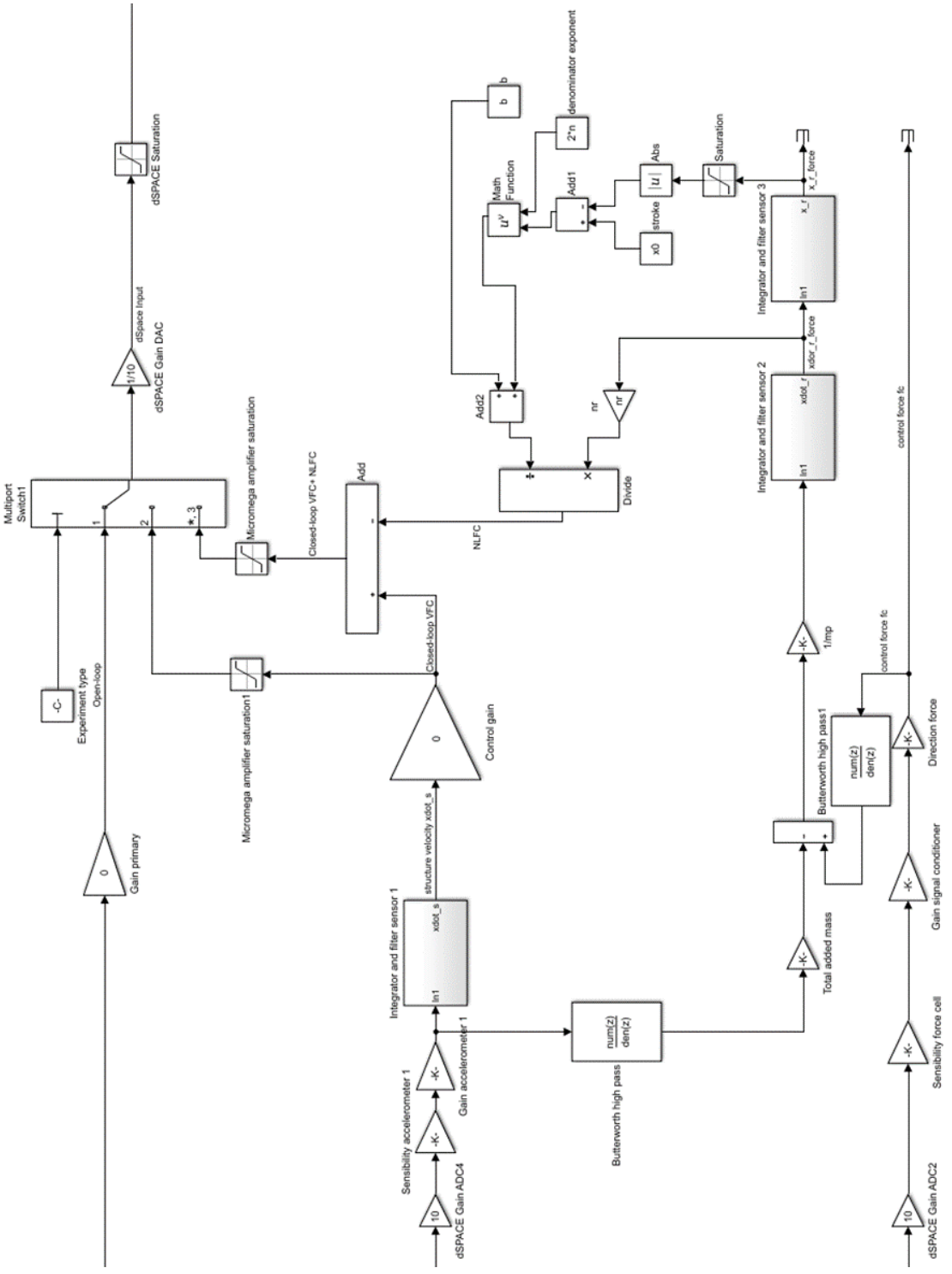

FIGURE E.2: Schematic of the Simulink model used in the NLFC+ VFC experiments.

Appendix F

Experimental results NLFC

This appendix shows the experimental results of the NLFC implementation under several scenarios of excitation level and velocity feedback gains.

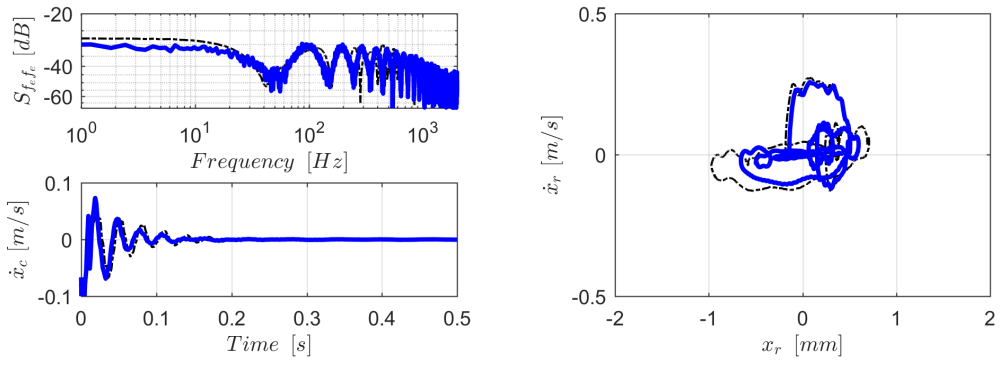

(a) (b)

FIGURE F.1: (a) Spectrum of the excitation force and time history of the velocity signal at the control point; (b) Phase-space trajectory of the relative proof mass displacement and velocity. Dash-dotted black line for the single VFC scenario using $h_s = 8\% h_{s,max}$ and solid blue line for the VFC+NLFC scenario using $h_s = 8\% h_{s,max}$.

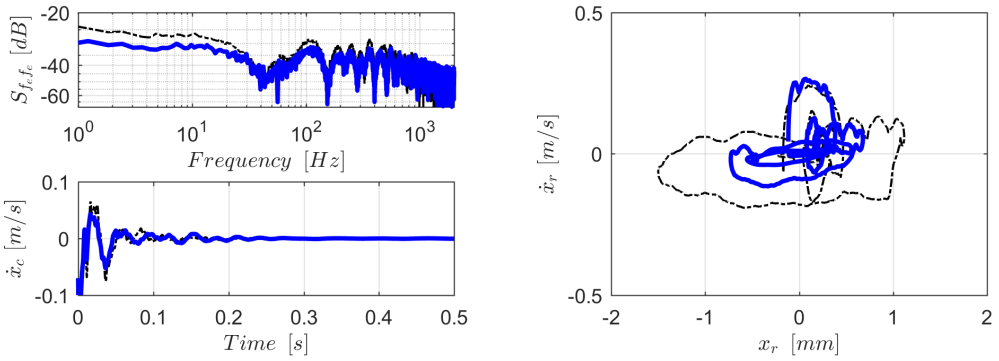

(a) (b)

FIGURE F.2: (a) Spectrum of the excitation force and time history of the velocity signal at the control point; (b) Phase-space trajectory of the relative proof mass displacement and velocity. Dash-dotted black line for the single VFC scenario using $h_s = 16\%h_{s,max}$ and solid blue line for the VFC+NLFC scenario using $h_s = 16\%h_{s,max}$.

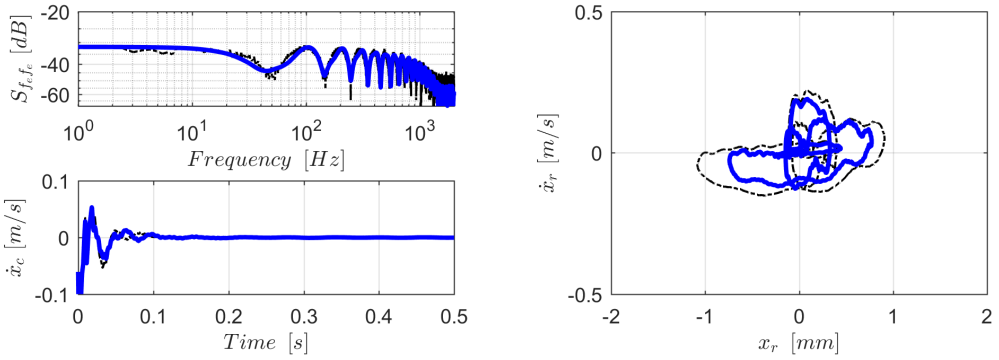

(a) (b)

FIGURE F.3: (a) Spectrum of the excitation force and time history of the velocity signal at the control point; (b) Phase-space trajectory of the relative proof mass displacement and velocity. Dash-dotted black line for the single VFC scenario using $h_s = 24\%h_{s,max}$ and solid blue line for the VFC+NLFC scenario using $h_s = 24\%h_{s,max}$.

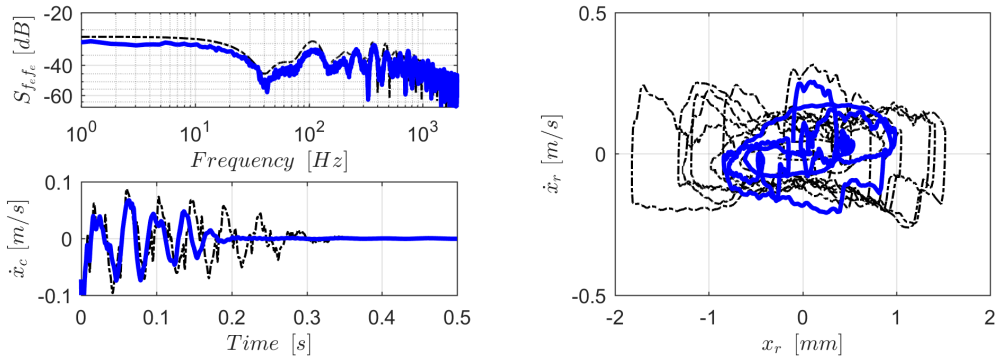

(a) (b)

FIGURE F.4: (a) Spectrum of the excitation force and time history of the velocity signal at the control point; (b) Phase-space trajectory of the relative proof mass displacement and velocity. Dash-dotted black line for the single VFC scenario using $h_s = 32\%h_{s,max}$ and solid blue line for the VFC+NLFC scenario using $h_s = 32\%h_{s,max}$.

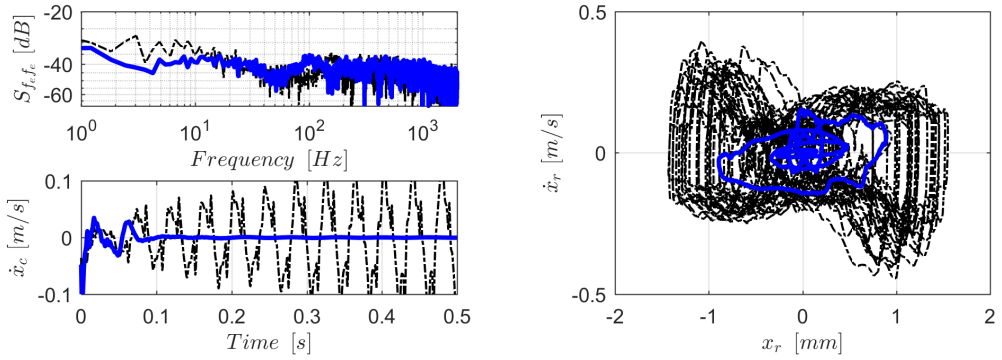

(a) (b)

FIGURE F.5: (a) Spectrum of the excitation force and time history of the velocity signal at the control point; (b) Phase-space trajectory of the relative proof mass displacement and velocity. Dash-dotted black line for the single VFC scenario using $h_s = 48\%h_{s,max}$ and solid blue line for the VFC+NLFC scenario using $h_s = 48\%h_{s,max}$.

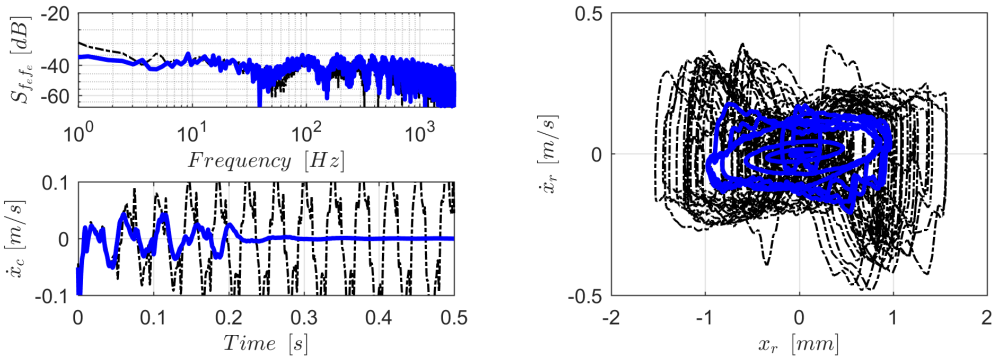

(a) (b)

FIGURE F.6: (a) Spectrum of the excitation force and time history of the velocity signal at the control point; (b) Phase-space trajectory of the relative proof mass displacement and velocity. Dash-dotted black line for the single VFC scenario using $h_s = 56\% h_{s,max}$ and solid blue line for the VFC+NLFC scenario using $h_s = 56\% h_{s,max}$.

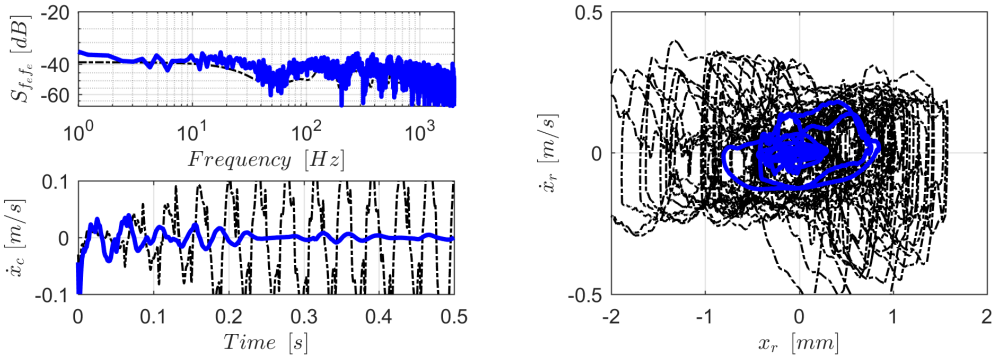

(a) (b)

FIGURE F.7: (a) Spectrum of the excitation force and time history of the velocity signal at the control point; (b) Phase-space trajectory of the relative proof mass displacement and velocity. Dash-dotted black line for the single VFC scenario using $h_s = 64\% h_{s,max}$ and solid blue line for the VFC+NLFC scenario using $h_s = 64\% h_{s,max}$.

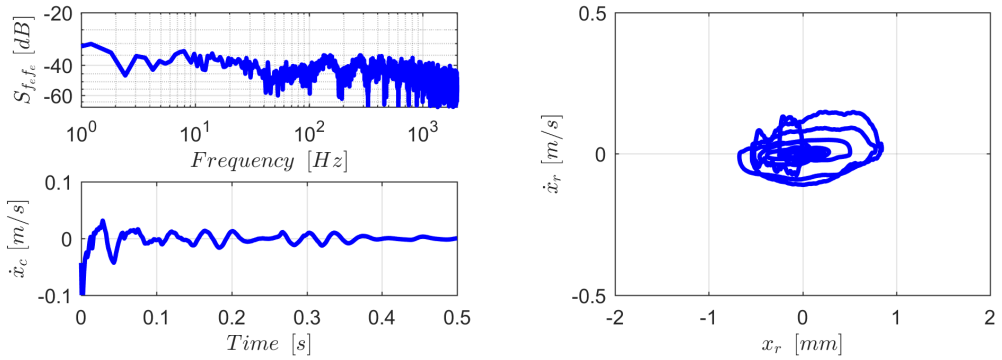

(a) (b)

FIGURE F.8: (a) Spectrum of the excitation force and time history of the velocity signal at the control point; (b) Phase-space trajectory of the relative proof mass displacement and velocity. Solid blue line for the VFC+NLFC scenario using $h_s = 72\% h_{s,max}$.

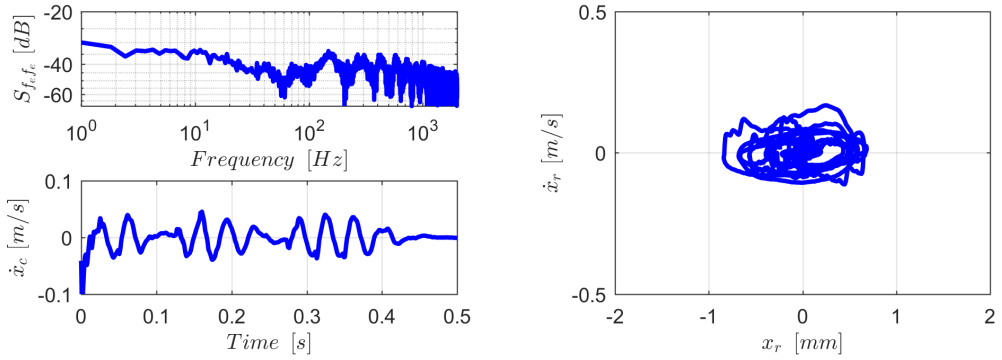

(a) (b)

FIGURE F.9: (a) Spectrum of the excitation force and time history of the velocity signal at the control point; (b) Phase-space trajectory of the relative proof mass displacement and velocity.Solid blue line for the VFC+NLFC scenario using $h_s = 80\% h_{s,max}$.

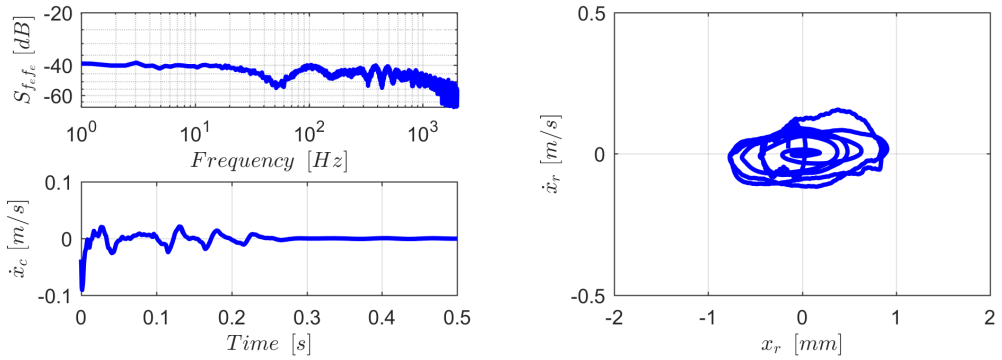

(a) (b)

FIGURE F.10: (a) Spectrum of the excitation force and time history of the velocity signal at the control point; (b) Phase-space trajectory of the relative proof mass displacement and velocity. Solid blue line for the VFC+NLFC scenario using $h_s = 88\% h_{s,max}$.

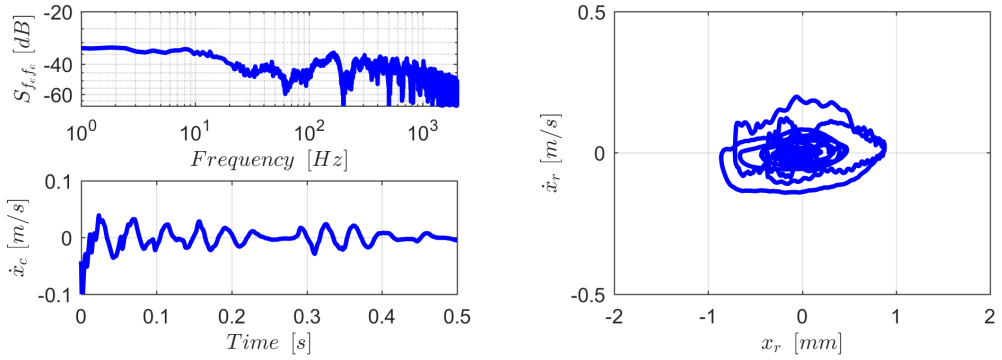

(a) (b)

FIGURE F.11: (a) Spectrum of the excitation force and time history of the velocity signal at the control point; (b) Phase-space trajectory of the relative proof mass displacement and velocity. Solid blue line for the VFC+NLFC scenario using $h_s = 96\% h_{s,max}$.

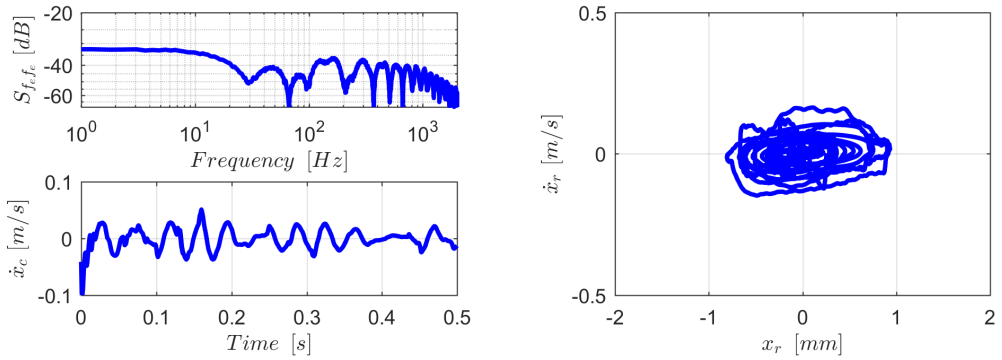

(a) (b)

FIGURE F.12: (a) Spectrum of the excitation force and time history of the velocity signal at the control point; (b) Phase-space trajectory of the relative proof mass displacement and velocity. Solid blue line for the VFC+NLFC scenario using $h_s = 104\% h_{s,max}$.

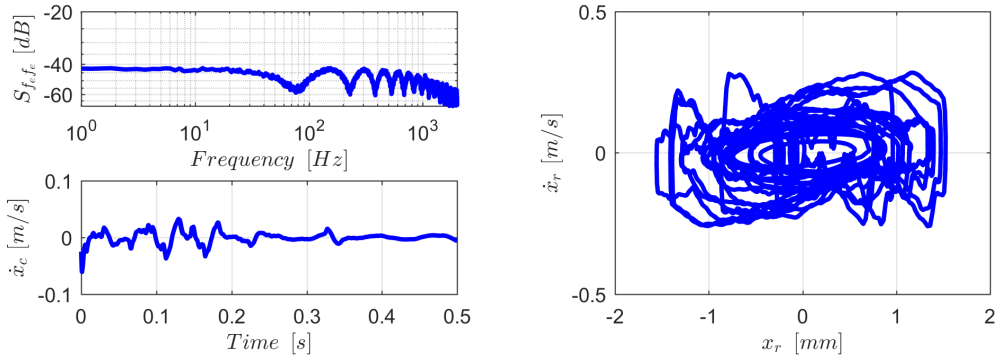

(a) (b)

FIGURE F.13: (a) Spectrum of the excitation force and time history of the velocity signal at the control point; (b) Phase-space trajectory of the relative proof mass displacement and velocity. Solid blue line for the VFC+NLFC scenario using $h_s = 112\% h_{s,max}$.